Alcohol Dehydrogenations Catalyzed by Iron(III) and Chromium(III) Catalysts

Hansen, Nicolai S.B.

Publication date:
2023

Document Version
Publisher's PDF, also known as Version of record

Alcohol Dehydrogenations Catalyzed by Iron(III) and Chromium(III) Catalysts

Ph.D. Thesis

Nicolai S.B. Hansen

May 2023

Department of Chemistry

Technical University of Denmark

Supervisor: Professor Robert Madsen

Co-supervisor: Professor Mads H. Clausen

Preface

This PhD thesis is the result of research performed between November 2019 and May 2023 at the Department of Chemistry, Technical University of Denmark, under the supervision of Professor Robert Madsen. Furthermore, three months were dedicated to conducting research at the Division of Theoretical Chemistry and Biology, KTH, Sweden, in the research group of Professor Mårten Ahlquist.

In addition to the work on the research project, coursework totaling 30 ECTS credits was completed, and mandatory teaching activities were undertaken. The research project was made possible through financial support provided by the Independent Research Fund Denmark.

Acknowledgements

First and foremost, I would like to thank Professor Robert Madsen for giving me the opportunity to conduct my research under his supervision.

I would like to extend my appreciation to past and present members of the research group for their camaraderie. A special thanks to Emil Krogh Nielsen for intellectual exchange related to the computational aspects of my research. Thanks to Fabrizio Monda, Frederik Simonsen Bro, Xiyue Liu and Sofie Latt Hjort Pedersen for providing valuable experimental results related to the projects described in this thesis.

I am grateful to the Department of Chemistry, DTU for providing me with resources and facilities to conduct my research. A special thanks to Charlie Johansen for technical assistance with the GC-MS and LC-MS instruments.

I would like to thank Professor Mårten Ahlquist for allowing me to conduct my external research stay in his research group at KTH in Stockholm. The techniques and insights I acquired throughout the stay have played a pivotal role in shaping the trajectory of this thesis.

I would like to acknowledge the funding provided by the Independent Research Fund Denmark.

Extremely sincere thanks to Bjarni Jørgensen for leaving me his bike, which provided me with a physically and mentally healthy way to commute from Nørrebro to DTU (when the weather allowed).

I am deeply thankful to my friends and family for their love and encouragement throughout this challenging endeavor. Their constant support and understanding have kept me afloat throughout this journey. A special thanks to Niels Andreas Bonde for proofreading and providing valuable feedback.

Lastly, it would be stupid not to thank Lea. You have been pretty great and I would not have completed this endeavor without your support. I should probably also mention Pelle, although he did not exactly act as a catalyst for the thesis-writing. Luckily, his cuteness makes up for it. Overall, I cannot wait to begin a new chapter with you two by my side.

Nicolai Steen Broberg Hansen
Copenhagen, May 2023

Abstract

In this thesis, new approaches to acceptorless alcohol dehydrogenation (AAD) with cheap and readily available Fe(III)- and Cr(III)-based catalysts have been investigated.

In the first project, an Fe(III)-salen catalyst system has been found effective for the coupling of benzylic alcohols and amines to yield imines. Previous members of the Madsen group have optimized the reaction parameters and performed mechanistic studies that indicated operation by homogeneous, molecular catalysis. Further mechanistic investigations have been conducted with Density Functional Theory (DFT) calculations, but insurmountable energy barriers have been calculated and poor correlation between the experimental and computational results have been observed.

To check for heterogeneous catalysis, poisoning studies with PMe_3 and Hg have been conducted and have shown inhibition of catalytic activity. Investigation of previously recorded LC-MS data and newly performed LC-MS studies have revealed extensive degradation of the Fe(III)-salen catalyst.

These control experiments have led to the conclusion that the catalytically active species are not molecular Fe(III)-salen derivatives but rather heterogeneous small iron particles as shown in Figure i.

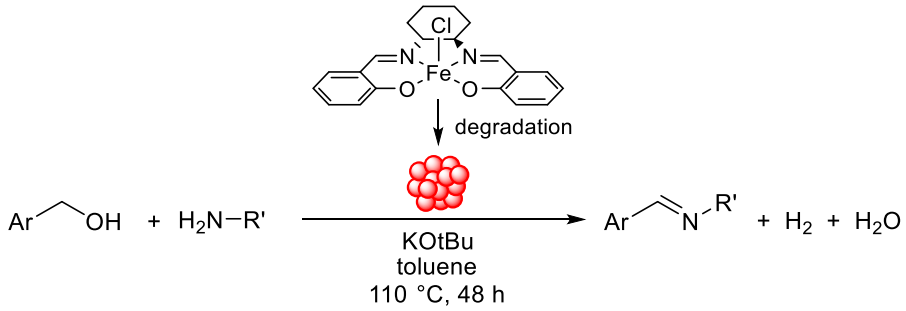

Figure i: Heterogeneous small iron particles have been suggested as the most likely catalyst for the coupling of benzylic alcohols and amines.

Despite endeavors to isolate and characterize these presumed catalyst particles, no success has been achieved.

In the second project, attempts to develop the AAD reaction between benzyl alcohol and cyclohexylamine using Cr(III)-salen and Cr(III)-salan catalysts have been described. After extensive optimization of reaction parameters, a maximum imine yield of only 30% has been achieved.

No evolution of hydrogen gas during the reaction has been detected and therefore, no AAD pathway has been discovered. Control experiments conducted under an air atmosphere have revealed that aerobic oxidation can be a significant side reaction, which may explain the high imine yields that have been reported in previous iterations of the Cr(III)-salen project.

LC-MS studies have confirmed the reduction Cr(III)-salen to Cr(III)-salan and provided evidence of catalyst dimerization. Furthermore, DFT calculations have been employed to

investigate different reaction mechanisms and catalyst derivatives, but no low-energy AAD pathways have been identified. Highly stable alkoxo-Cr(III)-salan intermediates have been suggested as resting states that inhibit catalytic activity.

In the last chapter, a previously published AAD protocol using a Cr(III)(TPP)Cl catalyst has been revisited. DFT calculations have been used to study the energetics of several proposed reaction mechanisms, but no low-energy pathways have been identified.

Repetition of key experiments from the paper under carefully controlled conditions has resulted in imine yields ranging from 15-20%, in contrast to the 60-86% reported in the original paper. Furthermore, no evolution of hydrogen gas has been detected during the reactions. Lastly, performing the reactions under an air atmosphere have revealed that aerobic oxidation can be a significant side reaction, leading to the high imine yields and formation of byproducts. Examination of several old chromatograms associated with the original paper has revealed the presence of these byproducts, suggesting that the presence of air may have led to erroneous conclusions in the original paper.

Resume

I denne afhandling er der blevet undersøgt nye metoder til oxidation af alkoholer under frigivelse af brint, også kaldet acceptorløs alkohol dehydrogenering (AAD). Katalysatorer baseret på jern og chrom er blevet undersøgt, da disse metaller er billige og lettilgængelige.

I det første projekt er en Fe(III)-salen katalysator blevet brugt til at syntetisere iminer ud fra benzyliske alkoholer og aminer. Tidligere studerende i Madsen-gruppen har optimeret reaktionsbetingelserne og udført mekanistiske undersøgelser, der indikerede, at der var tale om homogen, molekylær katalyse. Yderligere studier af mulige reaktionsmekanismer er blevet udført ved hjælp af Density Functional Theory (DFT) beregninger, men de beregnede energibarrierer er fundet uoverkommelige under reaktionsbetingelserne. Desuden er der udvist utilfredsstillende sammenhæng mellem de eksperimentelle og beregnede resultater.

For at undersøge om det katalytiske system opererer homogent eller heterogent er der udført forgiftningsstudier med PMe_3 og Hg, som begge resulterede i hæmning af den katalytiske reaktion. Desuden har undersøgelse af det katalytiske system med LC-MS afsløret at Fe(III)-salen katalysatoren nedbrydes under reaktionsbetingelserne.

Disse forsøg har ført til den konklusion, at den aktive katalysator ikke er molekylære Fe(III)-salen komplekser, men derimod jernpartikler, som vist i Figur ii. Det er imidlertid ikke lykkes at isolere og karakterisere disse katalysatorpartikler.

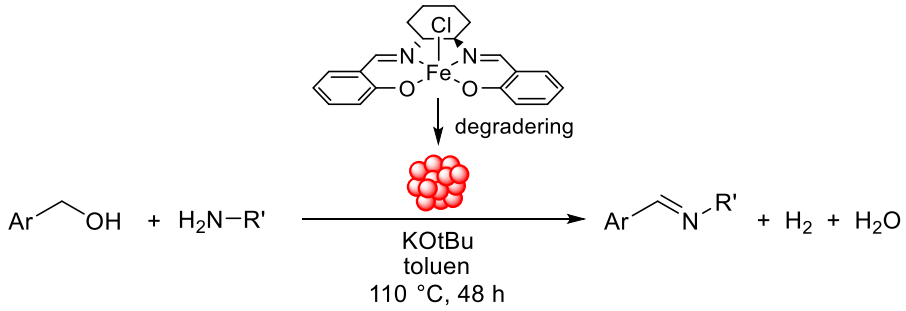

Figur ii: Jernpartikler, der dannes ved degradering af den oprindelige katalysator, er blevet foreslået som den aktive katalysator, der katalyserer koblingen mellem benzyliske alkoholer og aminer.

I det andet projekt er forsøget på at udvikle en Cr(III)-katalyseret AAD-reaktion mellem benzylalkohol og cyclohexylamin blevet beskrevet. Efter omfattende optimering af reaktionsbetingelserne er et udbytte på maks. 30% blevet realiseret.

Udvikling af brint under reaktionen er ikke blevet påvist, så der er ikke tale om en AAD-reaktion. Reaktionen er desuden blevet foretaget med tilstedeværelse af atmosfærisk luft, hvilket resulterede i markant højere udbytter. Dermed er oxidation med ilt en betydelig sidereaktion.

Forsøg med LC-MS har bekræftet at Cr(III)-salen komplekserne reduceres til Cr(III)-salan komplekser under reaktionsbetingelserne, og der er fundet evidens for dimerisering af disse komplekser.

Derudover er der blevet anvendt DFT-beregninger til at undersøge forskellige reaktionsmekanismer, men de beregnede energibarrierer er høje, hvilket kan forklare den

manglende reaktivitet. Alkoxo-Cr(III)-salan komplekser er blevet foreslået som yderst stabile komplekserne, der hæmmer den katalytiske aktivitet.

I det sidste kapitel er en tidligere udviklet AAD-reaktion, der gør brug af en anden Cr(III)-baseret katalysator, blevet undersøgt. DFT-beregninger er blevet brugt til at undersøge energierne for flere foreslåede reaktionsmekanismer, men de beregnede energibarrierer er generelt for høje.

Gentagelse af eksperimenter fra det tidligere studie under nøje kontrollerede betingelser har resulteret i lave udbytter mellem 15-20%, hvilket står i kontrast til de 60-86%, der blev rapporteret i den oprindelige artikel. Desuden har det ikke været muligt at påvise udvikling af brintgas under reaktionerne. Til slut har udførelsen af reaktionerne under atmosfærisk luft afsløret at oxidation med ilt kan være en betydelig sidereaktion, der kan føre til højere udbytter og dannelse af sideprodukter. Undersøgelse af flere gamle kromatogrammer, der blev optaget til den oprindelige artikel, har afsløret tilstedeværelsen af disse sideprodukter. Dermed er det fundet sandsynligt, at tilstedeværelsen af ilt kan have ført til højere udbytter i det oprindelige studie.

Table of contents

Preface i

Acknowledgements iii

Abstract v

Resume vii

List of Abbreviations xi

Chapter 1. Introduction **1**

1.1. Green chemistry 2

1.2. Derivatization of alcohols by acceptorless alcohol dehydrogenation (AAD) 4

1.3. Early examples of AAD catalysis 5

1.4 A new wave of catalysts: metal-ligand cooperation and bifunctionality 8

1.5 DFT investigations of (de)hydrogenative transformations 15

Chapter 2. AAD catalyzed by Fe(III)-salen catalysts **18**

2.1. Introduction 19

2.2. Previous work on Fe(III)-salen AAD catalysis in the Madsen group 28

2.3. Computational investigation of the catalytic cycle 35

2.4. Return to the laboratory: additional control experiments and investigations 48

2.5. Conclusion 57

2.6. Experimental 59

Chapter 3. Development of AAD reactions catalyzed by Cr(III)-salen and Cr(III)-salan complexes **75**

3.1. Introduction 76

3.2. Previous work on Cr(III)-salen catalysis performed in the Madsen group 82

3.3. First round of Cr(III)-salen experimental investigations 83

3.4. Synthesis of Cr(III)-salen and Cr(III)-salan derivatives 88

3.5. Second round of Cr(III)-salen and Cr(III)-salan experimental investigations 93

3.6. Computational investigation of the catalytic cycle 115

3.7. Conclusion 130

3.8. Experimental 131

Chapter 4. Revisiting alcohol oxidation catalyzed by Chromium(III) Tetraphenylporphine Chloride **169**

4.1. Introduction 170

4.2. Computational study of the CrTPP catalytic cycle 173

4.3. Repetition of experiments 177

4.4. Conclusion 180

4.5. Experimental 181

Conclusions and outlook **188**

Publications **190**

Bibliography **191**

List of Abbreviations

AAD	Acceptorless alcohol dehydrogenation
Ac	Acetyl
Acac	Acetylacetonate
AE	Atom economy
Ar	Aryl
Bn	Benzyl
Cat	Catalyst
CCDC	Cambridge Crystallographic Data Center
COD	1,5-Cyclooctadiene
CSA	Camphorsulfonic acid
Cy	Cyclohexyl
Cyp	Cyclopentyl
d	Doublet
DBU	1,8-Diazabicyclo[5.4.0]undec-7-ene
DCE	Dichloroethane
DCM	Dichloromethane
Deut	Deuterated
DFT	Density functional theory
DIBAL	Diisobutylaluminium
DMAP	4-Dimethylaminopyridine
DMF	Dimethylformamide
DMP	Dess-Martin periodinane
E	Environmental factor or energy
EDG	Electron donating group
EI	Electron ionization
EIC	Extracted ion chromatogram
eq.	Equivalent(s) or equation
ESI	Electrospray ionization
ESR	Electron spin resonance
Et	Ethyl
EWG	Electron withdrawing group
FTIR	Fourier-Transform Infrared Spectroscopy
GC	Gas chromatography
GC-MS	Gas chromatography-mass spectrometry
HMDS	Hexamethyldisilazane
HPLC	High-performance liquid chromatography
HS	High spin
iPr	Isopropyl
IS	Intermediate spin or internal standard
J	Coupling constant
KIE	Kinetic isotope effect
LC-MS	Liquid chromatography–mass spectrometry

LS	Low spin
m	Multiplet
m/z	Mass over charge number of ions
Me	Methyl
MLC	Metal-ligand cooperation
MS	Mass spectrometry or molecular sieves
NMR	Nuclear magnetic resonance
NSBH	Nicolai Steen Broberg Hansen
OTf	Triflate
PCC	Pyridinium chlorochromate
PDC	Pyridinium dichromate
Ph	Phenyl
ppm	Parts per million
PPNO	4-Phenylpyridine *N*-oxide
PPN	Bis(triphenylphosphine)iminium
Prot	Protonated
q	Quartet
rt.	Room temperature
s	Singlet
SLHP	Sofie Latt Hjort Pedersen
STEM	Scanning transmission electron microscopy
t	Triplet
tBu	Tert-butyl
TEMPO	(2,2,6,6-Tetramethylpiperidin-1-yl)oxyl
THF	Tetrahydrofuran
TIC	Total ion chromatogram
TPP	Tetraphenylporphyrin or tetraphenylporphine
TS	Transition state
UV	Ultraviolet
VIS	Visible
ZPE	Zero-point energy
δ	Chemical shift
Δ*G*	Change in Gibbs free energy
Δ*H*	Change in enthalpy
Δ*S*	Change in entropy

Chapter 1. Introduction

Abstract

In this chapter, several concepts related to acceptorless alcohol dehydrogenations have been introduced. The importance of green chemistry and increasing the sustainability of chemical transformations have been underscored, and acceptorless alcohol dehydrogenations have been advocated as an important transformation that has the potential to lead to a wide range of value-added products.

Different early approaches to acceptorless alcohol dehydrogenations have been outlined, relying mainly on Ru-catalysis. The concept of metal-ligand cooperation (MLC) has been introduced, and different mechanisms related to the MLC strategy have been outlined. Furthermore, a range of catalyst systems relying on MLC have been introduced, with a particular focus on catalytic systems employing cheap and readily available base-metals such as Co and Mn.

Lastly, a few studies using Density Functional Theory (DFT) calculations to substantiate reaction mechanisms have been highlighted. Special attention has been given to a previously reported Mn(III)-salen system,[1] as this study has shaped the research presented later in this thesis.

1.1. Green chemistry

Chemists have increasingly recognized the impact of chemical processes on the environment and human health, giving rise to sustainable chemistry, also known as green chemistry. The goal of green chemistry is to minimize the harmful effects of chemical production, usage, and disposal by designing sustainable chemical products and processes.

In 1998, Anastas and Warner introduced the 12 principles of green chemistry.[2] These are outlined and explained below.

1. *Prevention:* It is better to prevent waste generation and environmental pollution than clean up afterwards.
2. *Atom economy:* Maximizing the efficiency of chemical reactions by designing processes that use all the starting materials, minimizing waste generation.
3. *Less hazardous chemical syntheses:* Designing and using synthetic methods that minimize or eliminate the use of toxic substances.
4. *Designing safer chemicals:* Developing and using chemical products that have reduced toxicity.
5. *Safer solvents and auxiliaries:* Using safer solvents and auxiliary reagents in chemical reactions to minimize their environmental impact.
6. *Design for energy efficiency:* Designing chemical processes that are energy-efficient and minimize energy consumption.
7. *Use of renewable feedstocks:* Utilizing renewable raw materials and feedstocks in chemical synthesis to reduce reliance on non-renewable resources.
8. *Reduce derivatives:* Minimizing the use of unnecessary derivatization steps in chemical reactions, which can lead to increased waste generation.
9. *Catalysis:* Maximizing the use of catalysts to increase reaction rates.
10. *Design for degradation:* Designing chemical products that break down into non-toxic substances after their use.
11. *Real-time analysis for pollution prevention:* Developing and implementing real-time monitoring and control techniques to prevent the formation and release of hazardous substances.
12. *Inherently safer chemistry for accident prevention:* Designing chemical processes and products to minimize the potential for accidents.

These principles serve as a guideline for promoting sustainable practices in the field of chemistry, aiming to minimize the environmental impact and improve the overall sustainability of chemical processes.

The 2nd principle raises the point of atom economy (AE),[3] and a related metric is the environmental factor (E).[4,5] These metrics are used to evaluate the sustainability of chemical reactions or processes and are calculated as shown in Eq. (1) and Eq. (2)

$$AE = \frac{M_w\ of\ product}{M_w\ of\ reagent(s)} \cdot 100\% \qquad \textbf{Eq. (1)}$$

$$E = \frac{Total\ mass\ of\ waste}{Mass\ of\ final\ product} \qquad \textbf{Eq. (2)}$$

The AE of a given reaction can be easily calculated from the reaction scheme and a couple of examples are given in Figure 1.1.

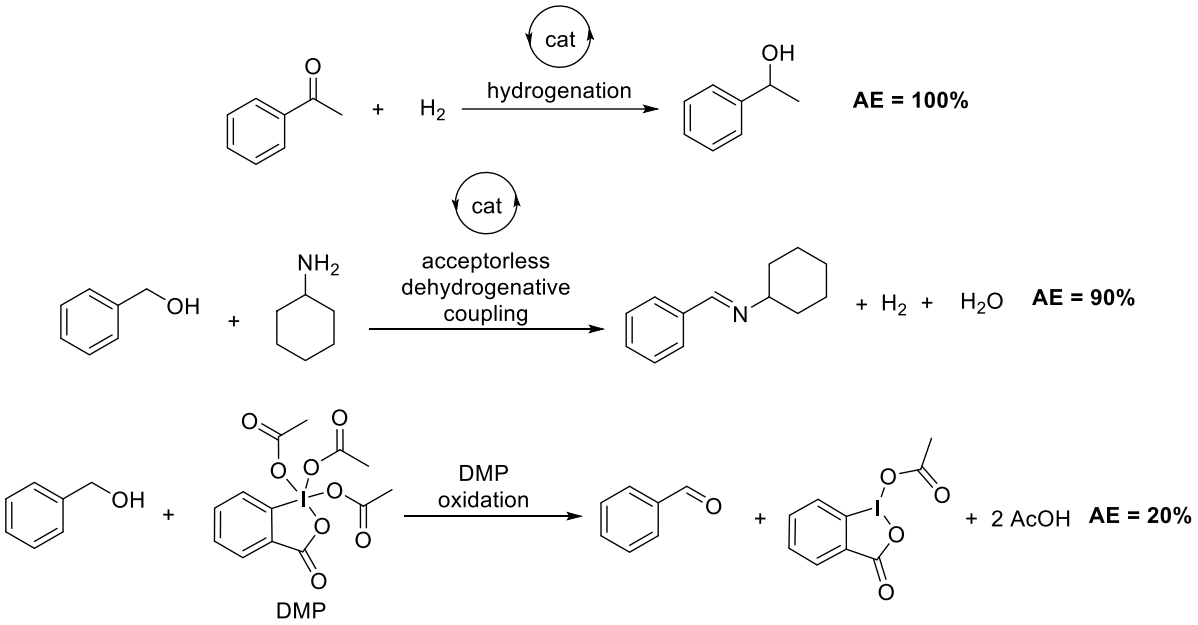

Figure 1.1: Both catalytic hydrogenation and acceptorless dehydrogenative coupling are processes with a high atom economy. Alcohol oxidation with DMP has a lower atom economy as the atoms of the DMP reagent are not utilized in the final product.

Evidently, the catalytic hydrogenation and the acceptorless dehydrogenative coupling to form imines present high AEs in the 90-100% range, whereas the oxidation of benzyl alcohol with Dess-Martin periodinane (DMP) presents an AE of only 20%. These examples highlight how catalysis, the 9th principle of green chemistry, enables effective utilization of atoms. As such, catalytic pathways typically result in reduced waste generation, as opposed to approaches relying on stoichiometric addition of reagents.

Importantly, the AE metric fails to account for solvents that may be used in the reaction or waste generation related to the work-up of the reaction. Consequently, the E-factor has been introduced, where the total mass of generated waste is considered in relation to the mass of the final product.[4,5] The E-factor is more laborious to calculate as careful assessment of the generated waste throughout the whole process is required. However, it is safe to say that reactions involving work-up procedures such as flash column chromatography may not exhibit favorable E-factors due to excessive solvent consumption.

The research conducted in this thesis delves into catalytic derivatization of alcohols. In the following section, the derivatization of alcohols by acceptorless alcohol dehydrogenation (AAD) is outlined.

1.2. Derivatization of alcohols by acceptorless alcohol dehydrogenation (AAD)

Alcohols are ubiquitous in nature and a commonly encountered functional group in synthetic organic chemistry. Importantly, a range of alcohols can be obtained from various renewable resources, such as biomass. It is therefore important to recognize the potential of alcohols as a sustainable starting material in the development of green chemical processes.

New methodologies for efficient and sustainable conversion of inexpensive, simple alcohols into value-added products are continuously sought. One of the preferred derivatizations of alcohols is based on oxidation. Several methodologies relying on addition of stoichiometric oxidants such as $KMnO_4$[6] or Dess-Martin periodinane[7] have long been preferred, but the generation of stoichiometric waste presents an important drawback of these methods.

In response, chemists have been actively pursuing the development of sustainable methods for alcohol oxidations. Among these methods, AAD stands out as a promising pathway as AAD results in alcohol oxidation with H_2 as the sole byproduct. Several reagents can be used in conjunction with the AAD transformation, which allows transformation of alcohols into a wide range of value-added products such as esters, carboxylic acids, amides, amines, and imines. A range of general pathways are shown in Figure 1.2.

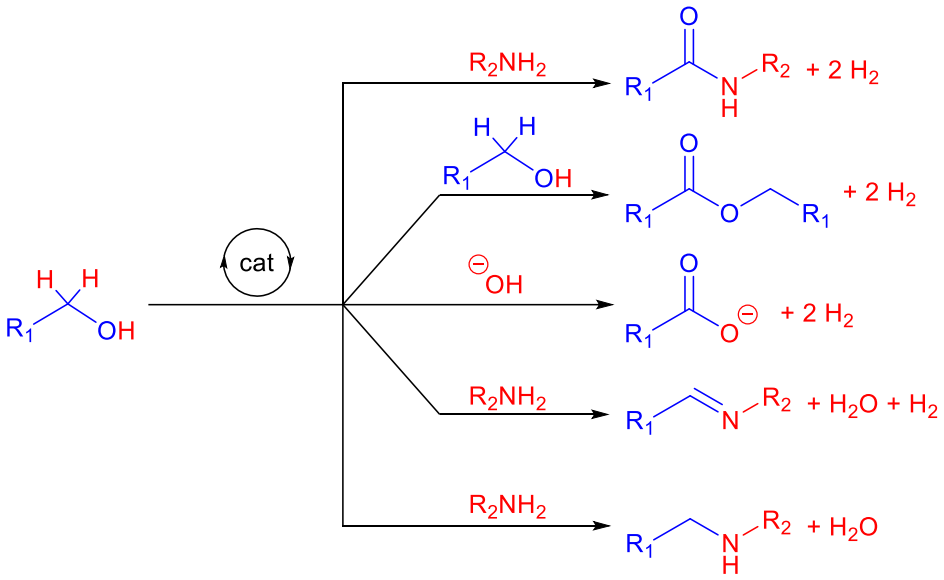

Figure 1.2: Dehydrogenative transformations of alcohols can lead to a variety of value-added products.

Evidently, the only byproduct is hydrogen gas, and occasionally water, which are environmentally benign byproducts. Therefore, transformations relying on the AAD methodology generally provide a more sustainable approach to alcohol derivatization.[8–10]

The projects described later in this thesis have primarily focused on the development of catalytic AAD pathways that enable coupling of primary alcohols with primary amines. A range of different products can be envisioned depending on the employed catalyst and reaction conditions. These pathways are elaborated in Figure 1.3.

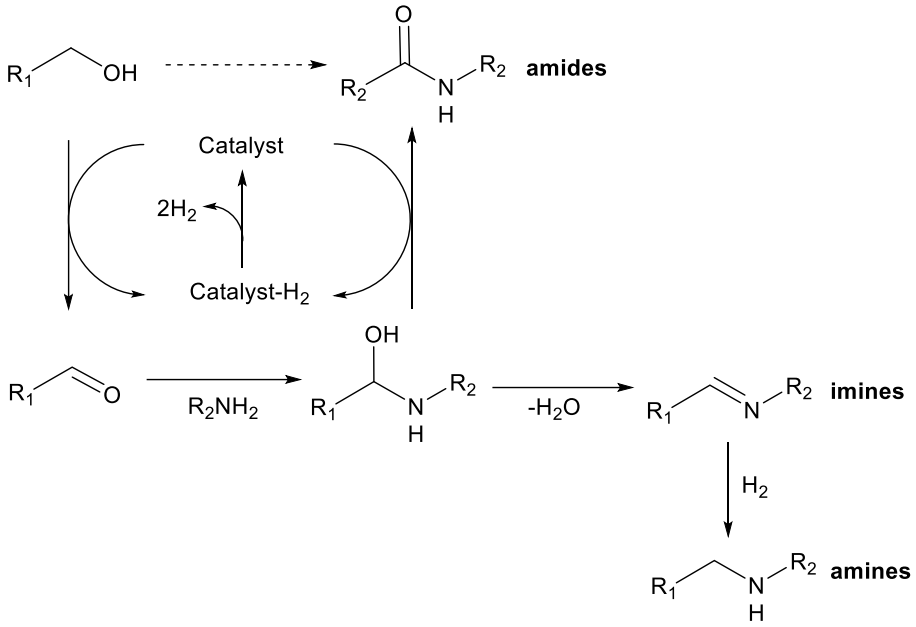

Figure 1.3: Acceptorless dehydrogenative coupling between alcohols and amines can result both in amides, imines and amines depending on the catalyst.

The coupling of aldehyde and amine leads to the formation of a hemiaminal, which can undergo two different reactions. In one pathway, the hemiaminal can be further transformed into an amide through a second dehydrogenative process. Alternatively, the hemiaminal can undergo dehydration to yield an imine as the final product. The last possible route involves hydrogenation of the imine, resulting in the formation of an amine coupling product. The last process is commonly referred to as hydrogen autotransfer or borrowing hydrogen.[11]

Ultimately, the AAD methodology can enable sustainable conversion of alcohols into a diverse array of functional groups. The following section will outline some of the catalyst systems that were developed during the early stages of AAD catalysis.

1.3. Early examples of AAD catalysis

Some of the early examples of AAD catalysis were realized using catalysts based on Ru and Rh. Figure 1.4 outlines two protocols developed by the Morton group in the late 1980s.[12,13]

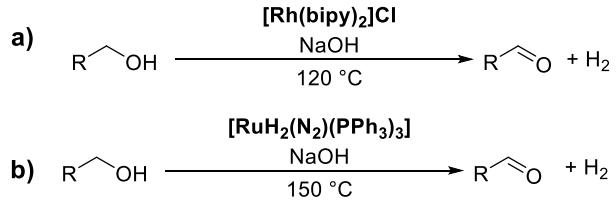

Figure 1.4: Early examples of acceptorless alcohol dehydrogenation catalyzed by Ru and Rh-complexes.[12,13]

The Morton group found that simple Rh and Ru-complexes were able to dehydrogenate small, aliphatic alcohols such as ethanol and isopropanol when heated in the presence of NaOH. However,

in the Rh-based protocol, byproducts stemming from aldol-type reactions and decarbonylations were observed, which limited the synthetic applicability of the protocol.

In the mid-2000s, several research groups progressed the field of dehydrogenative transformations catalyzed with Ru. Two notable examples of Ru-based AAD catalysis were developed in the Beller and Madsen group.[14–16] The protocols are shown in Figure 1.5.

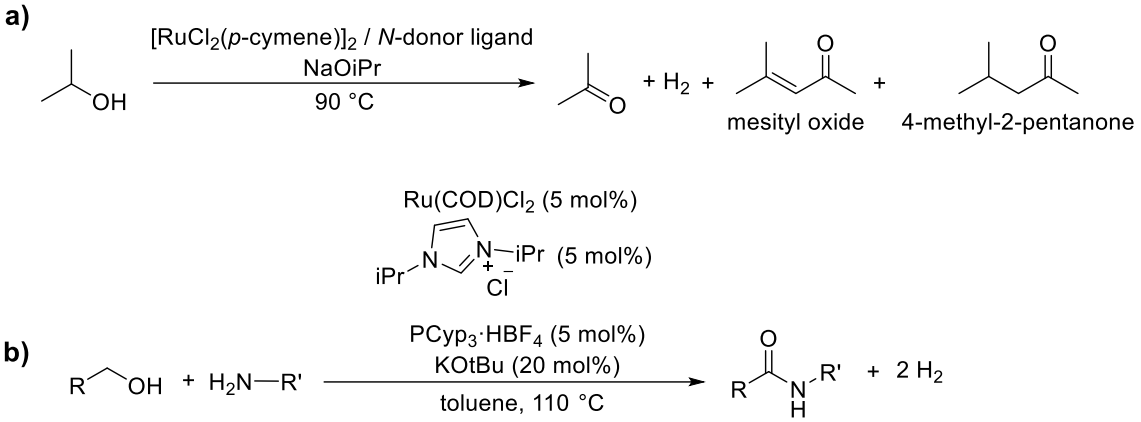

Figure 1.5: **a)** Ru-based acceptorless dehydrogenation of isopropanol developed in the Beller group.[14] **b)** Protocol for dehydrogenative coupling of alcohols and amines to form amides developed in the Madsen group.[15]

Figure 1.5 **a)** shows the protocol developed in the Beller group.[14] Isopropanol was efficiently dehydrogenated by a mixture of $[RuCl_2(p\text{-cymene})]_2$ and an *N*-donor ligand in the presence of strong base. No comments on the nature of the active catalyst or the reaction mechanism were made, and aldol-type byproducts were observed.

Figure 1.5 **b)** shows how dehydrogenative amide synthesis from alcohols and amines were achieved in the Madsen group.[15] Mixing a Ru(II)-salt, an *N*-heterocyclic carbene (NHC) precursor, a phosphine ligand and KOtBu results in an active catalyst system that effectively couples alcohols and amines to form amides. Later, Madsen and coworkers isolated an active Ru-catalyst employing an NHC ligand.[16] This catalyst was subsequently used to extend the applicability of the Ru-NHC-system to include dehydrogenative synthesis of carboxylic acids[17], imines[18], esters[19] and self-coupling of primary and secondary alcohols.[20] These findings highlight the multiple pathways of alcohol derivatization made possible by dehydrogenative transformations.

The operative reaction mechanism in the early examples of AAD catalysis with Ru-based systems has been widely investigated and two different pathways are commonly invoked.[21–24] The two pathways are shown in Figure 1.6.

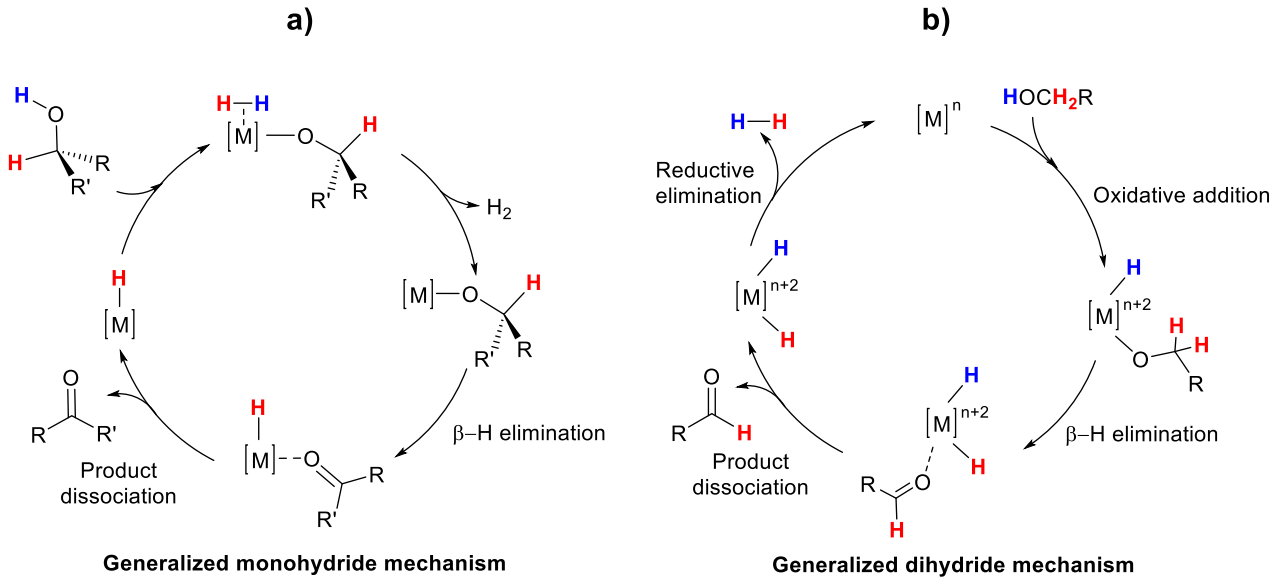

Figure 1.6: **a)** Acceptorless alcohol dehydrogenation by an inner-sphere monohydride mechanism. **b)** Acceptorless alcohol dehydrogenation by an inner-sphere dihydride mechanism.

Most importantly, the dihydride mechanism relies on oxidative addition of the O–H bond and reductive elimination of the [M]–H bond, which leads to cycling between different oxidation states of the metal-center. Furthermore, the identity of the C_α–H and O–H hydrogens is lost during the dihydride mechanism, which leads to scrambling of the C_α–H and O–H protons. This effect becomes observable in mechanistic studies with deuterated substrates.[24]

Conversely, the monohydride mechanism relies on heterolytic bond cleavages to facilitate dehydrogenation. Here, β-hydride elimination from a metal-alkoxo intermediate results in a monohydrido intermediate, that releases H_2 upon protonation by an alcohol. No scrambling of the C_α–H and O–H protons can occur during this catalytic cycle and the two possible mechanisms can therefore be distinguished by employing deuterium-labelled substrates.

Indeed, the Madsen group conducted a thorough mechanistic investigation of the Ru-NHC catalyzed coupling of alcohols and amines to amides.[25] Experiments with deuterium-labelled substrates revealed H/D scrambling suggesting a dihydride mechanism and NMR spectroscopic evidence of dihydrido intermediates was obtained. Furthermore, the kinetic isotope effect (KIE) was measured to 2.29, a Hammett plot with a small negative slope of ρ = -0.15 was constructed and a DFT-calculated catalytic cycle with an energy span of 28.4 kcal mol^{-1} supported the experimental findings adequately.[25] This work demonstrated how several physical organic methods and DFT calculations can work in tandem to support a hypothesized reaction mechanism and the strategies employed in this work have shaped the work presented later in this thesis.

Conclusively, the early examples of AAD catalysis spurred much interest in the development of metal-catalyzed dehydrogenative transformations. So far, the presented protocols featured ligands that merely acted as spectators, stabilizing the metal-center, but not actively partaking in bond-formation or bond-breakage. With increased focus on developing efficient catalysts for dehydrogenative transformations, new strategies and ligand scaffolds arose. One of the most important strategies employs the concept of metal-ligand cooperation (MLC) to enable efficient heterolytic bond cleavages. The MLC concept will be further explored in the coming section.

1.4. A new wave of catalysts: metal-ligand cooperation and bifunctionality

In the classical metal catalysis paradigm, all key transformations happen solely at the metal-center with the ligands acting as spectators. However, an alternative to this paradigm was offered with the advent of metal-ligand cooperative (MLC) catalysts. The MLC strategy typically relies on a Lewis acidic metal-center collaborating with a Brønsted base functionality on the ligand. The proximity of the proton-responsive Brønsted base and the Lewis acidic metal-center enables efficient polarizing of challenging substrates such as H_2, which makes heterolytic cleavages the preferred pathway. Consequently, the MLC strategy has found wide success in both hydrogenative and dehydrogenative transformations.[26]

Before providing examples of a range of catalyst systems employing the MLC strategy, the commonly invoked AAD reaction mechanisms in the MLC paradigm will be outlined in the coming section.

1.4.1. Different AAD reaction mechanisms using the MLC strategy

Different reaction mechanisms have been proposed to describe AAD catalysis employing the MLC strategy. Figure 1.7 illustrates three generalized reaction mechanisms that provide an overview of the key steps that can be envisioned in the MLC paradigm.[10,21,27]

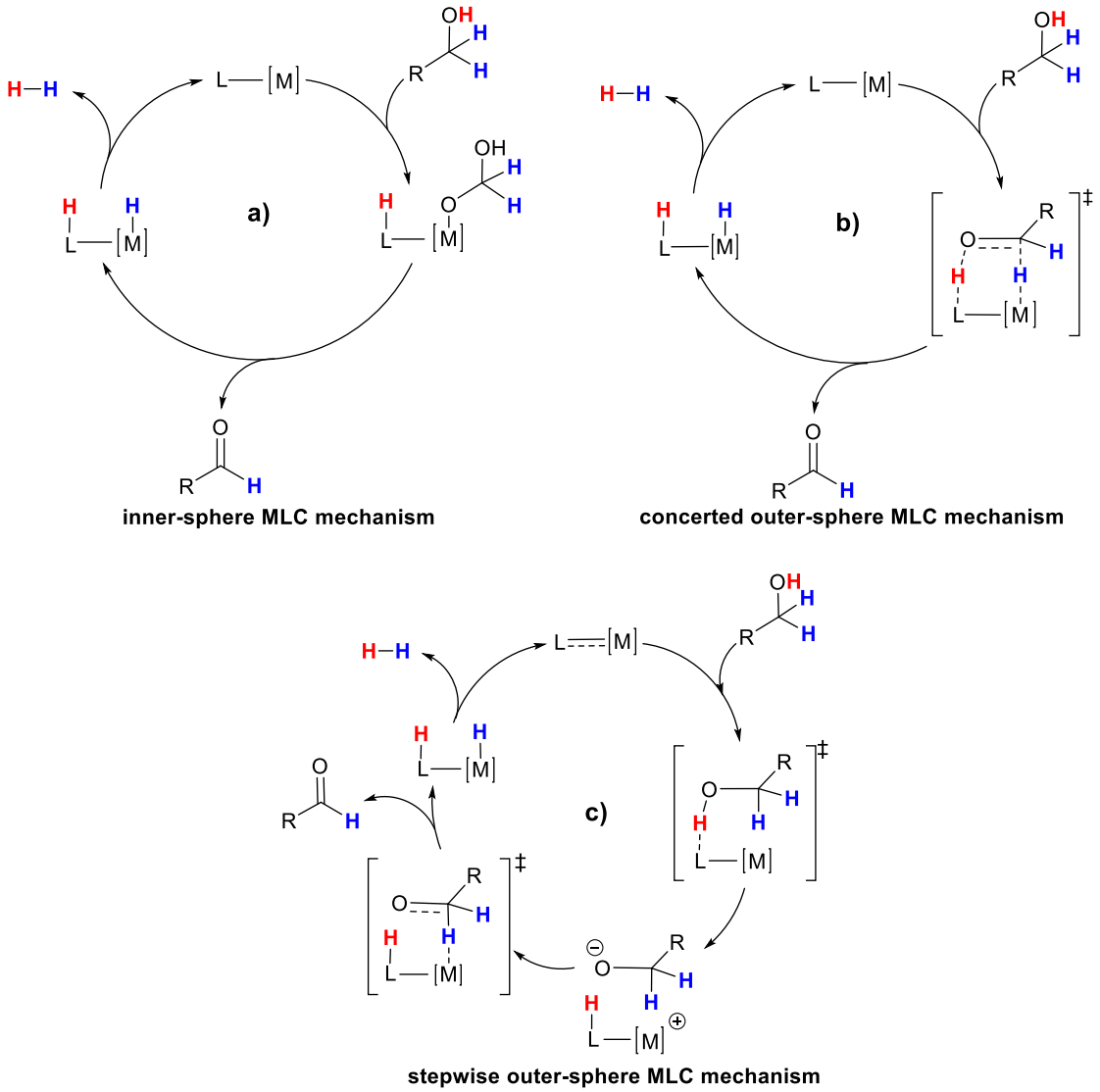

Figure 1.7: **a)** Inner-sphere MLC mechanism with formation of metal-alkoxo intermediate. **b)** AAD following a concerted outer-sphere MLC mechanism **c)** AAD by a stepwise outer-sphere MLC mechanism.

In the inner-sphere MLC mechanism (Figure 1.7 **a)**), the alcohol is deprotonated by the proton-responsive group of the ligand and a metal-alkoxo intermediate is formed. The C_{α}–H bond is subsequently cleaved by a traditional *β*-hydride elimination, leading to the oxidized product and a $H^{+}H^{-}$ pair on the catalyst. Release of H_2 sets up the catalyst for another cycle.

One caveat of the inner-sphere MLC mechanism is that the *β*-hydride elimination typically requires a vacant coordination site. This requirement can potentially limit the range of ligand scaffolds and metals that can operate by this reaction mechanism. For example, catalysts that employ the planar, tetradentate salen scaffold are not expected to perform alcohol oxidation by traditional *β*-hydride eliminations as no vacant coordination sites are readily available due to the salen *O,N,N,O* donor set.[1]

The alternative to an inner-sphere mechanism is an outer-sphere mechanism, that can be further divided into a "concerted outer-sphere" and a "stepwise outer-sphere" MLC mechanism. In the concerted outer-sphere mechanism (Figure 1.7 **b)**), the H^+H^- pair is transferred from the alcohol to the MLC catalyst in a 6-membered transition state. Therefore, no formation of a metal-alkoxo intermediate is predicted. The concerted transfer of the H^+H^- pair from an alcohol was first hypothesized in studies of Ru-catalyzed transfer hydrogenations by Noyori and Ikariya.[28,29] Later, thorough mechanistic investigations employing both DFT-calculations and KIE measurements found compelling evidence in favor of the concerted outer-sphere mechanism.[30–32]

The last noteworthy MLC mechanism is the stepwise outer-sphere mechanism (Figure 1.7 **c)**), that has been advocated by Dub and Gordon as a viable alternative to the concerted mechanism.[33–36] In this mechanism, the transfer of H^+ and H^- is asynchronous. As such, the initial step is the deprotonation of the alcohol, but instead of forming a metal-alkoxo intermediate, an ion-pair is formed. The envisioned ion-pair is stabilized by Coulombic interactions, L – H$\cdots$O$^-$ hydrogen-bonding and an agostic C – H$\cdots$ M$^+$ interaction. From this ion-pair, the C_α–H bond is heterolytically cleaved to give the oxidized product and the H^+H^- pair on the catalyst. This mechanism is likely preferred in polar and protic solvents that effectively stabilize charge-separated species.[35]

Ultimately, several reaction mechanisms for AAD are possible within the MLC paradigm, and it can be extremely difficult to distinguish between them experimentally. Therefore, DFT calculations are routinely applied to unravel the preferred reaction pathways in catalytic cycles. Section 1.5 will provide a brief introduction to the application of DFT calculations in AAD catalysis. However, before diving into that, some early examples of AAD catalysis utilizing the MLC strategy will be explored.

1.4.2. Early examples of AAD catalysis using the MLC strategy

RuPNP1 employs a PNP pincer ligand and is a classic example of a bifunctional catalyst that achieves efficient AAD by employing the MLC strategy. The catalyst was developed in the Beller group and found efficient for dehydrogenation of methanol,[37] isopropanol[38] and dehydrogenative synthesis of ethyl acetate from ethanol.[39] Furthermore, both a range of mechanistic experiments and DFT calculations indicated that breakage of the C_α–H bond happens in the inner-sphere of Ru.[40] The developed protocols are shown in Figure 1.8.

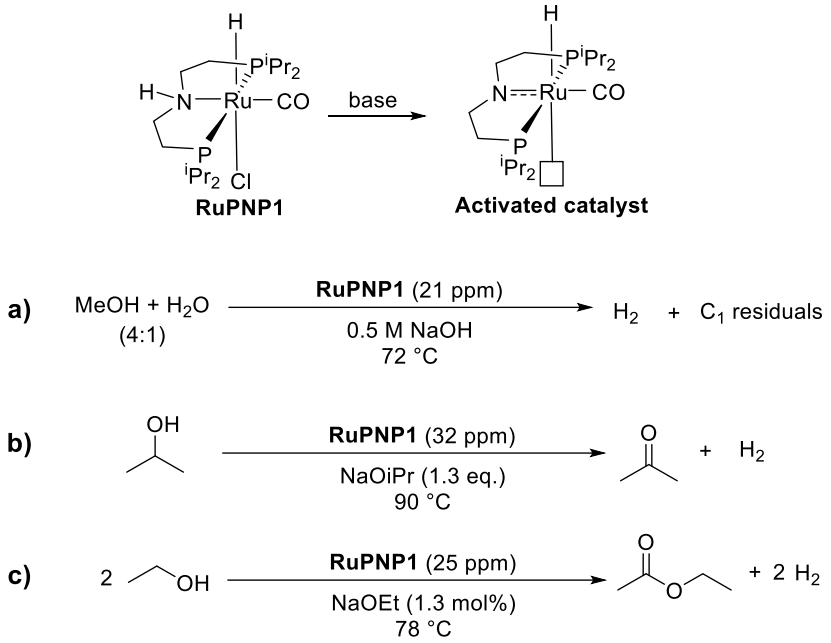

Figure 1.8: **a)** Methanol dehydrogenation with **RuPNP1**.[37] **b)** Dehydrogenation of isopropanol with **RuPNP1**.[38] **c)** Synthesis of ethyl acetate from ethanol by successive dehydrogenations catalyzed by **RuPNP1**.[39]

In **RuPNP1**, the proton-responsive group is the N-H functionality of the amine ligand. Upon treating **RuPNP1** with strong base, HCl is eliminated, and an amido-ligand is formed.[37] The basicity of the amido-ligand coupled with the Lewis acidity of the metal-center enables efficient heterolytic cleavage of the O–H and C_α–H bonds of alcohols with amido-group accepting the H^+ and the metal-center accepting the H^-. As the amido/amine couple is directly coordinated to the metal-center, the resulting H^+H^- pair resides in close proximity on the catalyst, which enables extrusion of H_2.

RuPNP1 is not the only pincer complex that enjoyed early success in AAD transformations. The Milstein group pioneered AAD transformations with catalyst systems utilizing Ru in combination with PNP or PNN pincer ligands.[8,41,42] Two noteworthy examples of dehydrogenative transformations developed in the Milstein group are shown in Figure 1.9.[43,44]

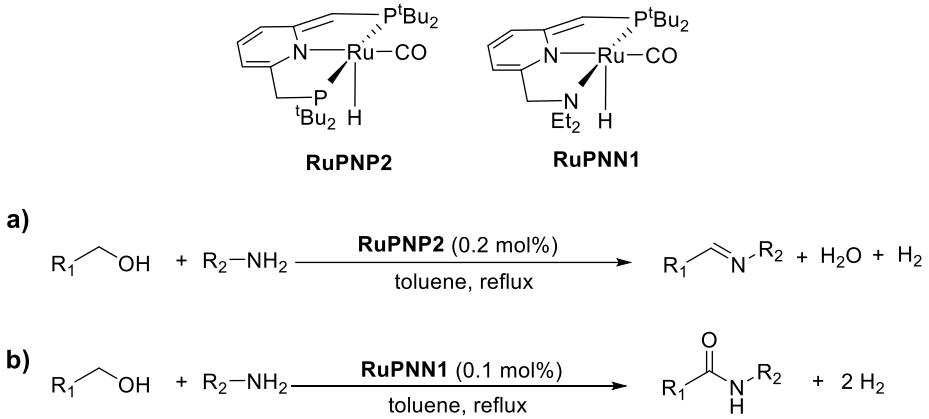

Figure 1.9: **a)** Dehydrogenative imine synthesis catalyzed by **RuPNP2**.[44] **b)** Dehydrogenative amide synthesis catalyzed by **RuPNN1**.[43]

The catalysts shown in Figure 1.9 rely on an MLC strategy based on aromatization/de-aromatization of the pyridine scaffold. The **RuPNP2** and **RuPNN1** catalysts represent the dearomatized mode of the catalyst, where the exocyclic C=C bond is the H^+ acceptor and the Ru-center is the H^- acceptor.[41]

Interestingly, Figure 1.9 **a)** shows how the **RuPNP2** catalyst facilitates imine synthesis from alcohols and amines,[44] whereas Figure 1.9 **b)** shows how the **RuPNN1** catalyst produces amides in the presence of alcohols and amines.[43] Evidently, dehydration is preferred in the case of **RuPNP2**, whereas successive dehydrogenation is preferred for **RuPNN1**. The differences in reactivity between the **RuPNP2** and **RuPNN1** systems were attributed to both steric and electronic factors. Furthermore, the lability of the tertiary amine donor in **RuPNN1** enables dissociation to create a vacant coordination site at the Ru-center, which was also deemed responsible for the observed selectivity.[45,46]

Lastly, it is noteworthy how these catalysts work in the absence of base, as the catalyst is added in the deprotonated, de-aromatized form, that is inherently ready to accept a H^+H^- pair.

1.4.3. AAD with base-metal catalysts relying on MLC

While catalyst systems based on precious metals, such as Ru, have demonstrated high activity for a wide range of dehydrogenative transformations, their utilization in catalysis presents certain drawbacks. The primary concern revolves around the scarcity and consequently, the high value of these noble metals. In pursuit of enhanced sustainability and cost-effectiveness, considerable efforts have been dedicated to achieving efficient AAD catalysis with earth-abundant base metals such as Mn, Fe, and Co.[47] This section will highlight a few notable examples of Mn and Co catalysis, while examples of Fe-catalyzed AAD reactions will be given in chapter 2.

Not surprisingly, homogeneous, base-metal catalyzed AAD reactions also largely rely on MLC and pincer ligands to achieve efficient catalysis. Two noteworthy examples of Co-catalyzed dehydrogenative transformations are shown in Figure 1.10.[48,49]

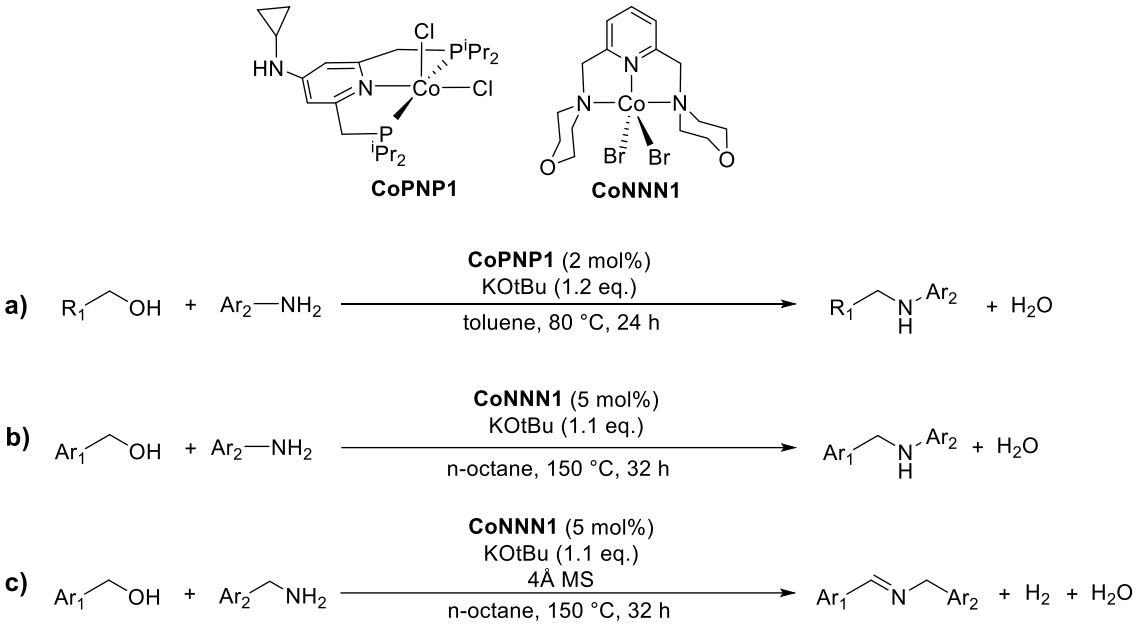

Figure 1.10: **a) CoPNP1**-catalyzed alkylation of aromatic amines by a hydrogen autotransfer mechanism.[48] **b)** Hydrogen autotransfer catalyzed by **CoNNN1**.[49] **c)** Dehydrogenative imination catalyzed by **CoNNN1**.[49]

Figure 1.10 **a)** shows how the **CoPNP1** catalyst enabled alkylation of aromatic amines by alcohols. The catalyst was developed in the Kempe group and was one of the first examples of homogeneous cobalt catalysis.[48] This system exemplifies the hydrogen autotransfer (or borrowing hydrogen) mechanism, where a H^+H^- pair is abstracted from the alcohol and subsequently used to hydrogenate the imine that results from the condensation of aldehyde and amine.

Figure 1.10 **b)** and **c)** presents later examples of Co-catalyzed dehydrogenative transformations reported by the Balaraman group.[49] The **CoNNN1** catalyst was found effective for alkylation of aniline-derivatives, whereas the reaction with benzylic amines furnished imines in good yields. The transformations require high temperatures, strong base and long reaction times, but it is noteworthy that the **CoNNN1** does not employ a phosphine-containing ligand. While phosphine-containing ligands are ubiquitous in homogenous metal catalysis, they are typically expensive and require inert handling as they are easily oxidized in the air.[50]

Mn-based catalysts have also found widespread application in dehydrogenative transformations. A few noteworthy examples of dehydrogenative Mn-catalysis are given in Figure 1.11.[1,51,52]

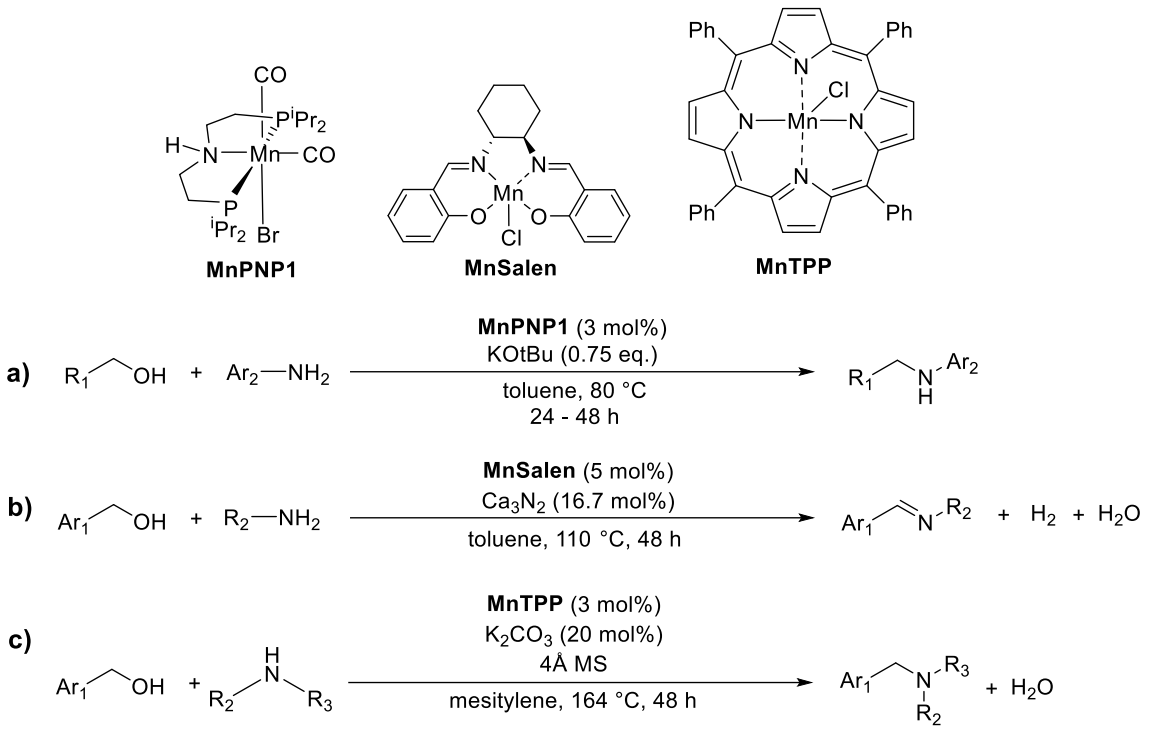

Figure 1.11: a) MnPNP1-catalyzed alkylation of aniline-derivatives a hydrogen autotransfer mechanism.[51] **b)** Dehydrogenative synthesis of imines catalyzed by a Mn(III)-salen complex.[1] **c)** Dehydrogenative synthesis of tertiary amines catalyzed by a Mn(III)-TPP complex.[52]

Figure 1.11 **a)** illustrates one of the first examples of molecular Mn-catalysis enabling C – N bonds by hydrogen autotransfer. The **MnPNP1** catalyst was developed in the Beller group and features a Mn(I)-center, which has been the most common oxidation state in Mn-based dehydrogenative catalysis.[51] Interestingly, the Madsen group reported two systems based on a Mn(III)-center. The Mn(III)-salen catalyst enabled dehydrogenative synthesis of imines from benzylic alcohols and amines (Figure 1.11 **b)**),[1] whereas the Mn(III)-TPP catalyst (and several related derivatives) enabled both imine synthesis and alkylation of secondary amines. (Figure 1.11 **c)**).[52]

To gain a comprehensive understanding of the Mn(III)-salen catalyst system, its mechanism was investigated through a combination of experimental techniques such as Hammett analysis and deuterium-labelling, as well as theoretical investigations employing DFT calculations.

As mentioned earlier, DFT calculations have provided an important tool to help unravel catalytic reaction mechanisms. In the following section, a few selected examples demonstrating the application of DFT in AAD catalysis will be provided, and the proposed mechanism of the Mn(III)-salen catalyst will be described.

1.5. DFT investigations of (de)hydrogenative transformations

A catalytic cycle involves a series of elementary steps that occur during a catalytic reaction, and DFT can be used to calculate the energies of the intermediates and transition states involved in these steps. By studying the energetics, DFT calculations can help identify the most favorable pathways, guiding the design and optimization of catalytic systems.[53]

As an in-depth explanation of the theoretical foundations behind DFT methodology lies outside the scope of this thesis, this section will merely present a couple of key examples that highlight application of DFT calculations in the realm of AAD catalysis with base-metal catalysts.

Table 1.1 summarizes a small selection of base-metal catalyst systems that have been studied with DFT.

Table 1.1: Examples where DFT calculations have been utilized to investigate the mechanism of AAD reactions performed with base-metal catalysts.

Entry	Key reaction	Catalyst type	Energy span	Reaction temperature	Rate-determining TS
1[54]	MeOH dehydrogenation	Fe(II)-PNP pincer	28 kcal mol^{-1}	120 °C	Coupling of H^- and H^+ to form H_2
2[55]	EtOH dehydrogenation	Mn(I)-PNP pincer	28.1 kcal mol^{-1}	110 – 150 °C	Coupling of H^- and H^+ to form H_2
3[1]	BnOH dehydrogenation	Mn(III)-salen	27.2 kcal mol^{-1}	110 °C	Breakage of C_α–H

In Entry 1, the study of MeOH dehydrogenation performed with an Fe(II)-PNP pincer catalyst was rationalized with DFT calculations. In the proposed reaction mechanism, MeOH is dehydrogenated through a concerted outer-sphere MLC pathway, which leads to an Fe(II)-amino-hydrido catalyst intermediate. Interestingly, the MeOH-assisted coupling of H^- and H^+ to liberate H_2 presents the most energetically demanding transition state, and the catalytic cycle presents an overall energy span of 28 kcal mol^{-1}, which was deemed acceptable under the employed reaction conditions.

Entry 2 provides an example of DFT studies of AAD catalysis with a Mn(I)-PNP pincer catalyst. In this study, a Mn(I)-alkoxide intermediate was identified as the resting state of the catalytic cycle and both concerted and stepwise outer-sphere dehydrogenation of EtOH were considered. The concerted transfer of the H^+H^- pair exhibited a barrier of 17.7 kcal mol^{-1}, whereas the stepwise transfer of the H^+H^- pair exhibited a barrier of 21.6 kcal mol^{-1}. Once again, the coupling of H^- and H^+ to liberate H_2 presented the most energetically demanding transition, resulting in an overall

energy span of 28.1 kcal mol^{-1}. The EtOH-mediated liberation of H_2 was also modeled, which decreased the energy span to 26 kcal mol^{-1}.

Entry 3 presents a study that is closely related to the Fe(III)-salen and Cr(III)-salen research that will be introduced in the main part of this thesis. As mentioned in Figure 1.11, the Mn(III)-salen catalyst proved effective for dehydrogenation of BnOH, followed by coupling with amines to produce imines. DFT calculations were utilized to devise a plausible reaction mechanism for the Mn(III)-salen system. The proposed activation of the Mn(III)-salen catalyst is shown in Figure 1.12.

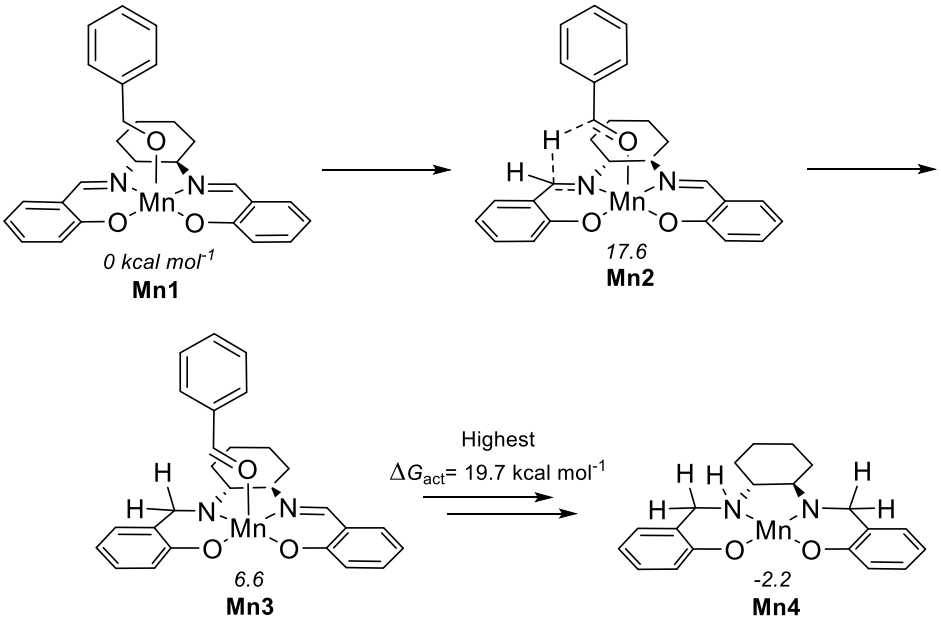

Figure 1.12: Proposed activation mechanism for the Mn(III)-salen catalyst.[1]

The alkoxo-Mn(III)-salen species **Mn1** was deemed a likely starting point for the activation mechanism, and a pathway consisting of a series of H^- and H^+ transfers led to the amine-amido intermediate **Mn4**. The highest calculated barrier along the activation pathway was 19.7 kcal mol^{-1}, and the reduction of the imino-bridges of the salen ligand was also experimentally verified with deuterium-labelled substrates.

The **Mn4** intermediate was labelled as the active catalyst, and the proposed catalytic cycle starting from **Mn4** is shown in Figure 1.13.

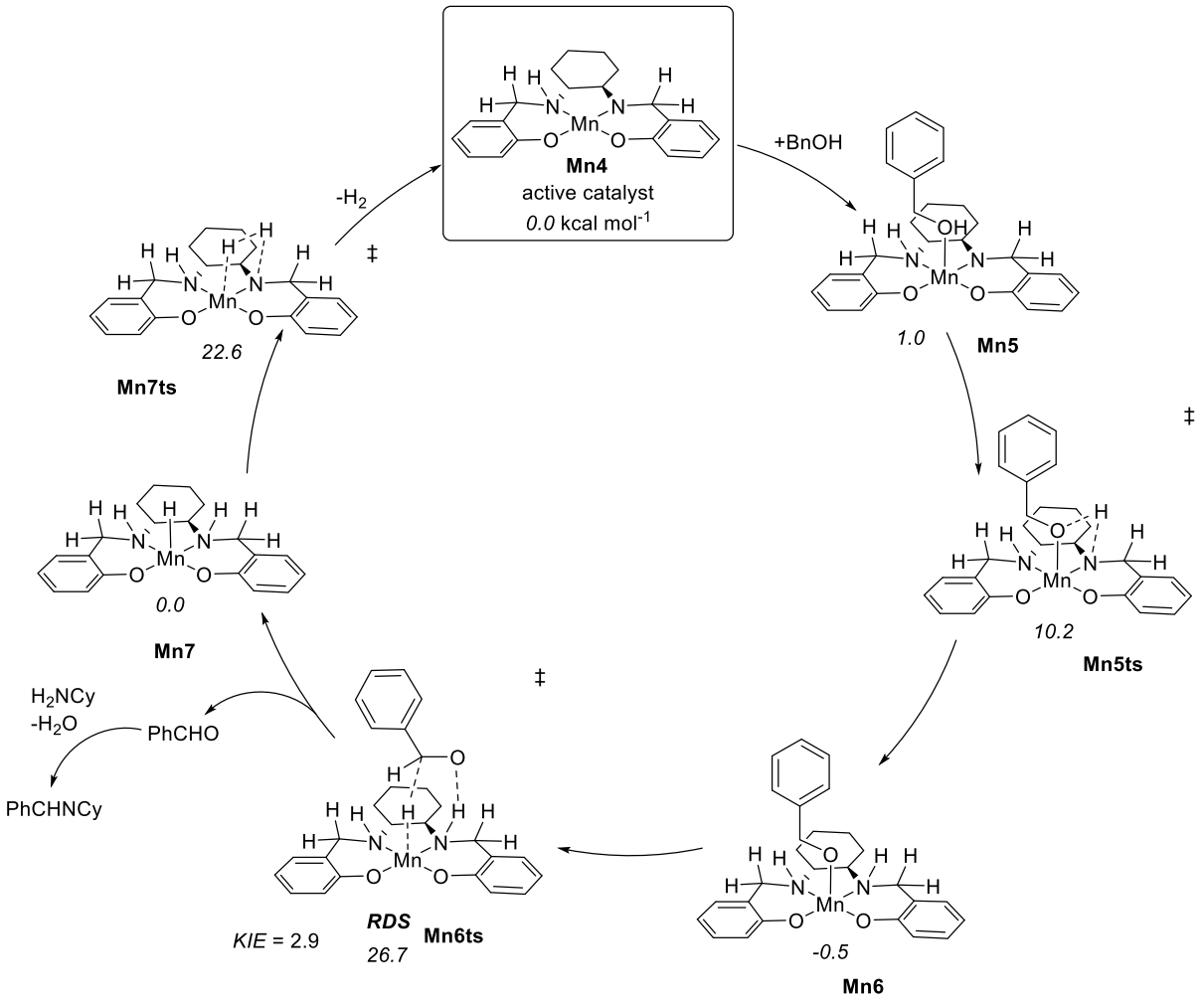

Figure 1.13: DFT-calculated catalytic cycle of the Mn(III)-salen AAD protocol.[1]

The catalytic cycle proceeds through a stepwise outer-sphere MLC mechanism, leading to the formation of **Mn7** and unassisted expulsion of H_2 completes the catalytic cycle. The most stable intermediate is the alkoxo-Mn(III) complex, **Mn6**, and the rate-determining step is the transfer of H^- to generate **Mn7**. The calculated energy span for the entire catalytic cycle is 27.2 kcal mol^{-1}, which is comparable to the energy spans reported in Table 1.1.

DFT calculations were also used to calculate the kinetic isotope effect (KIE) of the transformation and a theoretical Hammett analysis was also conducted. The DFT-calculated KIE was 2.9, which was found in reasonable agreement with the experimentally determined value of 2.0. The DFT-calculated Hammett plot also reproduced the experimentally determined Hammett plot nicely.

In conclusion, DFT calculations have been frequently used to rationalize AAD reaction mechanisms. Especially the DFT study conducted on the Mn(III)-salen system has served as a valuable source of inspiration and guidance for the DFT investigations conducted on the Fe(III)-salen and Cr(III)-salen systems. These systems will be presented in the coming chapters.

Chapter 2. AAD catalyzed by Fe(III)-salen catalysts

Abstract

In this chapter, the development of Fe(III)-salen catalysts for acceptorless dehydrogenative coupling of benzylic alcohols and amines to form imines has been described. Optimization studies have found that good imine yields are obtained when refluxing the benzylic alcohol and amine in toluene for 48 hours in the presence of 5 mol% catalyst and 20 mol% KOtBu. The AAD pathway of the reaction has been confirmed by the detection of H_2 gas. A Hammett plot with a slope of -0.80 has been measured and duplicate KIE values of 1.34 and 1.36 have been measured.

DFT calculations of a catalytic cycle similar to the previously published Mn(III)-salen cycle[1] have been attempted. All attempts at developing a DFT model that results in acceptable energy barriers and consistency with the experimental results have failed.

A series of control experiments have been conducted. Poisoning studies with PMe_3 and Hg have shown inhibition of catalytic activity. LC-MS studies have revealed extensive hydrolytic degradation of the catalyst and after prolonged reaction time, no Fe(III)-salen derivatives have been observable by LC-MS. Ultimately, the control experiments have indicated that the catalytically active species are heterogeneous small iron particles instead of molecular Fe(III)-salen derivatives. Efforts towards the isolation and characterization of the presumed catalyst particles have failed.

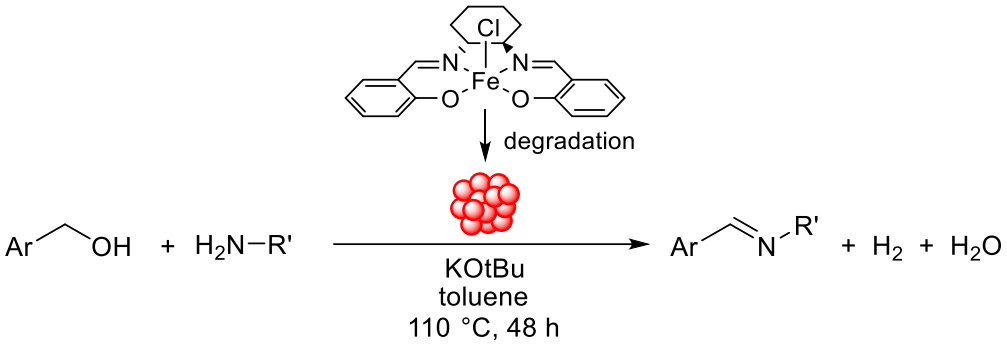

2.1. Introduction

Two of the most invoked examples of iron catalysis are the industrially relevant Fischer−Tropsch process[56,57] and the Haber−Bosch synthesis of ammonia.[58] The development of these processes has enabled modern lifestyle by providing fuel: the Fischer-Tropsch process produces fuel for combustion engines, whereas ammonia from the Haber-Bosch synthesis is an important ingredient in fertilizer and therefore indirectly fueling humans.

There are several advantages of utilizing iron in the development of efficient catalysts for organic transformations. For one, its wide range of oxidation states renders it suitable for both reductive and oxidative transformations.[59] Furthermore, iron is generally regarded as one of the safer transition metals, even though care should be taken when gauging the toxic effects of metal compounds.[60] Lastly, iron constitutes approximately 5% of the Earth's crust, ranks second in abundance among metals and fourth among all elements, following oxygen, silicon, and aluminum.[61] Consequently, iron is inexpensive, which makes it attractive for the development of cheap metal catalysts.

While heterogeneous catalysis with iron-based catalysts has been industrially applied for decades, the field of dehydrogenative transformations with iron catalysts is a relatively young research field with key contributions arising in the late 2000s.[27,62] Before delving into the development and investigation of an Fe(III)-salen catalyst for acceptorless alcohol dehydrogenations (AAD), the field of (de)hydrogenative transformations with iron-based catalysts will be briefly outlined in the coming sections.

2.1.1. Molecular Fe-based catalysts for (de)hydrogenative transformations

A wide range of iron complexes have been developed as homogeneous catalysts for (de)hydrogenation reactions. The most common ones include Fe(0) complexes with cyclopentadienone ligands[63–65], Fe(II)-PNP pincer complexes[54,66–74] and Fe(II)-PNNP complexes.[75–79] A few examples of hydrogenations catalyzed by an Fe(II)-PNP and an Fe(II)-PNNP complex are shown in Figure 2.1.

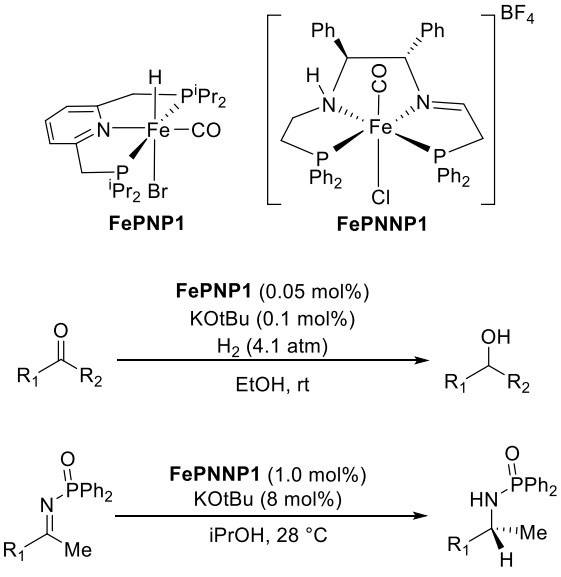

Figure 2.1: Hydrogenations catalyzed by **FePNP1** and **FePNNP1**.[74,80]

FePNP1 was employed by the Milstein group to achieve hydrogenation of ketones to alcohols in one of the earliest accounts of Fe(II)-catalyzed hydrogenations. The reaction relies on metal-ligand cooperation (MLC) by de-aromatization/aromatization cycles of the pyridine scaffold and a variety of ketones were efficiently reduced.[74] **FePNNP1** was developed in the Morris group and found as an efficient catalyst for asymmetric transfer hydrogenations of both ketones and imines. Again, metal-ligand cooperativity was important and cycling between an amido-eneamido complex and an amine-eneamido-hydride complex was proposed.[80]

Another class of Fe(II)-PNP complexes and some examples of dehydrogenative transformations are shown in Figure 2.2.

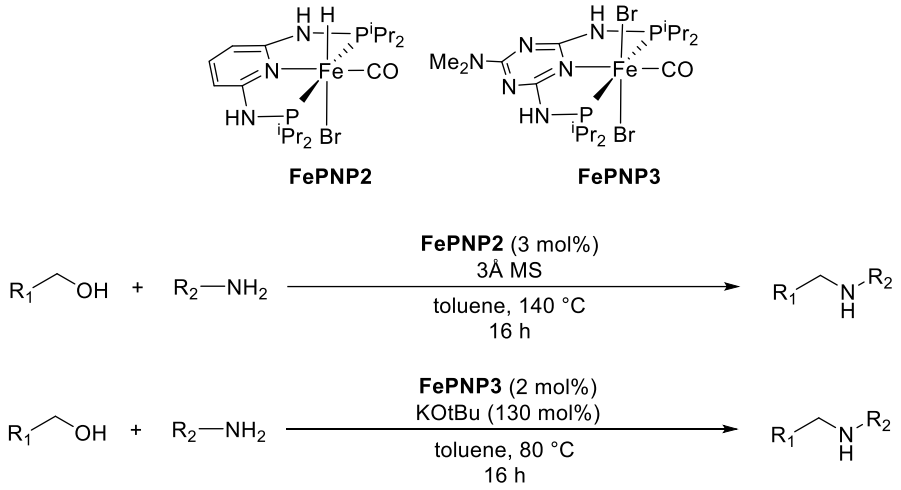

Figure 2.2: *N*-alkylation by hydrogen autotransfer catalyzed by **FePNP2** and **FePNP3**.[68,69]

Both **FePNP2** and **FePNP3** were employed in the coupling of alcohols and amines into secondary amines by the Kirchner group. A de-aromatization/aromatization cycle of the pyridine and triazine scaffold play a key part in the reaction mechanism, thus indicating the importance of MLC.[68,69]

Lastly, a few examples of hydrogenative and dehydrogenative transformations catalyzed by **FePNP4** and **FePNP5** are shown in Figure 2.3.

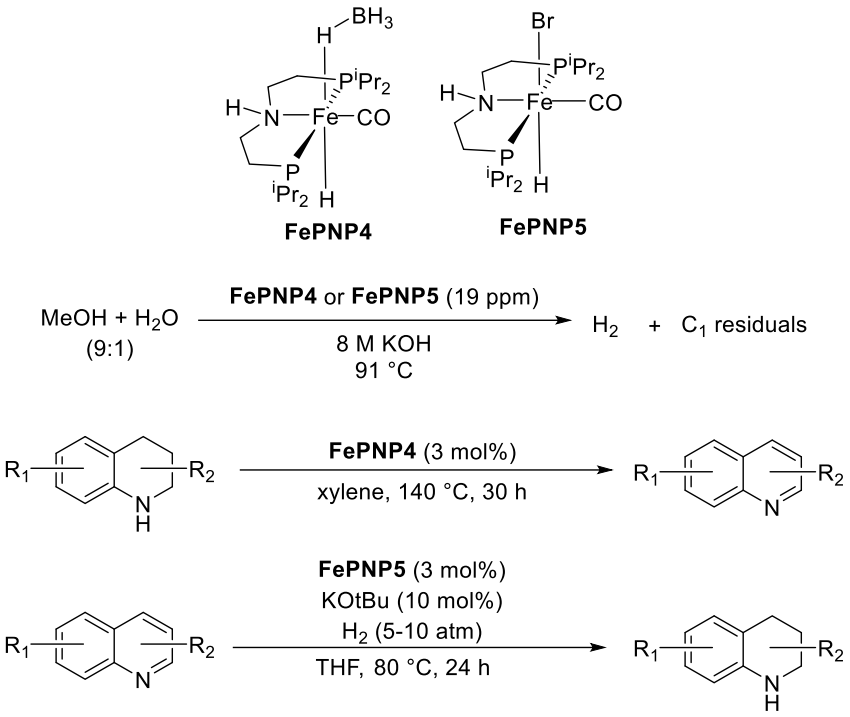

Figure 2.3: (De)hydrogenative transformations catalyzed by **FePNP4** and **FePNP5**.[66,72]

The Beller group reported acceptorless dehydrogenation of methanol catalyzed by both **FePNP4** and **FePNP5**. Cycling between an amido-hydrido Fe(II) complex and an amino-dihydrido Fe(II) complex is the generally accepted mechanism for acceptorless alcohol dehydrogenations with **FePNP4** and **FePNP5**, which is another example of an MLC mechanism.[81] Furthermore, the dehydrogenative synthesis of esters, ketones, lactones and lactams with **FePNP4** has been reported by the Jones and Beller research groups.[54,70]

Lastly, the Jones group reported **FePNP4** as a catalyst for the dehydrogenation of *N*-heterocycles and **FePNP5** was found to catalyze hydrogenation of *N*-heterocycles. In this study, the amido-hydrido Fe(II) complex was isolated and the amino-dihydrido Fe(II) complex was characterized by NMR.[66]

The examples listed in Figure 2.1 – 2.3 merely represent a small selection of Fe(II) complexes employing *N* and *P* donor ligands for (de)hydrogenative transformations. Generally, these reported Fe(II)-complexes rely on metal-ligand cooperation to achieve heterolytic bond cleavages. Ultimately, this strategy has enabled a plethora of Fe(II)-PNP and PNNP complexes to find tremendous success in homogeneous catalysis.

In contrary, few examples of homogeneous (de)hydrogenative transformations with Fe(III)-based catalysts have been described. A few examples of Fe(III)-based catalyst systems for (de)hydrogenative transformations are shown in Figure 2.4.

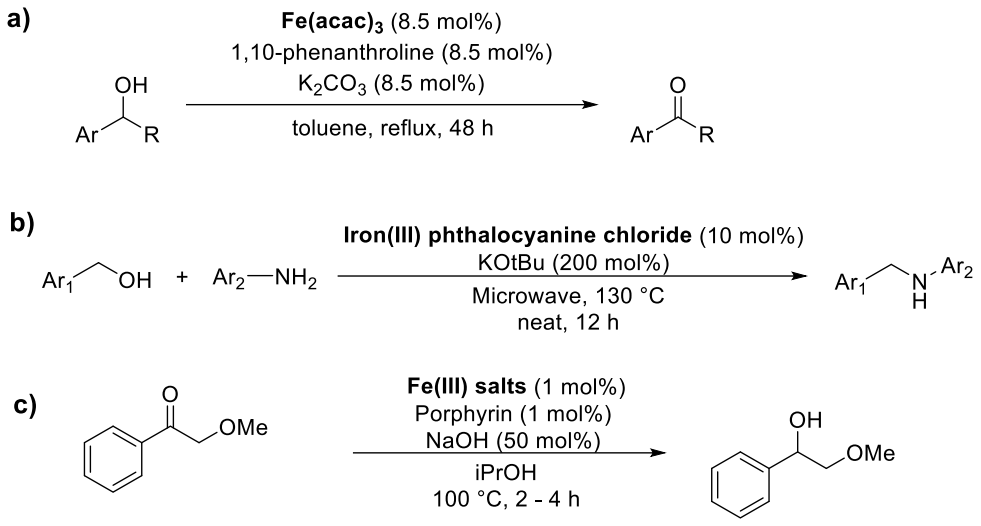

Figure 2.4: **a)** Acceptorless dehydrogenation of secondary benzylic alcohols with $Fe(acac)_3$ and 1,10-phenanthroline.[82] **b)** *N*-alkylation by hydrogen autotransfer catalyzed by an iron(III)-phthalocyanine complex.[83] **c)** Transfer-hydrogenation of ketones catalyzed by a range of Fe(III) salts in the presence of porphyrins.[84]

Figure 2.4 **a)** demonstrates how a system consisting of $Fe(acac)_3$ and 1,10-phenanthroline was found to efficiently catalyze AAD of secondary benzylic alcohols. Only secondary benzylic alcohols were found reactive, the active catalyst was not characterized, and the kinetic isotope effect was measured to 2.5.[82]

Figure 2.4 **b)** shows how *N*-alkylation of anilines with benzylic alcohols was catalyzed by a Fe(III)-phthalocyanine complex in the presence of KOtBu. No mechanistic investigation was performed, but generation of an benzyloxo-Fe(III)-phthalocyanine complex followed by transfer of the benzylic H^- to the Fe(III)-center was tentatively proposed. No experiments to elucidate the structure of the active catalyst were made.[83]

Lastly, Figure 2.4 **c)** illustrates how transfer hydrogenation of ketones was catalyzed by a catalyst system comprised of Fe(III) salts such as $FeCl_3$ and $Fe(acac)_3$ and porphyrin derivatives. Fe(II) or Fe(0) compounds could also be used as the source of Fe and no characterization of the active Fe-species was possible.[84]

Ultimately, the presented reports of Fe(III)-based catalysts for (de)hydrogenative transformations share several characteristics. For instance, all systems employ *N*-donor ligands, strong bases, and elevated temperatures to achieve reactivity. Importantly, the nature of the active catalyst was not experimentally substantiated in any of the reports, and this observation is in line with the conclusion presented at the end of this chapter.

2.1.2. Heterogeneous Fe-based catalysts for (de)hydrogenative transformations

The desire to develop new cost-effective and non-toxic base-metal catalysts has also resulted in the development of several heterogeneous Fe-based catalysts for (de)hydrogenative transformations. The main selling point of heterogeneous catalysts is that they are usually easily recovered from reaction mixtures by filtration, which allows efficient recycling of the catalyst material. Selected

examples of dehydrogenative and hydrogenative transformations catalyzed by heterogeneous Fe-based catalysts are shown in Figure 2.5.

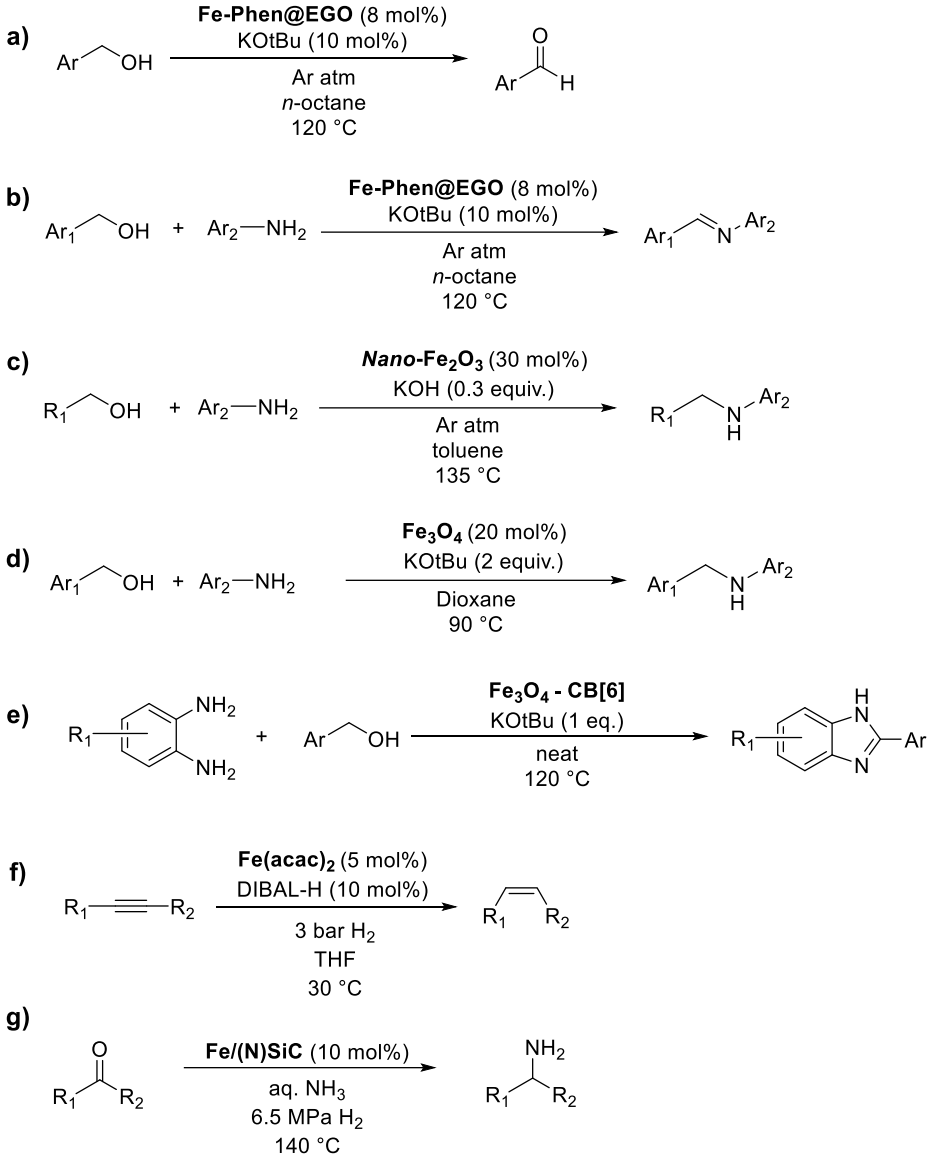

Figure 2.5: **a)** Acceptorless dehydrogenation of benzylic alcohols developed in the Balaraman group.[85] **b)** Fe-catalyzed dehydrogenative imine formation.[86] **c)** *N*-alkylation by hydrogen autotransfer catalyzed by nanoscale Fe_2O_3.[87] **d)** *N*-alkylation by hydrogen autotransfer catalyzed by commercial Fe_3O_4.[88] **e)** Dehydrogenative **s**ynthesis of benzimidazoles with cucurbit[6]uril-supported Fe_3O_4.[89] **f)** Stereoselective hydrogenation of alkynes with *in situ* generated Fe nanoclusters.[90] **g)** Reductive aminations catalyzed by Fe supported on *N*-doped SiC material.[91]

The protocols shown in Figure 2.5 entry **a)** and **b)** were developed in the Balaraman group.[85,86] The catalyst was prepared by complexation of $Fe(acac)_3$ and 1,10-phenanthroline followed by pyrolysis on an exfoliated graphene oxide support.[92] The scope of the reaction extended beyond the dehydrogenative synthesis of benzaldehyde; the catalyst allowed synthesis of quinoline from 1,2,3,4-tetrahydroquinoline, synthesis of imines and oxidation of secondary, benzylic alcohols to ketones.[85,86] Figure 2.5 entry **c), d)** and **e)** show how catalysts derived from Fe_2O_3 and Fe_3O_4 can catalyze dehydrogenative *N*-alkylation between benzylic alcohols and aniline derivatives.[87–89]

Figure 2.5 **f)** is an example of stereoselective alkyne hydrogenation catalyzed by iron particles that are generated by reduction of $Fe(acac)_2$ with DIBAL-H.[90] Figure 2.5 **g)** shows how iron supported on *N*-doped SiC acts as a catalyst for reductive aminations.[91]

The dehydrogenative transformations shown in Figure 2.5 generally require high temperatures, and in most cases, the optimal basic additive was found to be KOtBu. The addition of KOtBu was also found necessary in the development of the AAD protocol with the Fe(III)-salen catalysts, which will be discussed in the later sections of this chapter.

Before delving into the Fe(III)-salen project, a noteworthy paper by the Morris group is highlighted. It describes the serendipitous discovery of an Fe-based nanocatalyst for asymmetric transfer hydrogenation.[93] The developed protocol is shown in Figure 2.6.

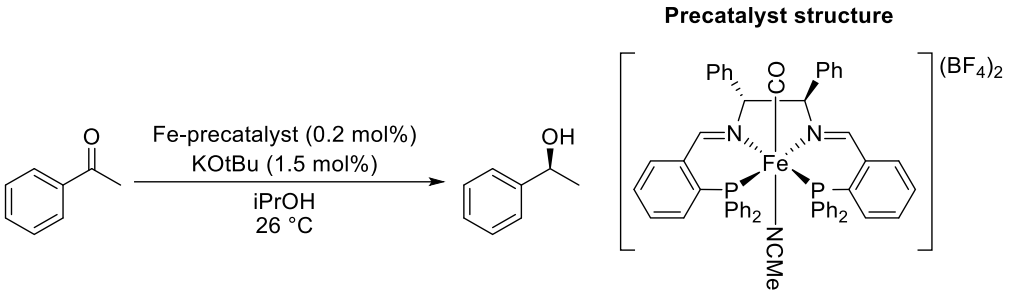

Figure 2.6: Asymmetric transfer hydrogenation catalyzed by an Fe nanocatalyst formed *in situ*.[93]

The precatalyst is a Fe(II)-PNNP complex with axially coordinated CO and MeCN. Interestingly, the employed PNNP ligand strongly resembles a salen ligand, but the precatalyst was found to quickly degrade when treated with KOtBu in iPrOH. Several experimental results supported the formation of nanoparticles. For example, a sigmoidal reaction profile was observed and pretreating the precatalyst with KOtBu removed the induction period. Furthermore, poisoning with substoichiometric amounts of phosphines and thiols was observed. Lastly, the nanoparticles were imaged with scanning transmission electron microscopy (STEM) and found to have a ~4.5 nm diameter. Ultimately, the envisioned homogeneous catalysis turned out to be of heterogeneous nature, even though no filtration of the heterogeneous catalyst was possible.[93] These results also prompted the Morris group to publish a thorough review of different methods to distinguish homogeneous and heterogeneous iron catalysis.[94]

In summary, heterogeneous iron catalysts have emerged as promising catalysts for several transformations, including hydrogenations with H_2, transfer hydrogenations, hydrogen autotransfers and AAD reactions. Heterogeneous iron catalysts are therefore offering an attractive alternative to homogeneous catalyst systems.

2.1.3. Structural aspects of Fe(III)-salen and Fe(III)-salan complexes

Before diving into the development of Fe(III)-salen catalysts for AAD reactions, a brief description of the structural aspects of Fe(III)-salen and Fe(III)-salan complexes is warranted. The salen and salan scaffolds are both tetradentate ligands capable of coordinating metal ions through their set of ONNO donor atoms. When complexed with Fe(III), 5-coordinate or 6-coordinate complexes typically result.[95] The most commonly adopted geometries are schematically shown in Figure 2.7.

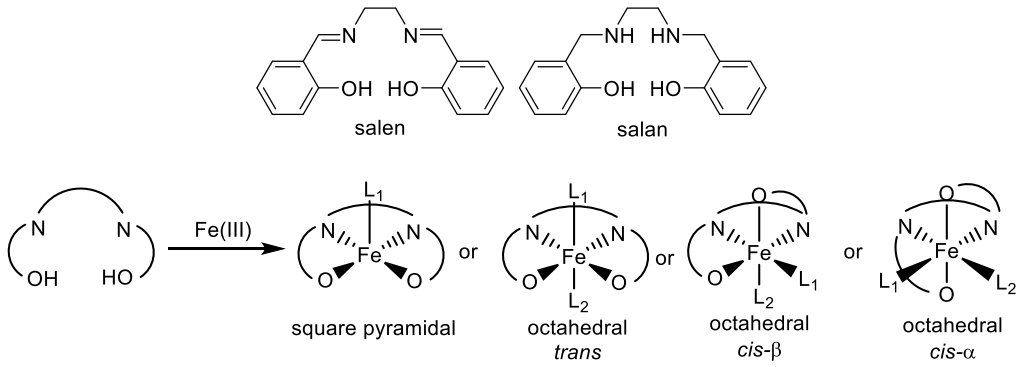

Figure 2.7: The structures of the simplest salen and salan ligands. Different geometries envisioned for Fe(III)-salen and Fe(III)-salan complexes.

One of the earliest reports of an Fe(III)-salen complex was published in 1933[96], but a more complete account of the structural aspects of Fe(III)-salen complexes with halide ligands was given by Gerloch and coworkers in the late 1960s.[97–99] They found that the Fe(III)-salen chloride could form either 5-coordinate square pyramidal monomers or 6-coordinate dimers depending on the solvent used for crystallization. Furthermore, it was shown that the Fe(III)-salen chloride complexes are monomeric in solution and magnetic measurements indicated a high-spin Fe(III) center.[99] The obtained crystal structures are shown in Figure 2.8.

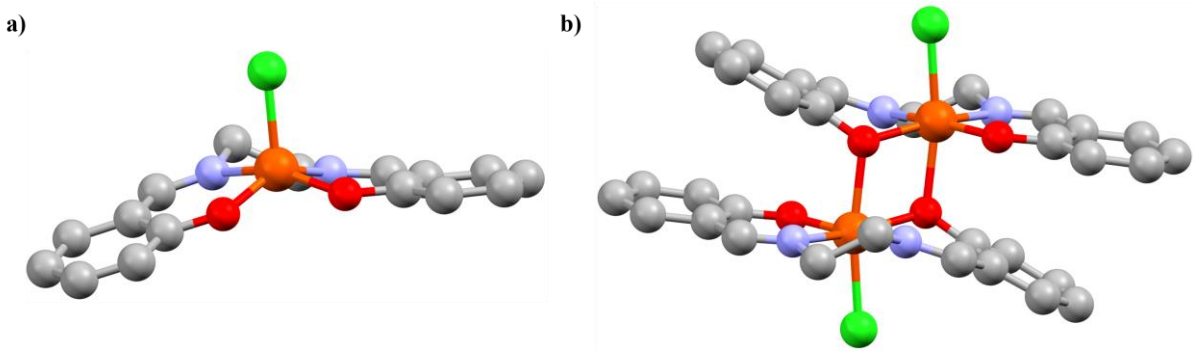

Figure 2.8: **a)** Fe(III)-salen chloride forms 5-coordinate square pyramidal monomers when crystallized from nitromethane.[97–99] **b)** 6-coordinate dimers of Fe(III)-salen chloride are formed when crystallized from acetone.[97–99]

The sp^2 carbons in the salen ligand causes a preference for coplanarity of the ONNO donor set. Therefore, square pyramidal and *trans*-octahedral geometry is prevalent for Fe(III)-salen complexes. However, octahedral *cis*-β geometry can also be observed if bidentate ligands such as acac are employed.[100]

Since the work of Gerloch and coworkers, the chemistry of the Fe(III)-salen scaffold has been widely explored. The AAD reactions described later in this chapter relies on coupling of alcohols and amines under highly basic conditions with concomitant release of water. Therefore, structures of the Fe(III)-salen scaffold incorporating alkoxo, hydroxo, amino or chemically similar ligands are of particular interest. Figure 2.9 shows examples of commonly encountered coordination geometries for Fe(III)-salen derivatives.

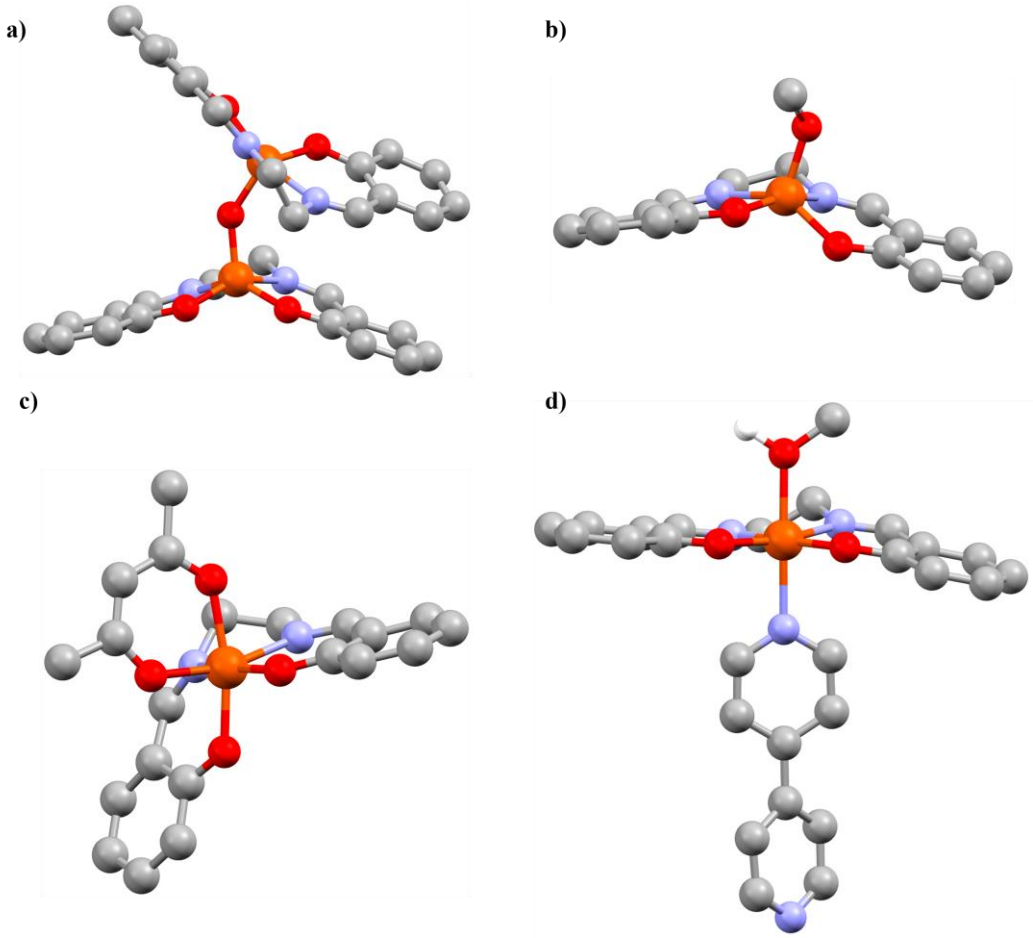

Figure 2.9: **a)** Square pyramidal oxo-bridged dimer of Fe(III)-salen (solvent hidden for clarity).[101] **b)** Distorted square pyramidal Fe(III)-salen scaffold with a methanolate ligand (substituents and solvent have been hidden for clarity.[102] **c)** Octahedral *cis*-β configuration of an Fe(III)-salen scaffold with acac.[100] **d)** Octahedral *trans* configuration of an Fe(III)-salen cation ligated by methanol and 4,4'-bipyridine (counterion has been hidden for clarity).[103]

Figure 2.9 **a)** and **b)** shows Fe(III)-salen derivatives adopting square pyramidal geometry, whereas Figure 2.9 **c)** and **d)** shows octahedral Fe(III)-salen derivatives with *cis*-β and *trans* geometry, respectively.

An interesting aspect of the Fe(III)-salen scaffold is the question of spin multiplicity of the Fe(III) center. Fe(III) is a d^5 system and low-spin ($S = {}^1/_2$), intermediate-spin ($S = {}^3/_2$) and high-spin ($S = {}^5/_2$) configurations are possible.[103,104] A detailed account of the spin behavior of Fe(III) systems is beyond the scope of this thesis, but it is worth noting that all Fe(III) centers depicted in Figure 2.9 adopt high-spin configurations.[100–103]

Reduction of the imino-bridges in the salen ligand results in the salan ligand and *N*-methylated derivatives are also known as salans. The salan ligand scaffold is more flexible due to the sp^3 carbons and a wider range of isomers is now possible. A range of crystal structures of Fe(III)-salan derivatives that corroborate this increased flexibility is shown in Figure 2.10.

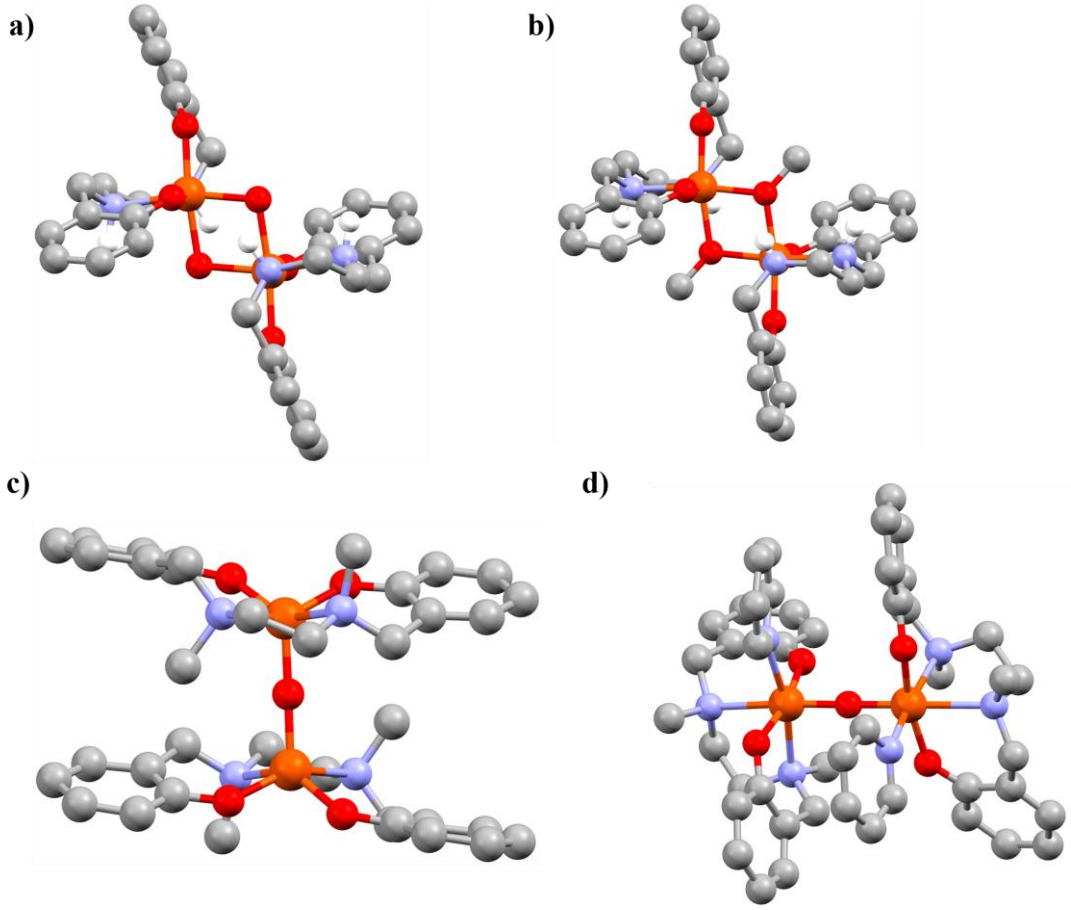

Figure 2.10: **a)** Octahedral *cis*-β configuration in a hydroxo-bridged dimer of Fe(III)-salan (solvent has been hidden for clarity).[105] **b)** Octahedral *cis*-β configuration in a methoxo-bridged dimer of Fe(III)-salan (solvent has been hidden for clarity).[106] **c)** Square pyramidal configuration of an oxo-bridged Fe(III)-salan scaffold (substituents have been hidden for clarity).[107] **d)** Octahedral *cis*-α configuration of an oxo-bridged Fe(III)-salan dimer with pyridine ligands (solvent has been hidden for clarity).[108]

Evidently both hydroxo-bridged, alkoxo-bridged and oxo-bridged structures of the Fe(III)-salan scaffold are known. Indeed, the increased flexibility of the salan ligand scaffold is underlined by the observation of both square pyramidal and octahedral complexes adopting both *cis*-β and *cis*-α configurations. Lastly, it should be noted that all Fe(III)-centers shown in Figure 2.10 adopt high-spin configurations like the Fe(III)-salen derivatives in Figure 2.9.[105–108]

Ultimately, the examples presented in Figure 2.9 and Figure 2.10 underline the ability of both the Fe(III)-salen and Fe(III)-salan scaffold to form a range of complexes with ligands coordinating through *N* or *O*. The observation of oxo, hydroxo and alkoxo ligands is a testament to the high oxophilicity of the Fe(III)-center and the structures provide valuable inspiration for possible intermediates under the catalytic reaction conditions. Lastly, it should be noted that the Fe(III)-centers in the provided examples adopt high-spin configurations, which is useful for the DFT calculations presented later in this chapter.

2.2. Previous work on Fe(III)-salen AAD catalysis in the Madsen group

My initial role in the Fe(III)-salen catalysis project was to provide computational support and mechanistic insight into an AAD reaction with a Fe(III)-salen catalyst that had been developed by previous Ph.D. student Fabrizio Monda. To provide the necessary background knowledge and relevant context for my contributions to the project, the experimental work performed prior to my involvement is outlined in the coming section. The sections in this chapter are presented in chronological order of discovery to illustrate the flow of experimental and computational evidence leading to the conclusion of the project. The whole story of AAD reactions with the Fe(III)-salen scaffold has been recently published.[109]

2.2.1. Synthesis of ligand and catalyst

The experiments outlined in this section were originally performed by previous Ph.D. student Fabrizio Monda. As the natural starting point of the Fe(III)-salen project, a catalyst was synthesized. A salen-type ligand employing a *trans*-cyclohexyl backbone was chosen due to its success in the Mn(III)-salen protocol and the ligand was prepared following the published procedure outlined in Figure 2.11.[1] Subsequently, the synthesis of the Fe(III)-salen complex was performed according to literature as shown in Figure 2.12.[110] Further details regarding synthesis and characterization can be found in section 2.6.3 and in the published paper.[109]

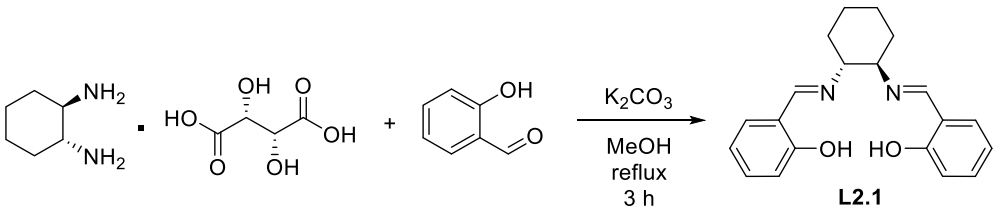

Figure 2.11: Synthesis of ligand **L2.1** employing a chiral cyclohexyl backbone.

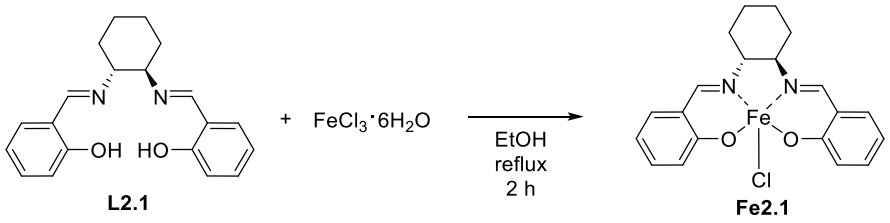

Figure 2.12: Synthesis of catalyst **Fe2.1**.

The synthesis of the ligand is straightforward and different derivatives containing electron withdrawing groups (EWGs) or electron donating groups (EDGs) on the phenols can easily be prepared in high yields.[109,111] The Fe(III)-salen complexes are synthesized by refluxing the salen ligand with an iron(III) source in EtOH. In the example shown in Figure 2.12, the chloride variant is synthesized by using $FeCl_3 \cdot 6H_2O$, but $FeBr_3$ can also be used as the metal source if the bromide variant is desired.[109] In all cases, the Fe(III)-salen complexes were isolated as black powders that were recrystallized from EtOH to obtain catalysts of high purity.[109,111]

2.2.2. Optimization of reaction conditions

In the early discovery phase, Ph. D. student Fabrizio Monda performed optimization of the reaction parameters. Both different ligand derivatives, different basic additives and the effect of molecular sieves were investigated. The yields were determined by GC-MS analysis and the results are shown in Figure 2.13.

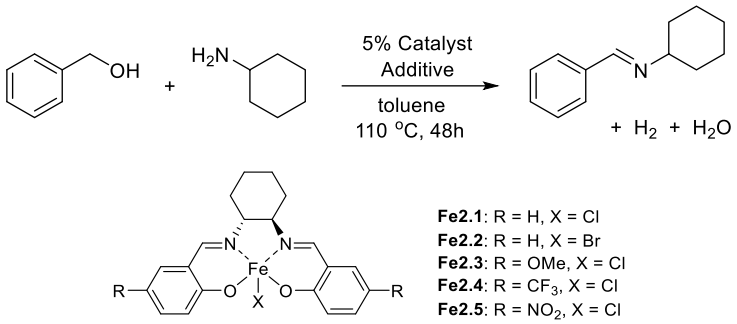

Entry	Catalyst	Additive	Yield [%][b]
1	**Fe2.1**	–	32
2[c]	**Fe2.1**	–	49
3	**Fe2.1**	4Å MS[d]	14
4	**Fe2.1**	KOtBu (15 mol%)	71
5	**Fe2.1**	KHMDS (15 mol%)	8
6	**Fe2.1**	Ca_3N_2 (15 mol%)	29
7	**Fe2.1**	KH (15 mol%)	10
8	**Fe2.1**	KOtBu (20 mol%)	92
9	–	KOtBu (20 mol%)	18
10	**Fe2.2**	KOtBu (20 mol%)	87
11	**Fe2.3**	KOtBu (20 mol%)	87
12	**Fe2.4**	KOtBu (20 mol%)	62
13	**Fe2.5**	KOtBu (20 mol%)	59

[a]Conditions: BnOH (1.0 mmol), $CyNH_2$ (1.0 mmol), catalyst (0.05 mmol), additive (0.2 mmol), tetradecane (0.5 mmol, internal standard), toluene (2 mL), reflux, 48 h. [b]GC yield based on the internal standard. [c]Reaction time 60 h. [d] With 150 mg of 4Å MS.

Figure 2.13: Optimization of reaction parameters originally performed by Fabrizio Monda.

Entry 3 shows that addition of 4Å molecular sieves was detrimental to the reaction, which stands in contrast to the observations made in the Mn(III)-salen case, where efficient desiccation was necessary for complete conversion into the desired imine.[1] Thus, water may play a role in the reaction, which is discussed later. Furthermore, KOtBu was identified as the best performing additive; KHMDS, Ca_3N_2 (which found success in the Mn(III)-salen project) and KH all resulted in

inferior yields. Interestingly, addition of 20mol% KOtBu without any catalyst resulted in an 18% yield, which is likely caused by traces of O_2 in the reaction vessel. Ultimately, addition of 20mol% KOtBu resulted in the highest imine yields and different catalyst derivatives were therefore tested under these conditions. Evidently, exchanging the counterion from chloride to bromide did not change the yield remarkably, which could indicate that the halide ion is substituted under the reaction conditions. Substitutions on the 4-position of the phenolate moiety did not lead to improvements; the yield was virtually unchanged with –OMe substitution, whereas slightly diminished yields were observed with $–CF_3$ and $–NO_2$ substitution. The detrimental effect of the EWGs is not understood, but Fabrizio Monda speculated that reduced solubility of **Fe2.4** and **Fe2.5** may have been responsible for the reduced reactivity.[111] Ultimately, **Fe2.1** and 20mol% KOtBu were chosen as the best performing combination for the AAD imination reaction.

2.2.3. Substrate scope

The substrate scope of the reaction was extended to include a variety of benzylic alcohols and amines. The results are shown in Figure 2.14.

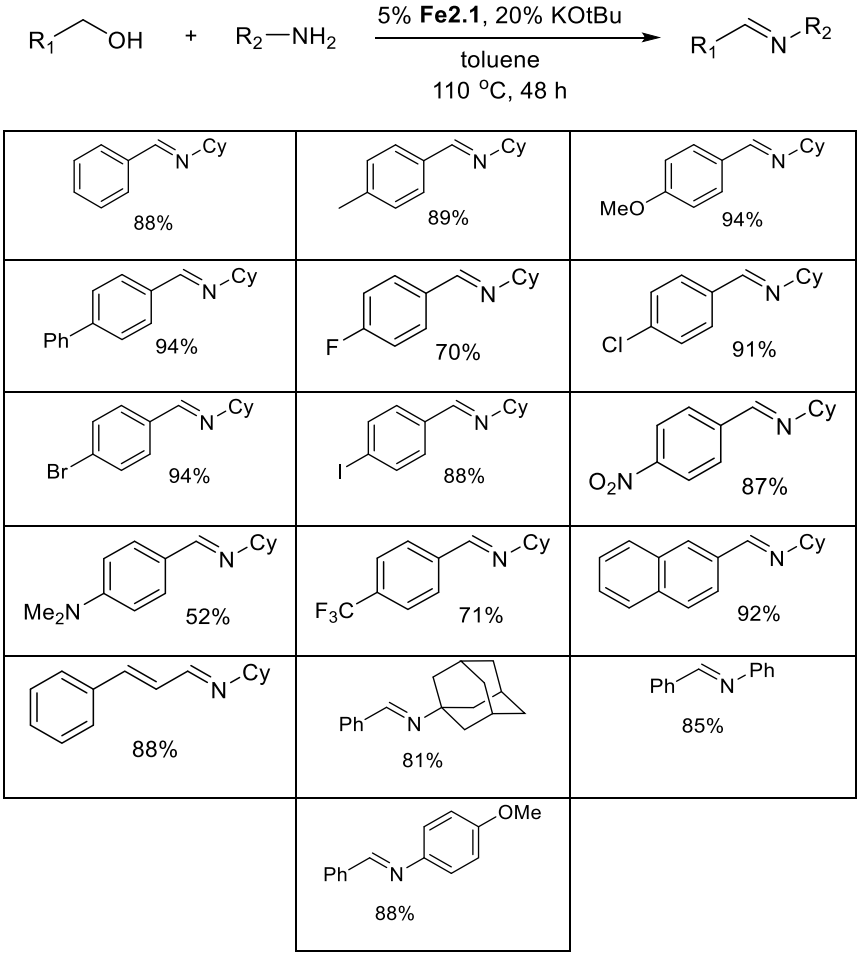

Figure 2.14: The substrate scope performed by Fabrizio Monda. Reaction conditions: alcohol (1.0 mmol), amine (1.0 mmol), **Fe2.1** (0.05 mmol), KOtBu (0.2 mmol), toluene (2 mL), reflux, 48 h. The reported yields are isolated yields.

Evidently, a range of benzylic alcohols and amines are tolerated. Both alcohols containing EWGs or EDGs are compatible with the developed protocol, and no dehalogenation or reduction of the $–NO_2$ group was observed.

2.2.4. Gas evolution and confirmation of identity

To confirm the dehydrogenative pathway of the reaction, Fabrizio Monda setup a reaction to capture any developed gases in a water-filled burette. The collected gas was successfully used to hydrogenate diphenylacetylene to 1,2-diphenylethane as shown in Figure 2.15. This experiment confirmed that the released gas was H_2 and indicated a dehydrogenative pathway.

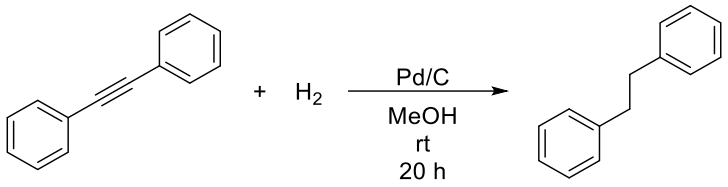

Figure 2.15: The gas released from the reaction was used to hydrogenate diphenylacetylene to 1,2-diphenylethane.

2.2.5. Initial LC-MS observations

To characterize possible catalyst intermediates, Fabrizio performed a short LC-MS study. Following the optimized protocol, the reaction mixture was sampled at t = 0 min and again at t = 30 min. The two obtained LC-MS chromatograms are shown in Figure 2.16.

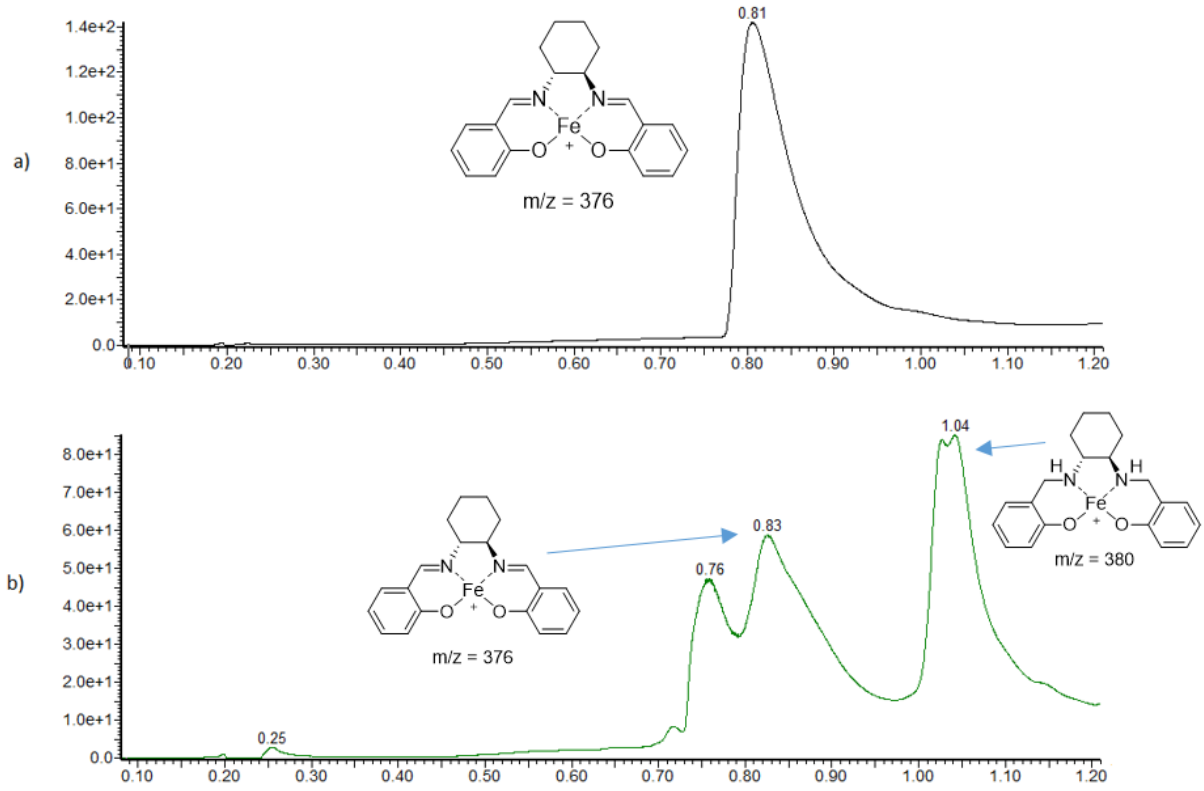

Figure 2.16: Initial LC-MS study performed by Fabrizio Monda. Top: LC-MS chromatogram at t = 0 min. Bottom: LC-MS chromatogram at t = 30 min. The formation of Fe(III)-salan species is observed.

At t = 0 min, only the Fe(III)-salen cation (m/z = 376 Da) was observed with a retention time of 0.81 min. At t = 30 min, a peak assigned to the Fe(III)-salan cation (m/z = 380 Da) was observed with a retention time of 1.04 min. This indicated that the imino-bridges in the Fe(III)-salen complex were rapidly reduced under the employed reaction conditions. The reduction of the imino-bridges in the salen ligand was also observed for the Mn(III)-salen protocol.[1] It was therefore hypothesized that the Fe(III)-salen and Mn(III)-salen catalyst systems may be operating by similar reaction mechanisms.

2.2.6. Determination of kinetic isotope effect and H/D scrambling

As further mechanistic investigations were desired, an experiment to determine the kinetic isotope effect of the reaction was conducted by project student Frederik Simonsen Bro. Comparing the reaction rate when using benzyl alcohol-α,α-d_2 to the reaction rate of non-deuterated benzyl alcohol resulted in Figure 2.17.

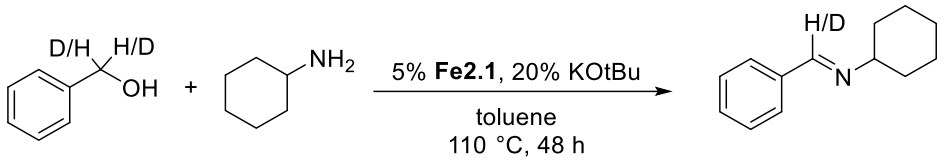

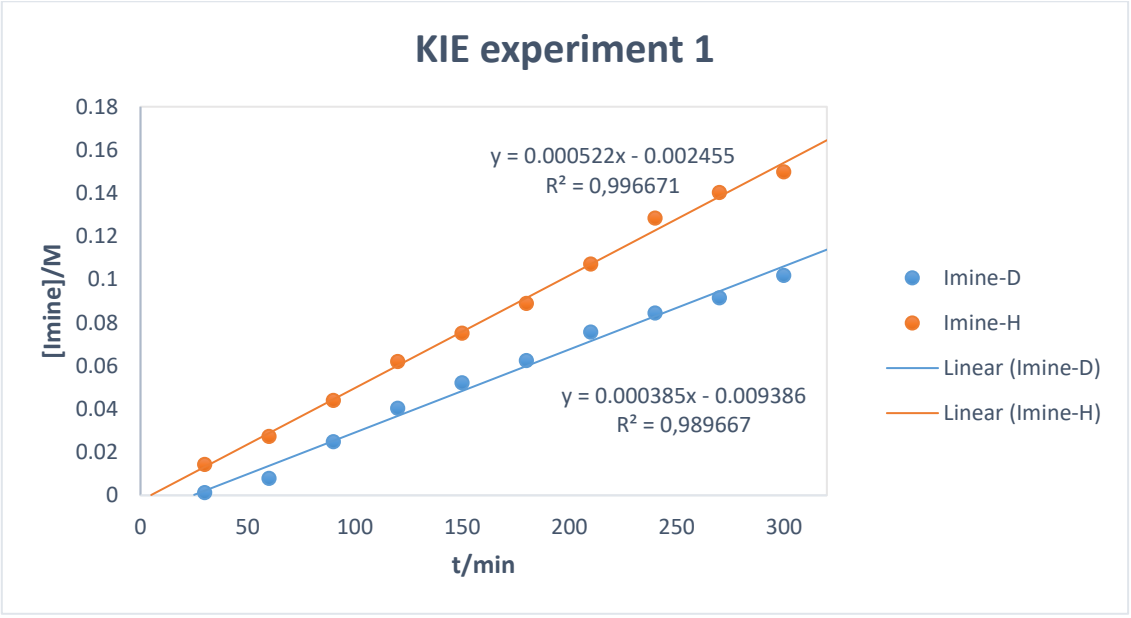

Figure 2.17: Data obtained in the 1st determination of the KIE of the reaction. Evidently, the non-deuterated benzyl alcohol reacts faster, and the KIE is determined to 1.36.

Based on this plot, the KIE of the reaction was determined to 1.36, which is rather low compared to the KIE of the Mn(III)-salen protocol and other AAD reactions where breakage of the C-H bond is thought to be one of the slow steps.[32,82,112–115] Puzzled by the low magnitude of the KIE, a second determination of the KIE was warranted and this was where my involvement in the project began. Under my supervision, BSc. student Xiyue Liu performed a repetition of the KIE experiment. The obtained results are shown in Figure 2.18.

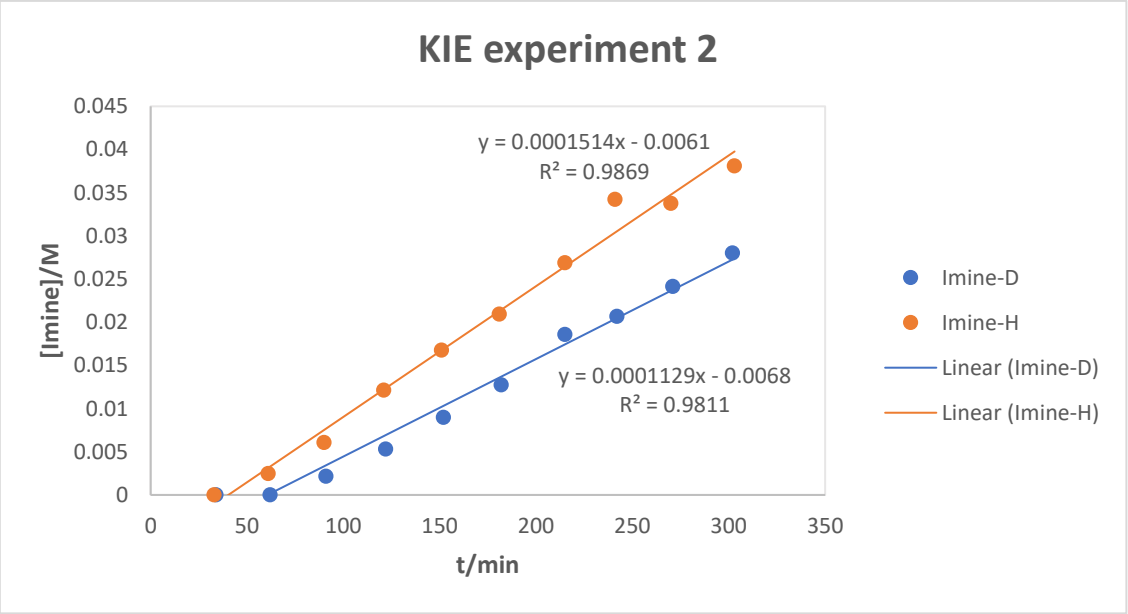

Figure 2.18: Data obtained in the 2nd determination of the KIE. The data reproduces the trend observed in the 1st iteration and the KIE is determined to 1.34.

The repetition of the KIE determination resulted in a value of 1.34, which was closely comparable to the initially determined KIE of 1.36. Consequently, the low KIE values were deemed trustworthy and possible explanations of the low value had to be sought.

In conjunction with the KIE experiments, possible scrambling of H/D in the product imine was investigated. In the experiment with benzyl alcohol-α,α-d_2, both NMR and GC-MS showed exclusive formation of the deuterated imine PhCD=NCy and no traces of hydrogen incorporation was observed (Figure 2.19).

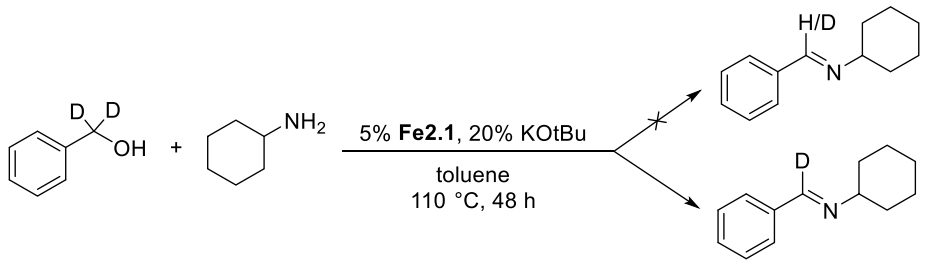

Figure 2.19: No H/D scrambling was observed by GC-MS or NMR when the reaction was performed with benzyl alcohol-α,α-d_2.

The same observation was made for the Mn(III)-salen protocol and is consistent with a monohydride mechanism involving only hydride transfer of the C_α-H to the metal.[21,23]

2.2.7. Hammett study

Further characterization of the reaction mechanism was performed in the form of a Hammett study. The Hammett study was carried out under my supervision by BSc. student Xiyue Liu. To perform the Hammett study, a series of competition experiments between benzyl alcohol and *para*-substituted benzyl alcohols were performed with the optimized protocol. The full details of the Hammett competition experiments and the corresponding rate plots are provided in section 2.6.3. From the obtained rate data, a Hammett plot based on the Hammett *para*-substituent constant σ_p was constructed. The plot is shown in Figure 2.20.

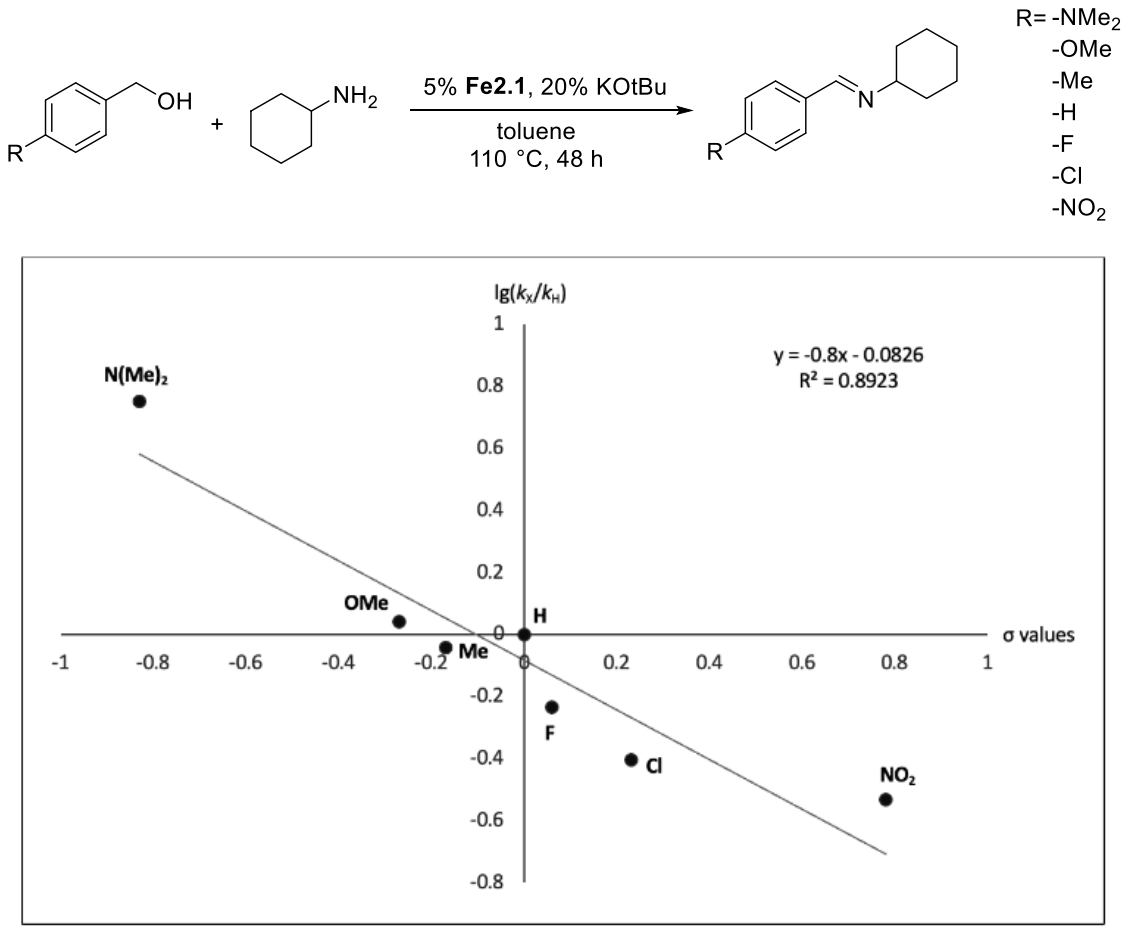

Figure 2.20: Hammett plot obtained from competition experiments between benzyl alcohol and *para*-substituted benzyl alcohol using the optimized Fe(III)-salen protocol.

The Hammett plot resulted in a straight line with a slope ρ = -0.8. For reference, the Hammett study in the Mn(III)-salen case resulted in a straight line with a slope ρ = -1.24.[1] The Hammett analysis is consistent with build-up of positive charge on the benzylic carbon, and the result supports the notion that hydride transfer from the alcohol could be one of the slow steps in the reaction.

2.2.8. Radical scavenger experiment

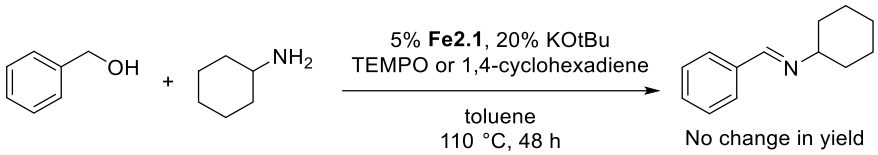

Figure 2.21: Radical scavenger experiments with addition of TEMPO or 1,4-cyclohexadiene.

In the Madsen group, KOtBu has previously been shown to initiate radical chemistry with benzyl alcohol and other reports of single electron transfer involving KOtBu are known.[116–118] Furthermore, single electron transfers are prominent in the field of iron catalysis.[59] Due to the low value of the KIE and the identification of KOtBu as the optimal base for the reaction, a radical scavenger experiment was performed by BSc. student Xiyue Liu to investigate possible involvement of radical intermediates. The standard reaction was run in the presence of either TEMPO or 1,4-cyclohexadiene as radical scavengers. If radicals are involved, a change in the yield of the imine is expected along with formation of byproducts resulting from radical couplings of the scavengers. However, no change in the yield of imine was observed in either case, and no byproducts associated with radical reactions of the scavengers could be identified by GC-MS. Therefore, no radical pathways were deemed operational.

2.3. Computational investigation of the catalytic cycle

An AAD reaction is clearly observed with the Fe(III)-salen catalyst, but the measured KIE is low if H^- transfer from benzyl alcohol is rate-determining, as it was determined in the Mn(III)-salen case.[1] To gain a better understanding of the reaction mechanism of catalysis, I was tasked with constructing a catalytic cycle based on DFT calculations. The goal was to construct a DFT model of the catalytic cycle that reasonably reproduced the observed kinetic isotope effect and Hammett plot. Furthermore, the calculated energy barriers should be comparable to those calculated for the Mn(III)-salen catalytic cycle as the reaction conditions of the two systems are similar. To save computation time, all catalyst intermediates were modelled with an ethylene backbone instead of the *trans*-cyclohexyl backbone.

2.3.1. Catalyst spin multiplicity

As mentioned in section 2.1.3, Fe(III) is a d^5 system and low-spin (doublet, $S = {}^1/_2$), intermediate-spin (quartet, $S = {}^3/_2$) and high-spin (sextet, $S = {}^5/_2$) configurations can be envisioned. Therefore, the first task was to determine the ground state spin multiplicity of the Fe(III)-center.

Based on the previous experience from the Mn(III)-salen catalytic cycle[1], a range of likely intermediates (shown in Figure 2.22) were chosen and their electronic energy was calculated with different spin multiplicities. The spin splittings were calculated using ORCA version 4.2.0.[119] Further details regarding the computational methods can be found in section 2.6.4.

The B3LYP functional[120,121] was chosen based on the computational method used in the Mn(III)-salen case.[1] The B3LYP functional has previously found success in spin state calculations of

Fe(III)-complexes.[122–125] Furthermore, this functional was also employed in the DFT study of alkoxo-Fe(III)-salen complexes.[102] To substantiate the results, the calculations were repeated using the PBE0[126] and OPBE[127,128] functionals. Both these functionals have been tested and found to perform well in DFT calculations of spin splittings in Fe(III)-complexes.[123,125,129,130]

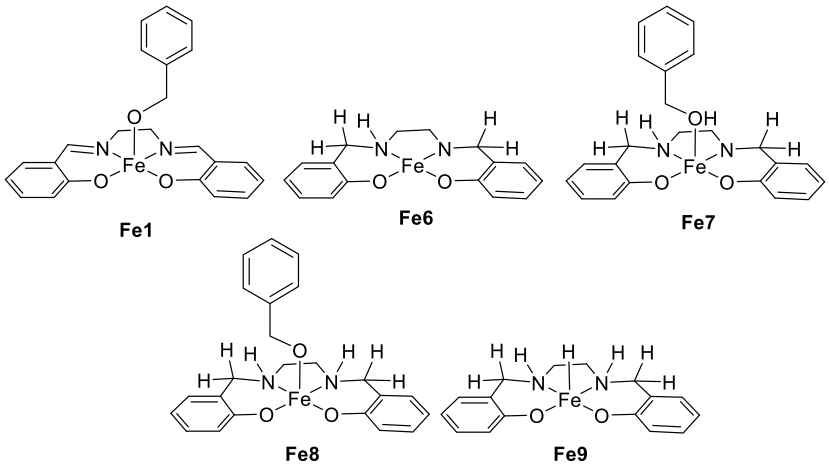

Figure 2.22: Structures of the Fe(III)-complexes included in the study of Fe(III) spin multiplicity.

The calculated electronic energies relative to the energy of the sextet configuration is shown in Table 2.1. The absolute electronic energies can be found in Figure 2.56 in section 2.6.4.

Table 2.1: Electronic energies in kcal mol^{-1} relative to the sextet configuration.

PBE0	doublet	quartet	sextet
Fe1	21.34886816	13.82514776	0
Fe6	13.65350987	-1.78127606	0
Fe7	22.31782971	1.907175572	0
Fe8	25.37718174	14.31665808	0
Fe9	11.62954876	9.475025455	0

OPBE	doublet	quartet	sextet
Fe1	8.250414119	6.064077434	0
Fe6	12.07311753	-3.8576971	0
Fe7	13.8581066	-2.00790114	0
Fe8	19.18497577	9.515531327	0
Fe9	1.787391457	1.610048931	0

B3LYP	doublet	quartet	sextet
Fe1	14.63658742	9.720783666	0
Fe6	7.491760809	-4.78139644	0
Fe7	18.73776921	-0.70029092	0
Fe8	19.13914698	11.47090212	0
Fe9	5.454474512	6.019869061	0

Evidently, the doublet state is energetically unfeasible across whole range of intermediates. For **Fe1**, **Fe8** and **Fe9**, the sextet is predicted to be the ground state by all three functionals. For **Fe6**, the quartet state is slightly favored (2 – 5 kcal mol^{-1}) by all three functionals and for **Fe7**, the OPBE and B3LYP functionals favor the quartet slightly, whereas the PBE0 functional predicts the sextet to be the ground state.

Ultimately, the possibility of a quartet ground state for intermediates containing an amido ligand (**Fe6** and **Fe7**) cannot be excluded, but spin changes during the catalytic cycle were deemed too complicated to account for. For the sake of simplicity, the ground state of all Fe(III) intermediates was therefore assumed to be the sextet in all further models.

2.3.2. Formation of octahedral complexes

With the establishment of the ground state spin multiplicity, the question of additional ligand coordination was tackled. Both cyclohexylamine and benzyl alcohol are present in excess compared to the catalyst, so the coordination of an additional axial ligand was hypothesized. It was experimentally established that reduction of the imino-bridges in the Fe(III)-salen scaffold takes place during the catalytic cycle. Therefore, coordination of benzyl alcohol and cyclohexylamine to both Fe(III)-salen and Fe(III)-salan intermediates was investigated with DFT calculations. The investigated equilibria are shown in Figure 2.23. The computational details can be found in section 2.6.4.

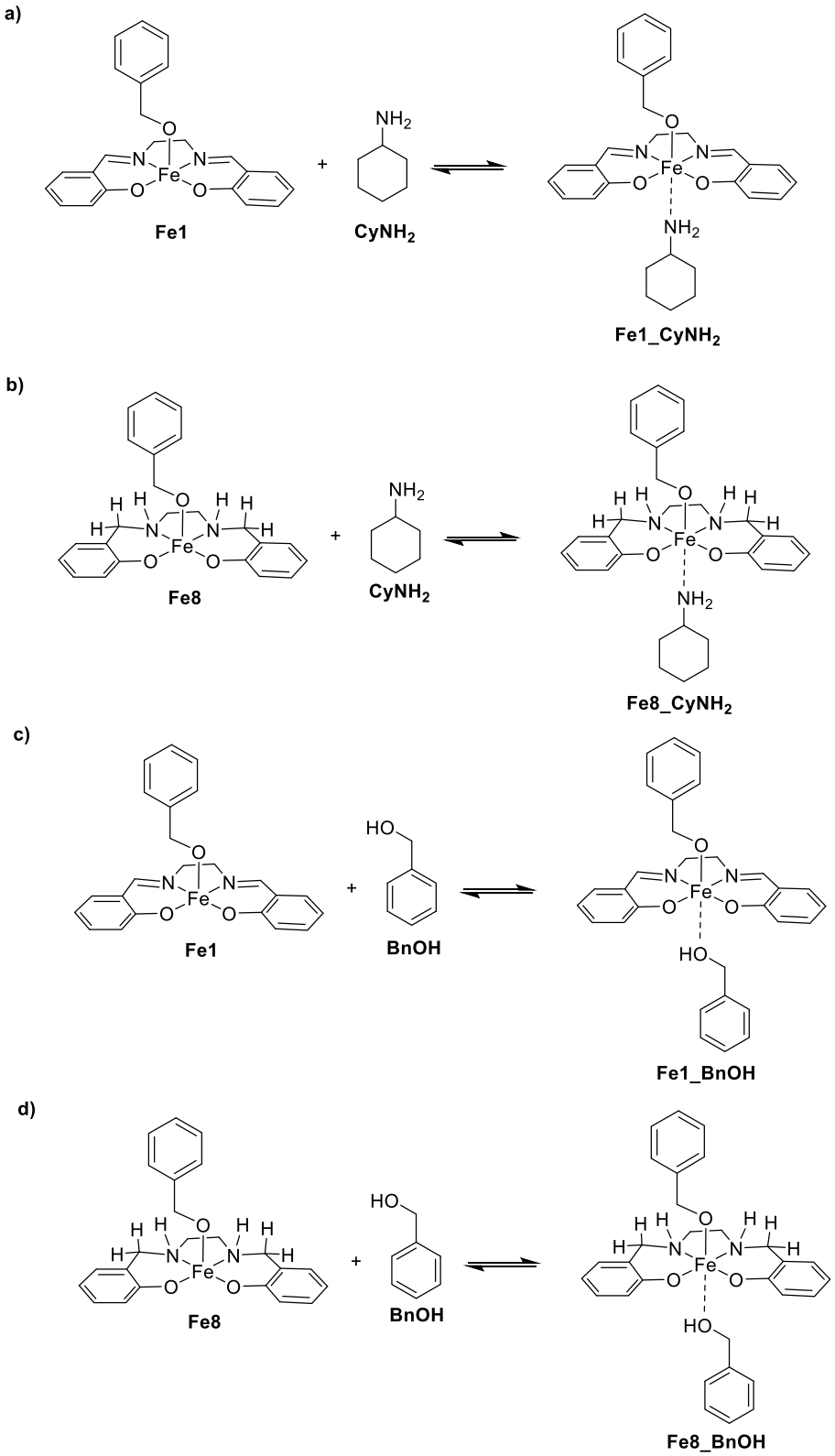

Figure 2.23: Equilibria of cyclohexylamine and benzyl alcohol coordinating to alkoxo-Fe(III)-salen and alkoxo-Fe(III)-salan complexes.

The calculated free energies of the structures in Figure 2.23 are presented in Table 2.2.

Table 2.2: Calculated free energies of the structures in Figure 2.23. The B3LYP-D3BJ\\def2-TZVP method was used with the SMD solvation model in toluene. The temperature was set to the boiling point of toluene (383 K).

Entry	ΔG(**Fe1**) + ΔG($CyNH_2$) / kcal mol^{-1}	ΔG(**Fe1_CyNH$_2$**) / kcal mol^{-1}	ΔG_{bind} (kcal mol^{-1})
a)	-1743588.409	-1743580.078	+8.331
Entry	ΔG(**Fe8**) + ΔG($CyNH_2$) / kcal mol^{-1}	ΔG(**Fe8_CyNH$_2$**) / kcal mol^{-1}	ΔG_{bind} (kcal mol^{-1})
b)	-1745068.803	-1745056.752	+12.05
Entry	ΔG(**Fe1**) + ΔG(BnOH) / kcal mol^{-1}	ΔG(**Fe1_BnOH**) / kcal mol^{-1}	ΔG_{bind} (kcal mol^{-1})
c)	-1778487.295	-1778476.104	+11.19
Entry	ΔG(**Fe8**) + ΔG(BnOH) / kcal mol^{-1}	ΔG(**Fe8_BnOH**) / kcal mol^{-1}	ΔG_{bind} (kcal mol^{-1})
d)	-1779967.688	-1779959.141	+8.547

In all cases, the coordination of either cyclohexylamine or benzyl alcohol is disfavored by 8 – 12 kcal mol^{-1}. Based on this result, the coordination of benzyl alcohol or cyclohexylamine to **Fe1** and **Fe8** to form octahedral intermediates does not seem likely. These DFT results are also corroborated by the fact that Fe(III)-salen complexes with anionic *O*-donor ligands were found to favor square pyramidal geometry.[102,131,132]

2.3.3. Activation of catalyst

With the observation of reduction of the Fe(III)-salen catalyst to Fe(III)-salan within the first 30 minutes of reaction (see section 2.2.5), an activation mechanism analogous to the mechanism proposed for the Mn(III)-salen catalyst was calculated with DFT.[1] To enable easy comparison to the calculations for the Mn(III)-salen mechanism, the B3LYP-D3\\LACVP** method was used. Further computational details can be found in section 2.6.4.

Due to the heavily basic reaction conditions and the comparatively weak coordination of chloride, the chloride present in the catalyst was assumed to be rapidly replaced by benzyl oxide, resulting in the starting structure **Fe1**. From **Fe1**, a series of H^- and H^+ transfers can lead to the amido-Fe(III)-salan **Fe6**, which is the hypothesized starting point of the catalytic cycle.

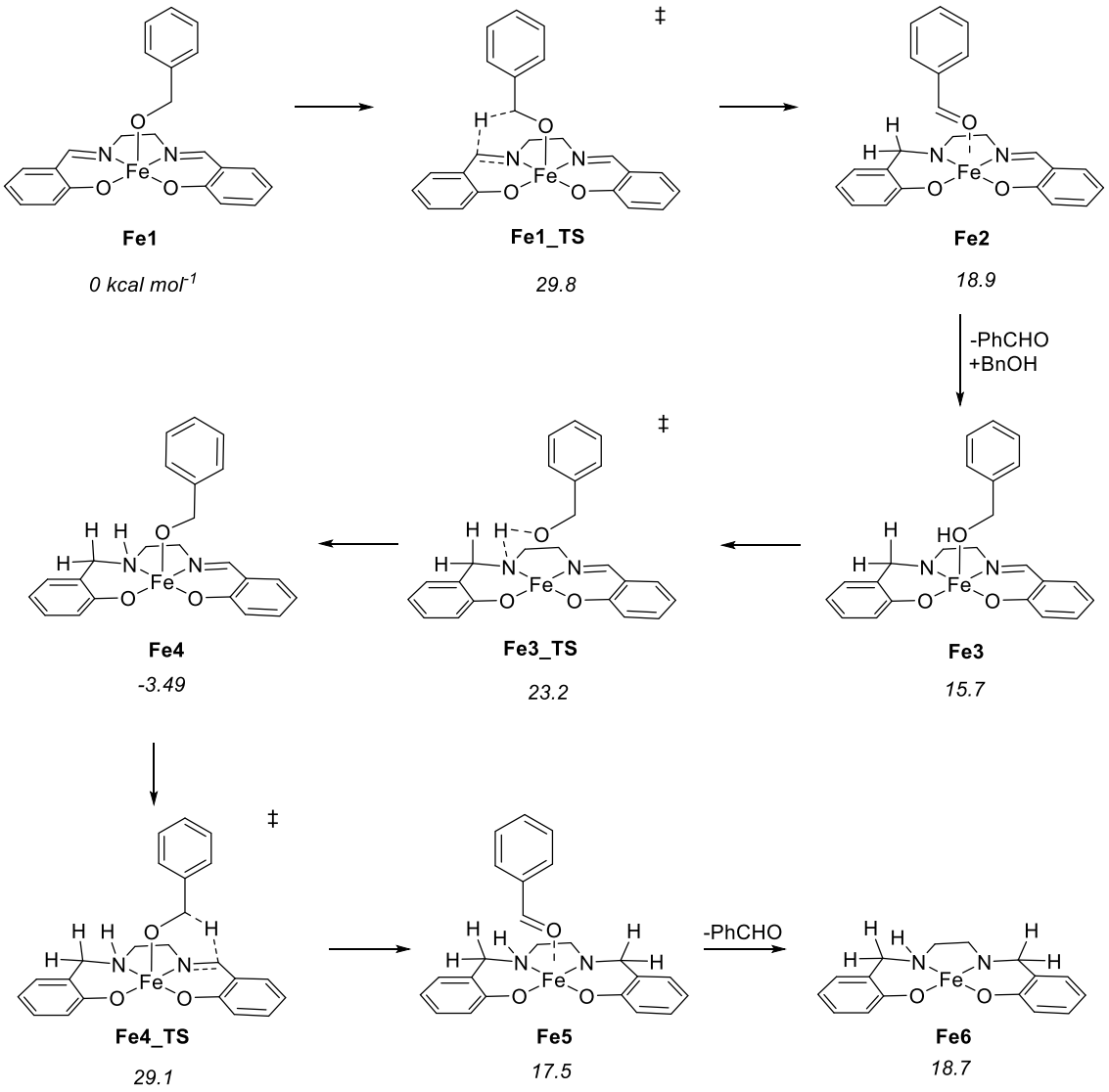

Figure 2.24: DFT-calculated activation mechanism based on square pyramidal Fe(III)-salen intermediates. The full computational details can be found in section 2.6.4.

It is worth noting the high activation energies of the H^- transfers to the ligand backbone. The initial hydride transfer (**Fe1→Fe1_TS**) presents a barrier of 29.8 kcal mol^{-1} and the subsequent hydride transfer (**Fe4→Fe4_TS**) presents a barrier of 32.6 kcal mol^{-1}. Comparatively, the same transitions for the Mn(III)-salen system presented much lower barriers of 17.6 kcal mol^{-1} and 19.7 kcal mol^{-1}, respectively. Therefore, the experimentally observed rapid reduction to form the Fe(III)-salan catalyst is not compatible with the high activation energies presented in Figure 2.24. Despite this conundrum, further calculations were employed in the mechanistic investigation of the catalyst activation.

Due to the calculated high activation energies, it was hypothesized that the catalyst activation could be rate-determining. Consequently, the kinetic isotope effect and a Hammett plot was calculated based on the transition **Fe4→ Fe4_TS**. The calculated KIE was 2.9 (Figure 2.26), which is in poor agreement with the experimentally observed values of 1.34 and 1.36. The calculated Hammett plot (Figure 2.25) had a slope of -1.53 and is not in good agreement with the experimentally determined slope of -0.80.

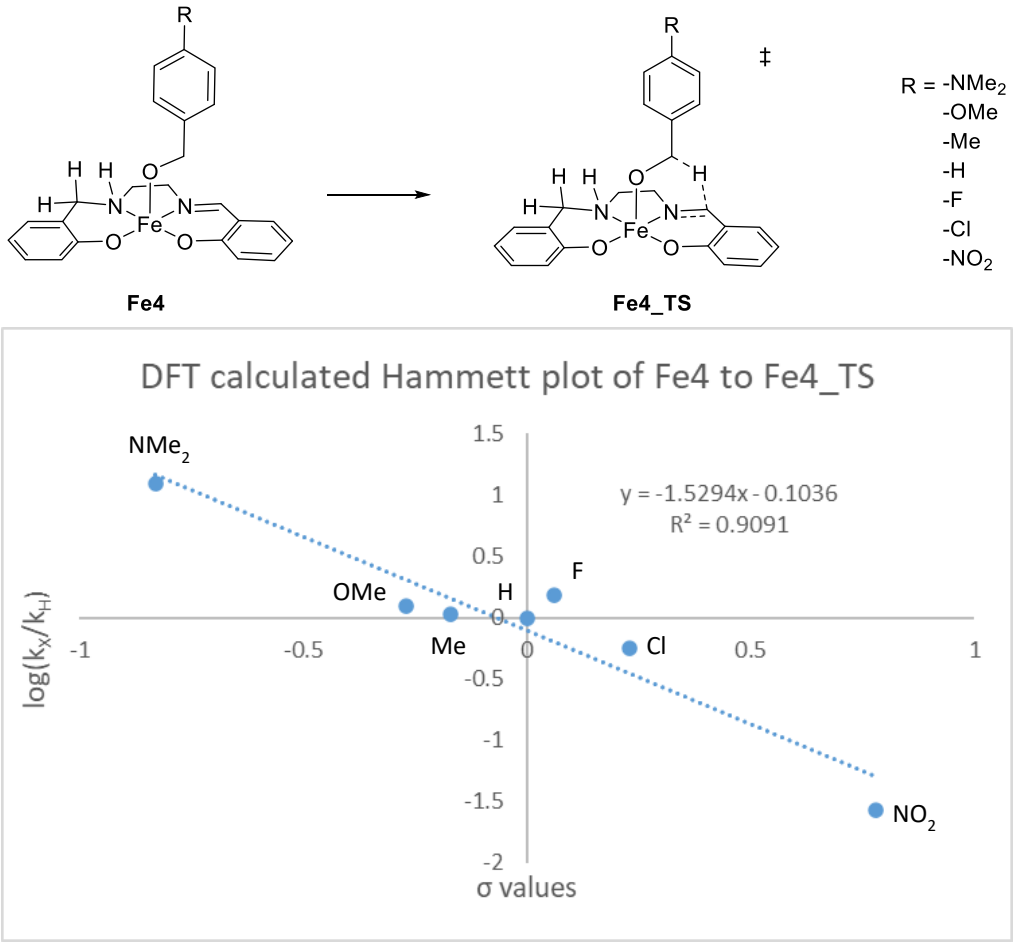

Figure 2.25: DFT calculated Hammett plot of the **Fe4→Fe4_TS** transition.

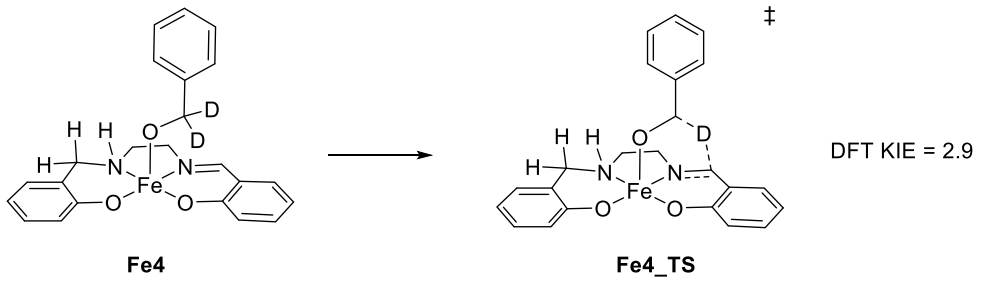

Figure 2.26: The DFT calculated KIE value for the **Fe4→Fe4_TS** transition was 2.9.

Ultimately, the proposed activation pathway does not reflect the experimental findings adequately, and the reason for this will become apparent later in the chapter.

2.3.4. Catalytic cycle with formation of Fe-H intermediate

Despite the high energy barriers presented in the activation mechanism, a full catalytic cycle analogous to the proposed catalytic cycle of the Mn(III)-salen system was calculated. The resulting catalytic cycle is shown in Figure 2.27.

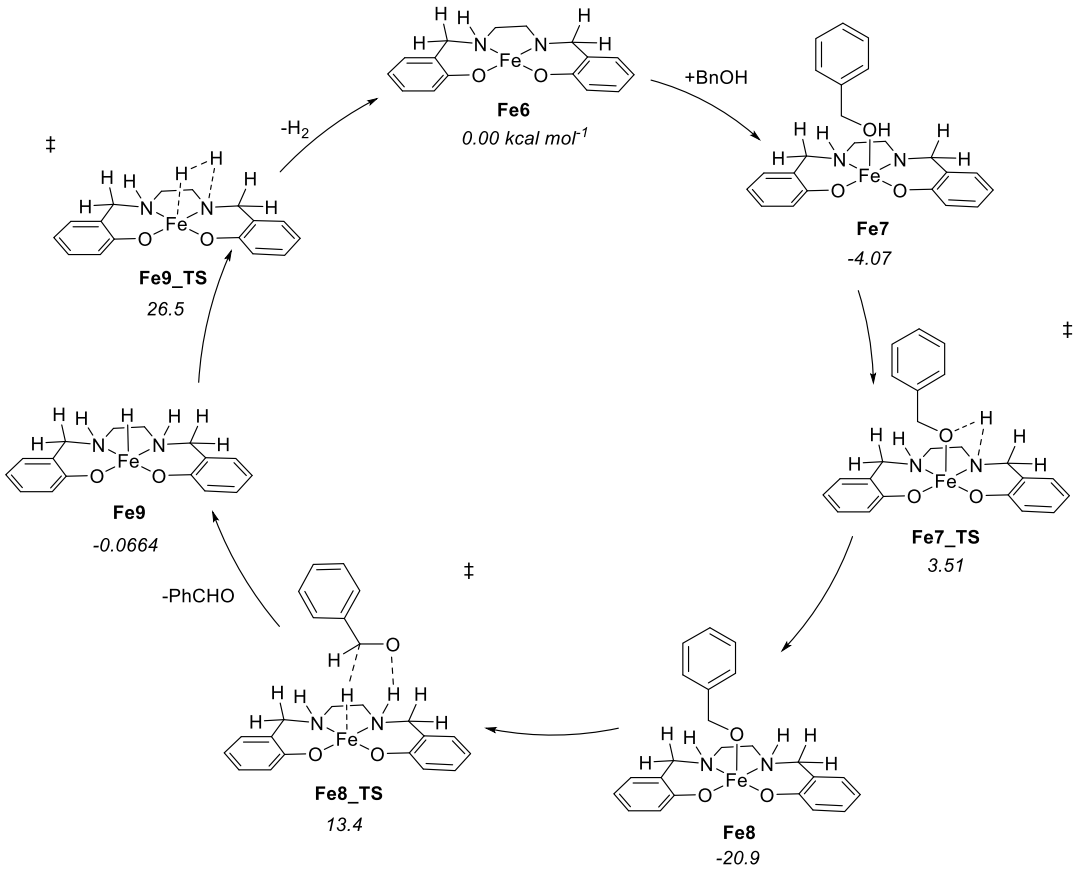

Figure 2.27: Calculated catalytic cycle of the Fe(III)-salen system analogous to the Mn(III)-salen system.

Starting from structure **Fe6**, coordination of benzyl alcohol followed by proton transfer from the alcohol to the amido nitrogen is highly energetically favored. Consequently, **Fe8** is predicted to be the resting state with a relative energy of -20.9 kcal mol^{-1}. **Fe8** is surprisingly stable, especially when compared to the analogous Mn(III)-salen mechanism where the Mn(III) variant of structure **Fe8** only had a relative energy of -0.5 kcal mol^{-1}.[1]

Due to the high stability of the **Fe8** intermediate, the subsequent outer-sphere H^- transfer (**Fe8_TS**) leading to formation of **Fe9** presents a high energy barrier of 34.3 kcal mol^{-1}. Closing the catalytic cycle by exclusion of H_2 through **Fe9_TS** results in the most energetically demanding transition with an energy span of 47.4 kcal mol^{-1}. Ultimately, the catalytic cycle outlined in Figure 2.27 is unlikely to be operative. Alternative explanations for the observed catalysis were therefore sought.

2.3.5. Calculation of Hammett plot and kinetic isotope effect

Even though the outer-sphere H^- transfer to the Fe(III)-center was not identified as the most energetically demanding transition, the breakage of the benzylic C-H bond (**Fe8→Fe8_TS**) was granted computational attention. This was done because the experimental Hammett study exhibited a negative slope of -0.8, which could indicate that breakage of the benzylic C-H is rate-determining. Consequently, a theoretical Hammett plot of the **Fe8→Fe8_TS** transition was calculated, which resulted in a slope of -0.94. The calculated Hammett plot is shown in Figure 2.28.

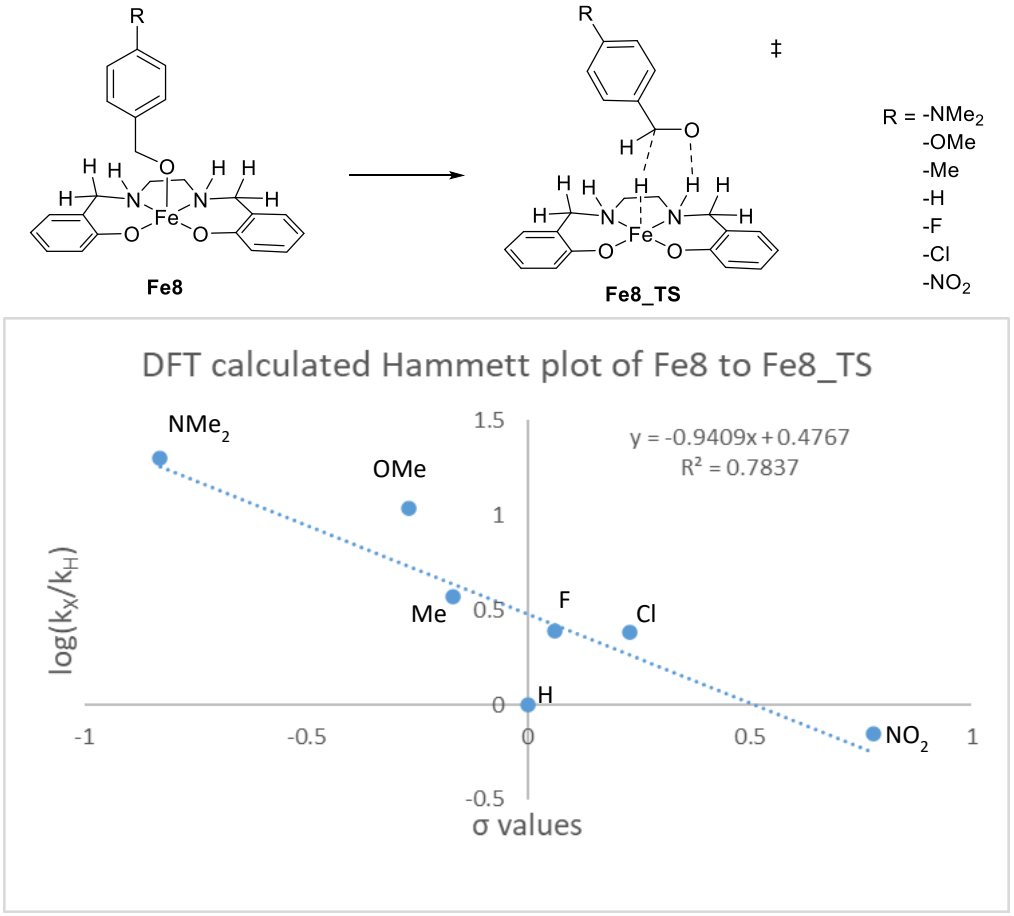

Figure 2.28: Calculated Hammett plot of the **Fe8→Fe8_TS** transition

The high similarity of the experimental and theoretical Hammett slope is thought to be coincidental as the kinetic isotope effect of the **Fe8→Fe8_TS** transition was calculated to 4.1 (Figure 2.29), which differs significantly from the experimentally determined values of 1.34 and 1.36.

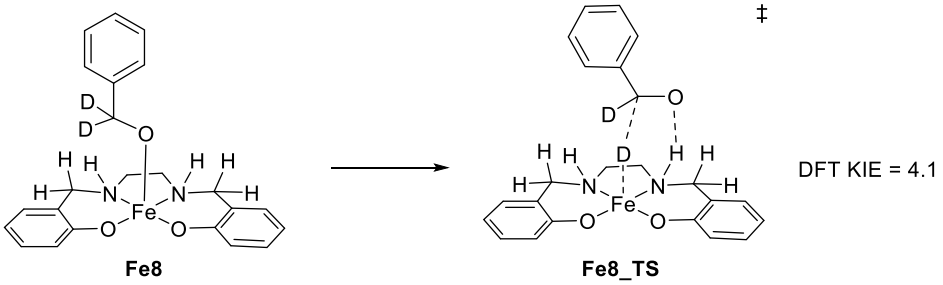

Figure 2.29: The DFT calculated KIE value for the **Fe8→Fe8_TS** transition was 4.1.

2.3.6. Catalytic cycle without formation of Fe-H intermediate

Due to the high energy barriers in the DFT model presented in Figure 2.27, an alternative reaction mechanism outlined in Figure 2.30 was hypothesized.

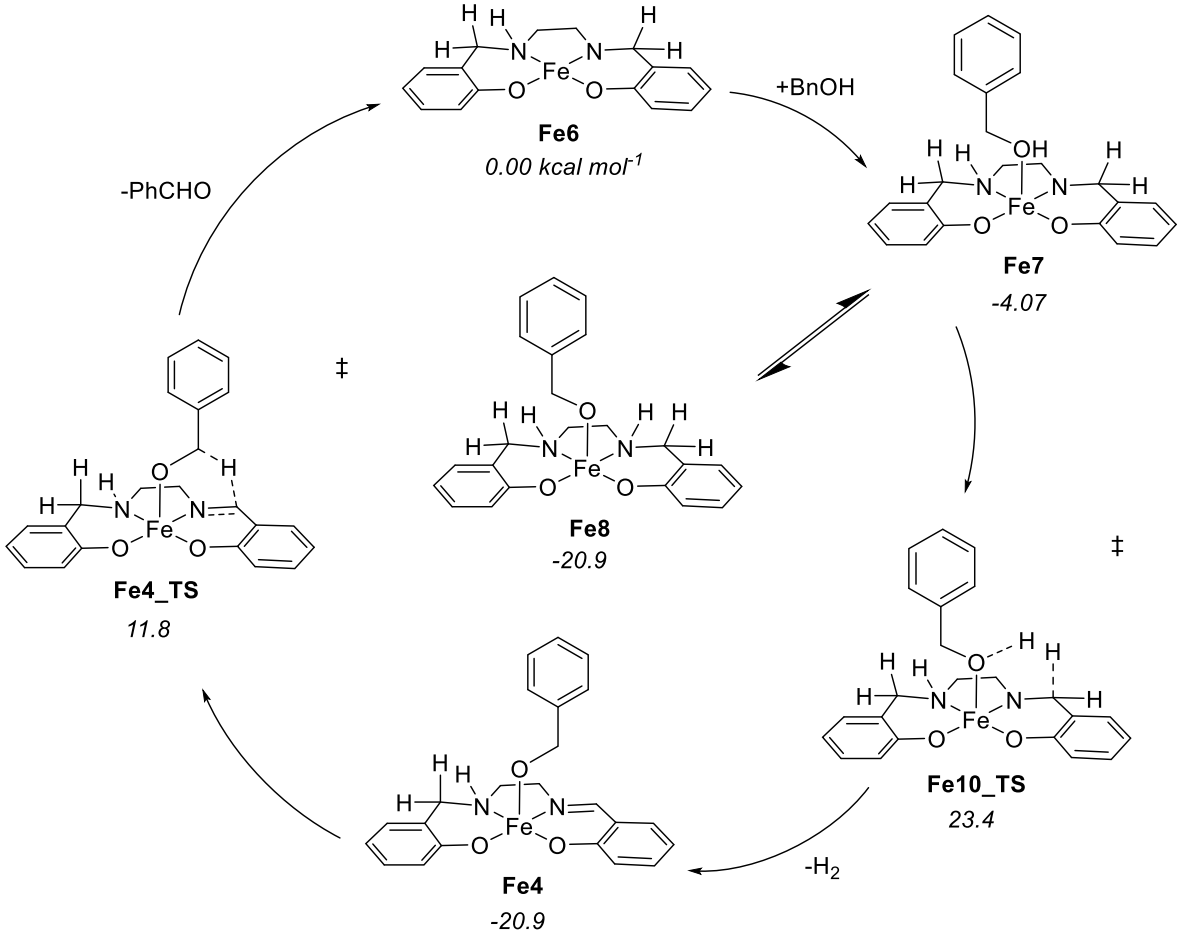

Figure 2.30: Alternative catalytic cycle with oxidation of the Fe(III)-salan backbone by reacting the a H^+ of benzyl alcohol with a H^- of the ligand backbone.

In this proposed catalytic cycle, an equilibrium between **Fe7** and **Fe8** is envisioned. The relative energies reveal that **Fe8** is energetically favored to the point where no appreciable concentration of **Fe7** is likely. Despite this, a direct transfer of H^+ from the alcohol of **Fe7** to the H^- equivalent in the ligand backbone was modelled. This step would oxidize the ligand back to **Fe4** and enable another hydride transfer from benzyl alkoxide (**Fe4_TS**), thereby closing the catalytic cycle. However, the transition state **Fe10_TS** was located with a relative energy of 23.4 kcal mol^{-1}. The overall energy span from **Fe8** to **Fe10_TS** is therefore 44.3 kcal mol^{-1}, which is too high to render this mechanism likely.

2.3.7. Key transitions with octahedral intermediates

So far, none of the presented mechanisms based on 5-coordinate complexes were found likely by DFT. Therefore, the search for a plausible reaction mechanism was extended to octahedral Fe(III)-salen and Fe(III)-salan derivatives, even though their formation seemed unlikely in the initial DFT studies.

The key transitions involving breakage of the benzylic C-H bond were recalculated for a range of octahedral complexes containing either an axial NH_3 ligand or a BnO^- ligand. The modelled transitions and their calculated activation energies are shown in Figure 2.31.

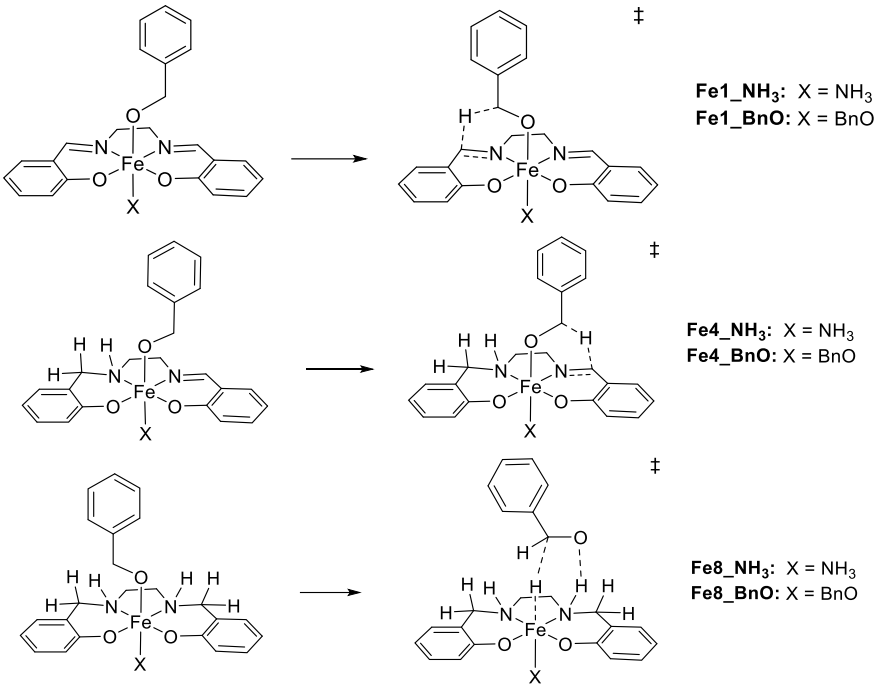

Entry	ΔG_{react} / kcal mol^{-1}	ΔG_{TS} / kcal mol^{-1}	$\Delta G^{\ddagger}$ / kcal mol^{-1}
Fe1	-845804.8224	-845774.9884	29.83
Fe1_NH3	-881302.5230	-881278.2244	24.30
Fe1_BnO	-1063096.562	-1063077.194	19.37
Fe4	-846552.9969	-846520.3855	32.61
Fe4_NH3	-882048.0414	-882025.0869	22.95
Fe4_BnO	-1063847.533	-1063827.143	20.39
Fe8	-847296.3793	-847262.1171	34.26
Fe8_NH3	-882795.8422	-882764.4654	31.38
Fe8_BnO	-1064599.727	-1064570.788	28.94

Figure 2.31: DFT modelling of the key H^- transfers in octahedral intermediates.

Evidently, the octahedral models with NH_3 and BnO^- result in dramatically lowered activation energies for the two initial H^- transfers to the ligand backbone. The effect is most pronounced for the BnO^- ligand, where the barrier for the 1st H^- transfer is lowered by ~10.5 kcal mol^{-1} compared to the 5-coordinate model and the barrier for the 2nd H^- transfer is lowered by ~12.2 kcal mol^{-1} compared to the 5-coordinate model. Rapid activation of the catalyst is observed experimentally,

and a possible explanation could be adoption of an octahedral coordination geometry during the catalyst activation, even though the previous DFT calculations suggested that coordination of neutral benzyl alcohol or cyclohexylamine was energetically unfeasible.

Upon investigation of the outer-sphere H^- transfer to the Fe(III)-center (**Fe8→Fe8_TS)**, lower activation energies are also observed with axial NH_3 and BnO^- ligands compared to the 5-coordinate model. The effect is not as dramatic as observed for the initial hydride transfers; a decrease in activation energy of ~2.9 kcal mol^{-1} is calculated for NH_3 and a decrease of 5.3 kcal mol^{-1} is calculated for BnO^-. Thus, the lowest energy barriers are associated with the octahedral BnO^- variant, which was not included in the initial DFT study of 5- vs. 6-coordinate intermediates. Consequently, a catalytic cycle based on the overall anionic, octahedral BnO^- derivative was constructed and the result is shown in Figure 2.32.

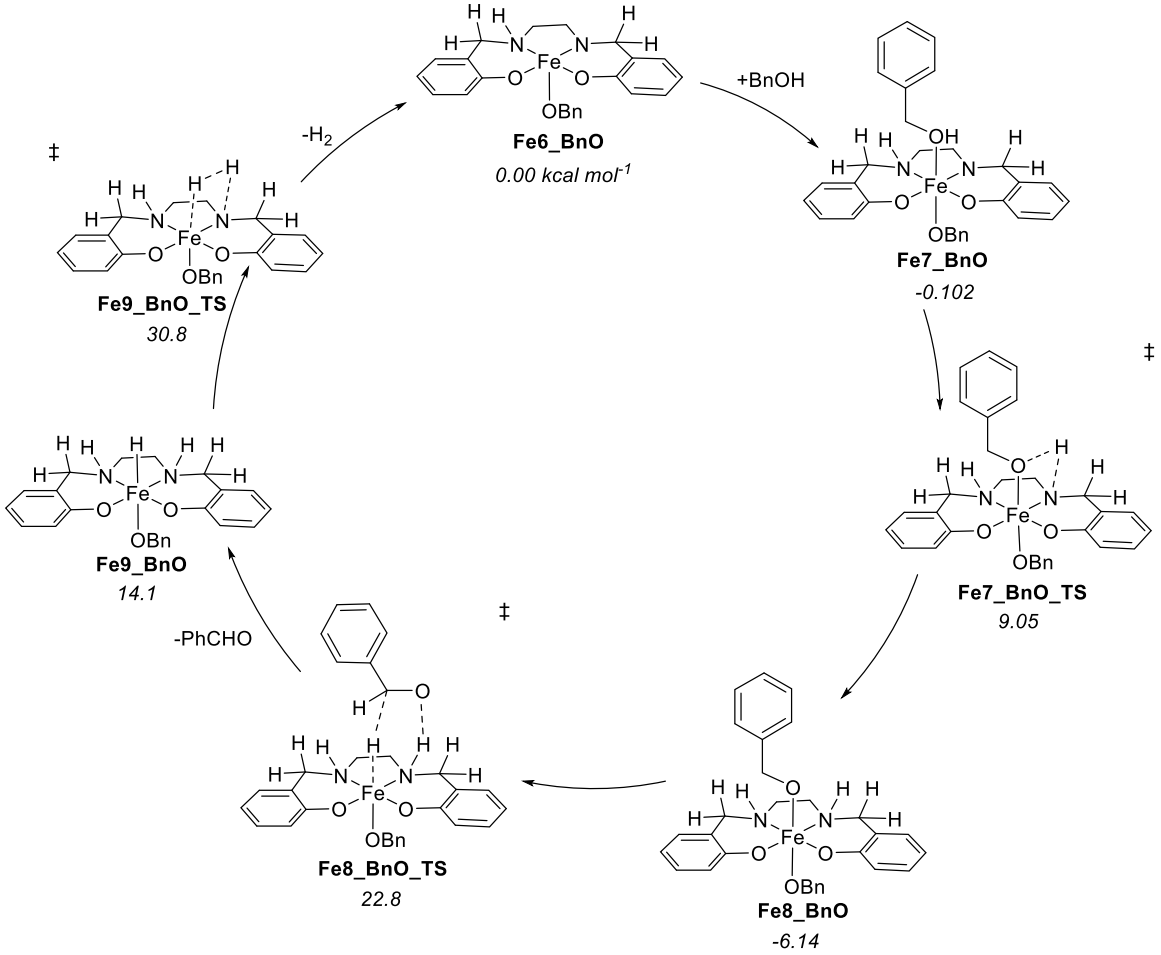

Figure 2.32: Anionic, octahedral BnO^- variant of the Fe(III)-salan catalytic cycle.

Coordination of BnOH to the amido complex **Fe6_BnO** is slightly favored by -0.1 kcal mol^{-1}, and the subsequent H^+ transfer to form **Fe8_BnO** is deemed likely as the transition is exergonic with a relatively low barrier of ~9 kcal mol^{-1}. It is noteworthy that the resting state **Fe8_BnO** now only presents a relative energy of -6.14 kcal mol^{-1}, which is much less stable compared to the analogous **Fe8** in Figure 2.27. Therefore, a low-lying minimum on the energy

surface is not predicted in the BnO^--ligated model, but the formation of the Fe(III)-hydride species **Fe9_BnO** remains highly endergonic with a barrier ~28.9 kcal mol^{-1}.

Analogous to the model of the 5-coordinate catalytic cycle (Figure 2.27), the exclusion of H_2 through **Fe9_BnO_TS** presents the highest barrier on the energy surface and is therefore the most energetically demanding transition with an overall energy span of 36.9 kcal mol^{-1}. Even though this is a marked improvement compared to the 5-coordinate catalytic cycle, the barriers are still deemed too high to render the catalytic cycle outlined in Figure 2.32 operative.

For the sake of completeness, the KIE of the **Fe8_BnO→Fe8_BnO_TS** transition was calculated (Figure 2.33).

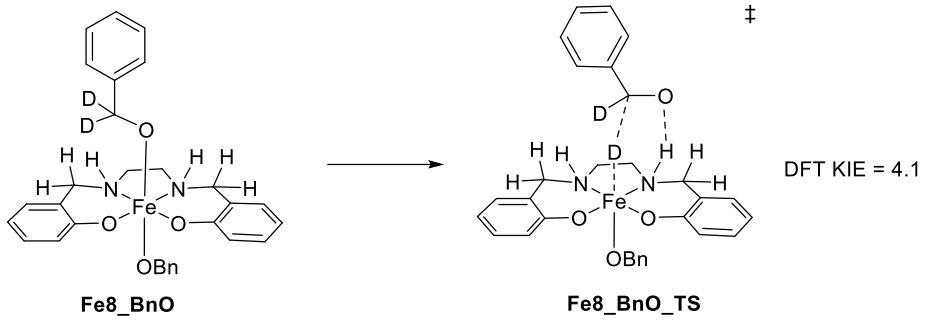

Figure 2.33: The DFT calculated KIE value for the **Fe8_BnO→Fe8_BnO_TS** transition was 4.1.

Interestingly, the DFT calculated KIE of 4.1 is identical to the value calculated for same transition in the 5-coordinate model. Still, this theoretical KIE value is not comparable to the experimentally determined values of 1.34 and 1.36.

2.3.8. Summary and conclusion of the computational investigation

The initial DFT calculations indicated that the preferred spin state of Fe(III) in a range of envisioned intermediates was high-spin. Furthermore, the coordination of an additional, neutral ligand in the form of either BnOH or $CyNH_2$ was found energetically unfeasible. Consequently, a reaction mechanism based on 5-coordinate model complexes was calculated by DFT, but the calculated energy barriers for both catalyst activation and different catalytic cycles were found too high to explain the observed reactivity. Furthermore, the calculated KIEs and Hammett plots for selected transitions did not correlate well with the experimentally determined values.

Employing a 6-coordinate model with either NH_3 or BnO^- as axial ligand resulted in lower energy barriers for catalyst activation, but the energy barriers in the catalytic cycle remained insurmountable. Ultimately, the computational study did not provide adequate support for a catalytic mechanism resembling the Mn(III)-salen system, which was originally envisioned. Therefore, the reaction mechanism of the Fe(III)-salen AAD catalysis remained unclear and a return to the laboratory to acquire further experimental evidence was found necessary.

2.4. Return to the laboratory: additional control experiments and investigations

Due to the difficulties producing a computational model that accurately reflected the experimental findings, further experiments were deemed necessary to establish the nature of the active catalyst and probe the reaction mechanism. The experiments in this section were all performed by me. The full experimental details can be found in section 2.6.3.

2.4.1. Radical clock and catalyst poisoning

Even though experiments with addition of radical scavengers such as TEMPO and cyclohexa-1,4-diene had previously been performed and no indication of radical reactivity was found, it was decided to recheck for radical reactivity. Therefore, 2-allylbenzyl alcohol was used as substrate to probe radical reactivity with an intramolecular radical reaction. It has been previously shown in the Madsen group that benzylic radicals can be generated when benzylic alcohols are reacted with KOtBu in boiling mesitylene.[116] Furthermore, it was found remarkable that the only reactive base in the Fe(III)-salen catalyzed imination was KOtBu, when additives such as Ca_3N_2, $MgSO_4$ and Na_2SO_4 gave high yields in the Mn(III)-salen system. A last radical experiment was therefore performed according to Figure 2.34.

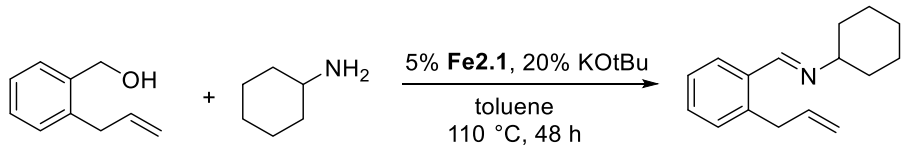

Figure 2.34: Fe(III)-salen imination with 2-allylbenzyl alcohol to investigate radical reactivity.

If benzylic radicals are generated during the catalysis, one should observe cyclization to form a range of possible byproducts shown in Figure 2.35.[116]

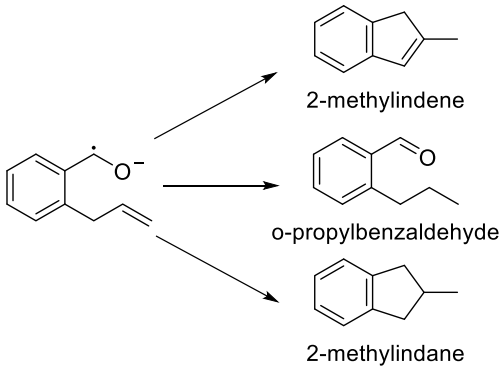

Figure 2.35: Possible byproducts arising from radical reactions of 2-allylbenzyl alcohol.

However, no byproducts were observed by GC-MS analysis; the only observed product was the imine presented in Figure 2.34, which was not quantified. Ultimately, the last radical experiment corroborates the previously performed radical scavenger studies and no radical intermediates seem to be involved in the reaction.

Due to the difficulties devising a molecular catalysis mechanism, the question of homogeneous vs. heterogeneous catalysis was raised. In the early stages of the project, Fabrizio Monda did identify

catalyst derivatives by LC-MS after 30 minutes of reaction, but further characterization of relevant intermediates over the full course of the 48-hour reaction was not performed.[111] Additionally, no attempts to isolate the catalyst after the 48-hour reaction period were made, so the fate of the catalyst remained ambiguous. The suspicions of particle formation during the catalysis were fueled by reports of particle formation when a similar precatalyst was treated KOtBu.[93,133,134] It was therefore decided to perform both a qualitative poisoning experiment with Hg and a sub-stoichiometric poisoning experiment with PMe_3.

The commonly performed Hg drop test is a poisoning experiment used to distinguish homogeneous molecular catalyst from heterogeneous particle catalysis. If particles are the responsible catalyst, the addition of Hg is expected to inhibit the catalysis.[135,136] The poisoning experiment with PMe_3 relies on the addition of a strongly coordinating ligand in sub-stoichiometric amounts. If the reaction is catalyzed by a homogeneous, molecular catalyst, only a minor reduction of the catalytic efficiency is expected due to partial inhibition of the molecular catalyst. However, if particles are formed during catalysis, the number of active sites is assumed to diminish due to aggregation.[93,94] Consequently, even a sub-stoichiometric amount of PMe_3 is expected to significantly inhibit the catalysis.

Therefore, poisoning experiments with addition of PMe_3 (2 mol%) and Hg at both $t = 0$ h and $t = 24$ h were performed (see section 2.6.3 for further details). The observed GC yields are shown in Figure 2.36.

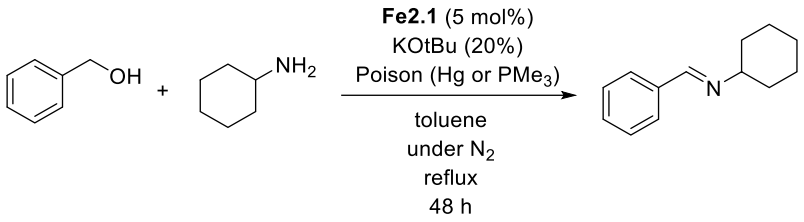

Entry	Poison	Yield (%)
1	None (for reference)	85
2	0.02 mmol PMe_3 (added at 0 h)	15
3	1 drop Hg (added at 0 h)	24
4	0.02 mmol PMe_3 (added after 24 h)	39
5	1 drop Hg (added after 24 h)	41

Figure 2.36: GC-MS yields of *N*-benzylidenecyclohexylamine in the poisoning experiments.

For both poisons, a significant inhibition of catalytic efficiency is observed. This observation indicates that the catalytically active species may be iron particles instead of the expected Fe(III)-salen derivatives. Catalysis with a heterogeneous iron catalyst would also explain the struggles of producing an accurate molecular model of the catalytic cycle. Based on the poisoning experiments, more thorough investigations of the fate of the Fe(III)-salen catalyst were performed with LC-MS.

2.4.2. Reinvestigation of previously recorded LC-MS chromatograms

The observation of Fe(III)-salan species after 30 minutes of reaction does not lend credence to the hypothesis of iron particles catalysis. The LC-MS chromatogram presented in the Ph.D. thesis of Fabrizio Monda was cropped to shown only the region of the chromatogram where Fe(III)-salen derivatives appear (0 – 1.2 min).[111] The whole chromatogram originally recorded by Fabrizio Monda is shown in Figure 2.37 and contains further information.

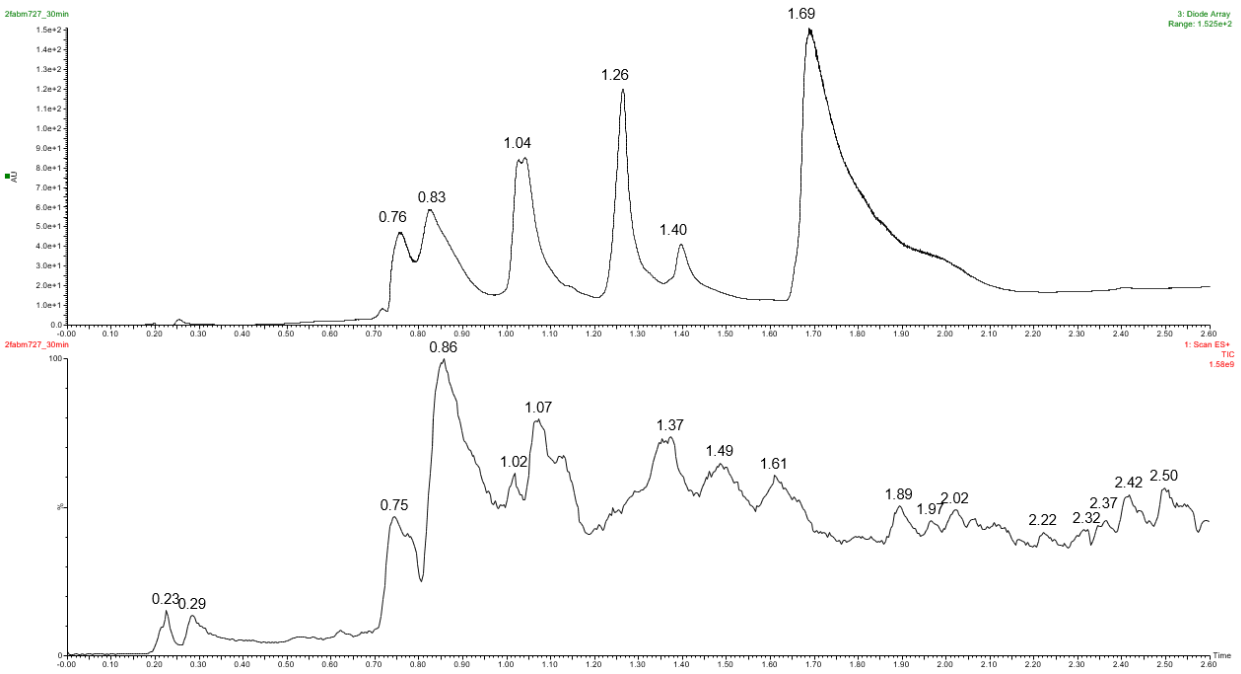

Figure 2.37: LC-MS chromatogram of the Fe(III)-salen reaction mixture after 30 minutes. Original data recorded by Fabrizio Monda. Top: UV-VIS chromatogram. Bottom: Total ion chromatogram (TIC).

The UV-VIS chromatogram contains several well-defined peaks, whereas the total ion chromatogram (TIC) indicates a highly complex mixture. Through investigation of the mass spectra at different retention times, possible catalytic intermediates or degradation products can be tentatively identified.

The mass spectrum of the region around 0.86 minutes is shown in Figure 2.38. The mass spectrum shows masses corresponding to products of ligand hydrolysis (206 Da and 221 Da), the fully reduced salan ligand (327 Da), the Fe(III)-salen catalyst (376 Da) and a curious mass of 374 Da. The 374 Da mass is tentatively assigned to a cyclohexene derivative of the Fe(III)-salen catalyst. It is currently unclear how this complex may be formed during the reaction, but the formation of a fully conjugated backbone could be a major driving force for the alkene formation.

Looking further into the chromatogram, the mass spectrum of the region around 1.0 – 1.1 minutes was examined. The resulting mass spectrum is shown in Figure 2.39 and several peaks corresponding to ligand hydrolysis (219 Da, 221 Da and 305 Da) and ligands with varying backbones (321 Da, 325 Da, 327 Da) were identified. Furthermore, masses corresponding to the fully reduced Fe(III)-salan complex (380 Da) and the previously assigned cyclohexene derivative of the Fe(III)-salen complex (374 Da) were found.

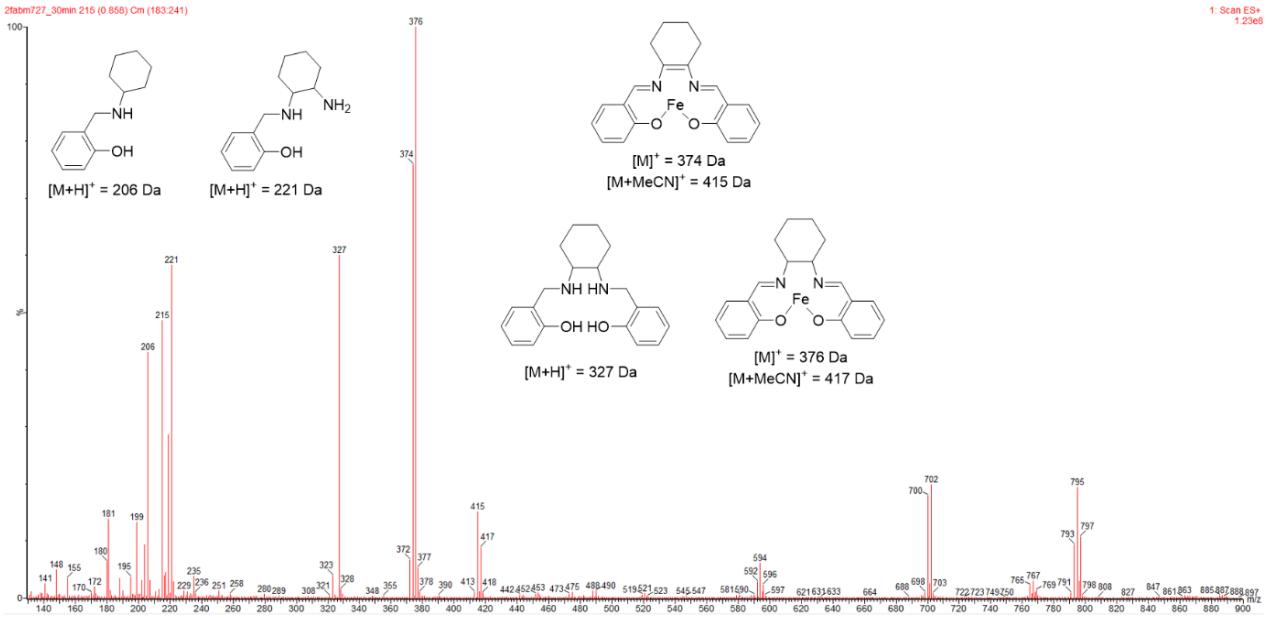

Figure 2.38: Mass spectrum of the region between 0.8 – 0.9 minutes. Masses corresponding to the fully reduced salan ligand, the Fe(III)-salen complex and possibly a cyclohexene derivative of the Fe(III)-salen complex were identified. Masses arising from hydrolysis of the ligand were also found.

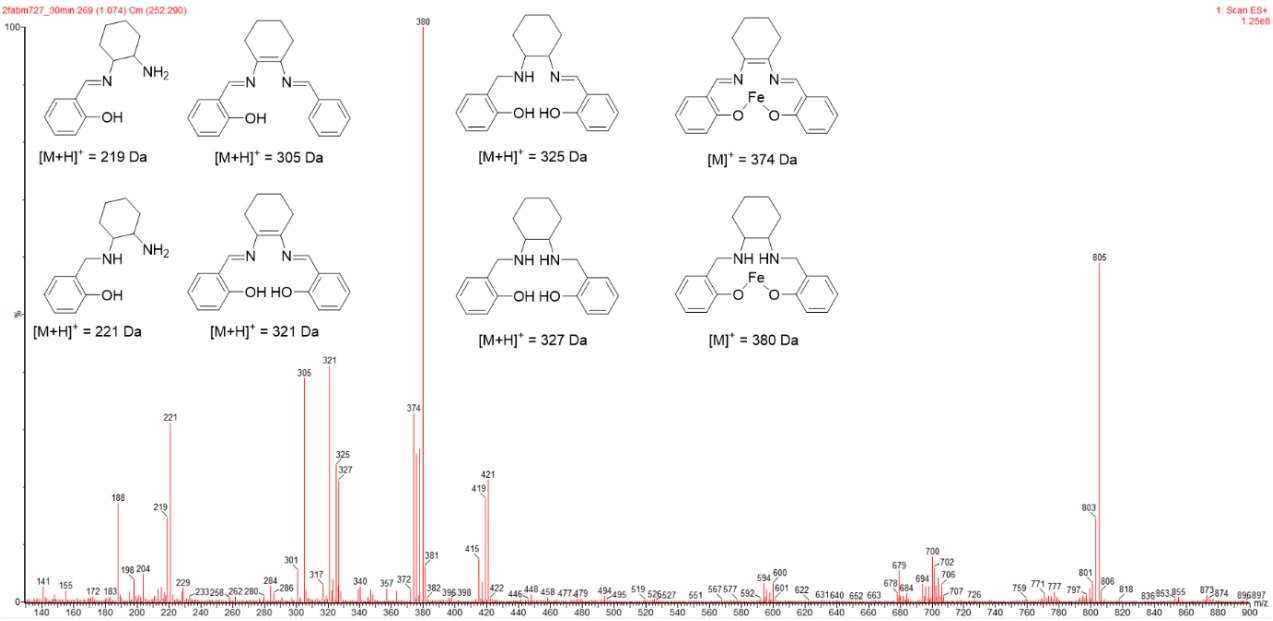

Figure 2.39: Mass spectrum of the region between 1.0 – 1.1 minutes. Masses corresponding to ligand hydrolysis products and various ligand derivatives were identified. Masses corresponding to the fully reduced Fe(III)-salan complex and a cyclohexene derivative of the Fe(III)-salen complex were identified.

Lastly, the mass spectrum of the region between 1.2 – 1.4 minutes and the mass spectrum of the region between 1.6 – 1.8 minutes were examined. The mass spectra are shown in Figure 2.40 and Figure 2.41, respectively.

Figure 2.40: Mass spectrum of the region between 1.2 – 1.4 minutes. The most prominent mass of 204 Da is assigned to the imine formed by coupling of cyclohexylamine and salicylaldehyde arising from hydrolysis of the salen ligand.

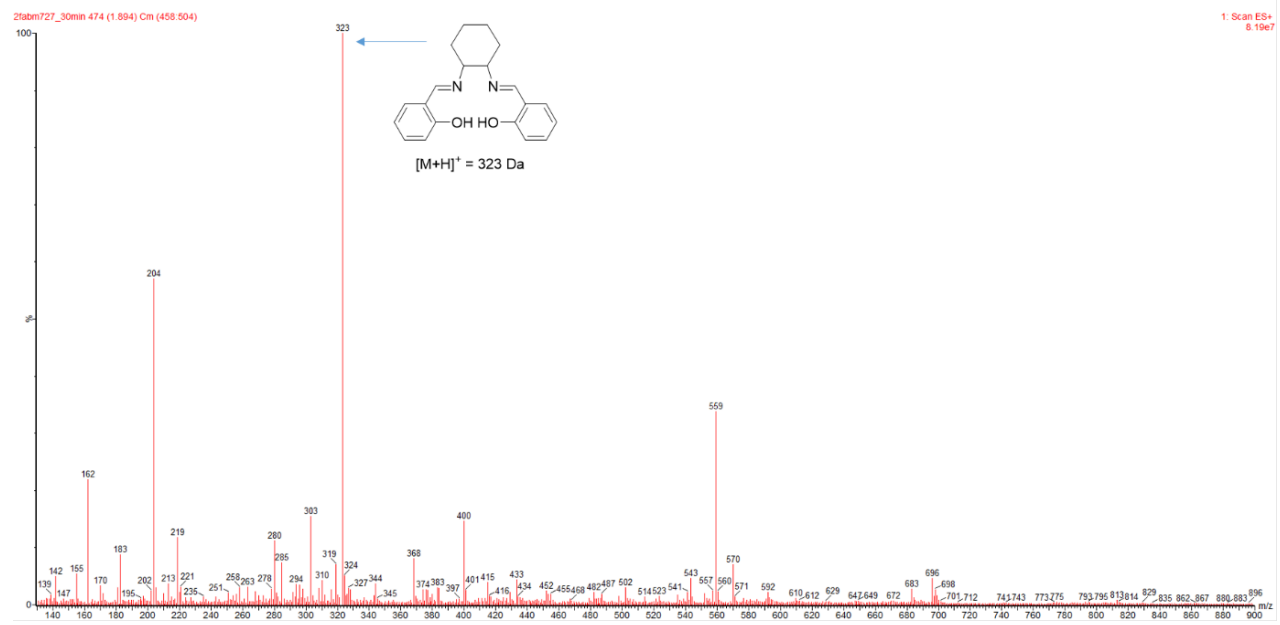

Figure 2.41: Mass spectrum of the region between 1.6 – 1.8 minutes. The most prominent mass of 323 Da corresponds to the free salen ligand.

The region between 1.2 – 1.4 minutes reveals the imine resulting from reaction between cyclohexylamine and salicylaldehyde stemming from ligand hydrolysis. The region between 1.6 – 1.8 minutes is dominated by a mass of 323 Da, which corresponds to the free salen ligand.

Upon re-examination of the original LC-MS chromatograms of the Fe(III)-salen system, a chromatogram of the same reaction measured by Fabrizio Monda after 18 hours of reaction was found. The original chromatogram is shown in Figure 2.42.

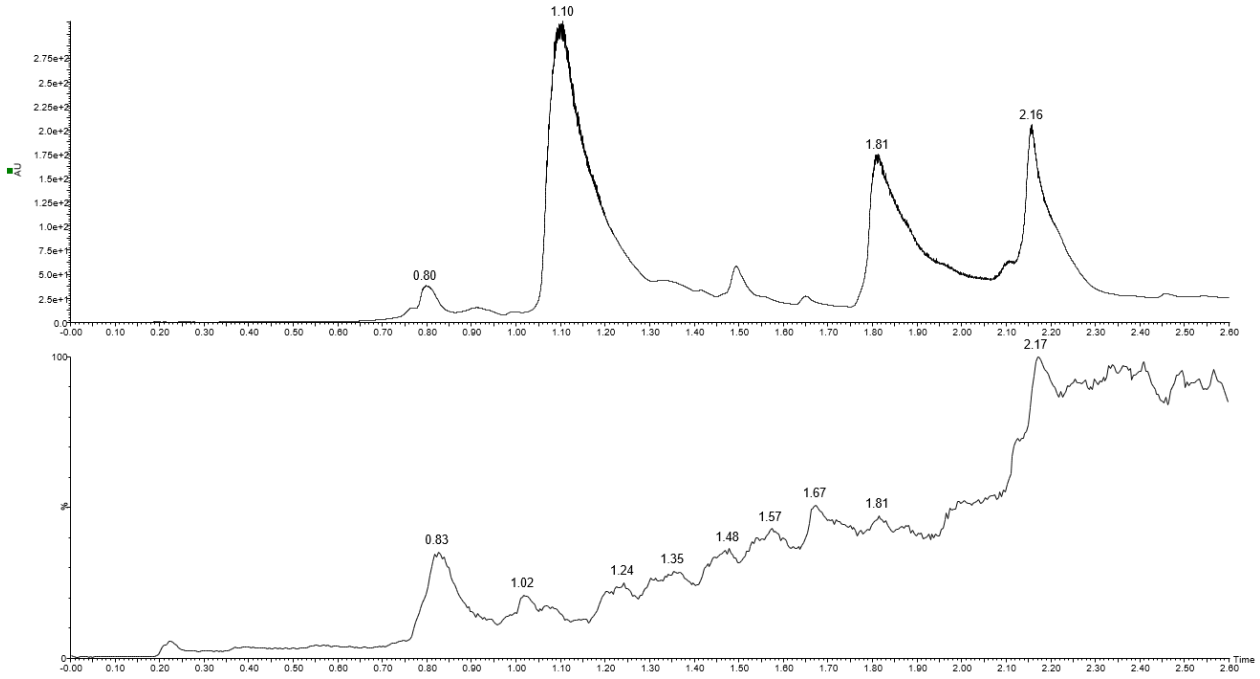

Figure 2.42: LC-MS chromatogram of the Fe(III)-salen reaction mixture after 18 hours. Original data recorded by Fabrizio Monda. Top: UV-VIS chromatogram. Bottom: Total ion chromatogram (TIC)

The integrated mass spectrum of the region between 0.8 – 1.0 minutes is shown in Figure 2.43.

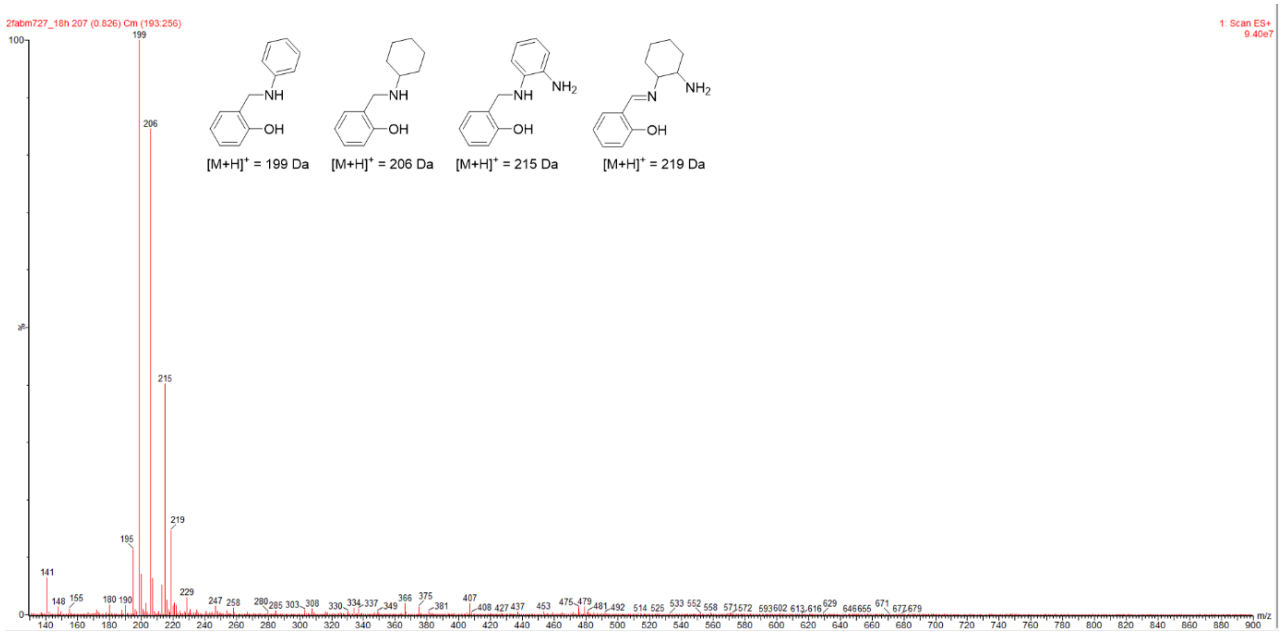

Figure 2.43: Mass spectrum of the region between 0.8 – 0.9 minutes. Masses corresponding to any Fe(III)-salen derivatives could no longer be identified in this region of the chromatogram. The observed low masses (199 Da, 206 Da, 215 Da and 219 Da) are tentatively assigned to products of ligand hydrolysis and oxidative dehydrogenation.

Notably, the Fe(III)-salen derivatives that were identified in this region of the chromatogram in the sample taken after 30 minutes could no longer be located after 18 hours. Instead, several low masses (199 Da, 206 Da, 215 Da and 219 Da) attributed to products of ligand hydrolysis and oxidative dehydrogenation were present. Products arising from oxidation of the cyclohexyl backbone are tentatively assigned, but there are examples of iron-based nanoparticles acting as catalysts for oxidative dehydrogenation of *N*-heterocycles under similar reaction conditions to those employed in this project.[85,137]. Lastly, the possible observation of cyclohexene backbones in both the free ligands and the Fe(III)-salen complexes could suggest that oxidative dehydrogenation leading to aniline backbones may be possible under the employed reaction conditions.

A further look into the chromatogram (1.0 – 1.2 minutes) of the reaction mixture after 18 hours results in the mass spectrum shown in Figure 2.44. No evidence of the previously observed intact Fe(III)-salen derivatives were found after 18 hours, and only masses corresponding to products from ligand degradation and oxidative dehydrogenation were observed.

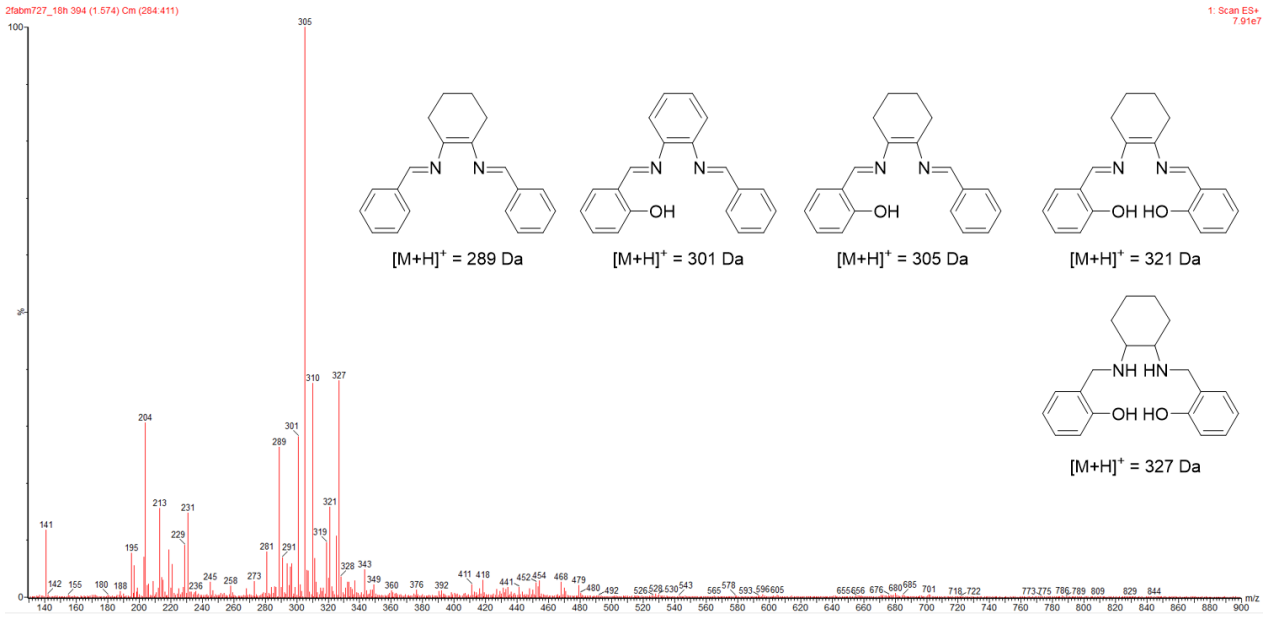

Figure 2.44: Mass spectrum of the region between 1.0 – 1.2 minutes. No masses corresponding to any Fe(III)-salen derivatives were identified in this region of the chromatogram either. The most prominent peaks are thought to result from ligand degradation and oxidative dehydrogenation.

The last region of the chromatogram from 1.8 – 2.2 minutes was combined into a single mass spectrum shown in Figure 2.45. Here, the 188 Da peak corresponds to the target imine, and the 204 Da peak corresponds to the previously observed coupling of salicylaldehyde and cyclohexylamine. Furthermore, the 285 Da and 287 Da peaks are thought to originate from coupling of benzaldehyde to *o*-phenylenediamine that may be formed by oxidative dehydrogenation. Lastly, it should be noted that a plethora of small peaks between 400 – 500 Da are present and no further attempts to assign these masses were made.

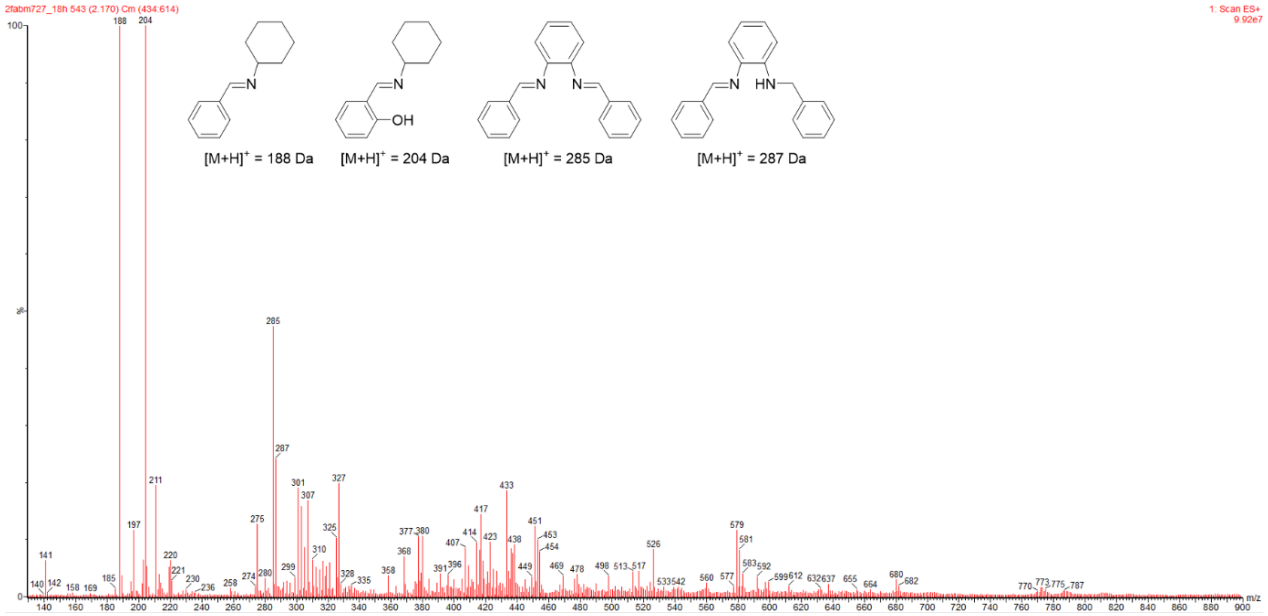

Figure 2.45: Mass spectrum of the region between 1.8 – 2.2 minutes. The mass 188 Da corresponds to the target product, 204 Da corresponds to the coupling of salicylaldehyde and cyclohexylamine. Lastly, two possible products of the coupling between *o*-phenylenediamine and benzaldehyde are tentatively assigned.

Ultimately, both previously recorded LC-MS chromatograms of the Fe(III)-salen reaction mixture after 30 minutes and 18 hours reveal highly complicated mixtures of ligand fragments and byproducts. Evidence of byproducts originating from hydrolysis of the complex and ligand is found along with evidence of structures thought to stem from oxidative dehydrogenation of the ligand.

Notably, no evidence of any Fe(III)-salen derivatives with masses between 374 – 380 Da could be identified in the LC-MS chromatogram taken after 18 hours of reaction. This indicates that degradation of the Fe(III)-salen complex into an unidentified, active catalyst is likely.

Lastly, the observed hydrolytic degradation of the catalyst could also explain why addition of molecular sieves to the reaction mixture was detrimental to the catalytic activity. The removal of water would hamper the hydrolysis of the catalyst and thereby the formation of the active catalyst.

2.4.3. Further investigation of catalyst degradation by LC-MS

To gain further evidence regarding the fate of the catalyst, it was decided to carry out a new LC-MS study of the degradation using a freshly prepared batch of catalyst **Fe2.1** and freshly opened reagents. A range of experiments were carried out and analyzed by LC-MS like in the previous section. The tested reaction conditions are listed in Table 2.3 and the structures of the observed degradation products are shown in Figure 2.46.

Table 2.3: Summary of the catalyst degradation study using LC-MS. All reactions were performed in refluxing toluene (2 mL) in a Schlenk flask under N_2.

Entry	Reaction time	Additive 1	Additive 2	Additive 3	Dominating masses
1	30 min	KOtBu (0.2 mmol)	N/A	N/A	219 Da, 376 Da
2	30 min	KOH (0.2 mmol)	N/A	N/A	204 Da, 376 Da
3	30 min	N/A	Benzyl alcohol (1.0 mmol)	Cyclohexylamine (1.0 mmol)	376 Da, 323 Da
4	60 h	KOtBu (0.2 mmol)	Benzyl alcohol (1.0 mmol)	Cyclohexylamine (1.0 mmol)	188 Da, 204 Da, 206 Da, 215 Da, 219 Da, 327 Da

Comparing entry 2 to entry 1 indicates that treatment of the **Fe2.1** with KOH results in rapid hydrolysis of the ligand as virtually no 219 Da mass is observed. In entry 3, no strong base was added and consequently, the only observed masses correspond to intact **Fe2.1** and the free salen ligand. In entry 4, the reaction was left running for 60 hours with addition of all additives according to the optimized procedure. This resulted in a complex mixture like the one observed previously by Fabrizio Monda, where the most prominent peaks correspond to hydrolysis byproducts and various ligand derivatives. Importantly, no evidence of any Fe(III)-salen derivatives was found in entry 4, which corroborates the previous results obtained by Fabrizio Monda.

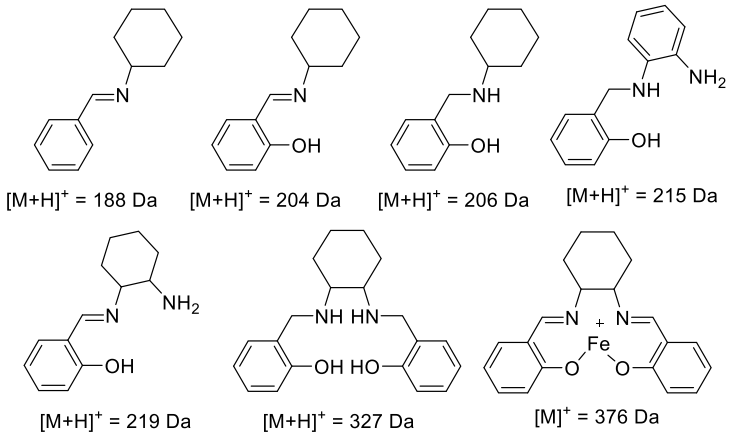

Figure 2.46: Structures of various products observed in the repeat LC-MS investigation of the Fe(III)-salen protocol.

Conclusively, the repeat investigation of catalyst degradation by LC-MS also shows evidence of extensive degradation of **Fe2.1** by hydrolysis and oxidative dehydrogenation. The active catalyst remains uncharacterized, but the most likely candidate is unspecified iron particles.

2.4.4. Visual characterization of the reaction mixtures

No accounts of color changes during the reactions were provided by Fabrizio Monda, but visual inspection of the reaction mixtures can provide important clues towards the active iron species. A closer look at the reaction mixtures was therefore taken and several color changes was observed during the reaction.

As **Fe2.1** is a black powder, the initially formed suspension of **Fe2.1** and KOtBu in toluene can be characterized as a black slurry. When the reaction mixture is heated, the black slurry turns into a cloudy, pale yellow suspension, which indicates interaction between KOtBu and **Fe2.1**. Once reflux is achieved, benzyl alcohol is added and immediately hereafter, the reaction mixture turns dark red and opaque, indicating yet another reaction. Addition of cyclohexylamine does not change the color, and the dark red color remains throughout the 48 hours of reaction. It should be noted that no black particles are deposited on the sides of the reaction vessel or on the magnetic stir bar. This would likely be observed if Fe(0) particles are produced during the reaction. On a similar note, attempts at isolation and characterization of the active catalyst failed.[109]

While the color changes are not easily interpreted, the dark red color can be speculatively associated with iron(III) oxides. As water is released during the imination and the reaction conditions are harsh and basic, hydrolysis of **Fe2.1** is a likely degradation pathway. As mentioned in the previous section, evidence of extensive hydrolysis was found by LC-MS, so the current hypothesis is that hydrolysis of **Fe2.1** leads to formation fine iron(III) oxide particles, that acts as the active catalyst. This hypothesis is supported by the fact that addition of molecular sieves, and thus removal of water, is highly detrimental to the catalytic activity of the system.

2.5. Conclusion

The development and mechanistic investigation of the AAD reaction with Fe(III)-salen catalysts has been long underway in the Madsen research group. A large portion of the experimental work, including optimization of reaction conditions, substrate scope and mechanistic experiments were carried out by previous Ph.D. student Fabrizio Monda with contributions from project student Frederik Simonsen Bro and BSc. student Xiyue Liu.

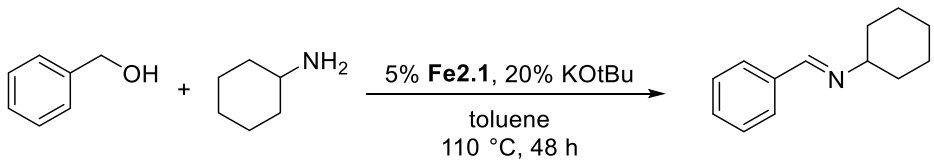

Figure 2.47: Optimal reaction conditions for acceptorless dehydrogenative coupling of alcohols and amines.

Early optimization studies found that good imine yields were obtained using the reaction conditions shown in Figure 2.47. Notably, addition of KOtBu was required to obtain adequate reactivity and addition of molecular sieves were detrimental to the catalytic activity. Subsequently, a range of experiments were performed by Fabrizio Monda, Frederik Simonsen Bro, and Xiyue Liu to shed light on the reaction mechanism.

The AAD pathway of the reaction was confirmed by detection of H_2 gas. The kinetic isotope effect of the reaction was measured twice to 1.34 and 1.36, respectively, which are small values compared to the KIE values usually observed for alcohol dehydrogenation reactions.[32,82,112–115] Another piece of the mechanistic puzzle was obtained by conducting a Hammett study, which resulted in a ρ value of -0.80. This is consistent with a build-up of positive charge on the benzylic position, indicating transfer of H^- from the alcohol. A similar result was obtained for the Mn(III)-salen protocol.[1]

To gain further insight into the mechanism of catalysis, DFT calculations were employed. Initial calculations revealed that the high-spin sextet was the preferred spin multiplicity of a range of envisioned catalyst intermediates. Furthermore, the coordination of cyclohexylamine and benzyl alcohol to form octahedral complexes was found unfavorable *in silico*, so the catalytic cycle was modeled with 5-coordinate complexes. However, all attempts at developing a DFT model that both demonstrated acceptable energy barriers and consistency with the experimental results failed.

Unable to devise a DFT model that adequately reproduced the experimental findings, a series of control experiments were conducted, and old LC-MS data recorded by Fabrizio Monda was re-examined. Poisoning studies with PMe_3 and Hg showed inhibition of the catalytic activity, and the previously recorded LC-MS data showed evidence of extensive catalyst degradation, primarily in the form of hydrolysis. A new series of degradation experiments also corroborated the observation of extensive catalyst hydrolysis; after prolonged reaction time, no Fe(III)-catalyst derivatives were observable.

Conclusively, an AAD coupling between alcohols and amines to furnish imines was developed using Fe(III)-salen catalysts. The catalysis was initially believed to be homogeneous and therefore one of the few examples of homogeneous AAD catalysis with Fe(III) complexes. However, poisoning studies and LC-MS investigations provided evidence of extensive catalyst degradation and particle formation during the reaction. The current view is therefore that the AAD reaction is catalyzed by unspecified iron particles generated *in situ* as summarized in Figure 2.48.

Efforts towards the isolation and characterization of the presumed catalyst particles have failed.

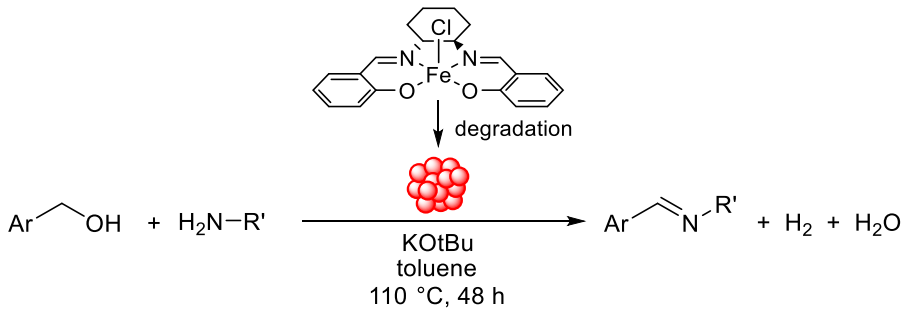

Figure 2.48: Generation of an active iron particle catalyst by degradation of the Fe(III)-salen catalyst.

Overall, the result highlights the importance of checking for heterogeneous catalysis early in the discovery phase, especially when dealing with iron catalysts performing reactions under reducing and hydrolytic conditions.

2.6. Experimental

In this section, the details of the experiments carried out by me are described. The only exception is the inclusion of the experimental details of the KIE determination (performed by both Frederik Simonsen Bro and Xiyue Liu) and the Hammett experiments (carried out by Xiyue Liu). These experiments were included as they were carried out under my supervision and provide important context to the computational study. If further details regarding the experiments carried out by Fabrizio Monda are wanted, one can refer to the published paper.[109]

2.6.1. General experimental details

All chemicals, except 2-allylbenzaldehyde, were purchased from either Merck or Fisher Scientific and used as received. 2-Allylbenzaldehyde was purchased from Combi-Blocks and used as received. The catalyst was kept in a vacuum desiccator to avoid degradation. Degassed, anhydrous toluene was prepared by freeze-pump-thaw cycles (repeated three times) followed by sparging with a flow of N_2 for 3 hours minimum. Freshly activated molecular sieves (4Å) was added and the solvent was kept under N_2 and allowed to dry for minimum 24 hours before use. Due to the hygroscopic nature of KOtBu, the base was handled rapidly to minimize exposure to air and the container was stored in a vacuum desiccator.

Manual flash column chromatography was performed using HPLC grade heptane and ethyl acetate. The separation was carried out on silica gel (35 - 70 μm) obtained from VWR Chemicals.

All catalytic reactions were performed in two-necked Schlenk reaction tubes using standard Schlenk techniques. The nitrogen feed of the Schlenk line was dried over a column of P_2O_5. To avoid cross-contamination, all glassware and magnets were thoroughly cleaned with *aqua regia* and oven-dried prior to use.

Gas chromatography was carried out on a Shimadzu GCMS-QP2010S instrument equipped with an Rtx-5MS column (30m x 0.25 mm x 0.25 μm). The carrier gas was helium, and the ionization was performed by electron impact (EI) at 70 eV. Table 2.4 outlines the GC settings that were employed in all analyses:

Table 2.4: Settings employed for GC-MS analysis.

Injection volume	1 μL
Injection mode	Split
Injection temperature	280 °C
Initial oven temperature	60 °C (hold 5 min)
Final oven temperature	300 °C (hold 5 min)
Temperature ramp rate	20 °C / min
Total run time	22 min

LC-MS was carried out on a Waters Acquity UPLC system equipped with PDA and SQD2 electrospray MS detector. Table 2.5 outlines the LC settings that were employed in all analyses:

Table 2.5: Settings employed for LC-MS analysis.

Flow rate	0.6 mL/min
Column type	Thermo Accucore C18 (2.6 µm, 2.1 × 50 mm)
Column temperature	50 °C
Eluent **A**	5 mM NH_4OAc in MeCN/water (95/5)
Eluent **B**	5 mM NH_4OAc in water
Eluent program	From 5% **A** - 100% **A** in 2.6 min

Standard ^{1}H and ^{13}C NMR spectra were recorded at 400 MHz and 101 MHz, respectively, on a Bruker Ascend 400 MHz spectrometer using residual $CHCl_3$ signals (δ_H 7.26 ppm, δ_C 77.2 ppm) as reference. All chemical shifts (δ) are quoted in ppm and coupling constants (*J*) are listed in Hz.

2.6.2. Construction of calibration curve

Procedure for the construction of calibration curves:

Stock solution **A** (0.100 M *N*-Benzylidenecyclohexylamine in diethyl ether) were prepared by dissolving freshly synthesized *N*-benzylidenecyclohexylamine (188 mg) in Et_2O in a 10 mL volumetric flask. Stock solution **B** (0.050 M tetradecane in diethyl ether) were prepared by dissolving tetradecane (100 mg) in Et_2O in a 10 mL volumetric flask. From the two stock solutions, the GC calibration samples were prepared according to Table 2.6 and the samples were subjected to GC-MS analysis using the standard method.

Table 2.6: Preparation of standards for the construction of the calibration curves.

Vial no.	1	2	3	4	5
V(**StockA**) / mL	0.1	0.2	0.3	0.4	0.5
V(**StockB**) / mL	0.5	0.5	0.5	0.5	0.5
V(Et_2O) / mL	0.4	0.3	0.2	0.1	0.0
c(*N*-Benzylidenecyclohexylamine) / M	0.01	0.02	0.03	0.05	0.05
c(tetradecane) / M	0.025	0.025	0.025	0.025	0.025

The obtained GC-MS chromatograms (example shown in Figure 2.49) were integrated across fixed retention times (reported in Table 2.7) to ensure consistent integration:

Table 2.7: Retention times used for reliable integration of the GC-MS chromatograms.

Compound	Retention time
Tetradecane	7.73 – 9.00 min
N-Benzylidenecyclohexylamine	12.0 – 13.0 min

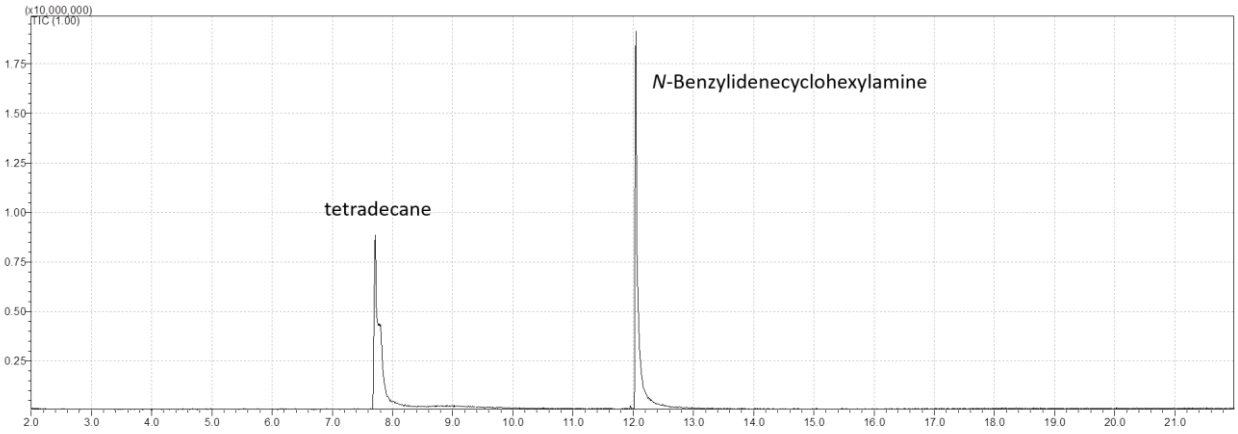

Figure 2.49: Example of a GC-MS chromatogram used to construct the calibration curves.

From the areas obtained by integration of the GC-MS chromatogram, the relative area (A_{imine}/A_{tet}) as a function of the relative concentration (c_{imine}/c_{tet}) were plotted, linear regression with a forced intercept through (0.0) was performed and the obtained slope was used to determine the concentrations of *N*-benzylidenecyclohexylamine in all catalytic experiments.

2.6.3. Synthetic protocols

Synthesis of **L2.1**:

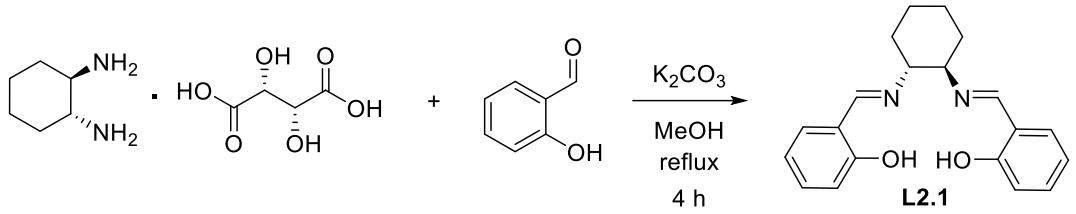

The synthesis was carried out according to literature.[1]

A mixture of (1*R*,2*R*)-(+)-1,2-diaminocyclohexane L-tartrate (2.11 g, 8.00 mmol), potassium carbonate (1.15 g, 8.32 mmol) and water (7 mL) was stirred until everything was dissolved. Methanol (50 mL) was added, and the reaction mixture was heated to reflux. A solution of salicylaldehyde (1.7 mL, 16 mmol) in methanol (20 mL) was prepared in an addition funnel and the mixture was added over 30 minutes during which the mixture turned yellow. The reaction mixture was further refluxed for 4 hours and cooled to room temperature. The reaction mixture was concentrated *in vacuo* and the residue was partitioned between ethyl acetate (30 mL) and water (20 mL). The aqueous layer was extracted with ethyl acetate (3 x 20 mL) and the combined organic phases were washed with water (2 x 15 mL), dried over sodium sulfate, and concentrated *in vacuo* to yield the product as a viscous, yellow oil that was used without further purification.

Yield: 2.47 g (96%)

^{1}H-NMR (400 MHz, $CDCl_3$): δ 8.26 (s, 2H), 7.28 – 7.21 (m, 2H), 7.15 (dd, *J* = 7.7, 1.7 Hz, 2H), 6.89 (dd, *J* = 8.3, 1.1 Hz, 2H), 6.79 (td, *J* = 7.5, 1.1 Hz, 2H), 3.37 – 3.27 (m, 2H), 2.00 – 1.83 (m, 4H), 1.80 – 1.67 (m, 2H), 1.56 – 1.41 (m, 2H).

^{13}C-NMR (101 MHz, $CDCl_3$): δ 164.9, 161.1, 132.4, 131.6, 118.8, 118.7, 116.9, 72.7, 33.2, 24.3.
NMR data are in accordance with literature values.[1]

Synthesis of **Fe2.1:**

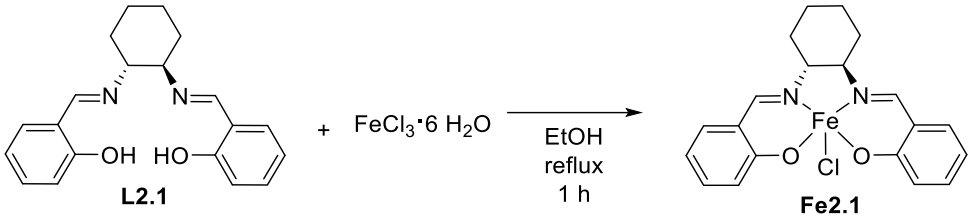

The synthesis was carried out according to literature.[110]

L2.1 (2.40 g, 7.44 mmol) and $FeCl_3 \cdot 6\ H_2O$ (2.21 g, 8.19 mmol) were mixed in absolute ethanol (150 mL) and refluxed for 1 h during which a dark precipitate formed. The precipitate was isolated by suction filtration on a sintered glass filter and washed with diethyl ether (3 x 5 mL). The crude product was recrystallized from absolute ethanol and the resulting black crystals were dried overnight *in vacuo* to yield the desired catalyst.

Yield: 1.50 g (49%)

MS (ESI+) *m/z*: 376.0 $[M\text{-}Cl]^+$, calc. 376.09.

Synthesis of *N*-benzylidenecyclohexylamine for calibration curves:

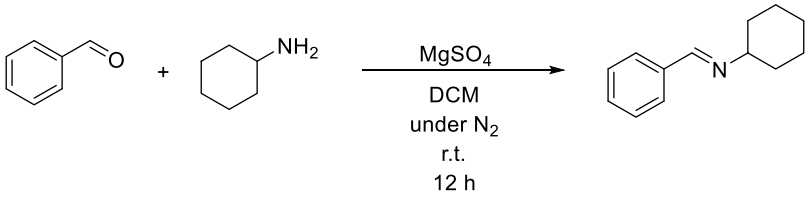

To a round-bottom flask was added CH_2Cl_2 (40 mL), benzaldehyde (2.0 mL, 19.7 mmol), cyclohexylamine (2.25 mL, 19.7 mmol) and $MgSO_4$ (2.4 g, 19.9 mmol). The reaction mixture was stirred for 12 h at room temperature under a flow of N_2. The reaction mixture was filtered, and the solvent was removed *in vacuo*. The crude product was loaded onto a silica gel column saturated with Et_3N and purified by flash chromatography in heptane/Et_3N (98:2). The fractions containing pure product were reduced *in vacuo* and the pure product was further dried under vacuum overnight to remove residual solvent.

Yield: 2.66 g (74%)

^{1}H-NMR (400 MHz, $CDCl_3$): δ 8.32 (s, 1H), 7.75-7.72 (m, 2H), 7.41-7.39 (m, 3H), 3.23-3.16 (m, 1H), 1.86-1.55 (m, 7H), 1.43-1.23 (m, 3H).
^{13}C-NMR (101 MHz, $CDCl_3$): δ 158.9, 136.7, 130.7, 128.7, 128.3, 70.0, 34.4, 25.8, 25.0
NMR data are in accordance with previously reported values.[1]

Determination of kinetic isotope effect:

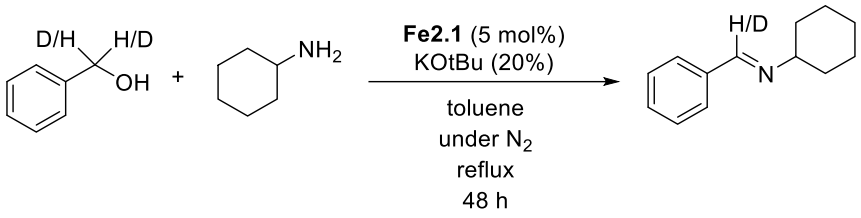

The KIE experiment was performed independently by project student Frederik Simonsen Bro and BSc. student Xiyue Liu under my supervision.

Fe2.1 (20.5 mg, 0.05 mmol) and KOtBu (22.5 mg, 0.2 mmol) were weighed into an oven-dried tube and the tube was placed in a Radley carousel. The tube was subjected to vacuum and N_2 refills (repeated three times). Freshly degassed anhydrous toluene (2 mL) was added by syringe and the reaction mixture was heated to reflux. Benzyl alcohol (108 mg, 1.0 mmol), cyclohexylamine (99 mg, 1.0 mmol) and tetradecane (0.13 mL, 0.50 mmol) were added. For 5 h, a sample of 50 µL was sampled every 30 minutes, transferred to a GC vial, diluted to 1 mL with diethyl ether and then subjected to GC-MS analysis to follow the formation of *N*-benzylidenecyclohexylamine and determine the initial rate *r*.

In the first experiment performed by Frederik Simonsen Bro, the initial rate for the transformation of benzyl alcohol was $r_H = 1.51 \cdot 10^{-4}$ M min^{-1}. The initial rate for the reaction of benzyl alcohol-α,α-d_2 was $r_D = 1.13 \cdot 10^{-4}$ M min^{-1}. The isotope effect was $k_H/k_D = 1.34$. The original data is shown in section 2.2.6 in Figure 2.17.

The determination of the KIE was repeated three months later by Xiyue Liu with new batches of substrates and catalyst **Fe2.1**. In this case, the initial rate for the transformation of benzyl alcohol was $r_H = 5.22 \cdot 10^{-4}$ M min^{-1} and the initial rate for the reaction of benzyl alcohol-α,α-d_2 was $r_D = 3.85 \cdot 10^{-4}$ M min^{-1}. Thus, the isotope effect was $k_H/k_D = 1.36$. The original data is shown in section 2.2.6 in Figure 2.18.

Synthesis of 2-allylbenzyl alcohol:

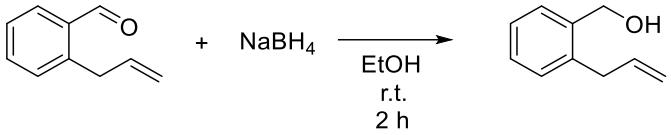

2-Allylbenzyl alcohol was prepared according to literature.[138]

2-Allylbenzaldehyde (2.22 g, 15.2 mmol) was dissolved in absolute ethanol (30 mL). The reaction flask was placed in an ice bath and $NaBH_4$ (840 mg, 21.9 mmol) was added in small portions. The reaction mixture was stirred at room temperature for 2 h before water (40 mL) was added. The mixture was transferred to a separatory funnel and extracted with CH_2Cl_2 (3 x 40 mL). The combined organic phases were dried over $MgSO_4$, filtered, and concentrated *in vacuo* to give the crude product that was further purified by flash column chromatography in heptane/EtOAc (4:1) to give a colorless oil.

Yield: 1.69 g (75%)

^{1}H-NMR (400 MHz, $CDCl_3$): δ 7.42-7.37 (m, 1H), 7.34-7.20 (m, 3H), 6.02 (ddt, J = 16.9, 10.2, 6.3 Hz, 1H), 5.09 (dd, J = 10.2, 1.7 Hz, 1H), 5.02 (dd, J = 17.0, 1.8 Hz, 1H), 4.72 (s, 2H), 3.50 (dd, J = 6.2, 1.8 Hz, 2H). NMR data are in accordance with literature values.[138]

Radical trapping experiment:

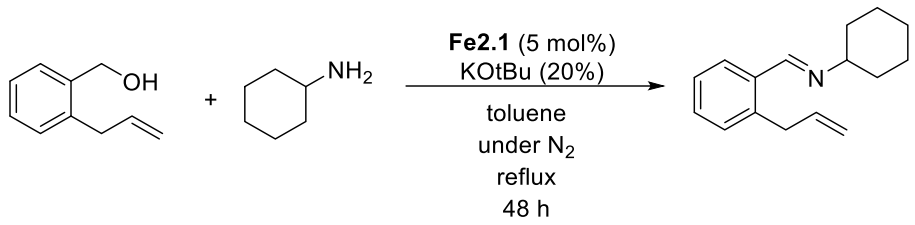

Fe2.1 (20.5 mg, 0.05 mmol) and KOtBu (22.5 mg, 0.2 mmol) were placed in an oven-dried Schlenk flask equipped with a cold finger. The flask was subjected to vacuum and N_2 refills (repeated three times). Freshly degassed anhydrous toluene (2 mL) was added by syringe and the reaction mixture was heated to reflux in an oil bath with stirring. Freshly prepared 2-allylbenzylalcohol (148 mg, 1.0 mmol), cyclohexylamine (99 mg, 1.0 mmol) and tetradecane (0.13 mL, 0.5 mmol) were added through the septum and the reaction mixture was refluxed for 48 h under a flow of N_2. At the 24-hour and 48-hour mark, aliquots of the reaction mixture (0.1 mL) were withdrawn through the septum and diluted to 1.0 mL with Et_2O. The sample was filtered through a nylon syringe filter (0.22 µm pore size) into a GC vial and subjected to GC-MS analysis to determine the presence of cyclized byproducts.

Preparation of stock solution of trimethylphosphine in toluene:

An ampoule containing pure trimethylphosphine (5 mL) was cracked and rapidly transferred into a flame-dried and purged Schlenk flask where it was kept under a flow of nitrogen. From this flask, trimethylphosphine (0.2 mL, 2 mmol) was transferred to a second flame-dried and purged Schlenk flask and diluted to 10 mL with freshly degassed, anhydrous toluene. The stock solution was prepared the same day as the poisoning experiments were performed.

Catalyst poisoning experiments:

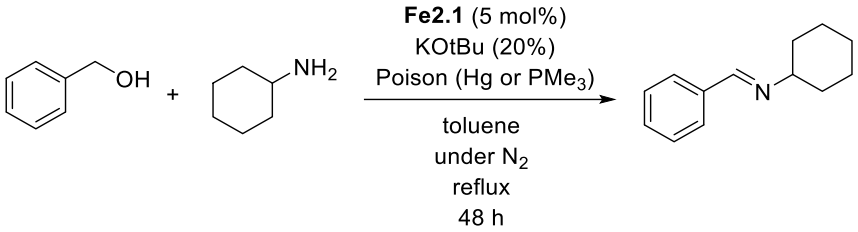

Fe2.1 (20.5 mg, 0.05 mmol) and freshly opened KOtBu (22.5 mg, 0.2 mmol) were placed in an oven-dried Schlenk flask equipped with a cold finger. The flask was subjected to vacuum and N_2 refills (repeated three times). Freshly degassed anhydrous toluene (2 mL) was added by syringe and the reaction mixture was heated to reflux in an oil bath with stirring. Benzyl alcohol (108 mg, 1.0 mmol), cyclohexylamine (99 mg, 1.0 mmol), tetradecane (0.13 mL, 0.5 mmol) and catalyst poison (either 1 drop of Hg or 0.1 mL of a freshly prepared 0.2 mol/L stock solution of trimethylphosphine in toluene) were added, and the reaction was refluxed while stirring under a flow of nitrogen for 48 h.

The experiment was repeated with addition of catalyst poison after 24 hours of catalysis. In all cases, the reaction progress was monitored by GC-MS using the following sampling procedure:

After 48 hours, a 0.1 mL aliquot was taken, diluted to 1.0 mL with Et_2O, filtered through a nylon syringe filter (pore size: 0.22 μm) and subjected to GC-MS analysis where the yield of *N*-benzylidenecyclohexylamine was quantified using a recently prepared calibration curve. The calculated GC yields are reported in the table below.

Entry	Poison	Yield (%)
1	None (for reference)	85
2	0.02 mmol PMe3 (added at 0 h)	15
3	1 drop Hg (added at 0 h)	24
4	0.02 mmol PMe3 (added after 24 h)	39
5	1 drop Hg (added after 24 h)	41

Hammett study:

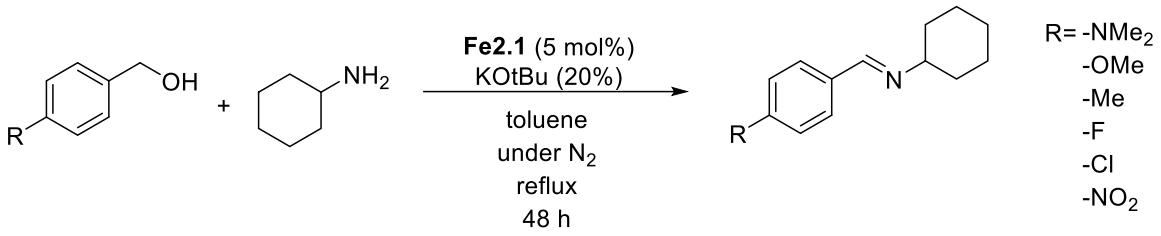

The Hammett study was performed by BSc. student Xiyue Liu under my supervision.

Fe2.1 (20.5 mg, 0.05 mmol) and KOtBu (22.5 mg, 0.2 mmol) were weighed into an oven-dried tube and the tube was placed in a Radley carousel. The tube was subjected to vacuum and N_2 refills (repeated three times). Freshly degassed anhydrous toluene (2 mL) was added by syringe and the reaction mixture was heated to reflux. Benzyl alcohol (0.5 mmol), 4-substituted benzyl alcohol (0.5 mmol), cyclohexylamine (1.0 mmol) and tetradecane (0.5 mmol) were added. For 5 h, a sample of 50 µL was sampled every 30 minutes, transferred to a GC vial, diluted to 1 mL with Et_2O and then subjected to GC-MS analysis to follow the formation of *N*-benzylidenecyclohexylamine and 4-substituted *N*-benzylidenecyclohexylamine to determine k_{rel}. The plots used to determine k_{rel} are shown in Figure 2.50 – Figure 2.55 later in this section. The final Hammett plot is shown in Figure 2.20 in section 2.2.7.

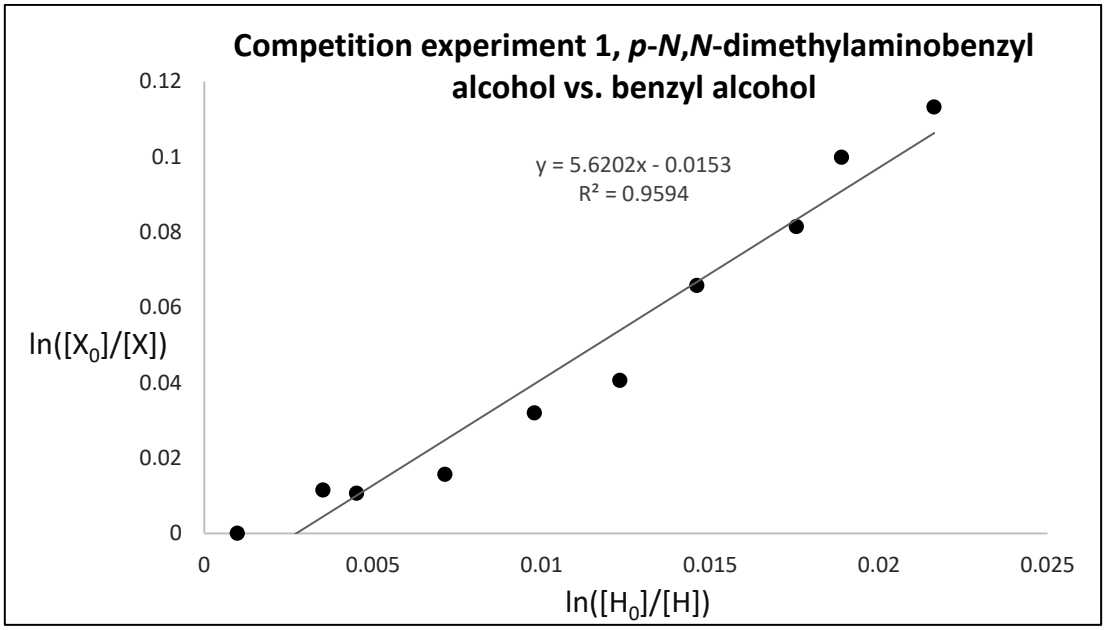

Figure 2.50: Competition experiment between *p*-dimethylaminobenzyl alcohol and benzyl alcohol.[109]

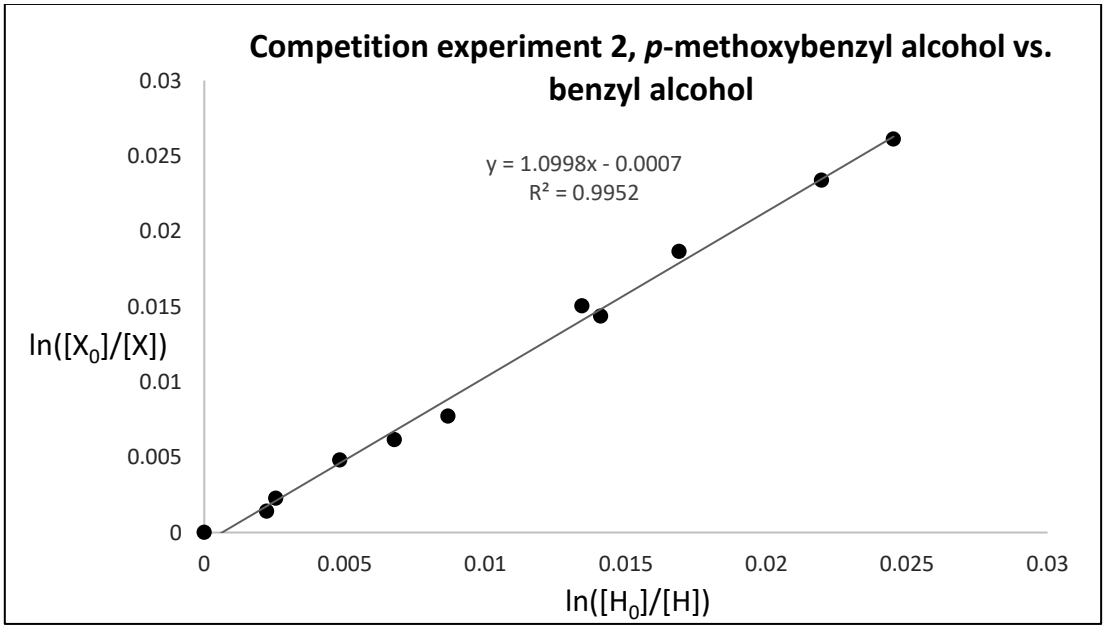

Figure 2.51: Competition experiment between *p*-methoxybenzyl alcohol and benzyl alcohol.[109]

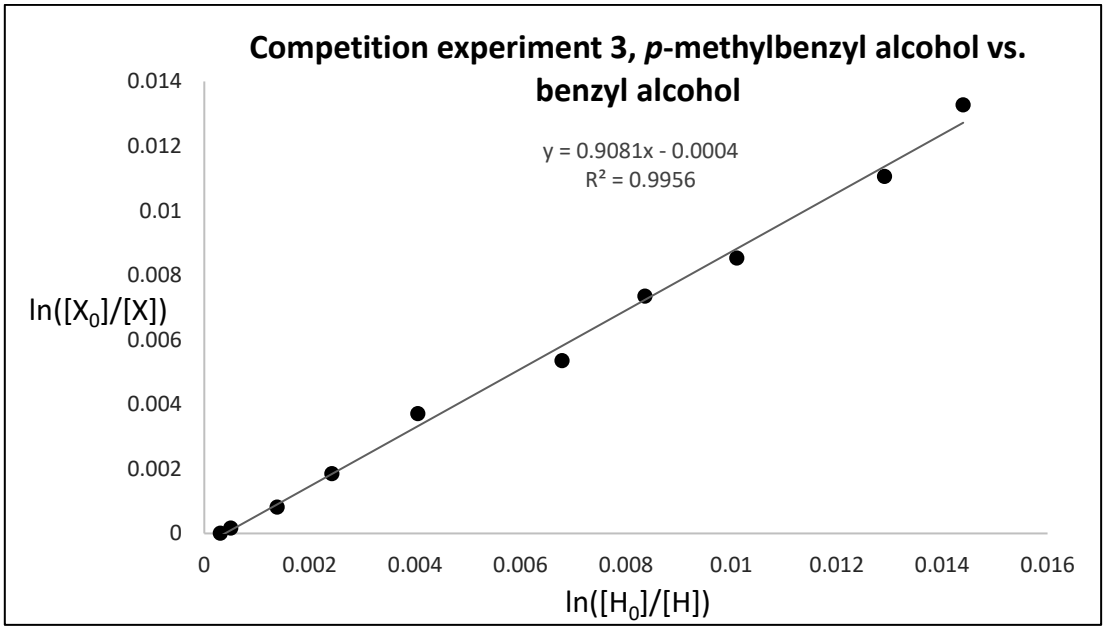

Figure 2.52: Competition experiment between *p*-methylbenzyl alcohol and benzyl alcohol.[109]

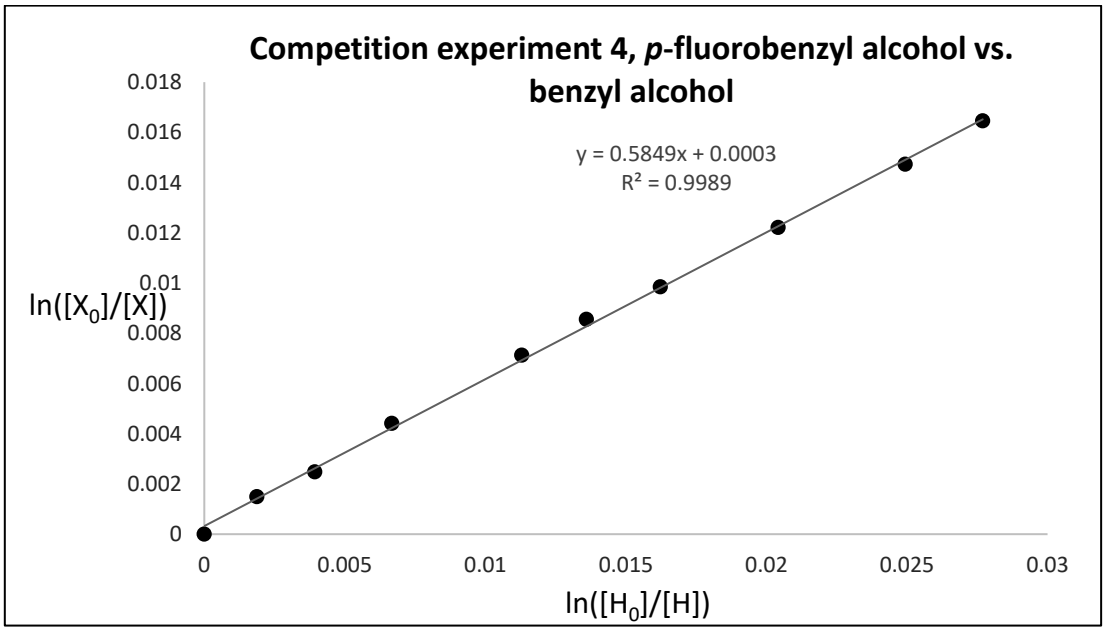

Figure 2.53: Competition experiment between *p*-fluorobenzyl alcohol and benzyl alcohol.[109]

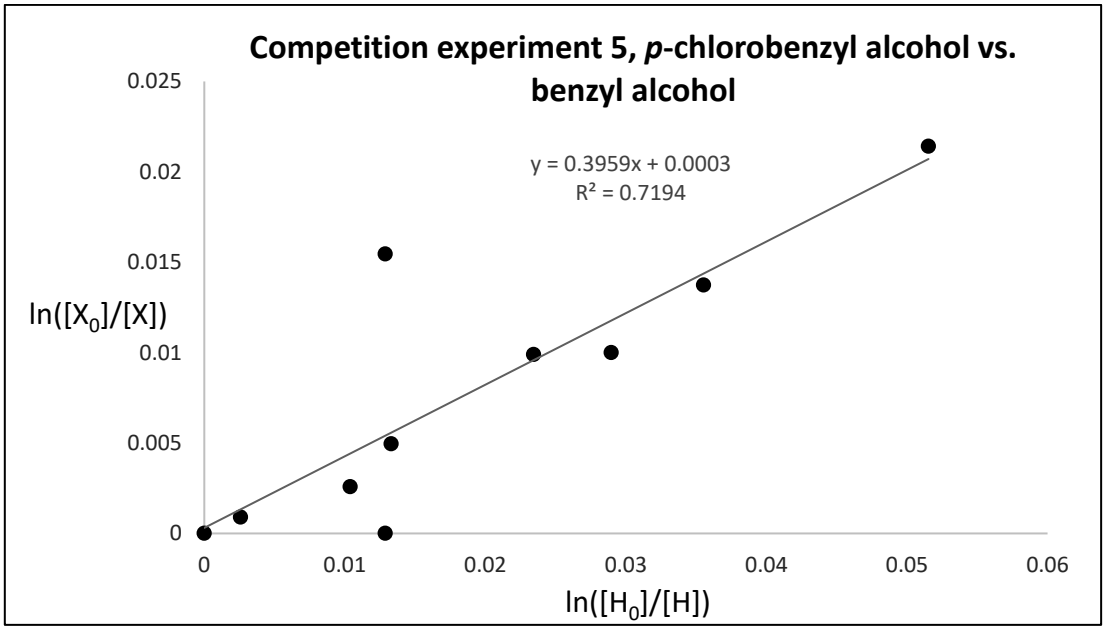

Figure 2.54: Competition experiment between *p*-chlorobenzyl alcohol and benzyl alcohol.[109]

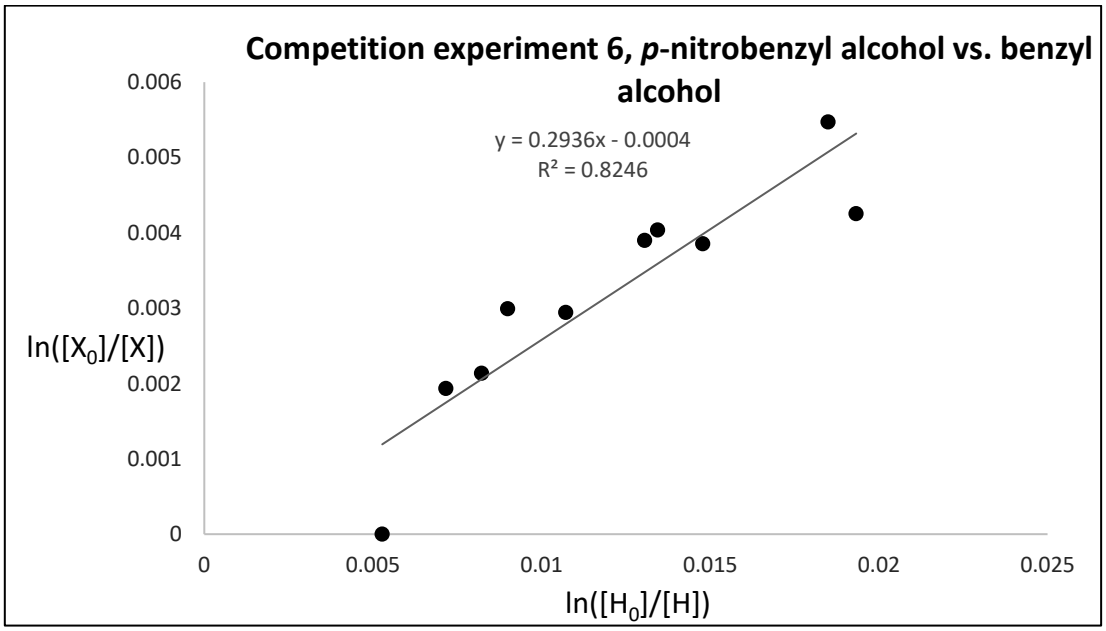

Figure 2.55: Competition experiment between *p*-nitrobenzyl alcohol and benzyl alcohol.[109]

2.6.4. Computational details

The DFT calculations used to determine the ground state multiplicity of different Fe(III) intermediates were performed with ORCA version 4.2.0.[119] For each intermediate, geometry optimizations in the gas phase were performed for each multiplicity (doublet, quartet, sextet) with three different functionals (PBE0[126], OPBE[127,128], B3LYP[120,121]). In all cases, the D3BJ[139] dispersion correction, the def2-TZVP basis set[140] and an unrestricted SCF spin treatment was employed. The electronic energy was used directly to determine the ground state multiplicity of the intermediates.

The DFT calculations used to investigate the coordination of a second axial ligand were performed with ORCA version 4.2.0. All structures were optimized in the gas phase using the B3LYP-D3BJ \\ def2-TZVP method and unrestricted SCF spin treatment (restricted SCF spin treatment was used for benzyl alcohol and cyclohexylamine). For Fe(III)-containing structures, a high-spin sextet was assumed. Vibrational frequencies and thermochemistry were calculated at T = 383 K and standard state (1 atm), which provided ΔG_{gas} directly. The free energy of solvation for each structure was calculated at the B3LYP-D3BJ \\ def2-TZVP level using the SMD model[141] with the standard parameters for toluene. Finally, the solvated Gibbs free energy of each structure was calculated as $\Delta G_{tot} = \Delta G_{gas} + \Delta G_{solv}$ and the binding energy of the additional axial ligand was calculated as $\Delta G_{bind} = \Delta G_{tot,\ 6coord} - (\Delta G_{tot,\ 5coord} + \Delta G_{tot,\ ligand})$.

The DFT calculations used to construct the final model of the reaction were performed with Jaguar (version 10.7, release 13) by Schrodinger LLC.[142] All geometry optimizations were performed in the gas phase using the B3LYP-D3 method[120,121,143] and the LACVP** basis set. Unrestricted SCF spin treatment was used in all calculations. Based on the initially calculated spin splittings, all Fe(III)-containing intermediates were assumed to be high-spin (HS). Frequency calculations were performed on all optimized structures to ensure that intermediates had no imaginary frequencies and that transitions states had one imaginary frequency. To match the experimental conditions, the frequency calculations were performed at the boiling point of toluene (383 K) and at standard state (1 atm). The solvation free energy ΔG_{solv} of structures containing Fe(III) were calculated with the PBF solver in Jaguar using the standard parameters for toluene and the B3LYP-D3 \\ LACVP** method. ΔG_{solv} of benzyl alcohol and benzaldehyde were calculated using the SM8 model[144] and the
B3LYP-D3 \\ 6-31G* method. To obtain more accurate electronic energies, the electronic energy of all complexes was recalculated with the larger basis set LACV3P**++. The final free energies were calculated as the sum $\Delta G_{tot} = E(\text{LACVP3**++}) + \Delta G_{solv} + ZPE + \Delta H - T\Delta S$. In all cases, T was set to the boiling point of toluene (383 K).

The theoretical Hammett study was conducted by calculating the free energy difference ($\Delta G^{\ddagger}$) between the appropriate reactant and transition state using the methodology described above. This calculation was repeated for all 4-substituted benzyl alkoxide ligands. The ratio of the rate constants was subsequently calculated by $k_x / k_H = \text{EXP}[(\Delta G^{\ddagger}(H) - \Delta G^{\ddagger}(x)) / RT]$ with T = 383 K and R = 0.001987204 kcal K^{-1} mol^{-1}.

The theoretical KIEs were calculated by performing frequency calculations on the appropriate reactant and transition state where the weights of the benzylic hydrogen atoms were set to 2. The thermochemistry calculated for the deuterium-containing structures was then employed in the calculation of the free energies using $\Delta G_{tot} = E(\text{LACVP3**++}) + \Delta G_{solv} + ZPE + \Delta H - T\Delta S$. From the calculated $\Delta G^{\ddagger}$(prot) and $\Delta G^{\ddagger}$(deut), the ratio k_H / k_D was calculated using k_H / k_D = EXP[($\Delta G^{\ddagger}$(deut) - $\Delta G^{\ddagger}$(prot)) / RT] with T = 383 K and R = 0.001987204 kcal K^{-1} mol^{-1}.

Study of Fe(III) multiplicity

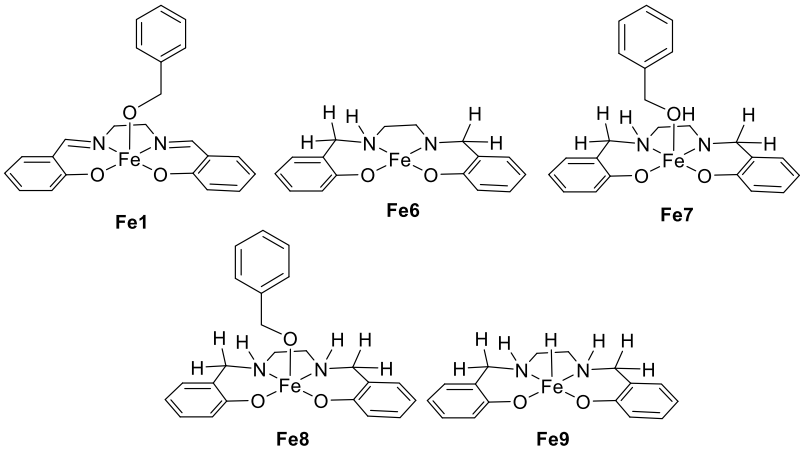

PBE0	doublet	quartet	sextet
Fe1	-2486.932813	-2486.944803	-2486.966835
Fe6	-2142.775369	-2142.799966	-2142.797128
Fe7	-2489.309272	-2489.341799	-2489.344838
Fe8	-2489.334815	-2489.352441	-2489.375256
Fe9	-2143.971064	-2143.974498	-2143.989597

OPBE	doublet	quartet	sextet
Fe1	-2488.537016	-2488.540501	-2488.550164
Fe6	-2144.072622	-2144.09801	-2144.091862
Fe7	-2490.931055	-2490.95634	-2490.95314
Fe8	-2490.949391	-2490.9648	-2490.979965
Fe9	-2145.280724	-2145.281007	-2145.283573

B3LYP	doublet	quartet	sextet
Fe1	-2487.860058	-2487.867892	-2487.883384
Fe6	-2143.477229	-2143.496788	-2143.489168
Fe7	-2490.22427	-2490.255247	-2490.254131
Fe8	-2490.254191	-2490.266412	-2490.284692
Fe9	-2144.673932	-2144.673031	-2144.682624

Figure 2.56: Investigation of ground state multiplicity of Fe(III). Absolute electronic energies calculated with B3LYP-D3BJ \\ def2-TZVP in ORCA version 4.2.0

2.6.5. Energies of structures

Table 2.8: Overview of structures and energies calculated in Jaguar.

	E(LACV3P**++)	ZPE	H	S	Solv
BnOH	-346.8833855	83.641	5.096	84.812	-4.494
PhCHO	-345.6767939	69.174	4.519	79.302	-4.014
Fe1	-1348.208136	248.038	25.414	192.371	-5.8911
Fe1_TS	-1348.157015	245.048	24.668	187.004	-6.4551
Fe2	-1348.173252	246.846	25.699	194.245	-7.2337
Fe3	-1349.391399	262.100	26.133	195.998	-5.7491
Fe3_TS	-1349.377856	259.808	25.500	192.465	-5.1515
Fe4	-1349.424427	263.785	25.686	193.494	-6.4317
Fe4_TS	-1349.368705	260.532	25.026	188.743	-6.6923
Fe5	-1349.385938	262.477	26.03	195.881	-7.6794
Fe6	-1003.673843	191.767	18.574	155.351	-7.2627
Fe7	-1350.603648	277.872	26.366	196.622	-6.6365
Fe7_TS	-1350.590454	275.517	25.766	193.493	-5.5745
Fe8	-1350.63268	279.251	26.001	194.772	-6.9269
Fe8_TS	-1350.570639	274.900	25.925	194.036	-7.4501
Fe9	-1004.878202	204.613	19.278	158.36	-8.6738
Fe9_TS	-1004.832248	200.756	19.026	157.25	-7.3066
Fe10_TS	-1350.551690	272.072	25.917	193.948	-6.4834
Hammett_Fe4_NMe_2_react	-1483.428312	309.585	29.709	214.476	-7.1099
Hammett_Fe4_NMe_2_TS	-1483.381944	306.653	29.042	210.288	-6.9417
Hammett_Fe4_OMe_react	-1463.979167	284.243	28.068	205.778	-7.0541
Hammett_Fe4_OMe_TS	-1463.930019	281.233	27.316	200.606	-7.0894
Hammett_Fe4_Me_react	-1388.746752	280.78	27.324	202.195	-6.9387
Hammett_Fe4_Me_TS	-1388.698582	277.99	26.576	197.013	-6.4697
Hammett_Fe4_F_react	-1448.685679	258.364	26.427	197.084	-6.5566
Hammett_Fe4_F_TS	-1448.637276	255.635	25.685	192.011	-6.5355
Hammett_Fe4_Cl_react	-1809.042451	257.553	26.722	199.21	-6.5606
Hammett_Fe4_Cl_TS	-1808.992938	254.768	25.986	194.173	-6.4163
Hammett_Fe4_NO_2_react	-1553.987502	265.296	27.918	205.567	-8.8024
Hammett_Fe4_NO_2_TS	-1553.934989	262.606	27.184	200.78	-8.2317
Hammett_Fe8_NMe_2_react	-1484.646521	325.28	30.067	216.449	-7.2912
Hammett_Fe8_NMe_2_TS	-1484.585188	320.844	29.988	215.994	-8.2238
Hammett_Fe8_OMe_react	-1465.192238	299.757	28.382	207.478	-7.6784
Hammett_Fe8_OMe_TS	-1465.133529	295.466	28.278	206.58	-8.2723
Hammett_Fe8_Me_react	-1389.963806	296.529	27.64	203.776	-6.9475
Hammett_Fe8_Me_TS	-1389.902152	292.17	27.554	203.094	-7.4029
Hammett_Fe8_F_react	-1449.902124	274.143	26.741	198.749	-7.1639
Hammett_Fe8_F_TS	-1449.841482	269.766	26.676	198.172	-7.5319
Hammett_Fe8_Cl_react	-1810.258508	273.313	27.037	200.792	-7.1328
Hammett_Fe8_Cl_TS	-1810.198005	268.946	26.967	200.248	-7.3542

	E(LACV3P**++)	ZPE	H	S	Solv
Hammett_Fe8_NO_2_react	-1555.201479	281.113	28.226	207.202	-9.1349
Hammett_Fe8_NO_2_TS	-1555.140776	276.783	28.143	206.535	-9.1187
Fe1_NH_3	-1404.811419	271.916	28.165	206.775	-6.1437
Fe1_NH_3_TS	-1404.768435	268.91	27.453	202.015	-6.9227
Fe1_BnO	-1694.572727	323.968	32.881	230.75	-22.547
Fe1_BnO_TS	-1694.536666	320.975	32.29	226.735	-23.762
Fe4_NH_3	-1406.0213	287.202	28.622	209.581	-7.1302
Fe4_NH_3_TS	-1405.982172	284.344	27.822	203.654	-7.3403
Fe4_BnO	-1695.792401	339.342	33.286	232.934	-23.115
Fe4_BnO_TS	-1695.758511	336.628	32.59	228.018	-22.464
Fe8_NH_3	-1407.238887	303.047	28.798	209.352	-7.004
Fe8_NH_3_TS	-1407.181273	299.039	28.547	207.202	-8.3442
Fe8_BnO	-1697.016215	355.161	33.558	233.8	-23.125
Fe8_BnO_TS	-1696.962422	351.218	33.474	233.673	-23.963
Fe6_BnO	-1350.079386	268.616	26.035	195.307	-24.861
Fe7_BnO	-1697.005574	354.531	33.694	235.556	-22.6032
Fe7_BnO_TS	-1696.986351	351.539	33.344	233.511	-22.9511
Fe9_BnO	-1351.258251	280.794	26.692	197.852	-27.5656
Fe9_BnO _TS	-1351.226898	276.853	26.69	198.295	-26.4729

The cartesian coordinates of all listed structures in Table 2.8 can be found by following the link or scanning the QR code below.

https://www.dropbox.com/sh/qnv83x67u1cy9wf/AACYPkwyR6frkPXuJUSH8slBa?dl=0

Chapter 3. Development of AAD reactions catalyzed by Cr(III)-salen and Cr(III)-salan complexes

Abstract

In this chapter, attempts to develop an efficient AAD reaction between benzyl alcohol and cyclohexylamine employing Cr(III)-salen and Cr(III)-salan catalysts have been described. After thorough optimization of reaction parameters including solvent, temperature, additives and catalyst structure, a maximum imine yield of ~30% has been realized using the conditions outlined below.

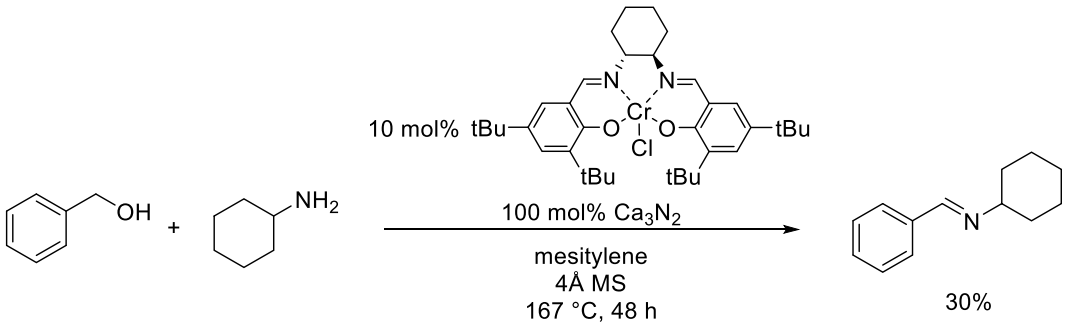

A Hammett plot with a slope of -0.73 has been measured and duplicate KIE values of 1.56 and 1.61 have been measured. No evolution of hydrogen gas during the reaction has been detected. Control experiments under an air atmosphere has revealed that aerobic oxidation can be a significant side reaction. Poisoning with Hg has not indicated involvement of heterogeneous species. LC-MS studies have shown that the Cr(III)-salen catalysts are reduced to Cr(III)-salan *in situ* and evidence of dimer formation has been found.

Furthermore, a range of DFT calculations have been employed to investigate the energetics of different reaction mechanisms and catalyst structures, but no low-energy AAD pathways have been identified. Ultimately, highly stable monomeric or dimeric alkoxo-Cr(III)-salan intermediates have been suggested as resting states that inhibit catalytic activity.

.

3.1. Introduction

In this chapter, the efforts towards efficient AAD reactions catalyzed by Cr(III)-salen and Cr(III)-salan complexes are described. The idea for this research project arose from the development of the Mn(III)-salen catalyzed imination previously published by the Madsen group.[1] Due to the structural similarities between Cr(III) and Mn(III), the Cr(III)-salen scaffold was hypothesized to catalyze the AAD reaction as observed in the Mn(III)-salen system.

Our interest in the development of an AAD catalyst based on the Cr(III)-salen scaffold was also compounded by the fact that only two Cr(III)-based protocols for AAD-derived reactions have been published[145,146]. These protocols are shown in Figure 3.1 and the protocol with Cr(III)(TPP)Cl is further discussed in Chapter 4.

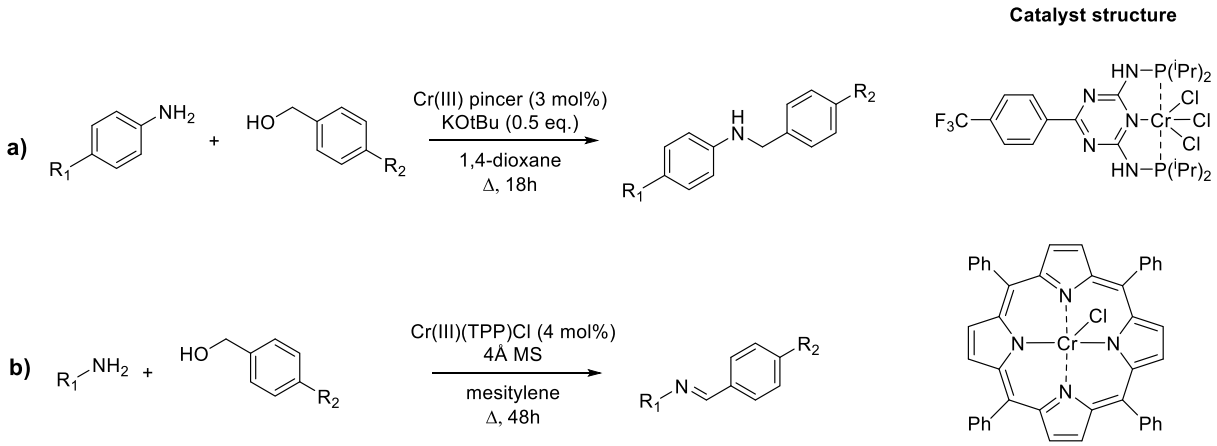

Figure 3.1: AAD-derived reactions catalyzed by Cr(III)-based catalysts. **a)** Alkylation of amines by alcohols via a hydrogen autotransfer mechanism catalyzed by a Cr(III) pincer catalyst developed in the Kempe group.[146] **b)** Protocol for imine-synthesis with a Cr(III)(TPP)Cl catalyst developed in the Madsen group.[145,147]

Ultimately, the discovery and development of new Cr(III) catalysts for AAD was deemed an unexplored field with untapped potential. Before getting into the results obtained during the work with the Cr(III)-salen catalysts, a brief introduction to some key results and concepts related to chromium-based reagents and catalysts is provided in the coming sections.

3.1.1. Traditional oxidation reagents based on chromium

The goal of the project was to develop new protocols for AAD reactions using Cr(III)-based catalysts and, as mentioned in Chapter 1, oxidation of alcohols by catalytic AAD reactions provides several advantages related to green and sustainable chemistry. Alcohol oxidations are synthetically important, and chromium has historically played an important role in the development of reagents for this transformation. More specifically, a range of Cr(VI)-based oxidizing agents (shown in Figure 3.2) have been widely used to oxidize primary and secondary alcohols. The simplest reagent is chromic acid, which is a strong oxidant that oxidizes primary alcohols to carboxylic acids and secondary alcohols to ketones.[148] The Collins reagent, a pyridine adduct of chromium trioxide, is slightly weaker and will selectively oxidize secondary alcohols into ketones and primary alcohols no further than into aldehydes.[149,150] Furthermore, it is a useful reagent for acid-sensitive compounds. However, Collins reagent is quite unstable and other reagents such as pyridinium

dichromate (PDC) and pyridinium chlorochromate (PCC) became preferred. Like the Collins reagent, these gentler oxidizing agents oxidize secondary alcohols into ketones and primary alcohols to aldehydes.[151,152]

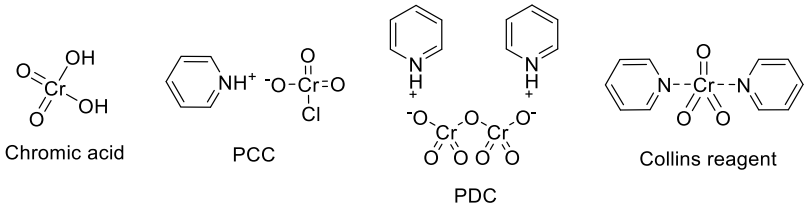

Figure 3.2: Traditional oxidation reagents based on Cr(VI).

While these reagents provide rapid and high-yielding alcohol oxidations, there are several drawbacks to their use. Firstly, alcohol oxidations with these reagents are not catalytic and thus requires stoichiometric amounts of oxidant, which in turn generates waste. Secondly, Cr(VI) is toxic and a known carcinogen, thus posing significant health risks to both humans and the environment.[153,154] Therefore, the Cr(VI)-based methods for alcohol oxidation are no longer preferable and greener, catalytic methods such as TEMPO catalysis or AAD reactions provide more environmentally friendly approaches to alcohol oxidations and is therefore an active field of research.[155,156]

3.1.2. Advantages and disadvantages of Cr(III)-based catalysts

The Madsen research group has developed several new protocols for AAD reactions, including catalyst systems based on Mn(III)-porphyrins[52], Co nanoparticles[157,158], $Mo(CO)_6$[159] and Ru *N*-Heterocyclic carbene complexes[15,16,18,20]. Recently, V(IV)-porphyrins and Cr(III)-porphyrins were also reported as catalysts for AAD reactions[145], and the Cr(III)-porphyrin system will be further discussed in Chapter 4. Overall, a wide range of metal complexes seems capable of catalyzing the AAD reaction, so it is suitable to analyze the advantages and disadvantages of employing Cr(III)-salen derivatives as catalysts for the transformation.

The main advantage of catalysts based on Cr(III) is first and foremost the cost and availability of chromium. Chromium is the 21th most abundant element in the earth crust[61] and consequently has a relatively low cost which makes it attractive in the development of cheap metal catalysts.[160] However, Cr(III)-based catalysts also have several disadvantages that one must take into account when developing new catalysts based on Cr(III).

Firstly, Cr(III) is a d^3 system, which heavily favors an octahedral coordination geometry around the Cr(III) center.[161] Octahedral complexes of Cr(III) are typically kinetically inert, so formation of saturated, octahedral and inert Cr(III) complexes may be detrimental to catalysis where fluxionality or rapid ligand exchanges may be needed.[162]

Moreover, the kinetic inertness of Cr(III) complexes has led them to be considered non-toxic, and they are certainly less toxic than Cr(VI) compounds.[163] However, the toxicity of metal ions is highly dependent on the structure of the encapsulating ligand.[60] Furthermore, the human body has a range of redox processes capable of cycling through the different oxidation states of chromium.[164] Interestingly, one study indicated that Cr(III) nutritional supplements may have

genotoxic side effects[165] and another study showed that Cr(III)-salen was an inhibitor of transcription factors binding to DNA, which is detrimental to gene expression.[166] Ultimately, one should be careful about making blanket statements about the toxicity of Cr(III) as the topic is not yet well-understood, but the uncertainty in the area should be considered a possible disadvantage of Cr(III)-based catalyst systems.

3.1.3. Catalysis with Cr(III)-salen and Cr(III)-salan complexes

Both Cr(III)-salen and Cr(III)-salan complexes have been previously studied and found to be effective catalysts in a variety of reactions. For example, Cr(III)-salen complexes have been employed as catalysts for epoxidation reactions[167–170], ring opening of epoxides[171–173], alcohol oxidations[174] and cross-coupling of phenols.[175] Furthermore, Cr(III)-salen complexes have found widespread application as catalysts for the coupling of CO_2 and epoxides, resulting in either cyclic carbonates or polycarbonates[176–179]. Figure 3.3 provides further details of catalysis achieved with the Cr(III)-salen scaffold.

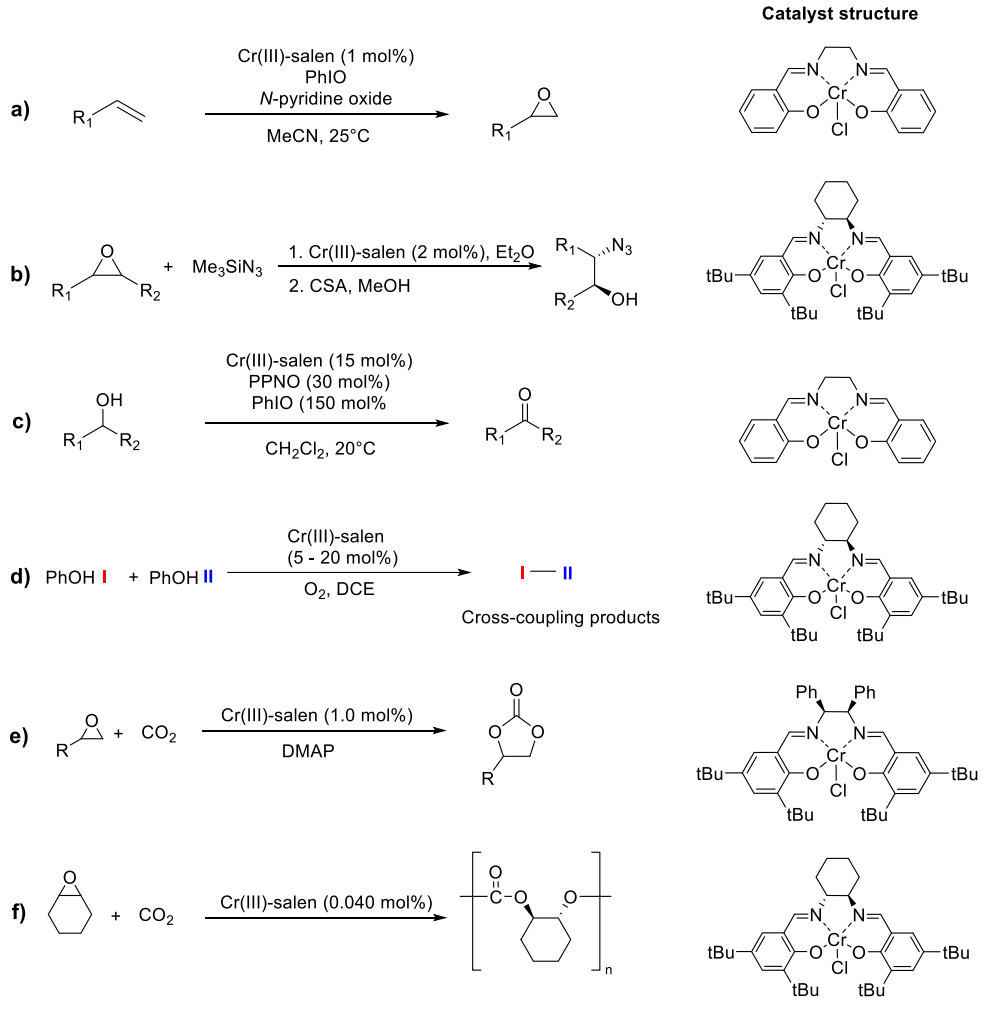

Figure 3.3: Overview of catalytic reactions with the Cr(III)-salen scaffold. **a)** Alkene epoxidation with *in situ* generated oxochromium(V).[167] **b)** Enantioselective ring opening of epoxides[173] **c)** Alcohol oxidation with *in situ* generated oxochromium(V).[174] **d)** Cross-coupling of phenols under aerobic conditions[175] **e)** Synthesis of cyclic carbonates from epoxides and CO_2.[176] **f)** Synthesis of polycarbonates from epoxides and CO_2.[178]

Reducing both imino-groups in the salen ligand results in the salan ligand. Cr(III)-salan complexes are not as well studied as the Cr(III)-salen scaffold and they have not found the same widespread application in catalysis. In fact, no examples of catalysis with the simplest Cr(III)-salan complex containing NH functionalities in the ligand have been found in the literature. However, analogous Cr(III)-salan derivatives containing methylated amino-groups in the ligand has found use in the polymerization of CO_2 and epoxides.[180,181] The protocol developed by the Darensbourg group is shown in Figure 3.4.

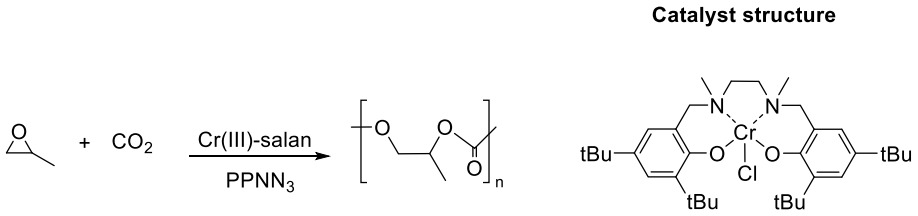

Figure 3.4: Polymerization of propylene oxide and CO_2 catalyzed by methylated Cr(III)-salan.[181]

To sum up, the Cr(III)-salen scaffold has been employed as catalysts in several organic transformations, sometimes using an external oxidant to generate reactive oxochromium(V) species. On the other hand, the applications of the Cr(III)-salan scaffold as catalyst has been limited to polymerization reactions.

3.1.4. Structural aspects of Cr(III)-salen and Cr(III)-salan complexes

To understand how catalysis with Cr(III)-salen and Cr(III)-salan complexes may function, it is important to understand the structural aspects and typical coordination geometries that these complexes may adopt under different reaction conditions. As noted in the section above, both Cr(III)-salen and Cr(III)-salan type complexes have been studied both in catalysis and fundamental inorganic chemistry and consequently, considerable efforts have been put into studying the structural aspects these complexes.

As mentioned earlier Cr(III) prefers to form octahedral complexes and thus, three configurations (*trans*, *cis*-β and *cis*-α) of an octahedral Cr(III)-salen or Cr(III)-salan complex are theoretically possible. These are schematically shown in Figure 3.5.[182,183]

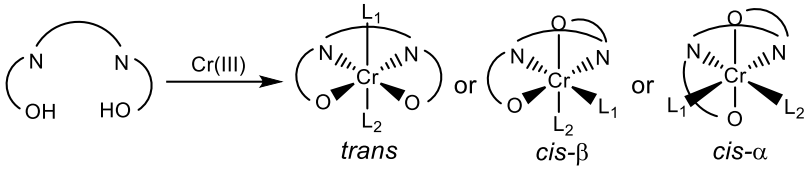

Figure 3.5: Three possible configurations of octahedral Cr(III)-salen and Cr(III)-salan complexes.

For the Cr(III)-salen scaffold, the most commonly observed configuration is *trans*-geometry due to the relatively rigid planarity of the salen skeleton leading to considerable strain in the *cis*-β and *cis*-α configurations.[182,183] No crystal structure of a *cis*-α Cr(III)-salen was found in the literature, but *cis*-β configurations around the Cr(III) center are possible and have been observed in a case with a bidentate oxalato ligand and in a hydroxo-bridged dimer of Cr(III)-salen and Cr(III)-salalen (the salalen ligand arises from reduction of only one the imines in salen).[184–186]

Apart from forming saturated, octahedral complexes, the Cr(III)-salen scaffold can also be crystallized as coordinatively unsaturated, pentacoordinate complexes if no suitable axial ligand is available. These complexes adopt a square pyramidal configuration with the salen donor atoms roughly in the same plane.[177] Crystal structures showcasing the most common configurations of Cr(III)-salen complexes are shown in Figure 3.6, and it should be noted that counterions, solvent molecules and phenolate-substituents have been removed for clarity.

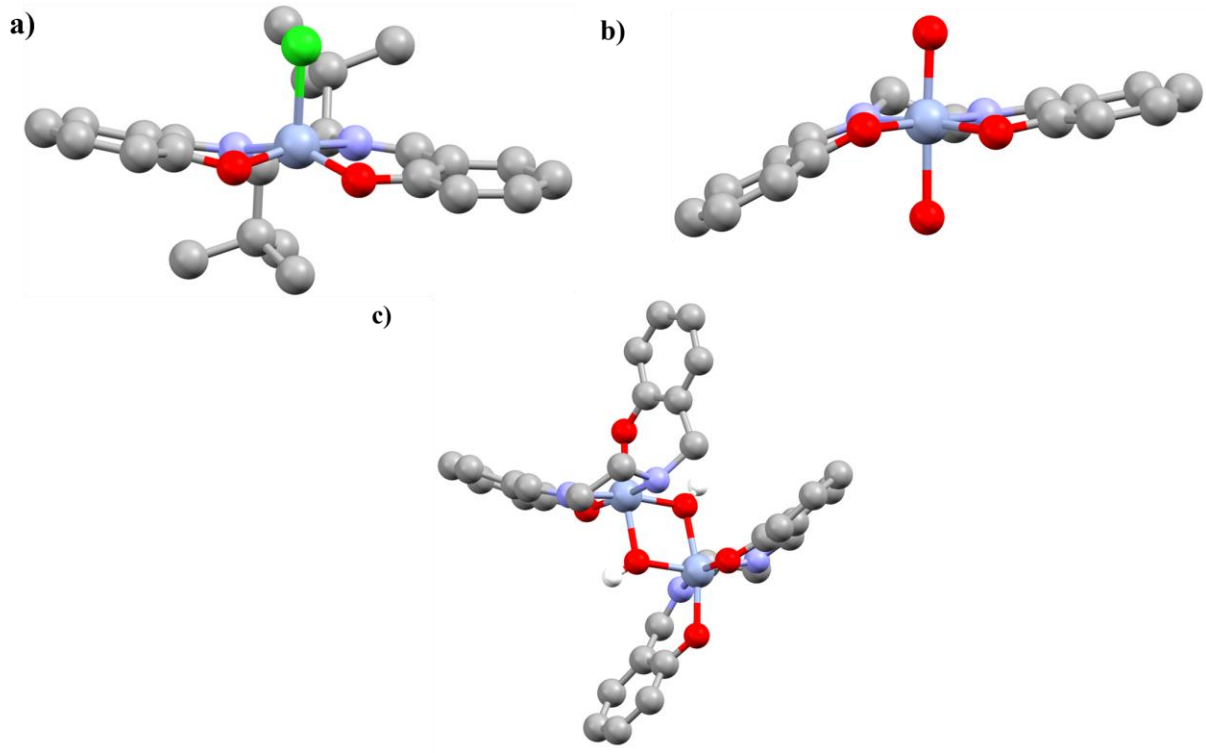

Figure 3.6: a) Pentacoordinate Cr(III)-salen with axial chloride.[177] **b)** Octahedral Cr(III)-salen cation coordinated by two water molecules.[187] **c)** Hydroxo-bridged dimer of Cr(III)-salen and Cr(III)-salalen where lower Cr(III)-salen unit adopts *cis*-β conformation.[185]

The structures of the Cr(III)-salan scaffold are more varying due to the increased flexibility of the ligand and a structure search in the CCDC database corroborates this increased flexibility and tendency to form dimers as a consequence hereof. In fact, the only monomeric structure of the fundamental Cr(III)-salan scaffold found in the CCDC database is a *cis*-β structure with ethylenediamine occupying the remaining two coordination sites.[188] A further look at the deposited structures in the CCDC database shows that the obtained crystal structures of the Cr(III)-salan scaffold are primarily dimeric and that the scaffold is capable of adapting both *trans*, *cis*-β and *cis*-α conformations, with the *cis*-β conformation being the most common.[189] Selected examples of the different conformations are shown in Figure 3.7, and it should be noted that counterions, solvent molecules and phenolate-substituents have been removed for clarity.

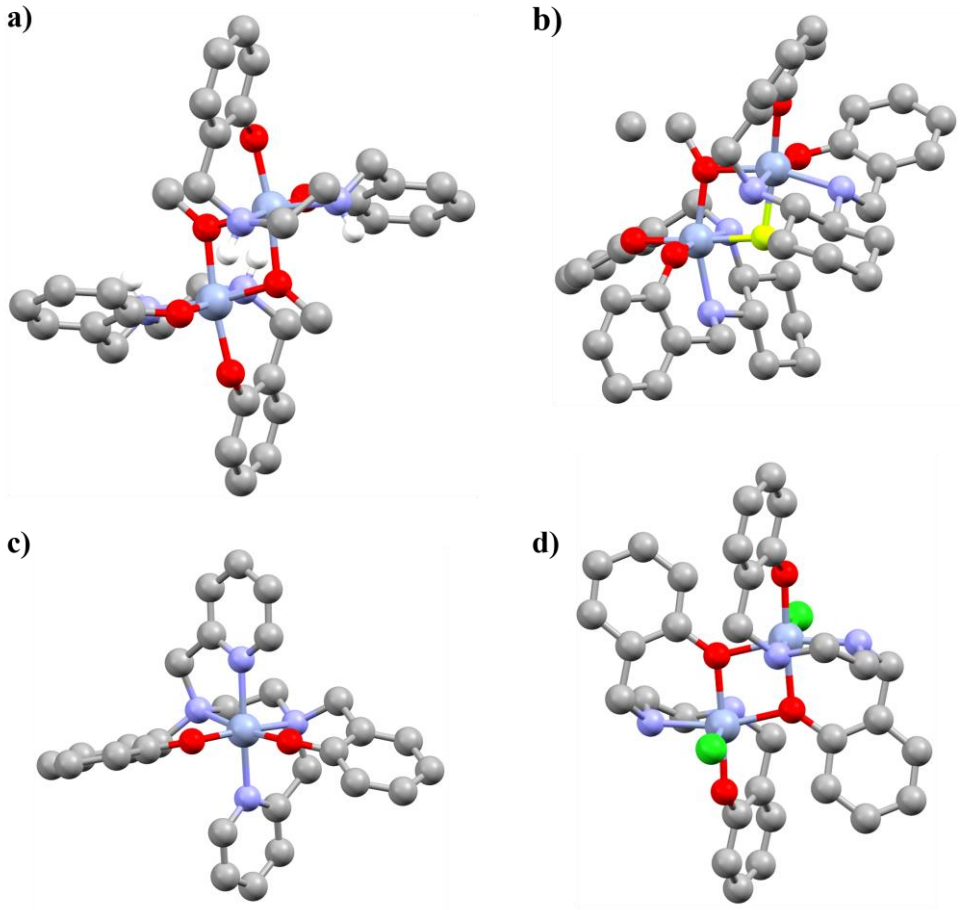

Figure 3.7: a) Cr(III)-salan dimer with bridging methoxide ligands and *cis*-β conformation.[188] **b)** Cr(III)-salan dimer with bridging ethoxide and fluoride ligands and *cis*-β conformation (-Me and -tBu groups have been removed).[190] **c)** *trans* conformation forced by pyridine ligands (-Me and -CH_2OH substituents on the phenolate have been removed).[191] **d)** Cr(III)-salan dimer with bridging phenolate ligands and *cis*-α conformation.[192]

From these examples, it is evident that the Cr(III)-salan scaffold can exist as different isomers and these are likely to have different properties, that influence their catalytic activities. Therefore, the conformational space of the Cr(III)-salan scaffold should be kept in mind if one wants to model the possible reaction mechanisms of these catalysts.

However, one thing is solid state structure, a more important factor is the solution structure of the catalyst under the reaction conditions. The solution structures of both the Cr(III)-salen and Cr(III)-salan scaffold in the presence of neutral Lewis bases such as amines or epoxides have been studied, especially in relation to polymerization catalysis. For the Cr(III)-salen scaffold, several studies based on mass spectrometry has confirmed the preference for octahedral coordination[193–195], and octahedral coordination in solution is supported by several mechanistic studies of the polymerization reactions catalyzed by the Cr(III)-salen scaffold.[196,197]

Detailed studies of solution structure for the Cr(III)-salan scaffold are scarce, but one study based on mass spectrometry found that the four-coordinate Cr(III)-salan scaffold only bound one equivalent of DMAP to form five-coordinate species preferentially.[195] However, in one of the early

descriptions of the Cr(III)-salan scaffold, evidence of octahedral *trans* configuration was found based on similarity in the ESR spectra of the Cr(III)-salan and Cr(III)-salen complexes.[198,199]

Ultimately, the previous studies indicate that octahedral *trans* configuration is preferred for Cr(III)-salen derivatives, whereas evidence for both six-coordinate and five-coordinate structures of Cr(III)-salan has been found. These findings lay the foundation for the DFT modelling of possible reaction pathways with the Cr(III)-salen system, that will be discussed later in this chapter. Before getting into the DFT modelling, the experimental investigations of AAD with Cr(III)-salen based catalysts are outlined in the coming sections.

3.2. Previous work on Cr(III)-salen catalysis performed in the Madsen group

With the basics of Cr(III)-salen and Cr(III)-salan catalysis established, the Madsen groups work with Cr(III)-salen catalysis performed prior to my involvement is outlined in this section. An international project student, Maryam Pirouz, had performed a series of screening experiments with the commercially available Cr(III)-salen catalyst **Cr3.1**. The results of her initial screening of reaction conditions are shown in Figure 3.8.

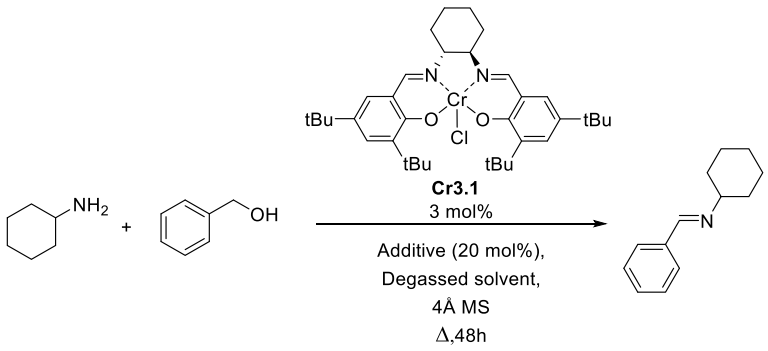

Entry	Additive	Solvent	Catalyst	GC Yield
1	NaOH	Toluene	**Cr3.1**	25%
2	NaOH	Toluene	-	54%
3	-	Toluene	**Cr3.1**	14%
4	-	Mesitylene	**Cr3.1**	70%
5	NaOH	Mesitylene	**Cr3.1**	69%
6	$CaCO_3$	Mesitylene	**Cr3.1**	99%
7	Et_3N	Mesitylene	**Cr3.1**	87%
8	CaO	Mesitylene	**Cr3.1**	91%
9	$MgBr_2$	Mesitylene	**Cr3.1**	95%
10	$AgBF_4$	Mesitylene	**Cr3.1**	72%
11	Na_2CO_3	Mesitylene	**Cr3.1**	87%
12	KOH	Mesitylene	**Cr3.1**	56%
13	$MgSO_4$	Mesitylene	**Cr3.1**	88%
14	Li_3N	Mesitylene	**Cr3.1**	81%
15	LiCl	Mesitylene	**Cr3.1**	72%
16	NaH	Mesitylene	**Cr3.1**	41%
17	Ca_3N_2	Mesitylene	**Cr3.1**	96%

Figure 3.8: Initial screening of reaction conditions performed by Maryam Pirouz.

Comparison of entry 1 and 2 shows that higher yield was obtained without addition of catalyst, which is strange and could indicate problems with the reaction setup. Nevertheless, a general improvement of the imine yield was observed when switching from toluene to mesitylene. This is expected as more thermal energy is available due to the higher boiling point of mesitylene. Looking at the role of the additives, good yields were generally observed, with the top performers being $CaCO_3$ (99%) and Ca_3N_2 (96%). Interestingly, good yields were also observed when non-basic additives such as $MgBr_2$, $AgBF_4$ and $MgSO_4$ were used, which is contrary to the observations made in the Mn(III)-salen system.[1] Here, a strong base with desiccating abilities (Ca_3N_2) was needed to drive the reaction to completion.

It should be noted that the reactions listed in Figure 3.8 were performed in a Radley carousel, which is now believed to have inflated the yields due to aerobic oxidation, as the seals in the Radley carousels were found to be prone to leakages. Nevertheless, the initial screenings performed by Maryam Pirouz laid the foundation for further investigations of the AAD reaction with Cr(III)-salen catalysts.

3.3. First round of Cr(III)-salen experimental investigations

With the promising screening experiments performed by Maryam Pirouz in hand, further investigation of the Cr(III)-salen catalyst system was deemed necessary. The experiments described in this section were carried out by BSc. students Emilie Lassen and Christian Petersen under my supervision and the reactions were performed in Radley carousels.

3.3.1. Optimization of reaction conditions

In the next iteration of Cr(III)-salen optimizations, Christian Petersen and Emilie Lassen, were working in tandem with me in an effort to optimize the yields of the AAD reaction with the commercially available Cr(III)-salen catalyst. The results of their optimization experiments are presented in Figure 3.9.

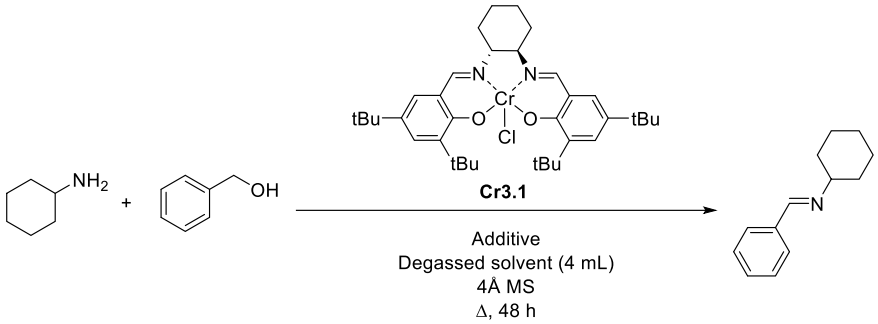

Entry	Catalyst loading (mol%)	Additive	Solvent	GC Yield
1	5	-	Toluene	10%
2	5	K_2CO_3 (20%)	Toluene	16%
3	5	K_2CO_3 (20%), 18-crown-6 (20%)	Toluene	56%
4	5	NaOH (20%)	Toluene	16%
5	5	$CaCO_3$ (20%)	Toluene	36%
6	5	-	Mesitylene	51%
7	-	KOtBu (20%)	Mesitylene	16%
8	5	KOtBu (20%)	Mesitylene	39%
9	5	K_2CO_3 (20%)	Mesitylene	34%
10	5	K_2CO_3 (20%), 18-crown-6 (20%)	Mesitylene	11%
11	5	$CaCO_3$ (20%)	Mesitylene	52%
12	5	NaOH (20%)	Mesitylene	67%
13	3	$CaCO_3$ (20%)	Mesitylene	49%
14	3	NaOH (20%)	Mesitylene	54%
15	3	Li_3N (20%)	Mesitylene	59%
16	10	Li_3N (20%)	Mesitylene	67%
17	10	Li_3N (15%)	Mesitylene	66%
18	10	NaOH (20%)	Mesitylene	61%
19	10	NaOH (15%)	Mesitylene	63%

Figure 3.9: Screening of reaction conditions performed by BSc. students Christian Petersen and Emilie Lassen.

From the optimization results, it is clear that toluene does not perform well, which stands in contrast to the observations made for the Mn(III)-salen and Fe(III)-salen protocols. The best result in toluene was obtained with the K_2CO_3/18-crown-6 combination, which furnished the imine in 56% yield. Due to the unsatisfactory yields obtained in toluene, a switch to mesitylene was made. Mesitylene is chemically similar to toluene but has a higher boiling point. If the poor yields in toluene result from a large activation energy, increasing the temperature should increase the yields. Indeed, performing the reaction in mesitylene resulted in generally higher yields, and a screening of basic additives was subsequently performed.

For reasons unknown, the K_2CO_3/18-crown-6 combination performed much worse in mesitylene (11% yield) compared to toluene (56% yield). In general, the best performing additives were NaOH and Li_3N, but full conversion of the starting materials was not achieved, not even when increasing

the catalyst loading to 10%. Ultimately, 5 mol% catalyst and 15 mol% Li_3N were selected by Christian Petersen and Emilie Lassen for further experiments.

3.3.2. Substrate scope

A limited substrate scope was performed by Christian Petersen and Emilie Lassen using the chosen conditions. The results are shown in Figure 3.10:

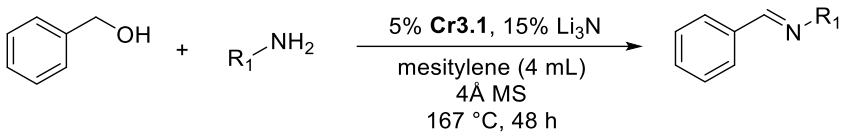

Entry	Amine	Product	Yield (%)
1	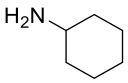	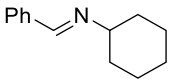	38
2	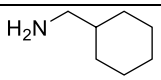	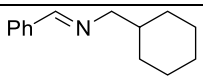	37
3	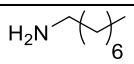	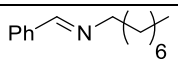	49
4	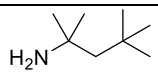	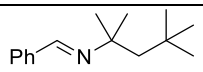	33
5	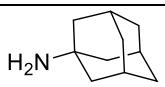	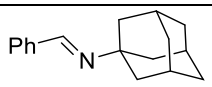	38
6	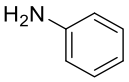	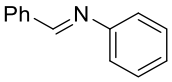	28
7	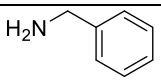	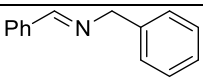	35

Figure 3.10: The substrate scope with respect to the amine was tested by Christian Petersen and Emilie Lassen using the optimized protocol. The noted yields are isolated yields.

The substrate scope revealed that a range of amines could partake in the imination reaction, and the yields were roughly comparable (30 – 50%). However, the isolated imine yields were not satisfactory compared to the high yields obtained with the Mn(III)-salen and Fe(III)-salen protocol, so further optimization was warranted.

3.3.3. Determination of kinetic isotope effect and H/D scrambling

To gain further insight into the reaction mechanism, experiments with benzyl alcohol-α,α-d_2 were conducted by Christian Petersen and Emilie Lassen. The aim was to determine the kinetic isotope effect and the possible deuterium/hydrogen scrambling in the product imine. Using the optimized protocol, reactions were performed with both deuterated and non-deuterated benzyl alcohol and the initial rates of reaction were determined by GC-MS monitoring of the product imine. The resulting plot is shown in Figure 3.11.

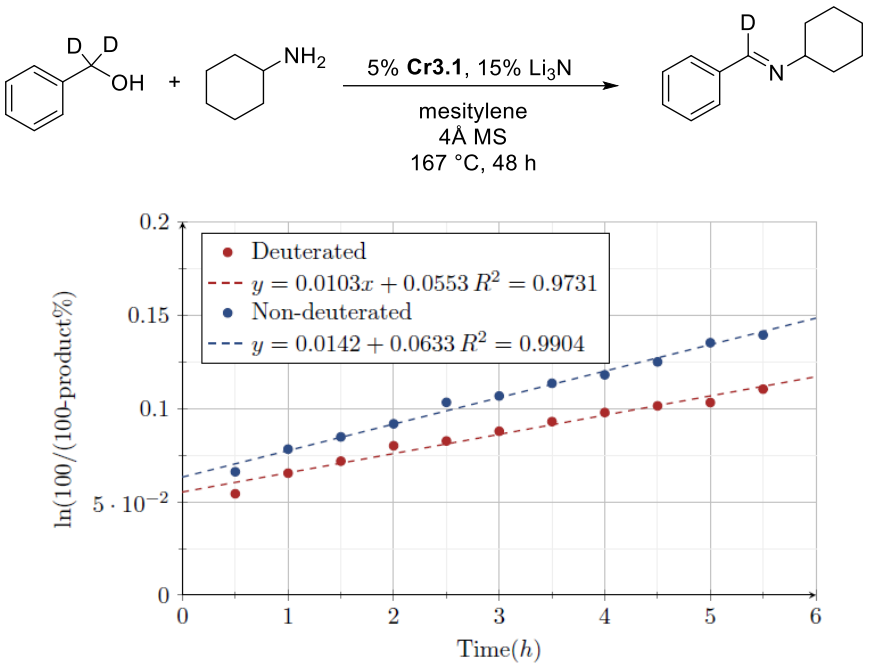

Figure 3.11: Monitoring the formation of imine as a function of time allowed determination of the initial rates of reaction for deuterated and non-deuterated benzyl alcohol, respectively.

From the rate plot shown in Figure 3.11, the kinetic isotope effect was determined to 1.38, which is very similar to the value determined for the Fe(III)-salen system. Again, the magnitude of the KIE is low compared to KIEs for H^- transfer from alcohols presented in the literature[32,82,112–115], and the cause for this is unknown.

3.3.4. Hammett study

To gain further understanding of the mechanism, a Hammett study was conducted by Christian Petersen and Emilie Lassen under my supervision.

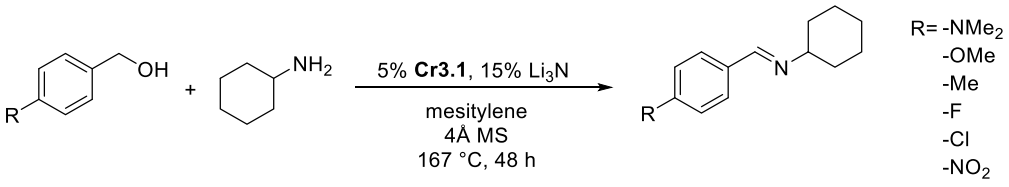

Figure 3.12: Conditions used in the Hammett study performed by BSc. students Christian Petersen and Emilie Lassen.

The Hammett study was performed by running competition experiments between non-substituted benzyl alcohol and a series of *para*-substituted benzyl alcohols. The conditions and included alcohols are shown in Figure 3.12. Due to experimental difficulties, the consumption of the alcohols could not be followed by GC-MS. Instead, the formation of imines was followed to determine the relative rates of reaction. From these, a Hammett plot based on the Hammett *para*-substituent constant σ_p was constructed. The plot is shown in Figure 3.13.

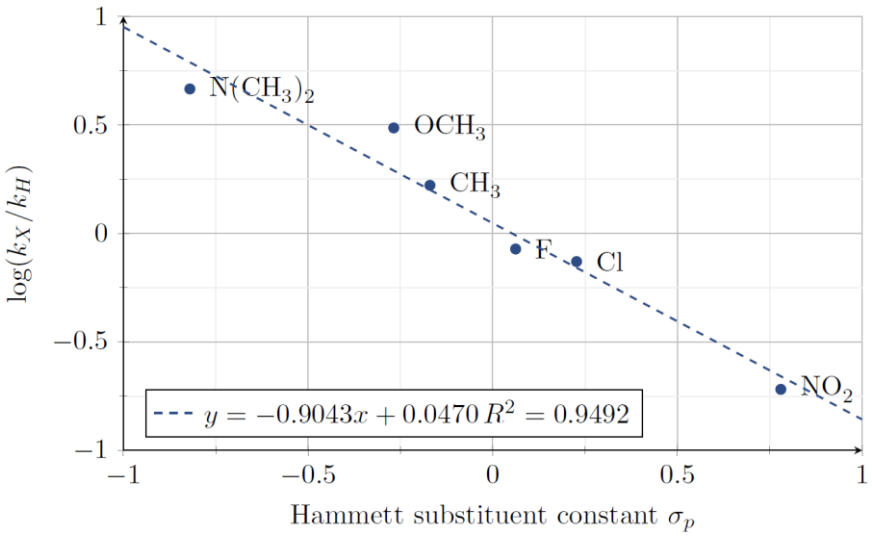

Figure 3.13: Hammett plot of the Cr(III)-salen imination determined by Christian Petersen and Emilie Lassen.

The Hammett plot resulted in a straight line with a slope ρ = -0.90, which is consistent with build-up of positive charge on the benzylic carbon. This indicates that hydride transfer from the alcohol could be one of the slow steps in the reaction.

3.3.5. Control experiments

As a last experiment in the first round of experimental investigations, the possible involvement of radicals was tested by Christian Petersen and Emilie Lassen. A reaction was performed in the presence of the radical scavenger 2,4-diphenyl-4-methyl-1-pentene according to Figure 3.14:

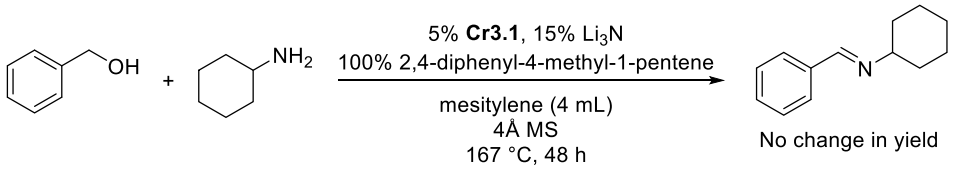

Figure 3.14: Presence of radical scavenger did not change the outcome of the reaction.

Neither change in imine yield nor conversion of the radical scavenger was observed by GC-MS, which renders a radical mechanism unlikely.

3.4. Synthesis of Cr(III)-salen and Cr(III)-salan derivatives

So far, inconsistent results and incomplete conversion of starting materials have plagued the development of the Cr(III)-salen catalyzed imination reaction. Only the commercially available **Cr3.1** had been used as the catalyst, but one of the important advantages of the salen ligand scaffold is the ease with which changes to the ligand structure can be made. Both the ligand backbone can be altered and the phenolates can be substituted with either electron donating groups (EDGs) or electron withdrawing groups (EWGs) to tune the electronic properties of the resulting catalyst. Furthermore, the salen ligands can be easily reduced to salan ligands, which may also impact the catalytic efficiency of the resulting catalysts due to increased flexibility and altered electronic properties.

The structural alterations are possible due to the relatively straightforward synthesis of both salen and salan-type ligands. In this section, the synthetic efforts towards derivatives of the salen and salan-type ligands and their corresponding Cr(III) complexes are outlined.

3.4.1. Ligand synthesis

The salen-type ligands and their corresponding metal complexes are ubiquitous in catalysis and inorganic chemistry in general.[200] One of the main reasons is the ease with which they are synthesized. In general, a diamine is condensed with two equivalents of salicylaldehyde to form the two imino-bridges. The reactions are typically carried out by refluxing the reactants in either MeOH or EtOH and the product usually precipitates cleanly out of the reaction mixture, allowing easy isolation of the salen-type ligands in high yields.[162] Changing the diamine allows synthesis of salen-type ligands with different backbones and changing the substitution pattern of the salicylaldehyde allows tuning of the electronic or steric properties of the ligand which may impact the catalytic activities of the resulting catalysts.[177,201]

As the structure of the catalyst is one of the main reaction parameters to optimize, a library of different salen ligand derivatives were synthesized in high yields according to the generalized reaction scheme presented in Figure 3.15.

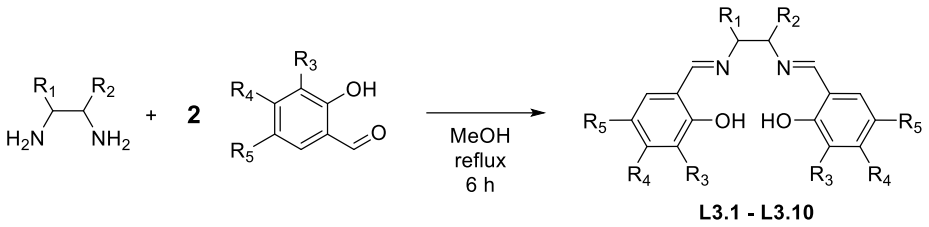

Ligand	Yield	Ligand	Yield
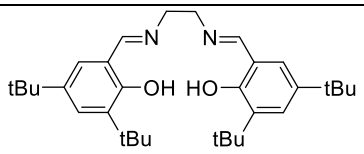 L3.1	92%	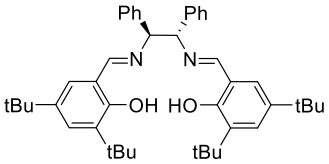 L3.2	95%
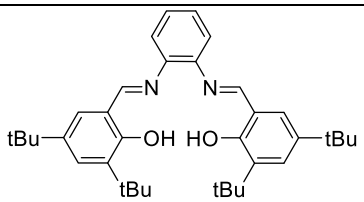 L3.3	88%	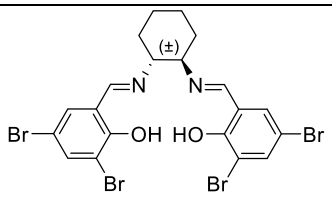 L3.4	90%
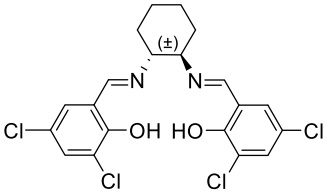 L3.5	94%	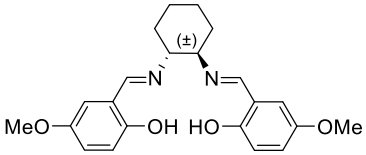 L3.6	93%
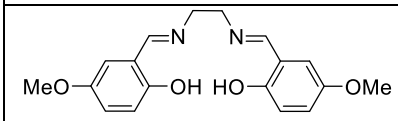 L3.7	89%	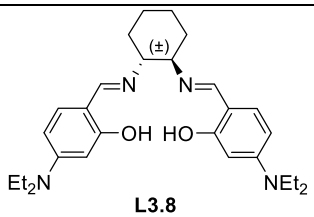 L3.8	89%
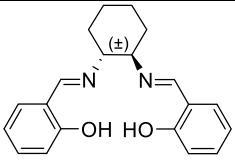 L3.9	80%	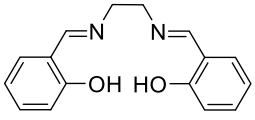 L3.10	94%

Figure 3.15: Overview of synthesized salen-type ligands and their isolated yields.

The different salen derivatives were chosen to test different factors such as the structural rigidity of the ligand (**L3.3**), the influence of solubility and steric bulk (**L3.1 – L3.3**), and the influence of EWGs or EDGs on the phenol moieties. Lastly, the syntheses were largely guided by the commercial availability of the starting materials. Overall, the syntheses of the salen ligand derivatives were straightforward and the full experimental details and characterization data for the salen ligands are provided in Section 3.8.3 and Section 3.8.4.

As *in situ* reduction of the diimino-backbone was observed in the Mn(III)-salen protocol[1], a similar pathway was hypothesized for the Cr(III)-salen protocol, and an investigation of the catalytic properties of Cr(III)-salan type catalysts was therefore deemed appropriate. The salan ligand derivatives are typically prepared by reduction of the imino-bridges in the salen ligand with either $NaBH_4$ or $NaBH_3CN$.[183,202,203] In this project, a method employing $NaBH_4$ in MeOH was chosen and a range of salan derivatives were synthesized according to Figure 3.16.

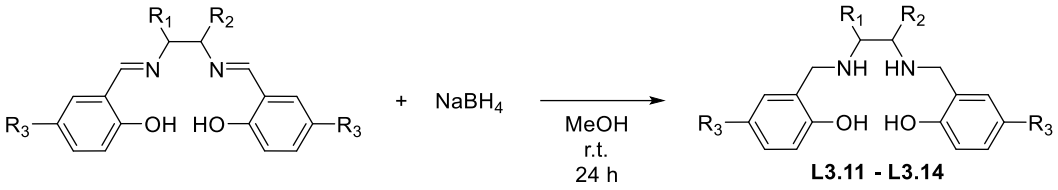

Ligand	Yield	Ligand	Yield
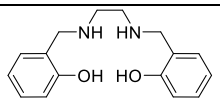 L3.11	79%	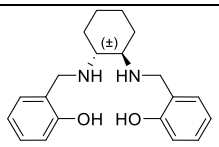 L3.12	96%
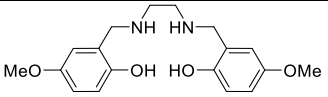 L3.13	89%	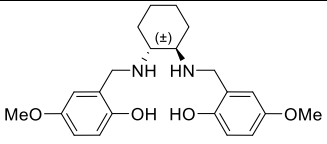 L3.14	92%

Figure 3.16: Overview of synthesized salan-type ligands and their isolated yields.

The reduction of the salen ligand is easy to follow visually as the yellow color gradually disappears and the reaction turns colorless. In general, high yields of the salan derivatives were obtained and the full details regarding synthesis and characterization are provided in Section 3.8.3 and Section 3.8.5. With a library of ligands in hand, the syntheses of the corresponding Cr(III)-salen and Cr(III)-salan complexes are described in the following section.

3.4.2. Synthesis of Cr(III)-salens

The most commonly adopted synthetic pathway to Cr(III)-salen complexes simply rely on mixing the salen ligand with a slight excess of anhydrous $CrCl_2$ in THF under water and air-free conditions. This method was employed both by the Jacobsen and the Darensbourg group in their studies of catalysis with Cr(III)-salen systems.[173,177] Using this method, a range of Cr(III)-salen derivatives were synthesized according to Figure 3.17. Further experimental details and characterization of the catalysts are provided in Section 3.8.3 and Section 3.8.6.

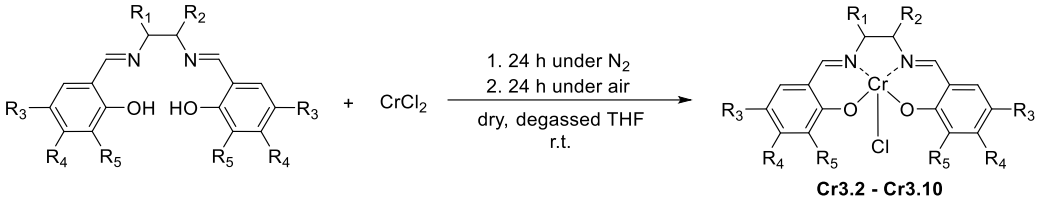

Complex	Yield	Complex	Yield
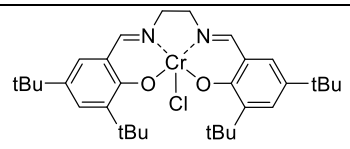 **Cr3.2**	71%	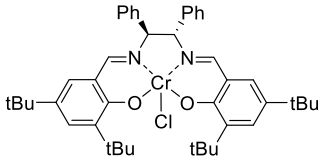 **Cr3.3**	89%
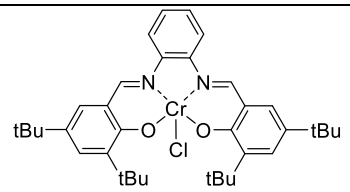 **Cr3.4**	68%	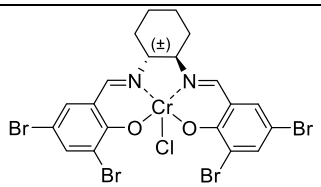 **Cr3.5**	55%
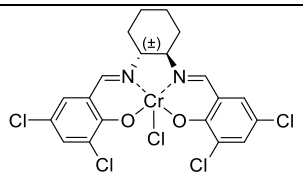 **Cr3.6**	76%	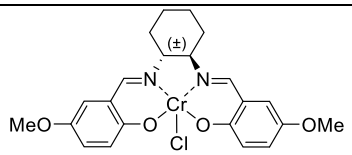 **Cr3.7**	68%
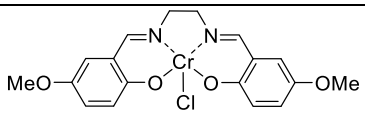 **Cr3.8**	45%	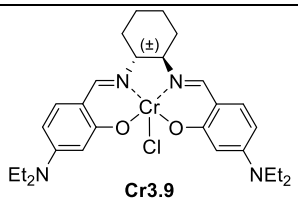 **Cr3.9**	48%
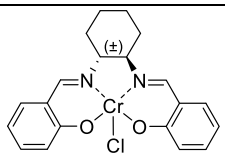 **Cr3.10**	73%		

Figure 3.17: The synthesis of catalysts based on the Cr(III)-salen scaffold.

The method involves stirring the reaction mixture for 24 hours under an inert atmosphere which allows complexation of the kinetically labile Cr(II). Subsequent introduction of air oxidizes Cr(II) to Cr(III) and, depending on the solubility of the resulting Cr(III)-salen complex in THF, the catalyst can be isolated in adequate yields by either filtration or aqueous work-up.

3.4.3. Synthesis of Cr(III)-salans

The Cr(III)-salan scaffold has not garnered the same research interest as the Cr(III)-salen complexes, and consequently, a plethora of literature syntheses of these complexes are not readily available. However, in the 1990s, the Elias research group pioneered the study of Cr(III)-salan complexes and discovered that dimers of the Cr(III)-salan scaffold can be prepared in good yields by refluxing the salan ligand, $CrCl_3 \cdot 6H_2O$, Et_3N and Zn in 2-methoxyethanol.[192] Using their method, four different catalysts based on the Cr(III)-salan scaffold was synthesized in good yields according to Figure 3.18. Further experimental details and characterization of the catalysts are provided in Section 3.8.3 and Section 3.8.7.

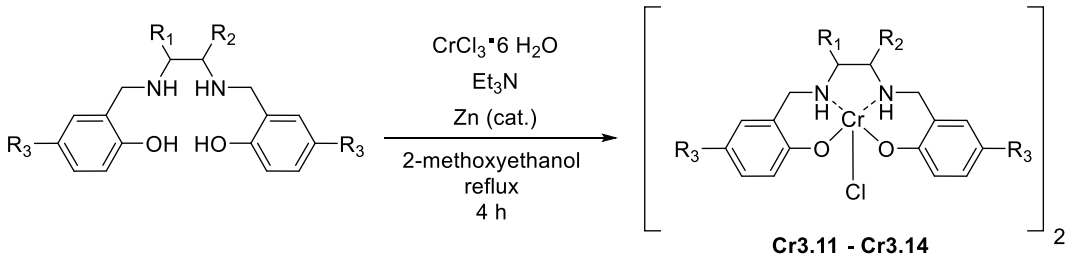

Complex	Yield	Complex	Yield
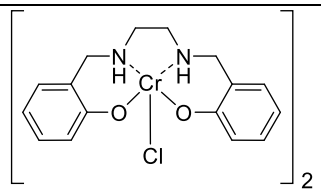 Cr3.11	69%	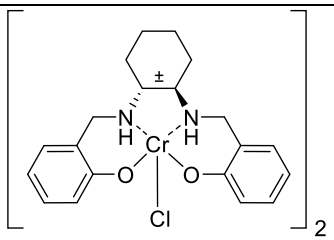 Cr3.12	75%
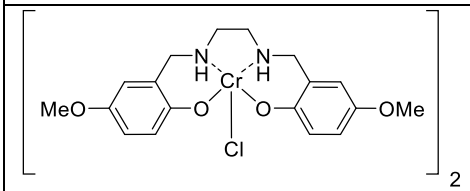 Cr3.13	53%	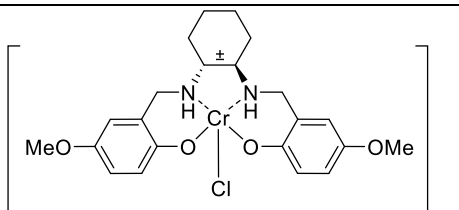 Cr3.14	67%

Figure 3.18: The synthesis of catalysts based on the Cr(III)-salan scaffold.

Presumably, the role of Zn is to reduce Cr(III) to Cr(II) to produce a kinetically labile metal center, and Et_3N facilitates deprotonation of the phenols. In all four cases, a fine blue-green powder precipitated during the reaction and subsequent filtration, washing and drying yielded the Cr(III)-salan derivatives in adequate yields.

With a range of Cr(III)-salen and Cr(III)-salan catalysts in hand, the experimental investigation and optimization of reaction parameters will be described in the coming section.

3.5. Second round of Cr(III)-salen and Cr(III)-salan experimental investigations

In the second round of investigations into the AAD reaction with Cr(III)-salen catalysts, several derivatives of both Cr(III)-salen and Cr(III)-salan were tested. Furthermore, the reactions were no longer performed in the Radley carousels due to issues with reproducibility arising from leakages. Rather, the reactions were performed in Schlenk reaction tubes equipped with a cold-finger, and actions were taken to minimize sources of error, including thorough degassing of solvents, keeping a high flow of N_2 over the reaction mixture to exclude oxygen and thorough cleaning of reaction vessels with *aqua regia* prior to use.

3.5.1. Optimization of reaction conditions

A large range of reaction conditions and catalysts were tested to improve the reactivity of the Cr(III)-salen based catalyst system. An overview of the tested Cr(III)-salen catalysts are shown in Figure 3.19 and an overview of the tested Cr(III)-salan catalysts are shown in Figure 3.20.

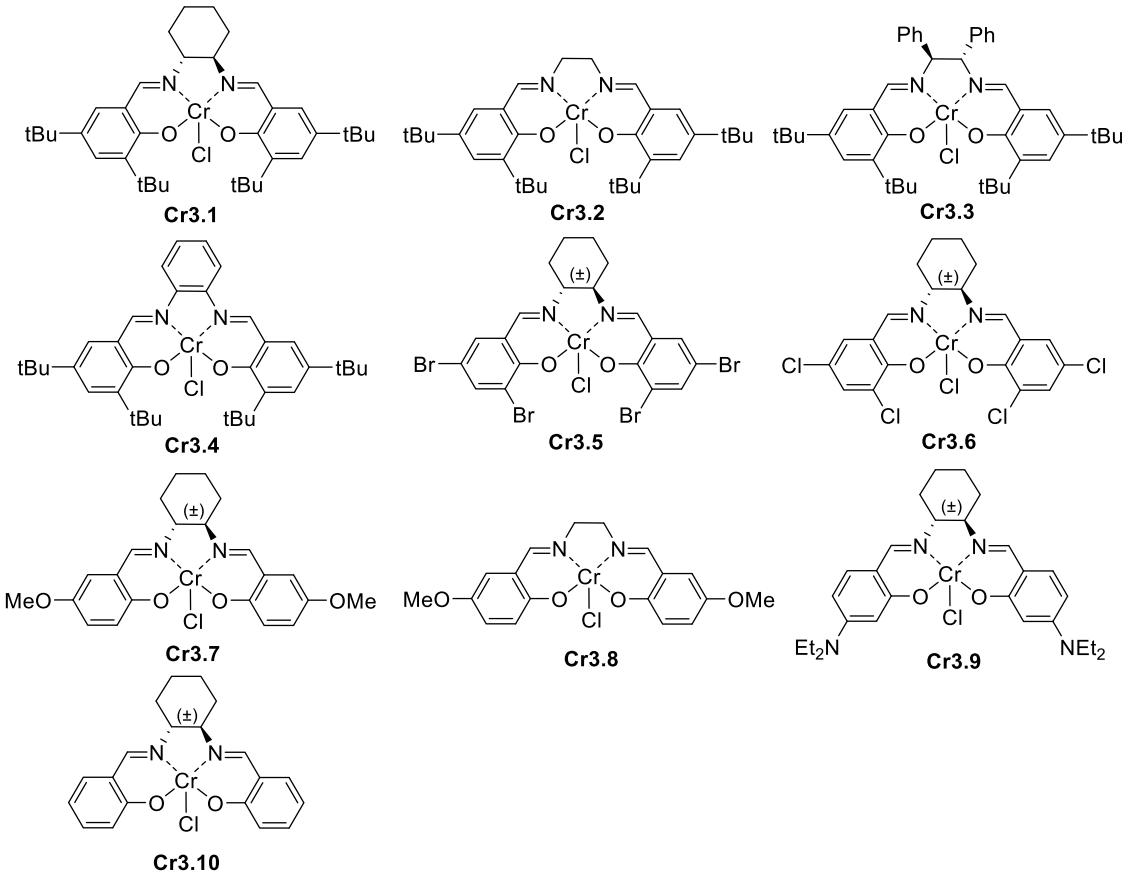

Figure 3.19: Overview of the tested Cr(III)-salen catalysts.

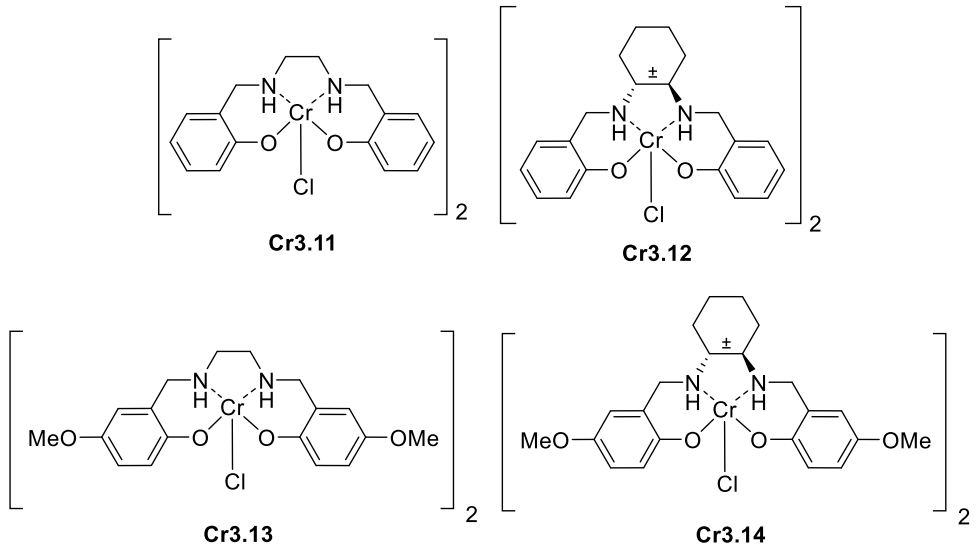

Figure 3.20: Overview of the tested Cr(III)-salan catalysts.

As in the previous iterations of the Cr(III)-salen investigations, the oxidation of benzyl alcohol and subsequent imine formation with cyclohexylamine was chosen as the trial reaction for the optimization experiments. Different catalysts, solvents, bases, desiccants, and additives were tested, and the yield of the reactions were determined by GC-MS. A daunting amount of optimization experiments were performed by me and MSc. student Sofie Latt Hjort Pedersen (SLHP). The full range of results are provided in Table 3.11 and Table 3.12 in Section 3.8.8 and Section 3.8.9. In the coming sections, the most illustrative results have been cherrypicked to more easily convey the different hypotheses that were addressed during the optimization experiments.

Influence of solvent

The solvent is an important factor in the optimization of reaction conditions and for the Mn(III)-salen and Fe(III)-salen protocols, toluene was determined as the optimal solvent.[1,111] The previous experiments with the Cr(III)-salen protocol outlined in Section 3.2 and Section 3.3 had determined mesitylene as the optimal solvent, indicating that high temperatures and a non-polar solvent is preferable. Evidently, high temperatures are needed to overcome the energy barriers and the non-coordinating nature of mesitylene is thought to allow efficient coordination of the reactants. To further corroborate that mesitylene is indeed the solvent of choice for the Cr(III)-salen protocol, a few experiments examining the solvent dependency is highlighted in Table 3.1.

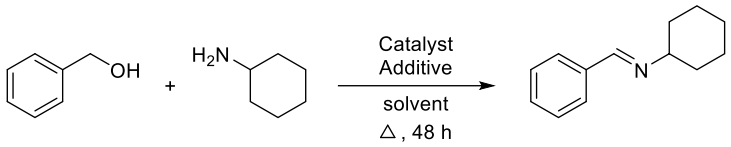

Table 3.1: Optimization entries highlighting the solvent dependency of the reaction.

Entry[a]	Catalyst	Catalyst load (mol%)	Base	Base load (mol%)	Solvent	Solvent amount (mL)	Desiccant	Yield[b] (%)
NH2	**Cr3.1**	5	KOtBu	20	toluene	4	4Å MS	18
NH7	**Cr3.1**	5	KOtBu	20	1,4-dioxane	4	4Å MS	<10
NH12	**Cr3.1**	5	KOtBu	20	mesitylene	4	4Å MS	23
NH76	**Cr3.12**	5	KOtBu	20	DMF	4	4Å MS	<10
NH81	**Cr3.12**	5	KOtBu	20	pyridine	4	4Å MS	<10
NH83	**Cr3.12**	5	KOtBu	20	toluene	4	4Å MS	<10
NH72	**Cr3.12**	5	KOtBu	15	mesitylene	4	4Å MS	<10
[a]Conditions: BnOH (1.0 mmol), CyNH2 (1.0 mmol), tetradecane (0.5 mmol, IS), reflux, 48 h. [b]GC-MS yield								

Evidently, the reaction occurs in both toluene and mesitylene, but the yield is slightly higher in mesitylene, presumably due to the higher temperature and thus faster reaction. Switching to the more polar and coordinating solvent 1,4-dioxane results in diminished reactivity, which is thought to stem from both the lower boiling point and coordinating ability of the solvent. The solvent dependency of the reaction with the Cr(III)-salan catalyst **Cr3.12** was also tested, but no appreciable conversion was observed in either DMF, pyridine, toluene or mesitylene. This is a testament to the low reactivity of the Cr(III)-salan derivatives, which will be discussed later.

Influence of base type

A wide range of base types had been tested in the previous iterations of the Cr(III)-salen protocol and the nitride bases Ca_3N_2 and Li_3N arose as lead candidates. In this iteration of optimization experiments, a wide range of bases were tested in an attempt to increase the reactivity of the Cr(III)-salen protocol. The addition of strong base is thought to facilitate formation of catalyst intermediates with benzyl alkoxide ligands, which are envisioned as important intermediates in the reaction. Furthermore, strong bases could also drive the imination by trapping released water as insoluble hydroxides. The results obtained with different bases are shown in Table 3.2.

Table 3.2: Optimization entries highlighting the dependency of the base type.

Entry[a]	Catalyst	Catalyst load (mol%)	Base	Base load (mol%)	Solvent	Solvent amount (mL)	Desiccant	Yield[b] (%)
SP11	**Cr3.1**	10	Ca_3N_2	100	mesitylene	4	4Å MS	30
SP15	**Cr3.1**	10	Li_3N	100	mesitylene	4	4Å MS	19
SP17	**Cr3.1**	10	Mg_3N_2	100	mesitylene	4	4Å MS	16
SP37	**Cr3.1**	10	KOtBu	100	mesitylene	4	4Å MS	22
SP39	**Cr3.1**	10	NaOtBu	100	mesitylene	4	4Å MS	17
SP40	**Cr3.1**	10	CaO	100	mesitylene	4	4Å MS	12
SP42	**Cr3.1**	10	DBU	100	mesitylene	4	4Å MS	14
SP47	**Cr3.1**	10	$Ca(OH)_2$	100	mesitylene	4	4Å MS	17
SP51	**Cr3.1**	10	NaOH	100	mesitylene	4	4Å MS	14
SP55	**Cr3.1**	10	KOH	100	mesitylene	4	4Å MS	17

[a]Conditions: BnOH (1.0 mmol), CyNH2 (1.0 mmol), tetradecane (0.5 mmol, IS), reflux, 48 h. [b]GC-MS yield.

The best performing base is Ca_3N_2, which resulted in a 30% yield of the imine. Ca_3N_2 was also identified as the optimal base in the Mn(III)-salen protocol.[1] The other tested bases performed roughly the same, with CaO being the worst performing base with a yield of 12%. It should be noted that, apart from DBU, KOtBu and NaOtBu, the tested bases were not fully soluble in mesitylene, so the actual base concentration is unknown. Overall, none of the tested bases incurred a large improvement in reactivity.

Influence of base amount

With the identification of Ca_3N_2 as the best performing base, different base amounts were tested. The hypothesis was that an increased amount of base would favor formation of benzyl alkoxide intermediates, which would be beneficial for the reactivity. The results are shown in Table 3.3.

Table 3.3: Optimization entries highlighting the dependency of the base loading.

Entry[a]	Catalyst	Catalyst load (mol%)	Base	Base load (mol%)	Solvent	Solvent amount (mL)	Desiccant	Yield[b] (%)
SP9	**Cr3.1**	10	Ca_3N_2	16.7	mesitylene	4	4Å MS	14
SP10	**Cr3.1**	10	Ca_3N_2	50	mesitylene	4	4Å MS	23
SP11	**Cr3.1**	10	Ca_3N_2	100	mesitylene	4	4Å MS	30
SP12	**Cr3.1**	10	Ca_3N_2	133	mesitylene	4	4Å MS	31
SP13	**Cr3.1**	10	Ca_3N_2	167	mesitylene	4	4Å MS	33

[a]Conditions: BnOH (1.0 mmol), CyNH2 (1.0 mmol), tetradecane (0.5 mmol, IS), reflux, 48 h. [b]GC-MS yield.

As the loading of Ca_3N_2 is increased, a slight increase in yield is also observed. The yield reaches a plateau around 30% with a loading of 100% Ca_3N_2, so increasing the base amount further was deemed futile.

Influence of desiccants

The condensation between cyclohexylamine and benzaldehyde is reversible, so it was hypothesized that addition of desiccants would be beneficial. Thus, a range of desiccants were tested, and the results are shown in Table 3.4.

Table 3.4: Optimization entries highlighting the influence of desiccants.

Entry[a]	Catalyst	Catalyst load (mol%)	Base	Base load (mol%)	Solvent	Solvent amount (mL)	Desiccant	Yield[b] (%)
NH49	**Cr3.2**	5	KOtBu	20	mesitylene	4	None	24
NH44	**Cr3.2**	5	KOtBu	20	mesitylene	4	4Å MS	24
NH103	**Cr3.1**	5	KOtBu	20	mesitylene	4	4Å MS	25
NH107	**Cr3.1**	5	KOtBu	20	mesitylene	4	$MgSO_4$ (1.0 eq.)	25
NH108	**Cr3.1**	5	KOtBu	20	mesitylene	4	Na_2SO_4 (1.0 eq.)	23
SP65	**Cr3.1**	10	KOtBu	100	mesitylene	4	$MgSO_4$ (1.0 eq.)	16
SP66	**Cr3.1**	10	KOtBu	100	mesitylene	4	K_2CO_3 (1.0 eq.)	17
SP74	**Cr3.1**	10	KOtBu	100	mesitylene	4	4Å MS	22

[a]Conditions: BnOH (1.0 mmol), CyNH2 (1.0 mmol), tetradecane (0.5 mmol, IS), reflux, 48 h. [b]GC-MS yield.

Evidently, the addition of different desiccants did not result in an improvement of the yield. In the presented cases, yields ranging from 16 – 25% were observed, and the variations are within the range of experimental error. Overall, the condensation between benzaldehyde and cyclohexylamine does not seem to be the troublesome reaction, rather it is the dehydrogenation of benzyl alcohol to form benzaldehyde that needs attention.

Influence of 18-crown-6 and $Al(OTf)_3$

Throughout the optimization experiments, a range of potassium salts were used as basic additives. To increase the basicity and solubility of the potassium bases, addition of 18-crown-6 was tried. 18-crown-6 (shown in Figure 3.21) is known to encapsulate the K^+ ion, thus increasing the solubility and basicity of the corresponding anion.[204]

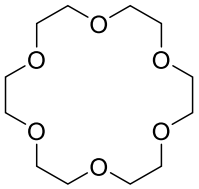

18-crown-6

Figure 3.21: Structure of 18-crown-6.

Furthermore, it was suspected that benzyl alkoxide ligands would bind too strongly to the Cr(III) center due to its high Lewis acidity. Therefore, the addition of a competing, strong Lewis acid in the form of $Al(OTf)_3$ was also tested. The results are shown in Table 3.5.

Table 3.5: Optimization entries highlighting the influence of other additives.

Entry[a]	Catalyst	Catalyst load (mol%)	Base	Base load (mol%)	Solvent	Solvent amount (mL)	Desiccant	Yield[b] (%)
NH44	**Cr3.2**	5	KOtBu	20	mesitylene	4	4Å MS	24
NH45	**Cr3.2**	5	K_2CO_3	20	mesitylene	4	4Å MS	19
NH41[c]	**Cr3.2**	5	KOtBu	20	mesitylene	4	4Å MS	25
NH42[c]	**Cr3.2**	5	K_2CO_3	20	mesitylene	4	4Å MS	23
SP23	**Cr3.3**	10	Ca_3N_2	100	mesitylene	4	4Å MS	20
NH130[d]	**Cr3.3**	10	Ca_3N_2	100	mesitylene	4	4Å MS	27

[a]Conditions: BnOH (1.0 mmol), CyNH2 (1.0 mmol), tetradecane (0.5 mmol, IS), reflux, 48 h. [b]GC-MS yield. [c]20 mol% 18-crown-6 was also added. [d]10 mol% $Al(OTf)_3$ was also added.

Evidently, the addition of 18-crown-6 did not result in a marked improvement of the reactivity. The addition of $Al(OTf)_3$ resulted in a small improvement from 20% to 27%, which indicates that addition of competing Lewis acids may increase reactivity slightly, but the effect was not large enough to warrant further investigations.

Influence of catalyst structure

The last considered parameter was the structure of the employed catalyst. After all, the salen ligand scaffold was chosen to allow easy modification of the catalyst and thereby easy tuning of both steric and electronic parameters. The tested catalysts are presented in Figure 3.19 and Figure 3.20 and across the range of catalysts, a range of parameters are varied. The main parameters include the solubility of the catalyst, the Lewis acidity of both the Cr(III)-center and the imino moiety, the flexibility of the catalyst and the presence of amino vs. imino groups in the catalyst backbone. The testing of the different catalysts was done over a long period of time during which different reaction conditions were thought optimal. The preferred conditions of 10 mol% catalyst and 100% Ca_3N_2 arose late in the project and therefore, the reaction conditions are not identical for each catalyst and the imine yields are therefore not directly comparable. Despite this, the main trend can still be extracted from the results presented in Table 3.6.

Table 3.6: Optimization entries highlighting the influence of catalyst structure.

Entry[a]	Catalyst	Catalyst load (mol%)	Base	Base load (mol%)	Solvent	Solvent amount (mL)	Desiccant	Yield[b] (%)
SP11	**Cr3.1**	10	Ca_3N_2	100	mesitylene	4	4Å MS	30
NH123	**Cr3.2**	10	Ca_3N_2	100	mesitylene	4	4Å MS	27
SP23	**Cr3.3**	10	Ca_3N_2	100	mesitylene	4	4Å MS	20
NH17	**Cr3.4**	5	KOtBu	20	mesitylene	4	4Å MS	24
NH87	**Cr3.5**	5	KOtBu	20	mesitylene	4	4Å MS	18
NH96	**Cr3.6**	5	Ca_3N_2	20	mesitylene	4	4Å MS	23
NH98	**Cr3.7**	5	Ca_3N_2	20	mesitylene	4	4Å MS	25
SP8	**Cr3.8**	5	Ca_3N_2	100	mesitylene	4	4Å MS	<10
SP27	**Cr3.9**	10	Ca_3N_2	100	mesitylene	4	4Å MS	18
SP60	**Cr3.10**	5	KOtBu	20	mesitylene	4	4Å MS	14
NH65	**Cr3.11**	5	KOtBu	20	mesitylene	4	4Å MS	<10
SP29	**Cr3.12**	10	Ca_3N_2	100	mesitylene	4	4Å MS	<10
SP31	**Cr3.13**	10	Ca_3N_2	100	mesitylene	4	4Å MS	<10
NH112	**Cr3.14**	10	Ca_3N_2	100	mesitylene	4	4Å MS	11

[a]Conditions: BnOH (1.0 mmol), CyNH2 (1.0 mmol), tetradecane (0.5 mmol, IS), reflux, 48 h. [b]GC-MS yield.

Overall, the performance of the different Cr(III)-salen catalysts are comparable; none of them work very well. It should be noted that only the –tBu substituted Cr(III)-salen complexes (**Cr3.1 – Cr3.4**) were fully soluble under the employed reaction conditions and full dissolution of the catalyst was not observed for the other catalysts (**Cr3.5 – Cr3.14**). This could be a contributing factor to the poor reactivity and the observation highlights the importance of –tBu substitution for increased solubility in non-polar solvents.

The attempts to increase the reactivity of the system by altering the structure of the backbone failed (**Cr3.1 – Cr3.4**); changing from the cyclohexyl backbone of **Cr3.1** to the alternatives **Cr3.2 – Cr3.4** did not improve reactivity. Altering the Lewis acidity of the catalyst was also attempted in

vain (**Cr3.5 – Cr3.10**); substituting various positions on the phenolate groups with –Br, -Cl, -OMe and –NEt_2 did not improve reactivity. Lastly, the imino groups were exchanged for amino groups as the Cr(III)-salan catalysts (**Cr3.11 – Cr3.14**) were tested. Evidently, this change was detrimental to the reactivity, which indicates that the imino groups play an important role in the system. Overall, none of the synthesized catalysts performed better than the commercially available **Cr3.1** and further optimization of the catalyst structure was not pursued.

3.5.2. Conclusion of the optimization experiments

In the second iteration of optimization experiments for the Cr(III)-salen protocol, a wide range of reaction conditions were tested, but no appreciable increase in reactivity was realized. Addition of 18-crown-6 to capture K^+, $Al(OTf)_3$, different desiccants, bases and catalysts did not result in substantial improvements, and a maximum imine yield of ~30% was realized. Interestingly, very low reactivity was observed for the Cr(III)-salan catalysts, which may be either due to their poor solubility in mesitylene, or due to the absence of imino moieties. Unable to reach adequate reactivity with the Cr(III)-salen protocol, the reason for the poor reactivity was targeted for further investigation. The reaction conditions chosen for further investigations was 10 mol% **Cr3.1** and 100% Ca_3N_2 as shown in Figure 3.22.

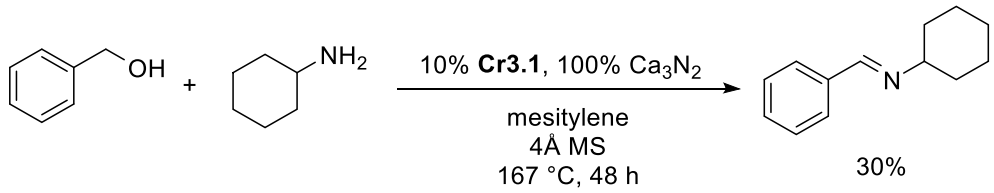

Figure 3.22: The best performing reaction conditions for the imination with Cr(III)-salen derivatives.

3.5.3. Kinetic isotope effect and deuterium labelling

To gain further mechanistic understanding, the kinetic isotope effect of the Cr(III)-salen reaction was measured in duplicate by me and SLHP. The protocol was performed with both regular benzyl alcohol and benzyl alcohol-α,α-*d*2. The rates of reaction were determined by monitoring the formation of the product imine by GC-MS. The results of the KIE experiment performed by me is shown in Figure 3.23 and the results of the KIE experiment performed by SLHP is shown in Figure 3.24. Further details of the KIE experiments can be found in Section 3.8.10.

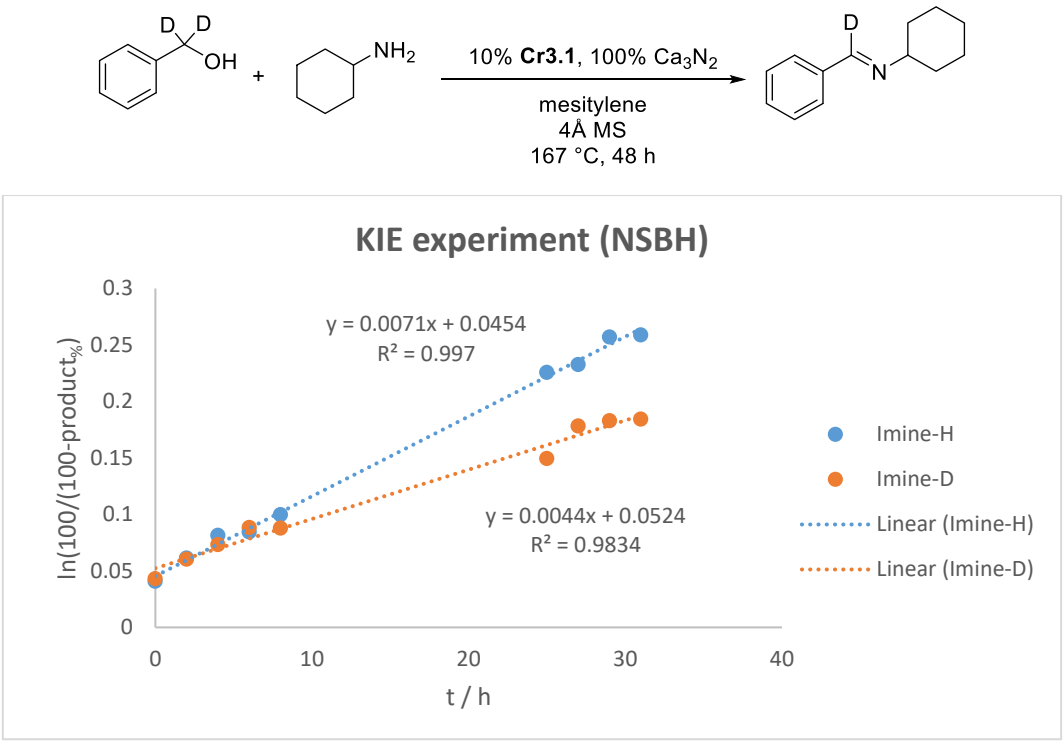

Figure 3.23: First determination of the kinetic isotope effect for the Cr(III)-salen protocol (performed by me).

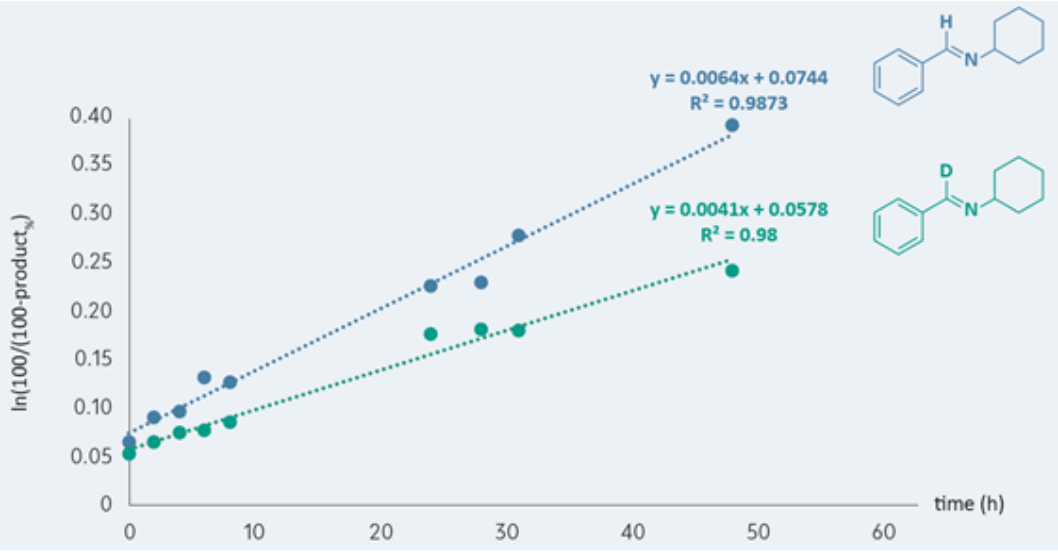

Figure 3.24: Second determination of the kinetic isotope effect for the Cr(III)-salen protocol (performed by SLHP, adapted from reference).[205]

The first KIE experiment resulted in a k_H/k_D = 1.61 and the second KIE experiment resulted in a k_H/k_D = 1.56. Comparatively, Christian Petersen and Emilie Lassen determined a k_H/k_D = 1.38 for their Cr(III)-salen protocol. Overall, the determined KIEs for the Cr(III)-salen protocols are similar and fall in the range 1.4 – 1.6. This value is low compared to the KIE of 2.0 observed in the Mn(III)-salen protocol and low compared to oxidations where breakage of C-H bond in the alcohol is thought to be the rate-determining step.[32,82,112–115]

As was done in the Mn(III)-salen and Fe(III)-salen protocols, the possible scrambling of H/D in the product imine was investigated. In the experiment with benzyl alcohol-α,α-d_2, GC-MS showed exclusive formation of the deuterated imine PhCD=NCy and no traces of hydrogen incorporation was observed (Figure 3.25).

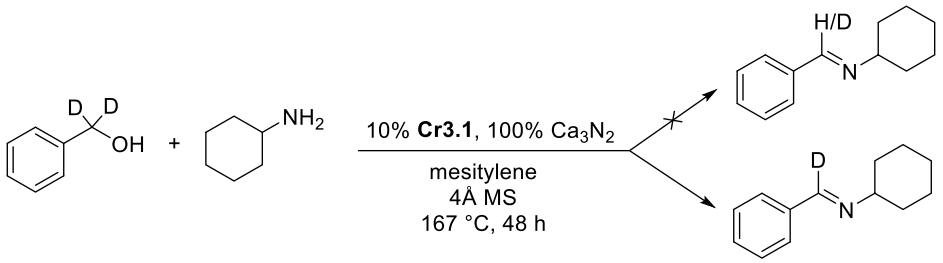

Figure 3.25: No H/D scrambling was observed by GC-MS when the reaction was performed with benzyl alcohol-α,α-d_2.

The absence of H/D scrambling is consistent with a monohydride mechanism involving only hydride transfer of the C_α-H to the metal.[21,23]

3.5.4. Hammett study

To characterize the Cr(III)-salen reaction mechanism further, a Hammett study was performed by SLHP under my supervision. A series of competition experiments between benzyl alcohol and *para*-substituted benzyl alcohols were performed with the newly optimized Cr(III)-salen protocol. Further details of the Hammett competition experiments, and the obtained rate plots are provided in Section 3.8.10 and Section 3.8.11. From the obtained rate data, a Hammett plot based on the Hammett *para*-substituent constant σ_p was constructed. The plot is shown in Figure 3.26.

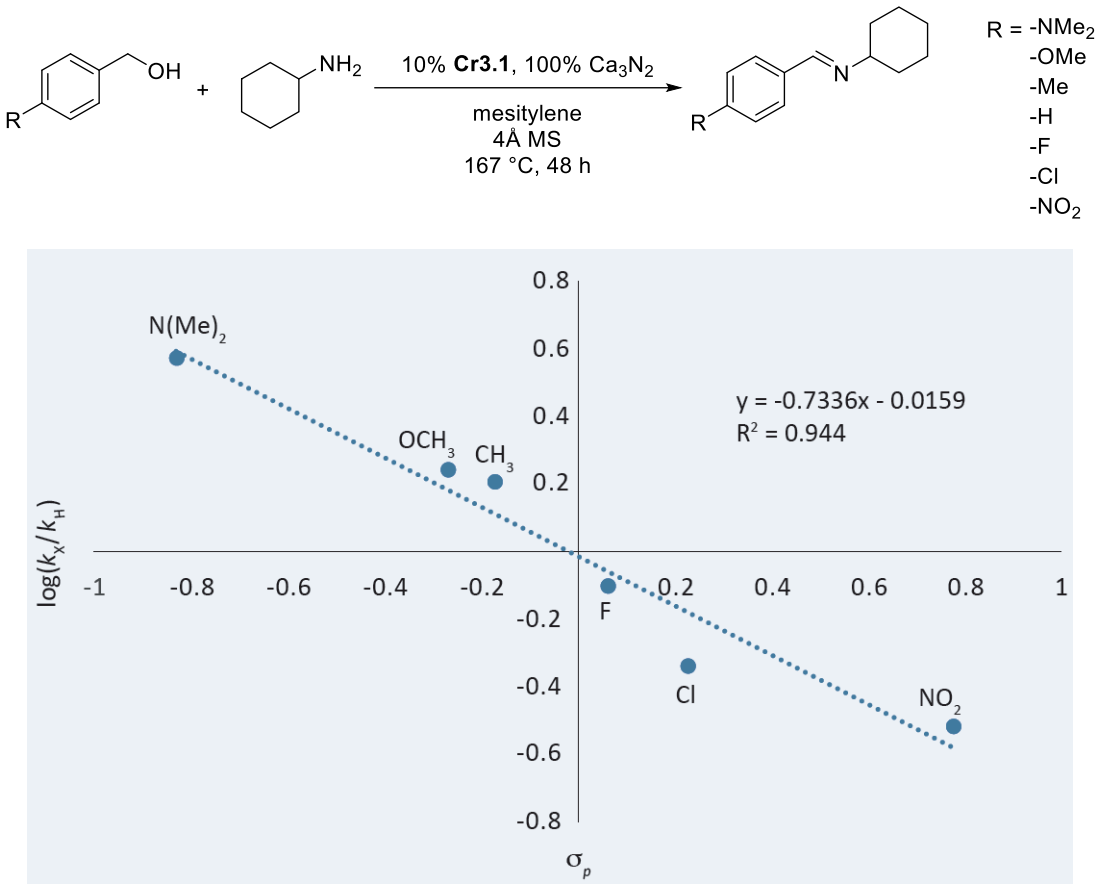

Figure 3.26: Experimental Hammett plot performed by SLHP (adapted from reference).[205]

A straight line with a slope ρ = -0.73 is obtained, which is similar to the value of ρ = -0.90 determined for Christian Petersen and Emilie Lassen's Cr(III)-salen protocol. Even though the slope is not as steep as expected for a H^- transfer from benzyl alcohol, the negative slope is consistent with build-up of positive charge on the benzylic carbon. The hypothesis that H^- transfer from the alcohol is one of the slow steps in the reaction mechanism is therefore maintained.

3.5.5. Gas evolution study

Throughout the vast optimization study, imine yields between 20 – 30% were frequently observed, with the optimal conditions yielding ~30% of the imine. To ascertain whether the observed oxidation was accompanied by a release of hydrogen gas, a reaction (Figure 3.27) was set up in a closed vessel with outlet to a water-filled burette residing in a water-filled crystallization bowl. If gas is developed during the reaction, the gradual displacement of the water in the burette would allow direct determination of the released gas volume.

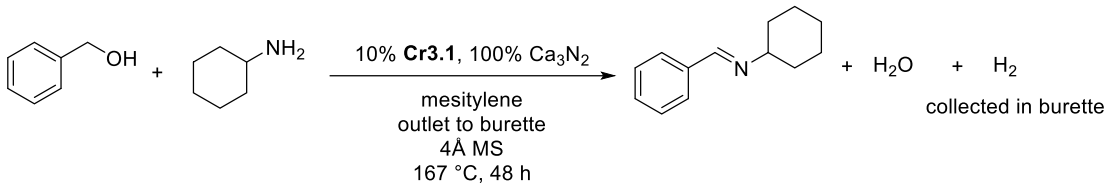

Entry	$V_{0\,h}$ / mL	$V_{24\,h}$ / mL	$V_{48\,h}$ / mL	GC Yield (48 h, %)
1	13.8	13.7	13.7	27
2	11.8	11.8	11.8	19
3^{SLHP}	14.1	14.1	14.1	30

Figure 3.27: Gas evolution experiments revealed no release of gas and thus, no dehydrogenative pathway is operational.

During the initial heating of the reaction vessel to 167 °C, displacement of water was observed, and this was attributed to thermal expansion of the dead volume of the Schlenk flask. Once thermal equilibrium was established at 167 °C, the gas evolution subsided completely, and the volume was noted. Checking the burette after 24 hours and 48 hours revealed no further gas evolution. The experiment was repeated twice by me and once by SLHP, and consistently, no release of gas was observed. Thus, a dehydrogenative pathway is not operational, and the reason for the observed imine yields between 20 – 30% will become apparent later in the chapter.

3.5.6. Control experiments

Due to the wildly varying yields between the different iterations of the Cr(III)-salen projects and the previous observation of particle catalysis in the Fe(III)-salen protocol, a series of control experiments were conducted by me and SLHP. The performed experiments are shown in Figure 3.28.

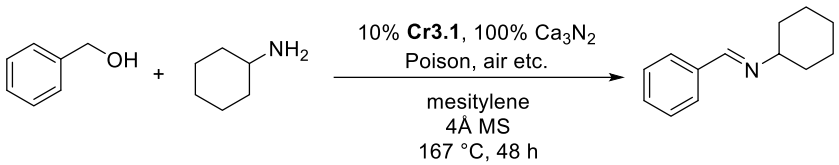

Entry	Alteration	GC Yield (48 h, %)
1	Under air atmosphere	80
2[SLHP]	No base	11
3[SLHP]	No catalyst	10
4[SLHP]	Under air atmosphere	86
5[SLHP]	1 drop of Hg added at 0 h	30
6[SLHP]	1 drop of Hg added at 24 h	29

Figure 3.28: Control experiments revealed aerobic oxidation, around 10% imine yield from alternate reaction pathways and no influence of mercury.

Entry 2 and 3 shows that around 10% imine can be formed in the absence of base or catalyst, and this background reaction is currently attributed to traces of oxygen in the reaction vessel. Furthermore, the possibility of particle formation and thus heterogeneous catalysis was checked by addition of Hg (entry 5 and 6). No inhibition of the reaction was found in the poisoned reactions and a yield of ~30% was observed, which is identical to the yield observed in reactions without added poison. Lastly, entry 1 and entry 4 makes it clear that running the reaction under an air atmosphere leads to very high yields of the desired imine due to aerobic oxidation. Thus, it is currently suspected that the high imine yields (>90%) reported previously by Maryam Pirouz and the good imine yields (50 – 70%) reported by Christian Petersen and Emilie Lassen are due to aerobic oxidation. All the reactions in these iterations of the Cr(III)-salen project were performed in Radley carousels that were later determined to be leaky by several members of the Madsen group. For illustrative purposes, Figure 3.29 presents a comparison of the GC-MS chromatograms for a typical air-free reaction and a reaction performed under air.

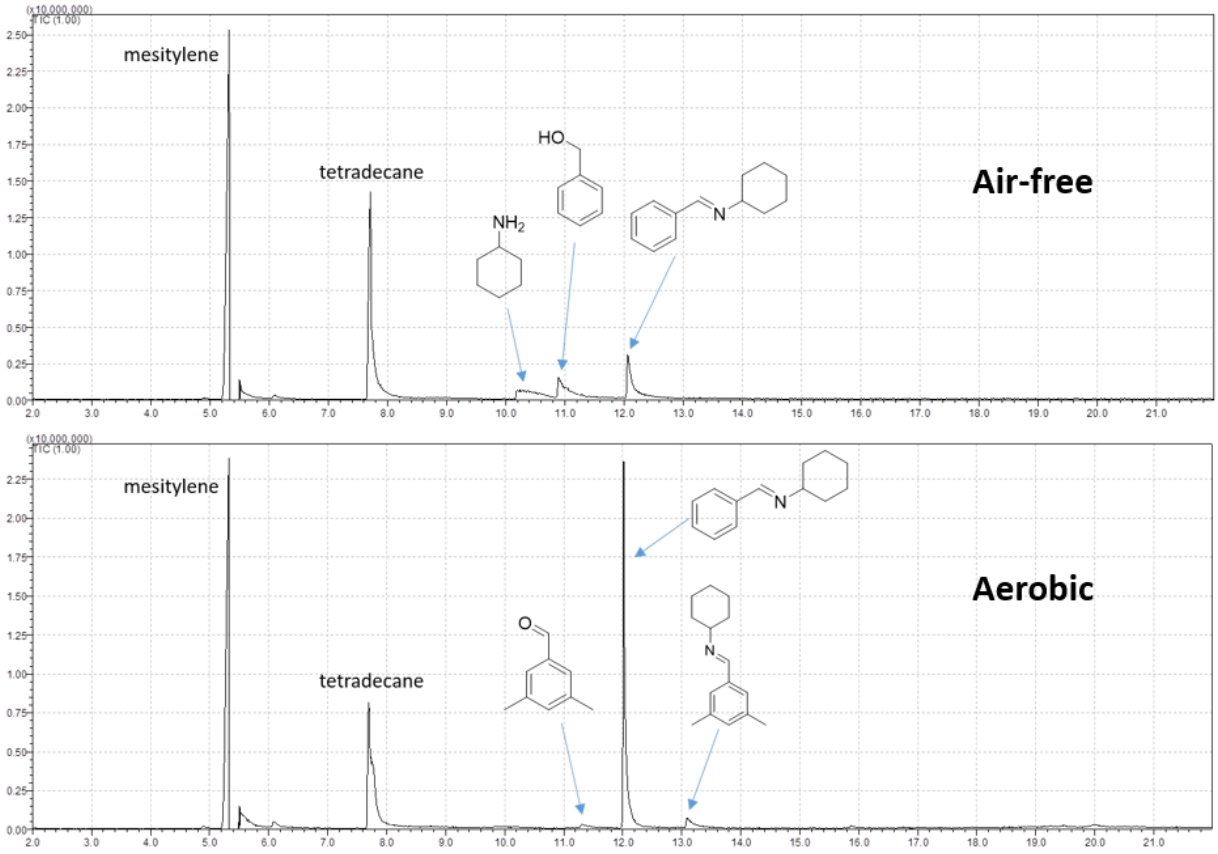

Figure 3.29: Comparison of GC-MS chromatograms of the Cr(III)-salen protocol run under air-free and aerobic conditions.

The difference between the chromatograms is stark; both $CyNH_2$, BnOH and a modest peak for the imine product is present in the chromatogram of the air-free reaction. Conversely, a large peak for the imine product is observed in the chromatogram of the aerobic reaction and no starting materials can be detected. Interestingly, an aldehyde and imine arising from the aerobic oxidation of mesitylene can be detected in the aerobic reaction, and the presence of these byproducts may function as a warning of aerobic conditions for future experiments conducted in boiling mesitylene.

3.5.7. LC-MS investigation of possible intermediates

As extensive catalyst degradation was observed by LC-MS in the Fe(III)-salen case, it was necessary to determine the fate of the Cr(III)-salen catalysts under the harsh reaction conditions. Furthermore, the LC-MS spectra can provide important information on possible catalyst intermediates, formation of dimers, reduction of the diimino-backbone etc. Therefore, an LC-MS study was performed to identify catalyst intermediates. An imination reaction was run with **Cr3.11** using the optimized protocol and analyzed by LC-MS after 24 hours. The total ion chromatogram (TIC) and two extracted ion chromatograms (EIC) of important ions are shown in Figure 3.30.

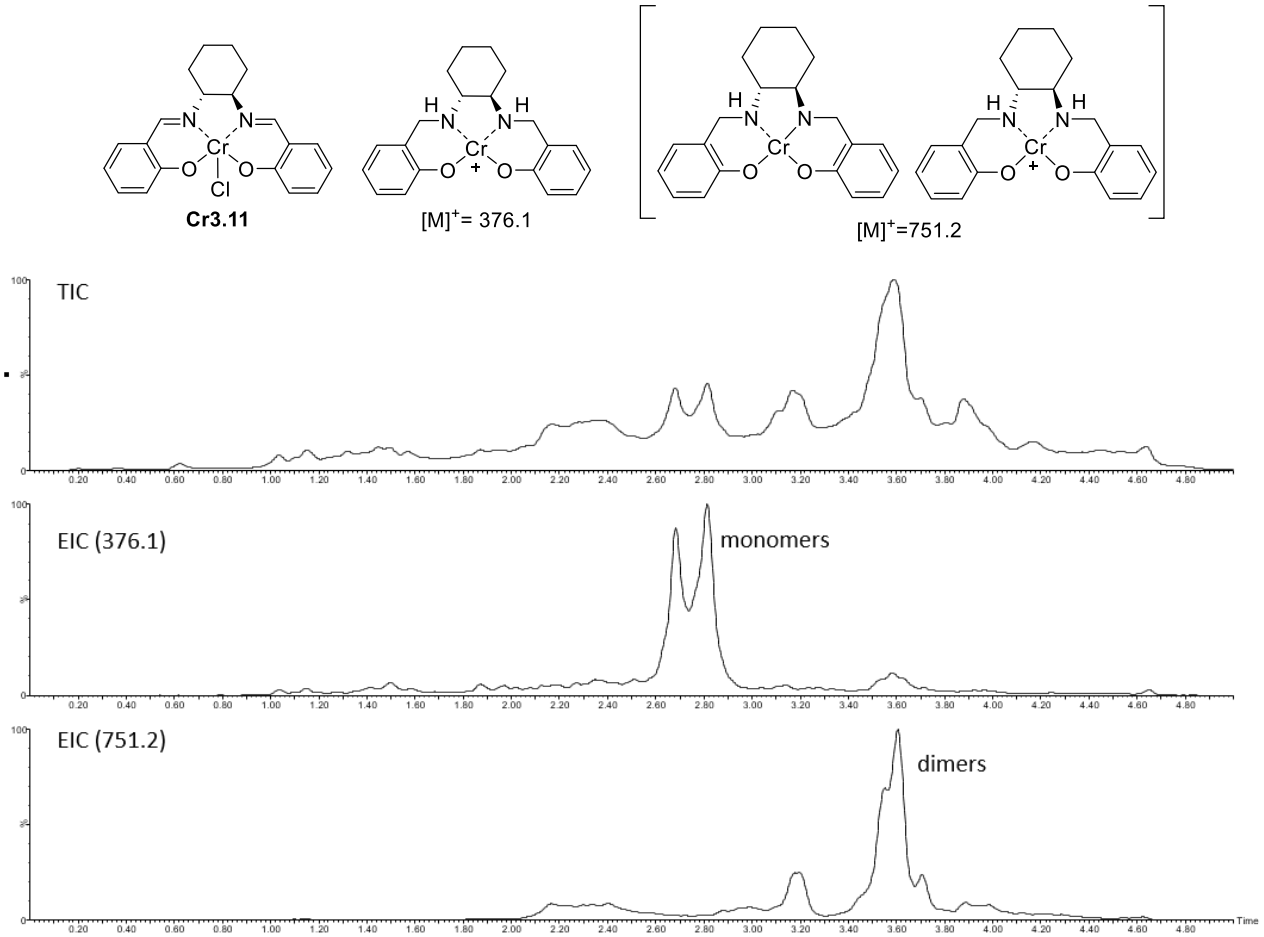

Figure 3.30: TIC, EIC(376.1) and EIC(751.2) of a reaction performed with **Cr3.11.** Monomers elute primarily from 2.60 – 3.00 minutes and dimers are observed between 3.40 – 3.80 minutes.

The TIC contains a plethora of peaks, indicating a complex mixture and the peak shapes are poor which makes interpretation difficult. EICs of the Cr(III)-salan monomer (376.1) and an observed dimer (751.2) are shown to ease interpretation. The EIC (376.1) shows two distinct peaks in the region from 2.60 – 3.00 minutes. The presence of two peaks could to stem from different isomers of the Cr(III)-salan complex, underlining the increased flexibility of the ligand scaffold. The EIC (751.2) shows that the dimeric species elute later (primarily between 3.40 – 3.80 minutes), and several peaks are observed which could indicate presence of different isomers.

In general, one should be careful assigning monomeric and dimeric species based on LC-MS spectra using electrospray ionization (ESI). The ESI technique can cause adduct formation of intrinsically monomeric species, which leads to observation of dimers, trimers etc.[206] However, the difference in retention time suggests that the observed dimeric species are intrinsic and likely not a result of the ESI method. To gain further information about catalytic intermediates, the combined mass spectrum of the region from 2.60 – 3.00 minutes was studied. The mass spectrum is shown in Figure 3.31.

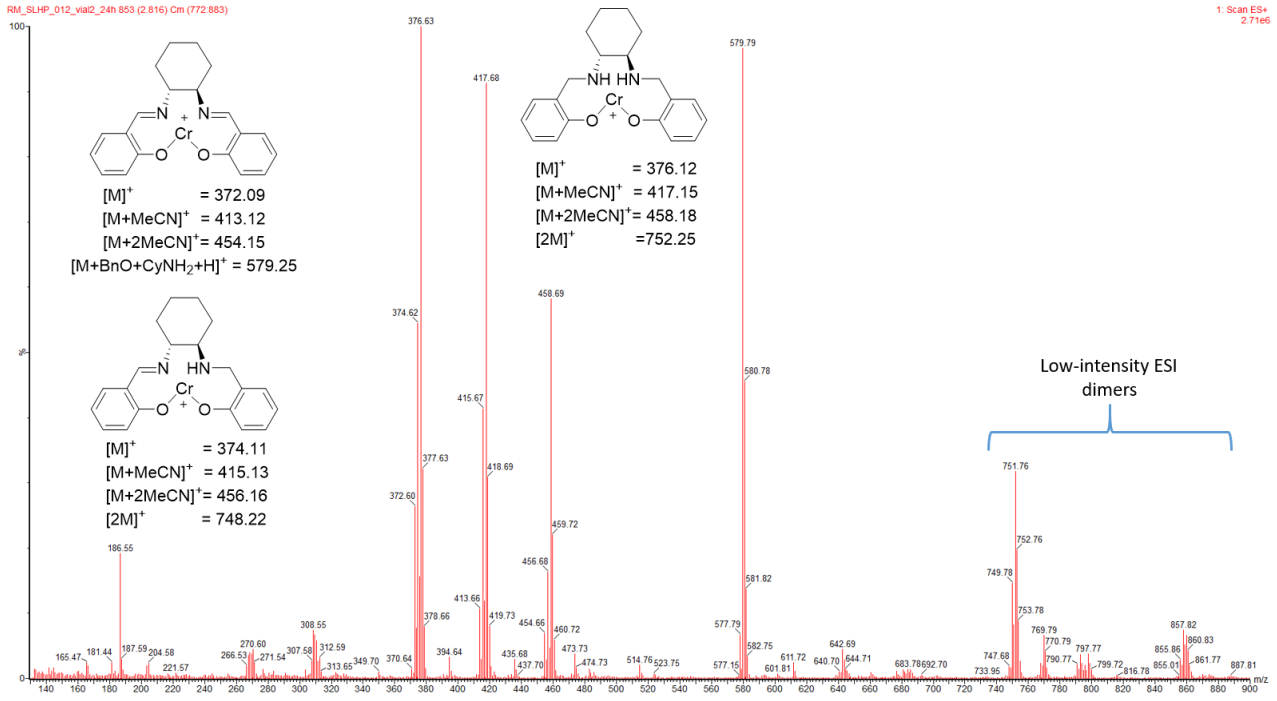

Figure 3.31: Combined mass spectrum of the monomer region ranging from 2.60 – 3.00 min. Presence of Cr(III)-salen, Cr(III)-salalen and Cr(III)-salan is evident and a mass corresponding to a Cr(III)-salen complex with $CyNH_2$ and BnO^- is also observed. The mass spectrometer was poorly calibrated, so the observed masses are consistently +0.5 units above the expected mass.

Reduction of the diimino-backbone is clearly observed as the peaks are bundled together with a mass difference of +2 Da per reduction. Furthermore, masses corresponding to coordination of both one and two MeCN are observed, which is expected from the eluent system. Interestingly, an intense peak with mass 579.8 Da is observed, and this mass is tentatively attributed to a Cr(III)-salen moiety coordinated by both $CyNH_2$ and BnO^-, which are both present under the reaction conditions. It is curious that this peak does not follow the pattern of +2 masses for the corresponding Cr(III)-salalen and Cr(III)-salan derivatives. The current hypothesis is that reduction of the diimino-backbone leads to increased flexibility of the ligand and therefore, alternative coordination modes (i.e., dimer formation) may be preferred for the reduced complexes. Lastly, masses corresponding to dimers do appear in the mass spectrum shown in Figure 3.31, but the intensity of the signals are relatively low and may stem from coelution or ESI-induced adduct formation.

The dimer-region in the LC-MS chromatogram (3.40 – 3.80 minutes) was also examined and the combined mass spectrum is shown in Figure 3.32.

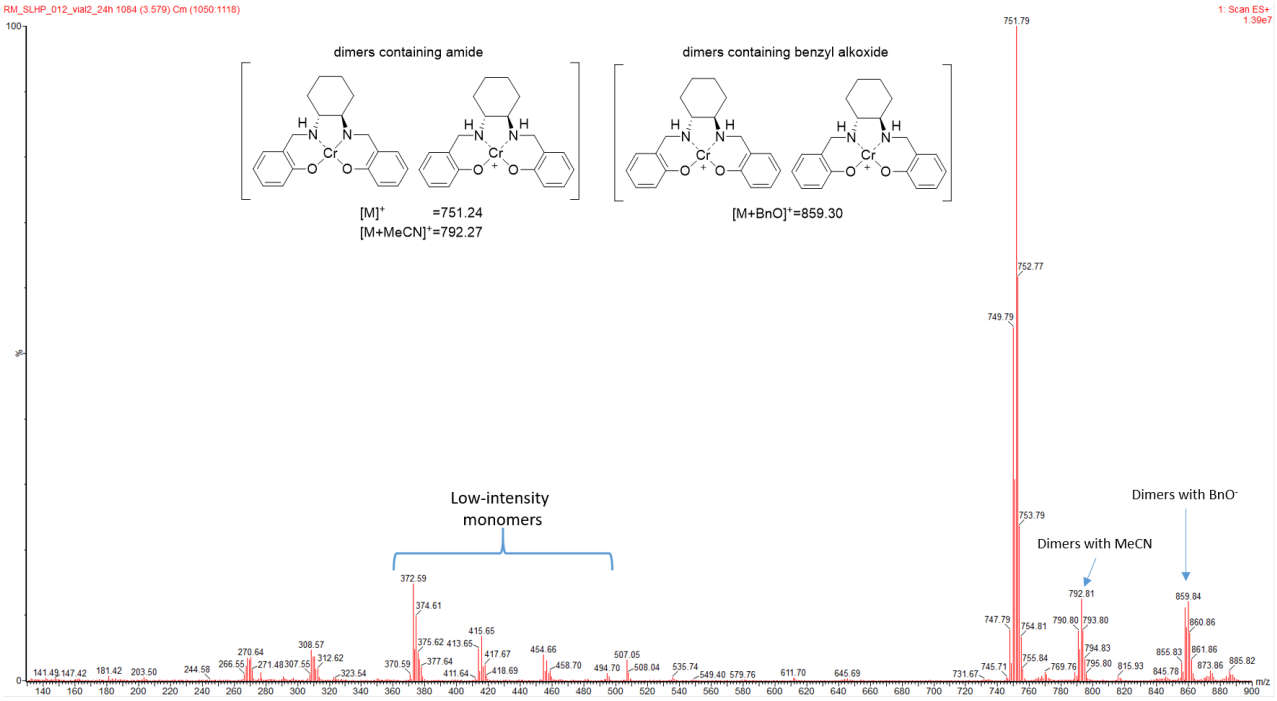

Figure 3.32: Combined mass spectrum of the dimer region ranging from 3.40 – 3.80 min. The mass spectrometer was poorly calibrated, so the observed masses are consistently +0.5 units above the expected mass.

The patterns in the mass spectrum reveal a complicated mixtures of dimers containing both Cr(III)-salalen and Cr(III)-salan and mixtures hereof. Furthermore, dimers with incorporation of MeCN and BnO^- are observed. It is worth noting that no masses corresponding to dimers of the initial Cr(III)-salen complex is observed, which is attributed to the low flexibility of the salen ligand. These observations corroborate the hypothesis that reduction of the diimino-backbone may lead to formation of dimers that are detrimental to the catalytic efficiency of the protocol.

For comparison, the reaction performed with the –OMe substituted Cr(III)-salan dimer **Cr3.14** was analyzed by LC-MS after 24 hours of reaction. The TIC and two extracted ion chromatograms of a monomeric and a dimeric ion are shown in Figure 3.33.

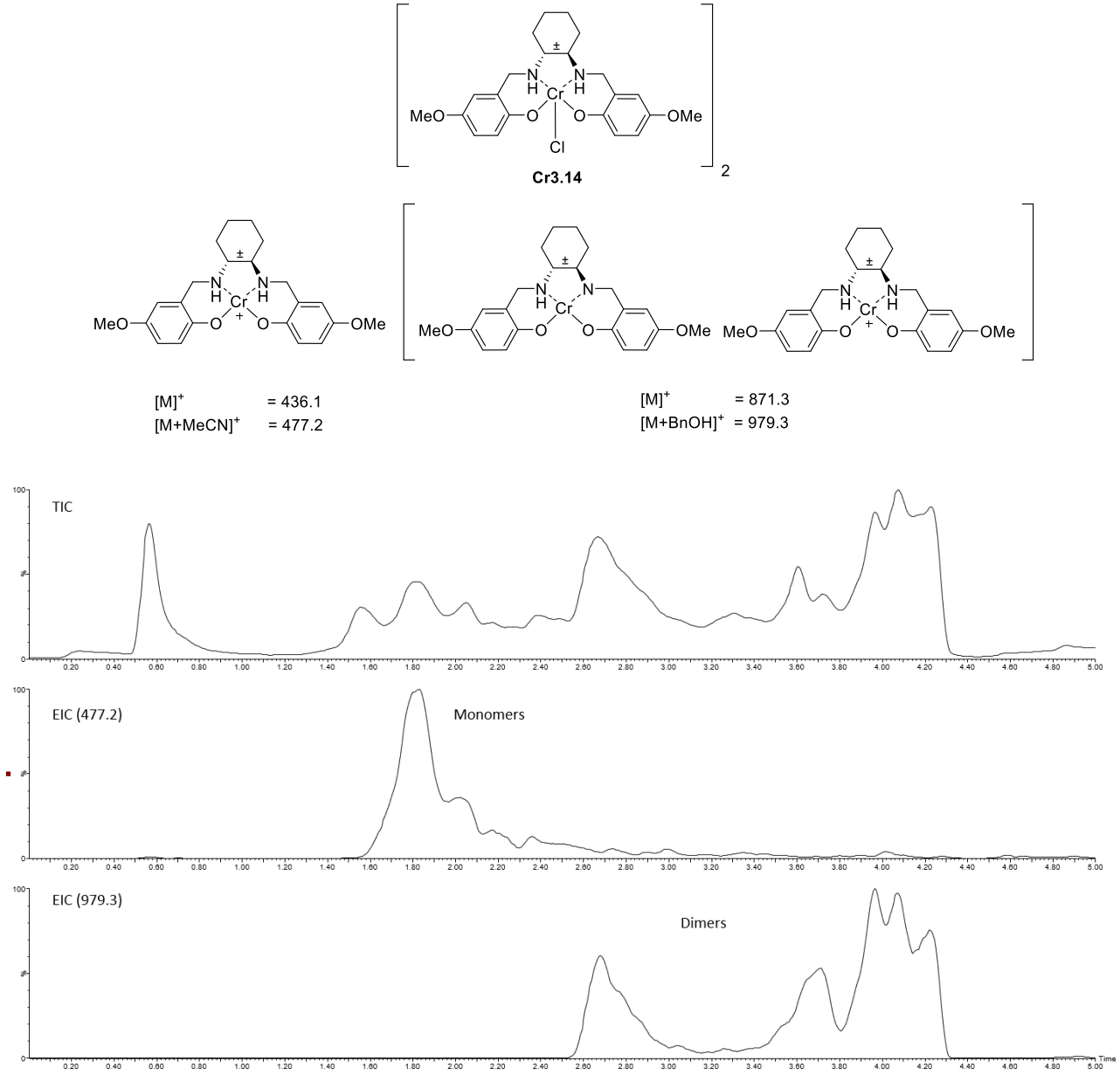

Figure 3.33: TIC, EIC(477.2) and EIC(979.3) of a reaction performed with **Cr3.14.** The sample was prepared after 24 hours of reaction. Monomers are present between 1.60 – 2.20 minutes and several dimer peaks are observed between 2.60 – 4.20 minutes.

Evidently, both monomeric and dimeric species are observed in the LC-MS chromatogram, and several peaks of a dimer with incorporation of BnOH are observed. The presence of several peaks may indicate the presence of different coordination isomers. To obtain further information, the combined mass spectrum of the monomeric region (1.60 – 2.20 minutes) is shown in Figure 3.34 and the combined mass spectrum of the dimeric region (2.60 – 4.20 minutes) is shown in Figure 3.35.

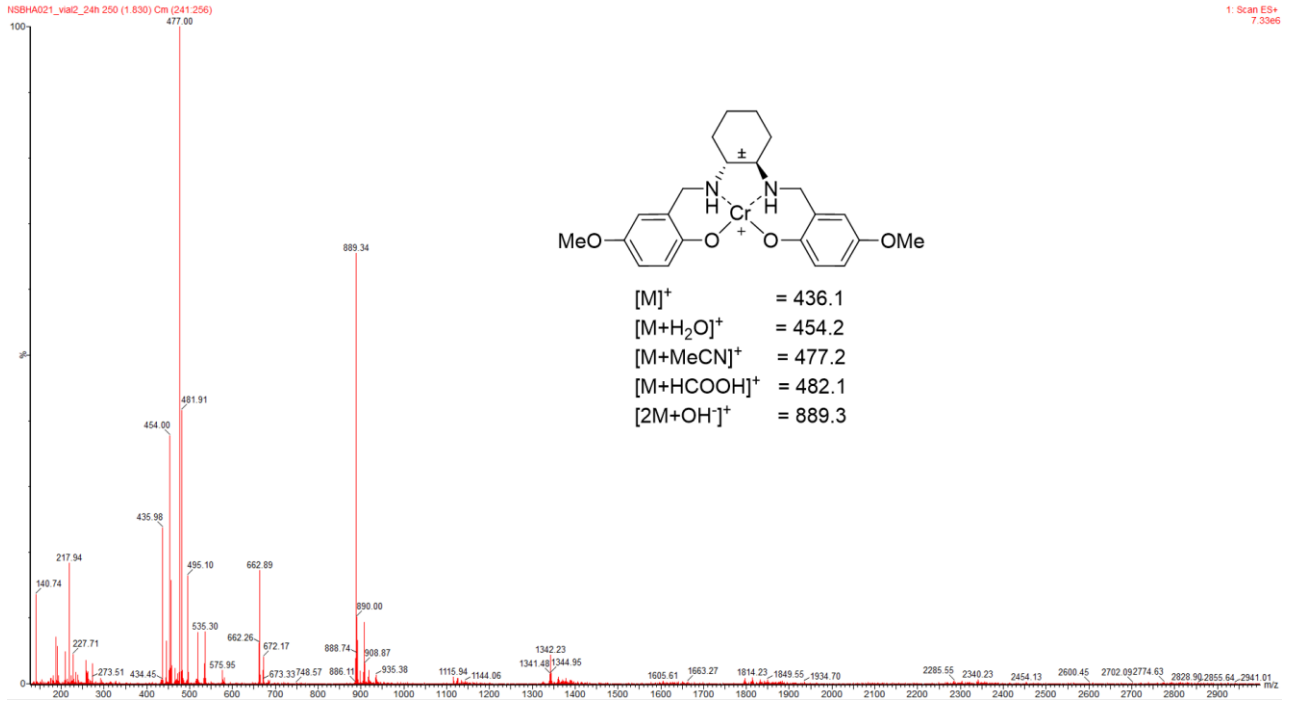

Figure 3.34: Combined mass spectrum of the monomeric region (1.60 – 2.20 minutes) for the reaction with **Cr3.14**. No masses corresponding to Cr(III)-salen or Cr(III)-salalen derivatives are present. The intense signal of 889.34 Da is tentatively assigned to a hydroxy-bridged dimer.

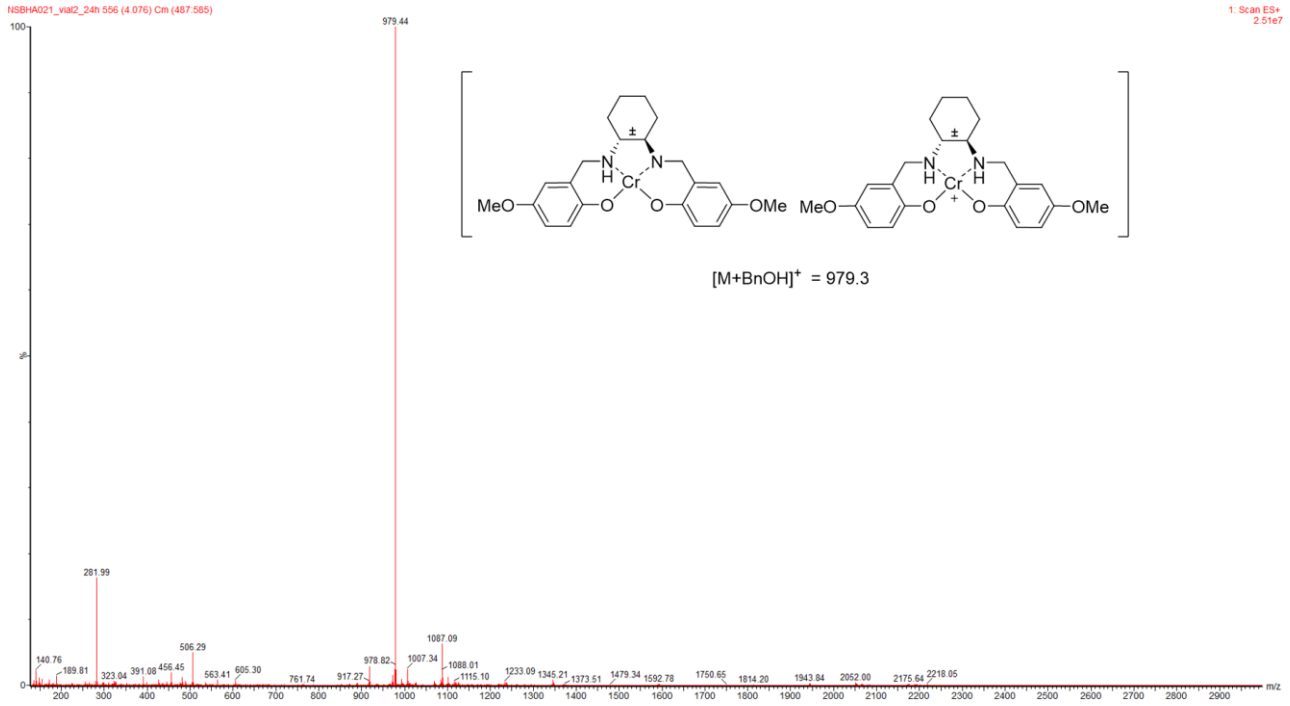

Figure 3.35: Combined mass spectrum of the dimeric region (2.60 – 4.20 minutes) for the reaction with **Cr3.14**. The intense signal of 979.44 Da is assigned to a benzyloxy-bridged Cr(III)-salan dimer. The simple pattern of the mass spectrum reveals no presence of Cr(III)-salen or Cr(III)-salalen derivatives.

The most important take-away from the LC-MS analysis of the reaction with **Cr3.14** is the absence of Cr(III)-salen and Cr(III)-salalen derivatives. This indicates that the diamino-backbone is not oxidized back to the diimino-backbone under the employed reaction conditions. Therefore, the observed reduction of the diimino-backbone when employing Cr(III)-salen catalysts seems to be irreversible. Furthermore, the observation of intense signals corresponding to both hydroxyl-bridged and benzyloxy-bridged dimers may indicate that these species are likely resting states for the catalyst.

Having established that dimer formation is likely for Cr(III)-salalen and Cr(III)-salan complexes without –tBu substituents, an LC-MS study was also carried out for the optimal catalyst, the commercially available **Cr3.1**. The role of the –tBu substituents is not only to increase solubility in organic solvents, the –tBu groups are also believed to hamper the formation of dimers due to steric repulsion.[207] Therefore, a typical reaction performed with **Cr3.1** was analyzed with LC-MS after 24 hours. The TIC and EIC of a Cr(III)-salan·MeCN complex (641.4 Da) is shown in Figure 3.36.

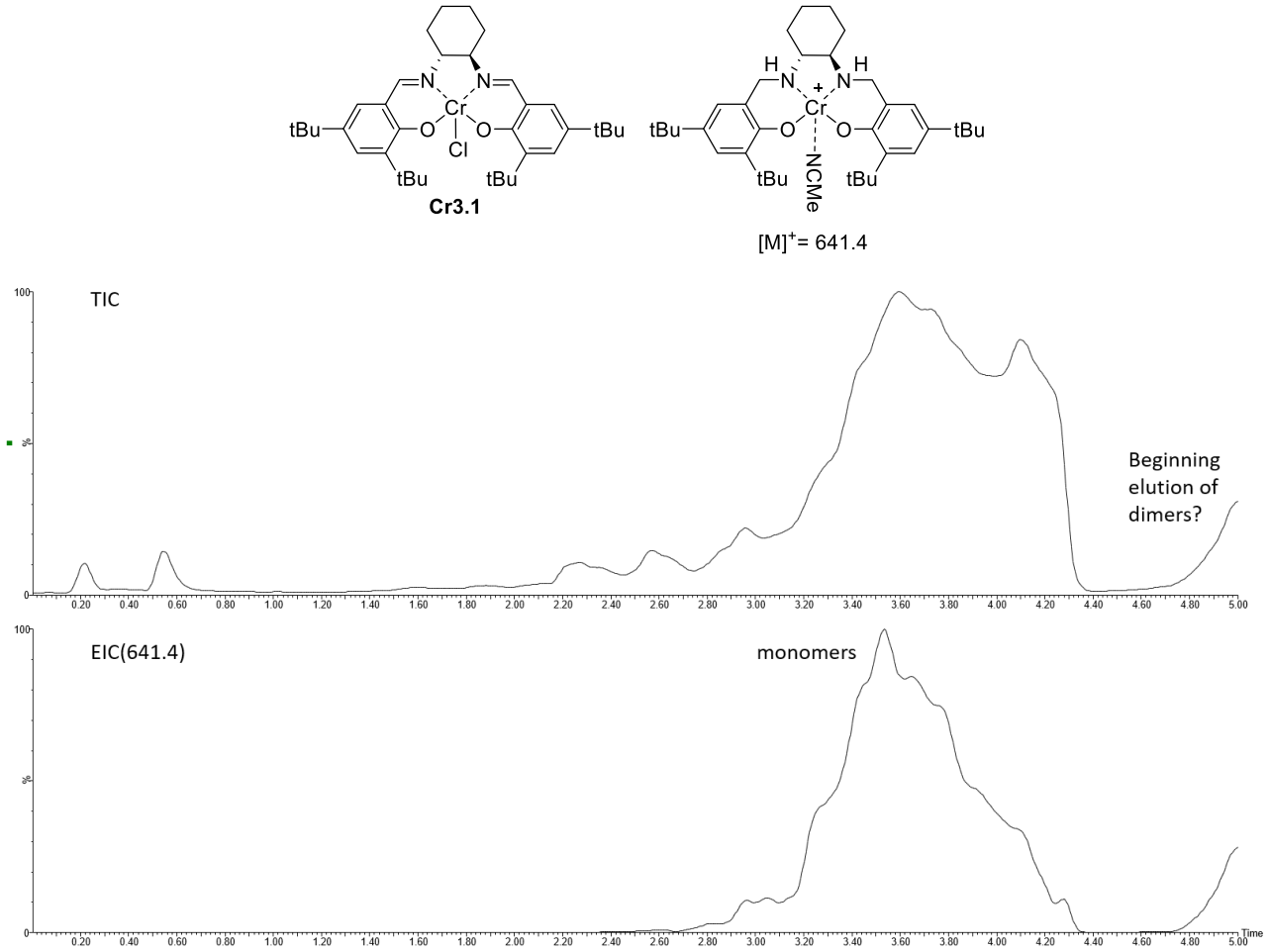

Figure 3.36: TIC and EIC(641.4) of a reaction performed with **Cr3.1.** The monomeric complexes elute in a broad band from 3.20 – 4.20 minutes.

Clearly, the employed chromatographic method is poorly suited to analysis of the –tBu substituted Cr(III) complexes. The high lipophilicity of the –tBu groups causes late elution of the monomeric species, and no significant mass peaks of dimers are observed. On one hand, the –tBu groups may

effectively hamper the formation of the previously observed dimers, but another likely explanation is that the high lipophilicity of the –tBu dimers causes the dimers to stick to the LC-MS column. A possible indication of this is seen in the end of the chromatograms, where the signal intensity starts to increase just before the end of the run.

The monomer region (3.20 – 4.20 minutes) of the chromatogram was studied and the combined mass spectrum is shown in Figure 3.37. Furthermore, the mass spectrum of an identically processed reaction performed with benzyl alcohol-α,α-d_2 is shown in Figure 3.38.

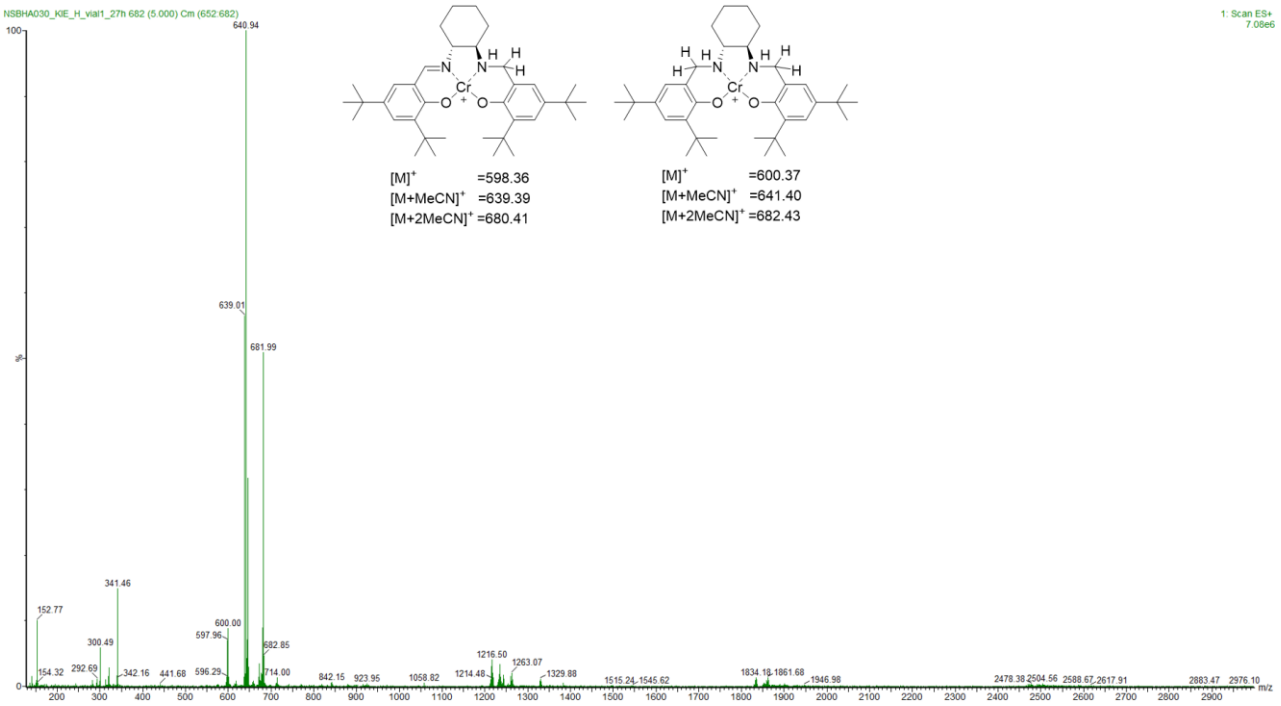

Figure 3.37: Combined mass spectrum of the monomer region ranging from 3.20 – 4.20 min. Both Cr(III)-salalen and Cr(III)-salan is observed, but no Cr(III)-salen is observed. The mass spectrometer was poorly calibrated, so the observed masses are consistently -0.4 units below the expected mass.

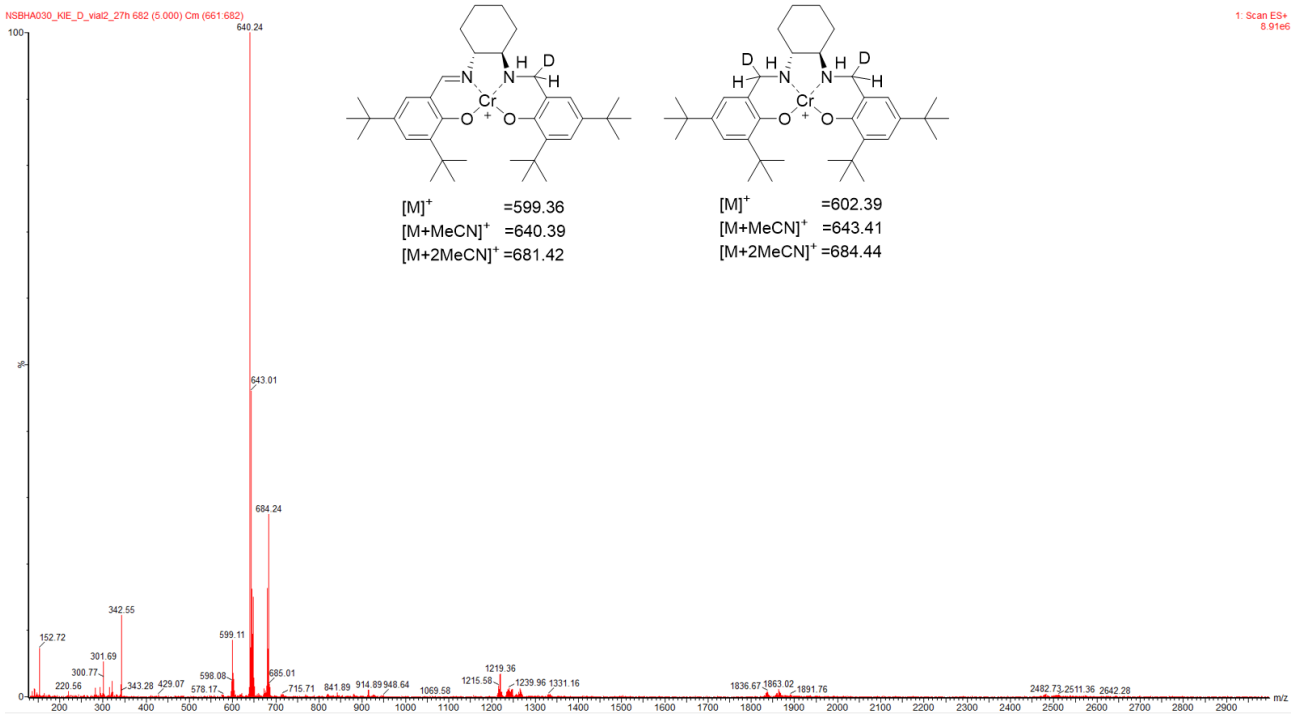

Figure 3.38: Combined mass spectrum (3.20 – 4.20 min) of the reaction with benzyl alcohol-α,α-d_2. The observed masses fit well with the transfer of one and two D^-, respectively. The mass spectrometer was poorly calibrated, so the observed masses are consistently -0.4 units below the expected mass.

In both cases, primarily monomers of Cr(III)-salalen and Cr(III)-salan and their MeCN adducts are observed, and the experiment with benzyl alcohol-α,α-d_2 shows increased masses consistent with transfer of one and two D^- as expected.

Overall, the LC-MS study of the Cr(III)-salen protocol shows reduction of the diimino-backbone resulting in formation of Cr(III)-salans and this was further confirmed by incorporation of deuterium in the complexes. Furthermore, evidence of dimer formation was found for **Cr3.11** (without –tBu groups), but no dimer formation of **Cr3.1** (with –tBu groups) could be unambiguously detected. Either the –tBu groups effectively hinder dimer formation or the highly lipophilic –tBu-substituted dimers stick to the LC-MS column, effectively hindering their detection. Lastly, the LC-MS study of the reaction performed with Cr(III)-salan dimer **Cr3.14** revealed no oxidation of the diamino-backbone to the diimino-backbone and masses corresponding to hydroxy-bridged and benzyloxy-bridged Cr(III)-salan dimers were observed. These dimers may be likely candidates for the resting state of the catalyst.

3.6. Computational investigation of the catalytic cycle

In tandem with the experimental development of the Cr(III)-salen based AAD reaction, DFT modelling of possible intermediates and transition states were used to obtain information on the energy landscape of the catalytic cycle. Similar to the cases of Mn(III) and Fe(III)-salen based catalysis, the goal was to construct a catalytic cycle with a plausible energy landscape that would also reproduce the experimental mechanistic data (Hammett slope and KIE values) reasonably well. Once a satisfactory DFT model was made, further *in silico* screening and optimization of catalyst structure was thought possible, as the salen ligand scaffold is highly customizable, both in the form of the substituents of the phenolates and structural variations in the backbone.

As the starting point for the DFT modelling of the Cr(III) catalysis, a crystal structure of an octahedral Cr(III)-salen derivative containing axially coordinated chloride and water was found.[177] Previous computational studies of polymerization mechanisms involving Cr(III)-salen derivatives involves equilibria between five-coordinate square pyramidal species and six-coordinate octahedral species.[208,209] Therefore, the question of coordination geometry under the catalytic reaction conditions was first to be tackled. In the following section, the possible coordination of additional ligands to form octahedral Cr(III)-salen complexes was studied *in silico* to obtain information on the preferred catalyst geometries under the employed reaction conditions.

3.6.1. Formation of octahedral complexes

Based on the aforementioned crystal structure of the octahedral Cr(III)-salen complex, a series of equilibria shown in Figure 3.39 was investigated *in silico*. The simple ethylene backbone was employed to minimize the computational requirements. As both cyclohexylamine and benzyl alcohol are present in excess during the reaction, these were deemed the most likely ligands (if only neutral ligands are considered). Furthermore, reduction of the imino-backbone during the reaction was an established experimental fact, so modelling of ligand coordination to both salen- and salan-type Cr(III) complexes was deemed appropriate. Lastly, the substitution of chloride by benzyl oxide was assumed rapid due to high oxophilicity of Cr(III), the highly basic reaction conditions and the observation of benzyl oxide-ligated Cr(III)-salen derivatives by LC-MS.

The free energies of the structures were calculated in ORCA at the B3LYP-D3BJ\\def2-TZVP level using the SMD solvation model with the parameters for toluene. The results are presented in Figure 3.39:

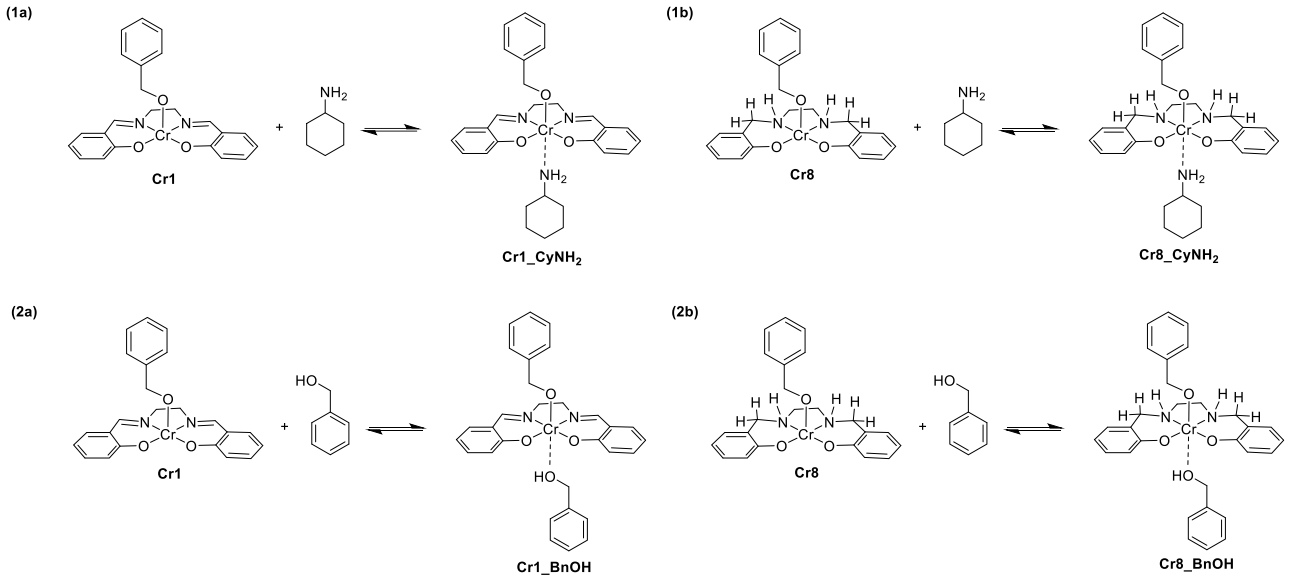

Method	ΔG(**Cr1**) + ΔG($CyNH_2$) / kcal mol^{-1}	ΔG(**Cr1_CyNH$_2$**) / kcal mol^{-1}	ΔG_{bind} / kcal mol^{-1}
B3LYP-D3BJ \\ def2-TZVP, SMD solvation	-1606040.916	-1606038.196	+2.72
B3LYP-D3 \\ LACVP**, PBF solvation	-1005256.408	-1005256.782	-0.374

Method	ΔG(**Cr8**) + ΔG($CyNH_2$) / kcal mol^{-1}	ΔG(**Cr8_CyNH$_2$**) / kcal mol^{-1}	ΔG_{bind} / (kcal mol^{-1})
B3LYP-D3BJ \\ def2-TZVP, SMD solvation	-1607516.275	-1607516.442	-0.166
B3LYP-D3 \\ LACVP**, PBF solvation	-1006743.223	-1006745.434	-2.21

Method	ΔG(**Cr1**) + ΔG(BnOH) / kcal mol^{-1}	ΔG(**Cr1_BnOH**) / kcal mol^{-1}	ΔG_{bind} / kcal mol^{-1}
B3LYP-D3BJ \\ def2-TZVP, SMD solvation	-1640939.598	-1640930.659	+8.94

Method	ΔG(**Cr8**) + ΔG(BnOH) / kcal mol^{-1}	ΔG(**Cr8_BnOH**) / kcal mol^{-1}	ΔG_{bind} / kcal mol^{-1}
B3LYP-D3BJ \\ def2-TZVP, SMD solvation	-1642414.957	-1642411.145	+3.81

Figure 3.39: Calculation of ΔG_{bind} for the equilibria shown above. All calculations were performed at the boiling point of mesitylene (438 K). For the coordination of cyclohexylamine, two different methods were used. In Orca, the B3LYP-D3BJ \\ def2-TZVP method with SMD solvation in toluene was used. In Jaguar, the B3LYP-D3 \\ LACVP** with PBF solvation in toluene was used.

Starting with the coordination of benzyl alcohol, a positive ΔG_{bind} is calculated for both the salen **Cr1** and salan **Cr8**, which indicates that coordination of benzyl alcohol is unfavorable. Therefore, axial coordination of additional benzyl alcohol was not pursued further.

For the coordination of cyclohexylamine, the initial calculations performed with Orca gave a positive ΔG_{bind} (+2.7 kcal mol^{-1}) for the **Cr1** case, whereas the ΔG_{bind} for the **Cr8** was slightly negative (-0.17 kcal mol^{-1}). To obtain a second opinion, the calculations were redone in Jaguar using a slightly different DFT method and solvation model. This resulted in slightly negative ΔG_{bind} for both **Cr1** and **Cr8** with values of -0.37 kcal mol^{-1} and -2.2 kcal mol^{-1}, respectively. Ultimately, the DFT calculations predict that coordination of cyclohexylamine is energetically feasible, especially in the case of the Cr(III)-salan type complexes, which are formed during the reaction. The hypothesis of octahedral Cr(III) intermediates are also supported by the observation of octahedral adducts of both MeCN, H_2O and $CyNH_2$ in the ESI+ mass spectra of the reaction mixtures. Thus, all further modelling was based on octahedral geometries around the Cr(III) center.

3.6.2. Catalyst activation

For the sake of simplicity and computational resources, the spectating cyclohexylamine ligand was replaced by NH_3 in the models presented in the coming sections. Due to the observation of Cr(III)-salan species during the reaction, an activation mechanism similar to the Mn(III)-salen activation mechanism was constructed. The individual steps and their relative energies are shown in Figure 3.40 and the computational details can be found in Section 3.8.12.

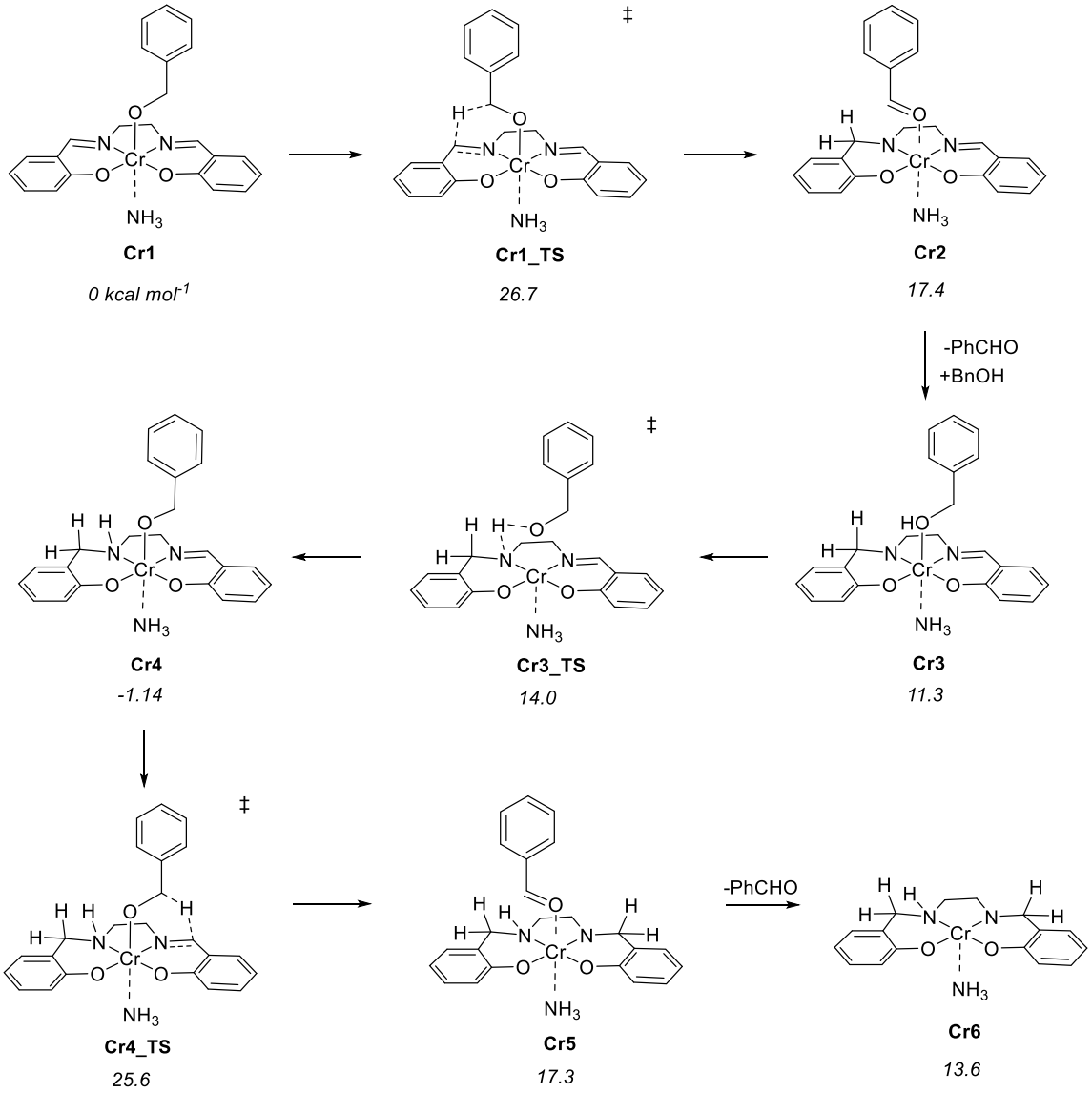

Figure 3.40: Proposed DFT model of activation of Cr(III)-salen. The denoted energies are relative Gibbs free energies calculated at 438 K using the B3LYP-D3 functional and PBF solvation in toluene.

The activation of the catalyst is thought to proceed by transfer of H^- from a coordinated benzyl oxide ligand to the imino-group of the salen ligand (**Cr1_TS**). The resulting benzaldehyde is displaced by benzyl alcohol, which can protonate the transient amide, resulting in a new benzyl oxide ligated complex (**Cr4**). Repetition of the steps ultimately leads to intermediate **Cr6**, which acts as the starting point for the modelling of a possible catalytic cycle. Throughout the activation mechanism, the highest energy barriers are the 1st and 2nd H^- transfer to the backbone, both with activation energies of around 26.7 kcal mol^{-1}. This is a considerable energy barrier, but it is deemed acceptable when the high temperature and long reaction time is considered. For reference, the rate-determining step of the Mn(III)-salen catalytic cycle had a calculated barrier of 27.2 kcal mol^{-1}, and this reaction takes place in boiling toluene instead of mesitylene.[1]

3.6.3. DFT calculated Hammett plot and kinetic isotope effect

To characterize the catalyst activation further, a Hammett plot and the kinetic isotope effect for the 2nd H^- transfer to the salen ligand was calculated. The resulting Hammett plot is shown in Figure 3.41.

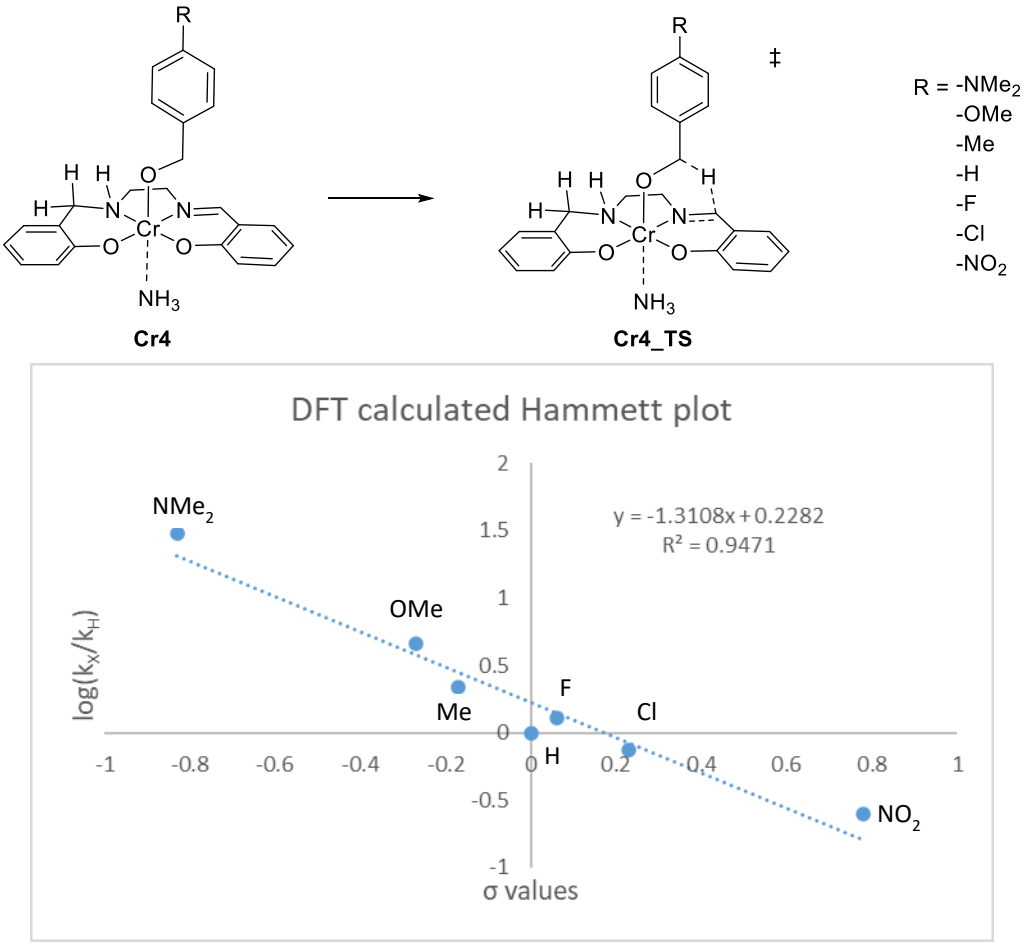

Figure 3.41: DFT calculated Hammett plot of the **Cr4 → Cr4_TS** transition.

An acceptable linear correlation with a slope of -1.31 is obtained, which is consistent with build-up of positive charge on the benzylic position as expected. Furthermore, the kinetic isotope effect of the transition **Cr4 → Cr4_TS** was calculated to 2.5, which is in poor agreement with the experimentally determined values of 1.56 and 1.61. However, it should be noted that in the Mn(III)-salen case, the measured KIE was 2.0, whereas the calculated KIE was 2.9. Thus, the mismatch between the calculated and measured KIEs are comparable to the Mn(III)-salen case, but the cause of the mismatch remains unknown.

3.6.4. Catalytic cycle with formation of a Cr-H intermediate

Having established a reasonable activation mechanism for the Cr(III)-salen system, the modelling of a plausible catalytic cycle was pursued. With the previously reported Mn(III)-salen mechanism in hand, the equivalent elementary steps for the octahedral Cr(III)-salen model was calculated. The resulting catalytic cycle with relative Gibbs free

energies is shown in Figure 3.42. Section 3.8.12 can be consulted for further details on the energy calculations.

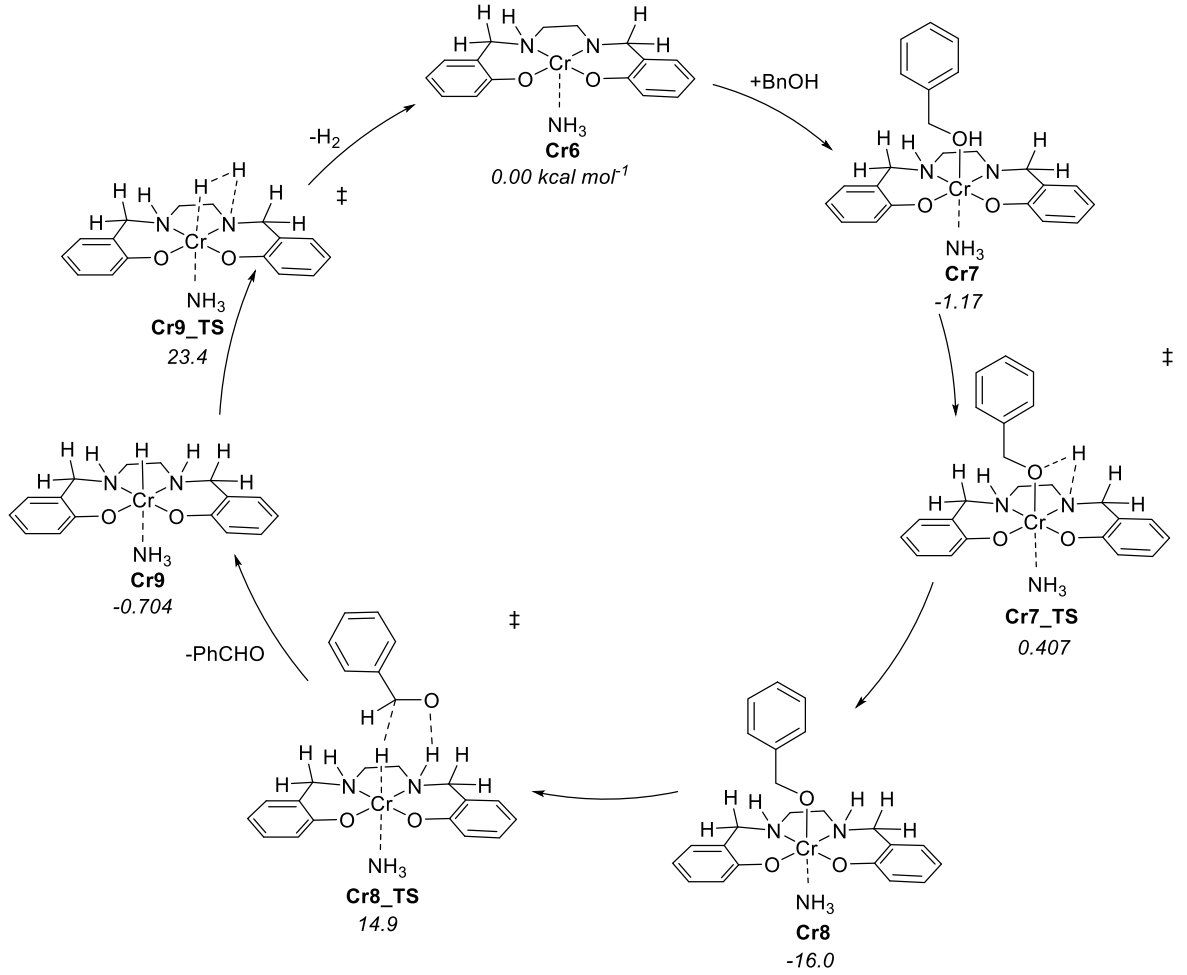

Figure 3.42: Octahedral Cr(III)-salen catalytic cycle based on the previously reported Mn(III)-salen mechanism. The denoted energies are relative Gibbs free energies calculated with the B3LYP-D3 method using PBF solvation in toluene.

Starting from the amido complex **Cr6**, the coordination of benzyl alcohol to form an octahedral intermediate **Cr7** is energetically favorable (-1.2 kcal mol^{-1}) and the following protonation of the amide nitrogen is virtually barrierless, leading to the highly stable benzyl oxide complex **Cr8**. This is likely the resting state of the catalytic cycle and masses corresponding to Cr(III)-salan ligated by benzyl oxide have been observed by LC-MS as shown in Section 3.5.7. Due to the high stability of **Cr8**, the outer-sphere, ligand-assisted H^- transfer to the Cr(III) center presents an energy barrier of 30.9 kcal mol^{-1}, which is deemed too high to occur with appreciable rate. It gets even worse when the expulsion of hydrogen gas from the hypothesized Cr(III)-hydride is calculated; the transition state **Cr9_TS** presents an energy 39.4 kcal mol^{-1} above the resting state **Cr8**, so this pathway is unlikely.

The highly stable nature of the **Cr8** (-16 kcal mol^{-1}) is remarkable, and a similar tendency was also observed in the calculations of the Fe(III)-salen system, where the relative energy of the Fe(III)-

salan alkoxide complex **Fe8** was calculated to -20.9 kcal mol^{-1}. As a reminder, the Mn(III) variant of structure **Fe8** only had a relative energy of -0.5 kcal mol^{-1} in the analogous Mn(III)-salen mechanism, and the absence of a low-energy resting state in the Mn(III)-salen catalytic cycle is likely contributing to the more efficient Mn(III) catalysis.[1]

Even though the exclusion of hydrogen is predicted to be the rate determining step of the catalytic cycle, a Hammett plot with a slope of –0.73 was determined experimentally, which indicates participation of benzyl alcohol. If the catalytic cycle in Figure 3.42 is operative, the transfer of H$^-$ to the Cr(III) center (**Cr8_TS**) is the most likely candidate for this type of Hammett correlation, so a DFT-calculated Hammett plot was constructed based on the **Cr8** → **Cr8_TS** transition. The Hammett plot is shown in Figure 3.43.

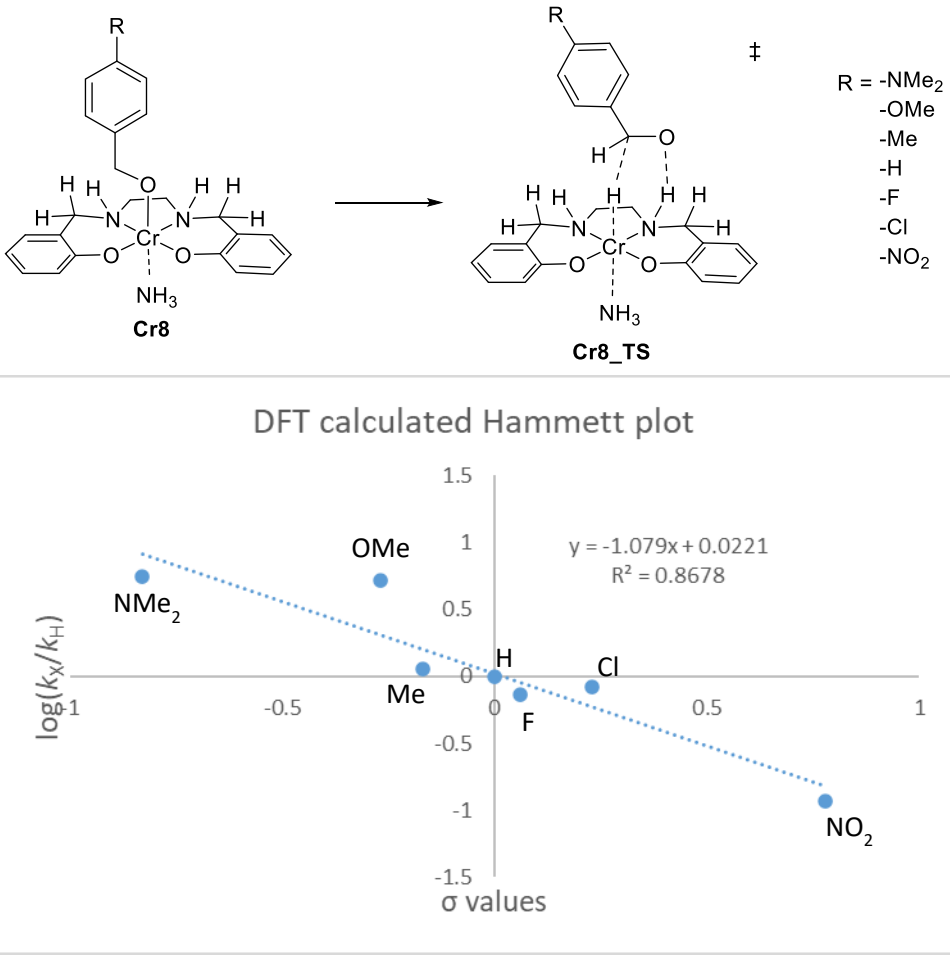

Figure 3.43: DFT-calculated Hammett plot of the **Cr8** → **Cr8_TS** transition

The slope of the DFT-calculated Hammett plot is -1.08, which is in relatively good agreement with the experimentally determined value of -0.73. However, the kinetic isotope effect based on the transition from **Cr8** → **Cr8_TS** was calculated to 2.6, which is too high compared to the experimentally determined values of 1.56 and 1.61. Due to the high energy barriers calculated for the mechanism in Figure 3.42, an alternative mechanism was considered.

3.6.5. Catalytic cycle with no formation of a Cr-H intermediate

Clearly, the catalytic cycle with a Cr(III)-hydride intermediate proposed in Figure 3.42 is energetically unfeasible, so an alternative cycle with no formation of a Cr(III)-hydride was investigated. This catalytic cycle is shown in Figure 3.44.

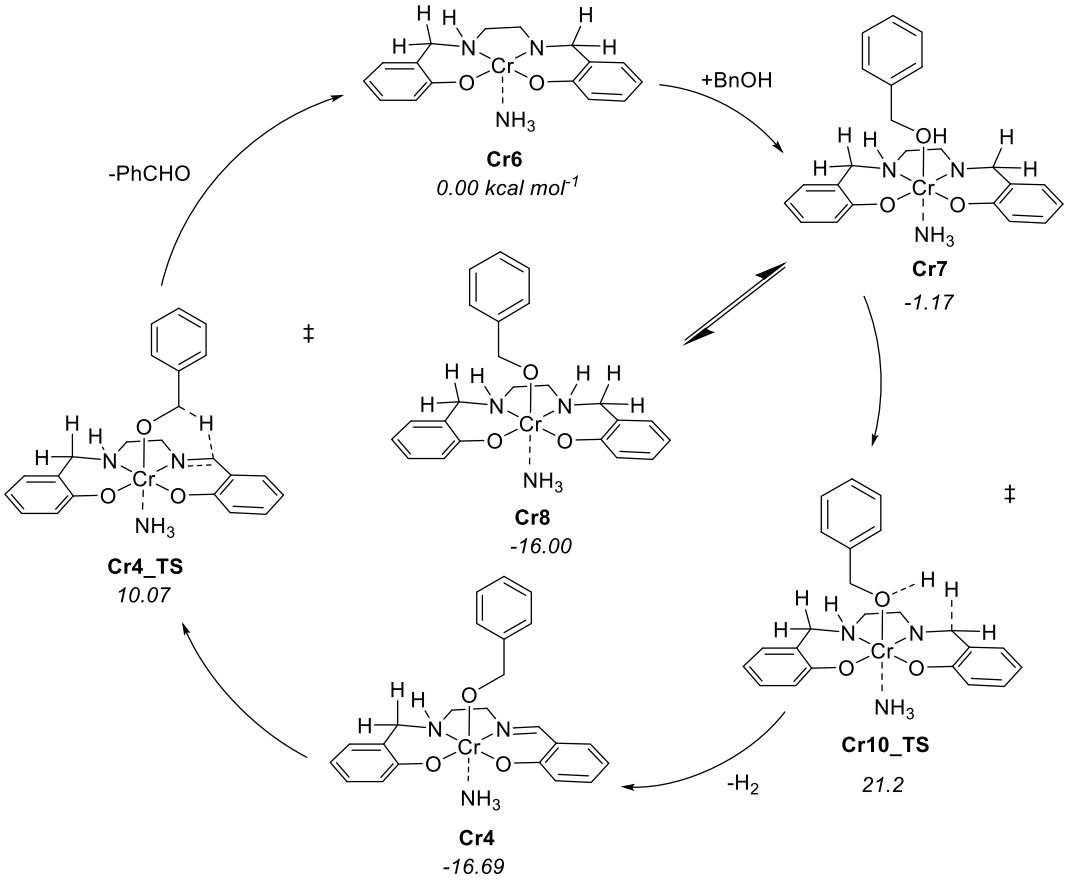

Figure 3.44: Catalytic cycle without formation of a Cr(III)-hydride intermediate. Exclusion of H_2 happens by reacting a H^+ from benzyl alcohol with a H^- from the ligand backbone (**Cr10_TS**)

In this model, an equilibrium between **Cr7** and **Cr8** is envisioned. Although the equilibrium heavily favors **Cr8**, the direct reaction between a H^+ of a coordinated benzyl alcohol with a H^- equivalent of the ligand backbone was hypothesized (**Cr10_TS**). The idea for this pathway came from the Mn(III)-salen catalytic system, where the fully oxidized Mn(III)-salen catalyst could be isolated after the reaction.[1] Thus, a mechanism leading to the reoxidation of the Mn(III)-salan back to Mn(III)-salen must be operative, and a transition state akin to **Cr10_TS** would satisfy this criteria.

However, applying this idea to the Cr(III)-salen system resulted in an overall energy barrier of 37.2 kcal mol^{-1}, so the catalytic cycle presented in Figure 3.44 was also deemed unlikely to occur.

3.6.6. Key transitions with variation of the axial ligand

So far, no models of the Cr(III)-salen system have resulted in energy profiles with barriers within the acceptable range, which coincides with the low observed reactivity of the Cr(III)-based catalysts. To leave no stone unturned, the three key transitions involving breakage of the benzyl oxide C-H bond were recalculated with both pentacoordinate Cr(III) complexes and negatively charged Cr(III) complexes containing two benzyl oxide ligands. These transitions are shown in Figure 3.45.

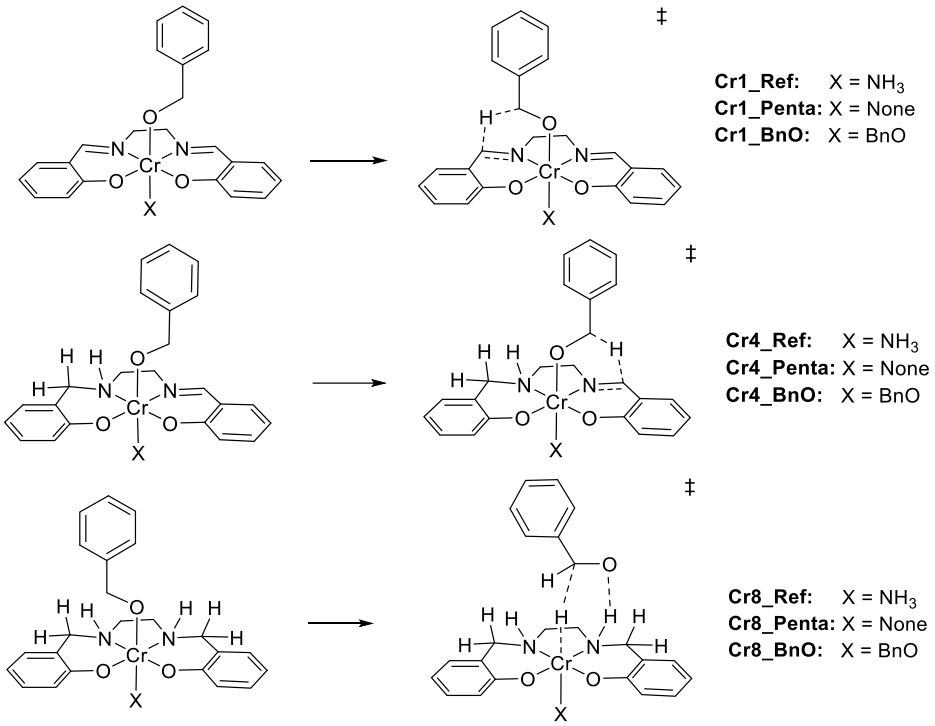

Entry	ΔG_{react} / kcal mol^{-1}	ΔG_{TS} / kcal mol^{-1}	$\Delta G^{\ddagger}$ / kcal mol^{-1}
Cr1_Ref	-858039.7164	-858013.0518	26.66
Cr1_Penta	-822531.5119	-822501.0583	30.45
Cr1_BnO	-1039839.968	-1039813.621	26.35
Cr4_Ref	-858784.0901	-858757.3345	26.76
Cr4_Penta	-823276.1139	-823245.2234	30.89
Cr4_BnO	-1040587.679	-1040562.650	25.03
Cr8_Ref	-859528.653	-859497.7211	30.93
Cr8_Penta	-824020.6277	-823981.1853	39.44
Cr8_BnO	-1041336.493	-1041307.036	29.46

Figure 3.45: The critical steps in the catalyst activation and the formation of Cr(III)-hydride were recalculated for both neutral, pentacoordinate Cr(III) derivatives and octahedral, anionic Cr(III) derivatives bearing two benzyl oxide ligands. The calculated energies for the NH_3 ligated derivatives are included for reference.

The main takeaway from these calculations is the high energy barriers calculated in the case of the pentacoordinate Cr(III) derivatives. The initial hydride transfers required for activation shows activation energies in the 30-31 kcal mol^{-1} range, whereas the transition leading to a pentacoordinate Cr(III)-hydride derivative has an activation energy of 39.4 kcal mol^{-1}. Bearing in

mind that reduction of the salen ligand is observed experimentally, a catalytic mechanism based on pentacoordinate Cr(III)-salen derivatives seems unlikely, as the activation energies are considerably higher than in the models based on octahedral Cr(III) intermediates. It is noteworthy that the energy barriers associated with the axial BnO^- ligand compared to the axial NH_3 results in no major differences in predicted reactivity; the calculated energy barriers are within 1-1.5 kcal mol^{-1} for all three examined transitions.

3.6.7. Effects of phenolate substitution: Catalyst activation

The ability to perform rapid *in silico* screening of a range catalyst derivatives is one of the major advantages of employing DFT calculations in reaction development. The salen scaffold allows substitution on the phenolates and in the ligand backbone. Both EWGs and EDGs were tested in an attempt to identify substitution patterns that could lead to increased reactivity of the Cr(III)-salen catalyst system. In the first *in silico* optimization, the 2nd H^- transfer from benzyl oxide to the ligand backbone was investigated. A range of substitutions on the phenolates were performed *in silico* to gauge the effect of EWGs (-Br, -Cl, $-CF_3$ and $-NO_2$) and EDGs (-OMe, $-NMe_2$) in varying positions on the phenolates. The hypothesis is that EWGs increases the electrophilicity of both the Cr(III)-center and the acceptor imino-carbon, which may lower the $\Delta G^{\ddagger}$ of the H^- transfer. The obtained results are shown in Figure 3.46.

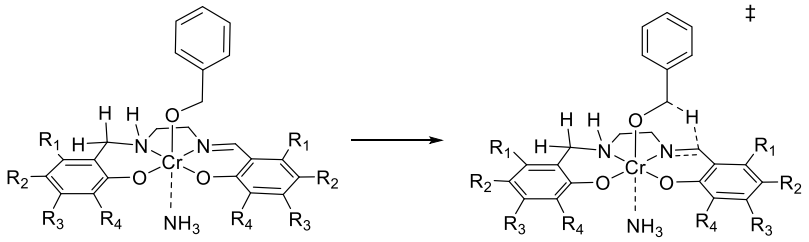

Cr4_Ref: $R_1=R_2=R_3=R_4=H$
Cr4_DiBr: $R_1=R_3=H$, $R_2=R_4=Br$
Cr4_DiCl: $R_1=R_3=H$, $R_2=R_4=Cl$
Cr4_mCF$_3$: $R_1=R_2=R_4=H$, $R_3=CF_3$
Cr4_mNMe$_2$: $R_1=R_2=R_4=H$, $R_3=NMe_2$
Cr4_mNO$_2$: $R_1=R_2=R_4=H$, $R_3=NO_2$
Cr4_mOMe: $R_1=R_2=R_4=H$, $R_3=OMe$
Cr4_pNO$_2$: $R_1=R_3=R_4=H$, $R_2=NO_2$
Cr4_pOMe: $R_1=R_3=R_4=H$, $R_2=OMe$

Entry	ΔG_{react} / kcal mol^{-1}	ΔG_{TS} / kcal mol^{-1}	$\Delta G^{\ddagger}$ / kcal mol^{-1}
Cr4_Ref	-858784.0901	-858757.3345	26.76
Cr4_DiBr	-890349.1853	-890326.1213	23.06
Cr4_DiCl	-2012472.472	-2012448.038	24.43
Cr4_mCF$_3$	-1281920.167	-1281893.272	26.90
Cr4_mNMe$_2$	-1026893.05	-1026861.891	31.16
Cr4_mNO$_2$	-1115524.851	-1115500.885	23.97
Cr4_mOMe	-1002526.444	-1002498.644	27.80
Cr4_pNO$_2$	-1115532.393	-1115508.434	23.96
Cr4_pOMe	-1002521.38	-1002493.705	27.67

Figure 3.46: *In silico* optimization of the 2nd H^- transfer in the activation of the Cr(III)-salen catalyst.

Evidently, substitution with -Cl or -Br in the *ortho*- and *para*-position of the phenolate leads to barriers in the 23-24 kcal mol^{-1} range and consequently faster catalyst activation is predicted for these substitution patterns. Similarly, -NO_2 substitution at both position R_3 and R_2 results in lowering of $\Delta G^{‡}$ to ~24 kcal mol^{-1} in both cases. Interestingly, a slight increase in $\Delta G^{‡}$ is calculated when placing a -CF_3 in the R_3 position, which breaks the trend of electron-withdrawing substituents leading to lower $\Delta G^{‡}$. Looking at the electron-donating substituents, the -OMe derivatives lead to an increase in $\Delta G^{‡}$ to ~27.7 kcal mol^{-1} for both position R_2 and R_3 and placing -NMe_2 in position R_3 leads to a dramatic increase in $\Delta G^{‡}$ to ~31.1 kcal mol^{-1}. Ultimately, the *in silico* optimization shows that placing EWGs on the phenolates lead to lower energy barriers for the catalyst activation.

3.6.8. Effects of phenolate substitution: H$^-$ transfer to Cr(III)

Even though EWGs on the phenolates are predicted to increase the rate of catalyst activation, the more important challenge is to optimize the hypothesized H$^-$ transfer to the Cr(III)-center. Consequently, the previously employed substituents patterns were tested in the *in silico* optimization of the outer-sphere H$^-$ transfer to the Cr(III)-center. The results are shown in Figure 3.47.

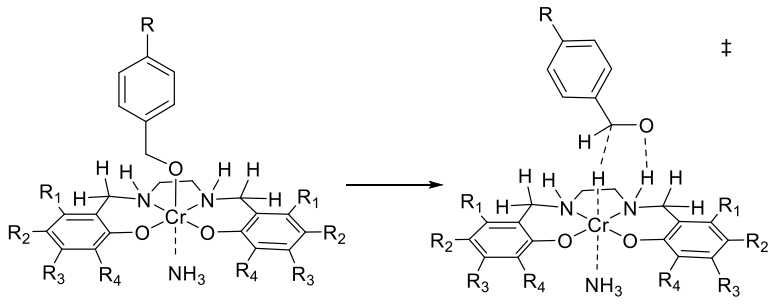

Entry	ΔG_{react} / kcal mol^{-1}	ΔG_{TS} / kcal mol^{-1}	$\Delta G^{‡}$ / kcal mol^{-1}
Cr8_Ref	-859528.653	-859497.7211	30.93
Cr8_DiBr	-891096.6712	-891065.2963	31.37
Cr8_DiCl	-2013219.017	-2013187.76	31.26
Cr8_mCF$_3$	-1282663.804	-1282632.794	31.01
Cr8_mNMe$_2$	-1027632.691	-1027602.411	30.28
Cr8_mNO$_2$	-1116271.38	-1116240.95	30.43
Cr8_mOMe	-1003269.681	-1003238.821	30.86
Cr8_pNO$_2$	-1116279.254	-1116247.108	32.15
Cr8_pOMe	-1003265.143	-1003233.865	31.28

Figure 3.47: *In silico* investigation of the outer-sphere H$^-$ transfer to the Cr(III)-center with catalysts containing different EWGs and EDGs.

Apparently, none of the tested substitution patterns leads to an appreciable decrease of the $\Delta G^{‡}$. Rather, a remarkably similar $\Delta G^{‡}$ is predicted for all substitution patterns, with the -NMe_2 derivative now showing the lowest $\Delta G^{‡}$ of 30.28 kcal mol^{-1}, which is only a 0.65 kcal mol^{-1} improvement compared to the reference transition. Ultimately, the *in silico* optimization study of different phenolate substituents does not predict them to have a pronounced effect on the outer-sphere H^- transfer to the Cr(III)-center.

3.6.9. Effects of backbone changes: Catalyst activation

Instead of manipulating the electrophilicity of the Cr(III)-center by introduction of either EWGs or EDGs, the ligand backbone was the next target for DFT studies. Three derivatives were investigated: a diphenyl-substituted backbone, a cyclohexyl-backbone and an *ortho*-phenylene backbone. The impact of the backbone variations on the $\Delta G^{‡}$ of the 2nd H^- transfer is summarized in Figure 3.48.

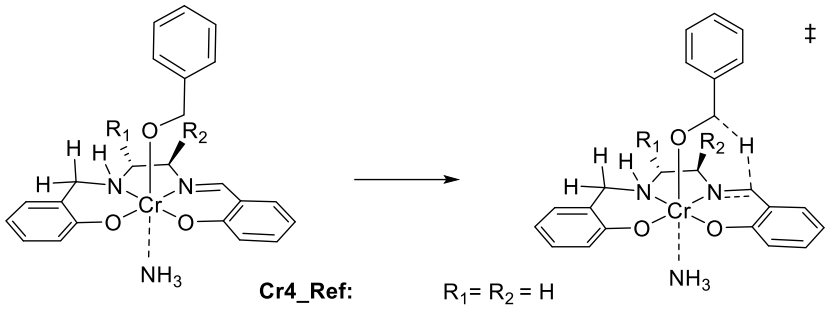

Entry	ΔG_{react} / kcal mol^{-1}	ΔG_{TS} / kcal mol^{-1}	$\Delta G^{‡}$ / kcal mol^{-1}
Cr4_Ref	-858784.0901	-858757.3345	26.76
Cr4_DiPhenyl	-1148748.044	-1148725.28	22.76
Cr4_Cyclohexyl	-956686.5467	-956660.5232	26.02
Cr4_Phenylene	-954445.0544	-954421.6149	23.44

Figure 3.48: *In silico* investigation of the 2nd H^- transfer (catalyst activation) with different ligand backbones.

Evidently, the catalyst activation with **Cr4_DiPhenyl** and **Cr4_Phenylene** is predicted to be faster due to the lowering of $\Delta G^{‡}$ by ~3-4 kcal mol^{-1}. The possibility of resonance stabilization of the negative charge can explain the decrease in $\Delta G^{‡}$ for **Cr4_Phenylene**, but no such stabilization is possible for **Cr4_DiPhenyl**. Consequently, the predicted 4 kcal mol^{-1} decrease in $\Delta G^{‡}$ for **Cr4_DiPhenyl** is curious, and the cause is unknown as no conformational or electronic change is immediately obvious. Lastly, **Cr4_Cyclohexyl** shows no marked difference in $\Delta G^{‡}$ compared to the reference, which is consistent with no significant change in sterics or conformation. Overall, faster transfer of H^- to the ligand backbone, and thus faster catalyst activation, is predicted for **Cr4_DiPhenyl** and **Cr4_Phenylene**, but once again, the main challenge lies in the outer-sphere H^- transfer to the Cr(III)-center, which is tackled next.

3.6.10. Effects of backbone changes: H^- transfer to Cr(III)

The variations in the catalyst backbone were also tested in the outer-sphere H^- transfer to the Cr(III)-center and the results are shown in Figure 3.49.

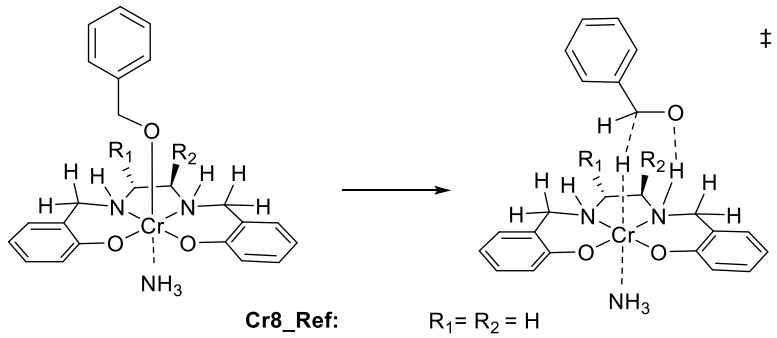

Cr8_Ref: $R_1 = R_2 = H$
Cr8_DiPhenyl: $R_1 = R_2 = Ph$
Cr8_Cyclohexyl: $R_1 = R_2 = -C_4H_8-$
Cr8_Phenylene: $R_1 = R_2 = -C_4H_4-$

Entry	ΔG_{react} / kcal mol^{-1}	ΔG_{TS} / kcal mol^{-1}	$\Delta G^{‡}$ / kcal mol^{-1}
Cr8_Ref	-859528.653	-859497.7211	30.93
Cr8_DiPhenyl	-1149494.946	-1149465.587	29.36
Cr8_Cyclohexyl	-957430.7701	-957400.8563	29.91
Cr8_Phenylene	-955184.8509	-955153.2364	31.61

Figure 3.49: *In silico* investigation of the outer-sphere H^- transfer to the Cr(III)-center with different catalyst backbones

Unfortunately, only minor differences in $\Delta G^{‡}$ for the different backbones are predicted and the most promising candidate is **Cr8_DiPhenyl** with a $\Delta G^{‡}$ of 29.4 kcal mol^{-1}. Ultimately, no radical difference in reactivity is deemed achievable through variation of the ligand backbone, so synthetic efforts may be better spent elsewhere.

3.6.11. Formation of alkoxo-bridged dimers: modeling of equilibria

As mentioned earlier, the increased flexibility of the salan ligand may lead to different coordination isomers as shown in Figure 3.5 and Figure 3.7. Furthermore, structures of phenoxo-bridged and alkoxo-bridged Cr(III)-salan dimers are known as shown previously in Figure 3.7.

It is suspected that the low reactivity of the Cr(III)-salen system may stem from the formation of highly stable dimers of *in situ* formed Cr(III)-salan moieties, possible bridged by benzyl oxide ligands. Evidence of such dimers have been observed by LC-MS, but further experimental evidence of their formation is warranted. To gauge the feasibility of dimer formation, a short DFT study was performed. As a starting point, a published crystal structure of a dimethoxo-bridged Fe(III)-salan complex was used.[106] The Fe(III)-center was changed to Cr(III) and the methoxide ligands were changed to benzyl oxide ligands followed by geometry optimization. The geometry of the pentacoordinate monomer was obtained by removing half of the dimer followed by geometry optimization. Based on these structures, the energetics of the dimerization equilibrium was calculated, and the results are shown in Figure 3.50.

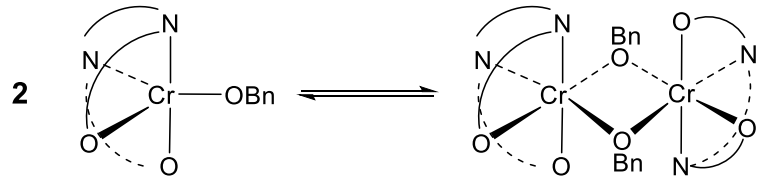

CrSalan_5Coord **CrSalan_Dimer**

2 x Δ*G*(**CrSalan_5Coord**) / kcal mol^{-1}	Δ*G*(**CrSalan_Dimer**) / kcal mol^{-1}	$\Delta G_{dimerization}$ / kcal mol^{-1}
-1648049.017	-1648085.349	-36.3

Figure 3.50: DFT study of the formation of a dimer from two pentacoordinate Cr(III)-salan complexes.

As expected, the formation of the dimer from two pentacoordinate monomers is highly energetically favorable due to the additional Cr-O bond and the resulting octahedral coordination around the Cr(III)-center. However, as established earlier, the monomer is most likely octahedrally coordinated. To account for this, a $CyNH_2$ ligand was coordinated to the monomer. The resulting equilibrium and the calculated energies are shown in Figure 3.51.

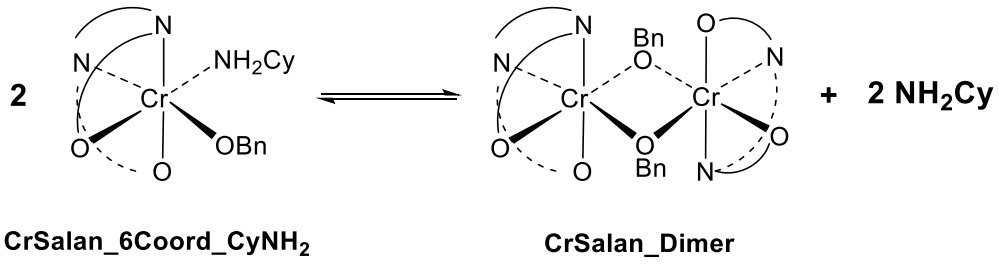

CrSalan_6Coord_CyNH$_2$ **CrSalan_Dimer**

2 x ΔG(**CrSalan_6Coord_CyNH$_2$**) / kcal mol^{-1}	ΔG(**CrSalan_Dimer**) + 2 x ΔG(**CyNH$_2$**) / kcal mol^{-1}	$\Delta G_{dimerization}$ / kcal mol^{-1}
-2013503.142	-2013530.54	-27.4

Figure 3.51: DFT study of the formation of a dimer from two CyNH$_2$-ligated Cr(III)-salan complexes.

In this case, the dimerization is still highly energetically feasible, albeit not as feasible as the case in Figure 3.50, which is expected. Overall, these DFT calculations support the hypothesis that reduction of Cr(III)-salen to Cr(III)-salan allows formation of highly stable benzyl oxide-bridged dimers. These dimers are currently perceived as the most likely candidate for the catalyst resting state and their high stability is thought to be the major issue causing low reactivity in the Cr(III)-salen AAD protocol.

3.7. Conclusion

In this chapter, the development of Cr(III)-salen and Cr(III)-salan AAD catalysts for efficient imination between benzyl alcohol and cyclohexylamine was endeavored. Based on preliminary optimization experiments performed by Maryam Pirouz, the project seemed promising as imine-yields in the 70–99% range were observed with a commercially available Cr(III)-salen catalyst. However, reproduction of the original experiments proved difficult, and switching from the previously used Radley carousel setup to individual Schlenk flasks reduced the imine-yields to the 0–30% range. Using the Schlenk flask setup, a wide range of additives, desiccants, solvents, and catalyst derivatives were investigated, both by me and by SLHP, in an effort to improve the reactivity of the Cr(III)-salen protocol. Ultimately, the best performing conditions resulted in imine-yields of ~30%, where 20% likely resulted from *in situ* reduction of Cr(III)-salen to Cr(III)-salan.

A range of experiments were conducted to probe the reaction mechanism; duplicate KIE values of 1.56 and 1.61 were measured, a Hammett plot with a slope of -0.73 was constructed by SLHP, poisoning with Hg did not show participation of heterogeneous species and lastly, no evolution hydrogen gas could be detected. Thus, an AAD pathway was not operative. Furthermore, LC-MS studies with both benzyl alcohol and benzyl alcohol-α,α-d_2 showed that the Cr(III)-salen scaffold was reduced to Cr(III)-salan *in situ* and evidence of dimer formation was also found by LC-MS.

In conjunction with the experimental investigations, extensive DFT calculations were employed to investigate different catalytic cycles, modifications of catalyst structure, different coordination modes and the possibility of catalyst dimerization. Overall, high energy barriers consistent with low reactivity were calculated for different catalytic cycles, and poor correlation between the experimental and computational KIE values and Hammett plot was found. Moreover, several derivatives of the Cr(III)-salen scaffold were investigated *in silico*, but no significant reactivity improvements were predicted by the DFT model. Lastly, DFT calculations indicated that formation of benzyl oxide-bridged Cr(III)-salan dimers was highly energetically favored, which corroborated the LC-MS observation of such species.

Conclusively, no AAD catalysis with Cr(III)-salen or Cr(III)-salan catalysts was realized. The current hypothesis is that alkoxo- or hydroxo-bridged dimers of Cr(III)-salan are highly stable resting states that effectively inhibit the catalytic activity of the system.

3.8. Experimental

3.8.1. General experimental details

All chemicals, including $CrCl_2$, diamines, salicylaldehyde derivatives, bases and other additives were purchased from either Merck or Fisher Scientific and used as received. The commercially available Cr(III)-salen catalyst, **Cr3.1**, was purchased from Merck and used as received. All moisture-sensitive chemicals (strong bases and catalysts) were either kept in a vacuum desiccator or flushed and stored under argon to avoid degradation. Degassed, anhydrous solvents (mesitylene, toluene, 1,4-dioxane, DMF, pyridine and THF) were prepared by freeze-pump-thaw cycles (repeated three times) followed by sparging with a flow of N_2 for 3 hours minimum. Freshly activated molecular sieves (4Å) was added and the solvent was kept under N_2 and allowed to dry for minimum 24 hours before use. Manual flash column chromatography was performed using HPLC grade heptane and Et_3N. The separations were carried out on silica gel (35 - 70 μm) obtained from VWR Chemicals and pre-saturated with Et_3N before loading the crude product.

All catalytic reactions were performed in two-necked Schlenk reaction tubes using standard Schlenk techniques. The nitrogen feed of the Schlenk line was dried over a column of P_2O_5. To avoid cross-contamination, all glassware and magnets were thoroughly cleaned with *aqua regia* and oven-dried prior to use.

Gas chromatography was carried out on a Shimadzu GCMS-QP2010S instrument equipped with an Rtx-5MS column (30m x 0.25 mm x 0.25 μm). The carrier gas was helium, and the ionization was performed by electron impact (EI) at 70 eV. The following GC settings were employed in all analyzes:

Table 3.7: Settings employed for GC-MS analysis.

Injection volume	1 μL
Injection mode	Split
Injection temperature	280 °C
Initial oven temperature	60 °C (hold 5 min)
Final oven temperature	300 °C (hold 5 min)
Temperature ramp rate	20 °C / min
Total run time	22 min

LC-MS was carried out on a Waters Acquity UPLC system equipped with PDA and SQD2 electrospray MS detector. The following LC-MS settings were employed in all analyzes:

Table 3.8: Settings employed for LC-MS analysis.

Flow rate	0.6 mL/min
Column type	Thermo Accucore C18 (2.6 μm, 2.1 × 50 mm)
Column temperature	50 °C
Eluent **A**	5 mM NH_4OAc in MeCN/water (95/5)
Eluent **B**	5 mM NH_4OAc in water
Eluent program	From 5% **A** - 100% **A** in 2.6 min

Standard ^{1}H and ^{13}C NMR spectra were recorded at 400 MHz and 101 MHz, respectively, on a Bruker Ascend 400 MHz spectrometer using residual $CHCl_3$ signals (δ_H 7.26 ppm, δ_C 77.2 ppm) as reference. All chemical shifts (δ) are quoted in ppm and coupling constants (*J*) are listed in Hz.

Standard IR spectra of the synthesized catalysts were recorded with a Bruker Alpha FT-IR spectrometer.

3.8.2. Procedure for the construction of calibration curves

Stock solution **A** (0.100 M *N*-Benzylidenecyclohexylamine in diethyl ether) were prepared by dissolving freshly synthesized *N*-benzylidenecyclohexylamine (188 mg) in Et_2O in a 10 mL volumetric flask. Stock solution **B** (0.050 M tetradecane in diethyl ether) were prepared by dissolving tetradecane (100 mg) in Et_2O in a 10 mL volumetric flask. From the two stock solutions, the GC calibration samples were prepared according to Table 3.9, and the samples were subjected to GC-MS analysis using the standard method outlined in Section 3.8.1.

Table 3.9: Preparation of standards for the construction of the calibration curves.

Vial no.	1	2	3	4	5
V(**StockA**) / mL	0.1	0.2	0.3	0.4	0.5
V(**StockB**) / mL	0.5	0.5	0.5	0.5	0.5
V(Et_2O) / mL	0.4	0.3	0.2	0.1	0.0
c(*N*-Benzylidenecyclohexylamine) / M	0.01	0.02	0.03	0.05	0.05
c(tetradecane) / M	0.025	0.025	0.025	0.025	0.025

The obtained GC-MS chromatograms (example shown in Figure 3.52) were integrated across fixed retention times (reported in Table 3.10) to ensure consistent integration:

Table 3.10: Retention times used for reliable integration of the GC-MS chromatograms.

Compound	Retention time
Tetradecane	7.73 – 9.00 min
N-Benzylidenecyclohexylamine	12.0 – 13.0 min

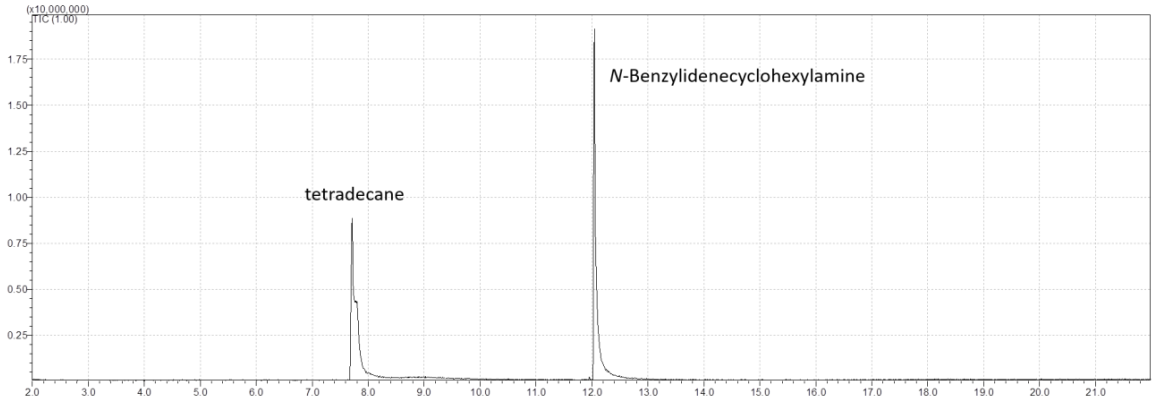

Figure 3.52: Example of a GC-MS chromatogram used to construct the calibration curves.

From the areas obtained by integration of the GC-MS chromatogram, the relative area (A_{imine}/A_{tet}) as a function of the relative concentration (c_{imine}/c_{tet}) were plotted, linear regression with a forced intercept through (0.0) was performed and the obtained slope was used to determine the concentrations of *N*-benzylidenecyclohexylamine in all further experiments.

3.8.3. Synthetic protocols

Synthesis of *N*-benzylidenecyclohexylamine for calibration curves:

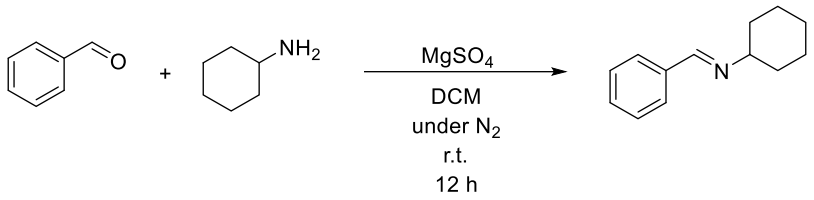

To a round-bottom flask was added CH_2Cl_2 (40 mL), benzaldehyde (2.0 mL, 19.7 mmol), cyclohexylamine (2.25 mL, 19.7 mmol) and $MgSO_4$ (2.4 g, 19.9 mmol). The reaction mixture was stirred for 12 h at room temperature under a flow of N_2. The reaction mixture was filtered and the solvent was removed *in vacuo*. The crude product was loaded onto a silica gel column saturated with Et_3N and purified by flash chromatography in heptane/Et_3N (98:2). The fractions containing pure product were reduced *in vacuo* to yield a pale yellow oil and the product was further dried under vacuum overnight to remove residual solvent.

Yield: 2.66 g (74%)

^{1}H-NMR (400 MHz, $CDCl_3$): δ 8.32 (s, 1H), 7.75-7.72 (m, 2H), 7.41-7.39 (m, 3H), 3.23-3.16 (m, 1H), 1.86-1.55 (m, 7H), 1.43-1.23 (m, 3H).
^{13}C-NMR (101 MHz, $CDCl_3$): δ 158.9, 136.7, 130.7, 128.7, 128.3, 70.0, 34.4, 25.8, 25.0
NMR data are in accordance with previously reported values.[1]

General procedure for the synthesis of **L3.1 – L3.10**:

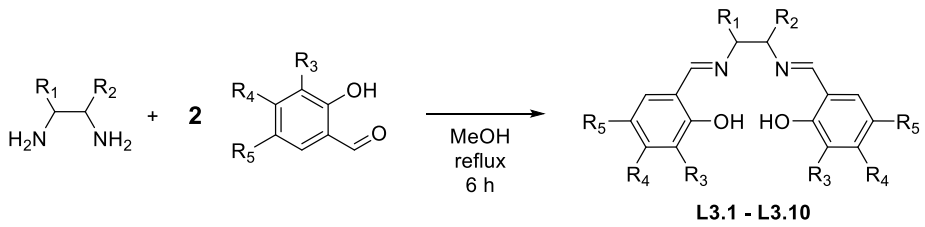

The exact parameters used, and yields obtained in each synthesis can be found in Section 3.8.4.

A round-bottomed flask was charged with the salicylaldehyde derivative (2.0 eq.) and MeOH. The mixture was heated and stirred until full dissolution was achieved. Then, the diamine (1.0 eq.) was added slowly to the reaction mixture, which immediately turned yellow. The flask was equipped with a reflux condenser and the reaction mixture was refluxed for 6 hours. The progress of the reaction was followed both by TLC and LC-MS. During the reaction, a yellow precipitate formed. After the reaction reached completion, the flask was allowed to slowly cool to temperature and subsequently placed in an ice bath. The yellow precipitate was filtered on a Büchner funnel, washed with cold MeOH and air-dried on the filter for 30 minutes followed by oven-drying at 70 °C for 24 h. The purity of the ligand was checked with ^{1}H-NMR and in all cases, the purity of the ligand was adequate for further reaction.

General procedure for the synthesis of **L3.11 – L3.14**:

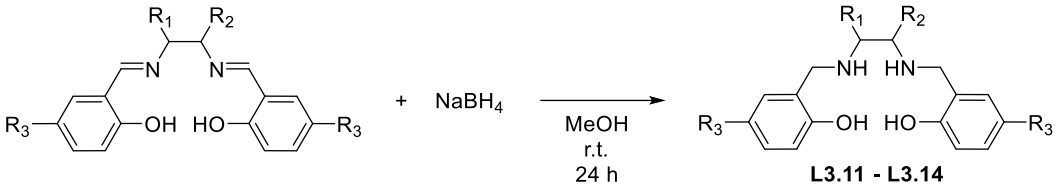

The exact parameters used, and yields obtained in each synthesis can be found in Section 3.8.5.

A round-bottomed flask was charged with the salen derivative (1.0 eq.) and MeOH. The yellow suspension was heated to reflux, resulting in partial dissolution of the salen derivative. The flask was cooled to room temperature, then $NaBH_4$ (1.0 eq.) was added in small portions. Bubbling and a gradual color change from yellow to colorless was observed. In some cases, the heterogeneous mixture turned homogeneous. In all cases, the progress of the reaction was followed by LC-MS. In most cases, the reaction completed within 2-3 hours, but occasionally 24 hours was needed to achieve full reduction. After the reaction reached completion, two different work-up procedures were employed depending on the homogeneity of the reaction mixture.

Work-up of homogeneous mixture:
MeOH was removed *in vacuo* and the residue was partitioned between water (50 mL) and DCM (70 mL). The organic phase was collected, and the aqueous phase was further extracted with DCM (2x30 mL). The organic phases were combined, dried over Na_2SO_4, filtered, and concentrated *in vacuo* to obtain the salan ligand as an off-white powder. The purity of the ligand was checked with ^{1}H-NMR and in all cases, the purity of the ligand was adequate for further reaction.

Work-up of heterogeneous mixture:
The precipitate was filtered on a Büchner funnel and the off-white product was washed with a 1:1 mixture of MeOH/water (50 mL), followed by cold MeOH (20 mL). The product was dried on the funnel for 30 minutes and the yield was determined. If the yield was low, the filtrate was concentrated *in vacuo* and the residue was recrystallized from EtOH/water to obtain a second crop of the product. The isolated powders were combined and oven-dried at 70 °C for 24 hours. The purity of the ligand was assessed with ^{1}H-NMR and recrystallization from EtOH/water was performed if deemed necessary.

General procedure for the synthesis **Cr3.2 – Cr3.10**:

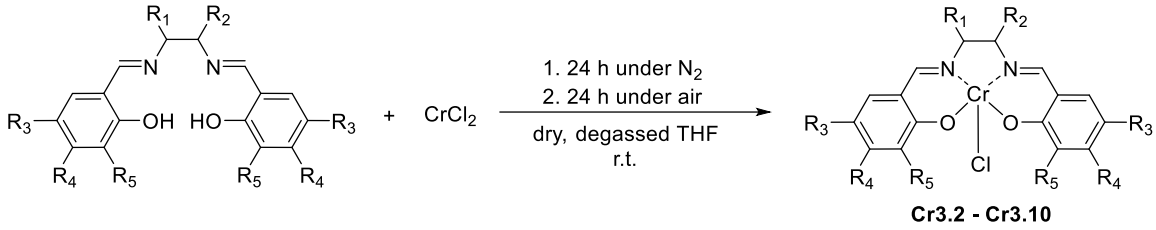

The exact parameters used, and yields obtained in each synthesis can be found in Section 3.8.6.

A flame-dried, round-bottomed Schlenk flask (250 mL) was charged with the salen ligand and dry, degassed THF (~150 mL). The resulting mixture was stirred under N_2 and dissolution of the ligand was observed. An ampoule containing anhydrous $CrCl_2$ (1.0 g) was carefully smashed with a hammer and the powdered $CrCl_2$ was rapidly added to the Schlenk flask under a counterflow of N_2. The flask was sealed with a septum and the reaction mixture was stirred under N_2 at room temperature for 24 hours during which the mixture turned dark brown. After stirring under N_2 for 24 hours, the flow of N_2 was stopped and the flask was opened to the atmosphere. The rate of stirring was increased to facilitate diffusion of O_2 and the mixture was vigorously stirred under air for 24 hours. For all complexes with -tBu substituted ligands, the reaction mixture remained dark brown and homogeneous. For all complexes without -tBu groups on the ligand, a fine light brown precipitate was observed. Thus, two different work-up procedures were employed depending on the homogeneity of the reaction mixture.

Work-up of homogeneous mixture:
The reaction mixture was poured into Et_2O (150 mL) in a separatory funnel and washed with saturated NH_4Cl (3x100 mL) and brine (3x100 mL). The organic phase was dried over Na_2SO_4, filtered into a round-bottomed flask and heptane (~75 mL) was added. The resulting mixture was concentrated *in vacuo* to ~50 mL and a fine brown precipitate appeared during rotary evaporation. The brown precipitate was filtered off on a Büchner funnel, washed with cold heptane (2x 20 mL) and air-dried on the filter for 30 minutes followed by oven-drying at 110 °C for 24 h. Thus, the Cr(III)-salen complex was isolated as a fine brown powder and LC-MS and IR analysis were performed to support the identity of the catalyst.

Work-up of heterogeneous mixture:
The fine brown precipitate was isolated by suction filtration on a Büchner funnel suction filtered on a Büchner funnel The reaction mixture was poured into Et_2O (150 mL) in a separatory funnel and washed with saturated NH_4Cl (3x100 mL) and brine (3x100 mL). The organic phase was dried over Na_2SO_4, filtered into a round-bottomed flask and heptane (~75 mL) was added. The resulting mixture was concentrated *in vacuo* to ~50 mL and a fine brown precipitate appeared during rotary evaporation. The brown precipitate was filtered off on a Büchner funnel, washed with cold heptane (2x 20 mL) and air-dried on the filter for 30 minutes followed by oven-drying at 110 °C for 24 h. Thus, the Cr(III)-salen complex was isolated as a fine brown powder and LC-MS and IR analysis were performed to establish the identity of the catalyst.

General procedure for the synthesis of **Cr3.11 – Cr3.14**

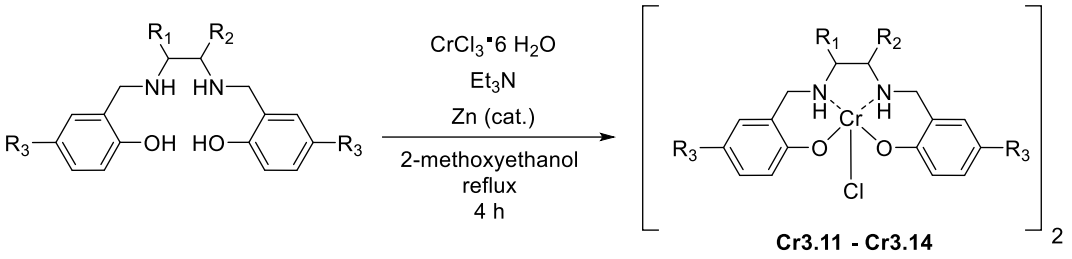

The exact parameters used and yields obtained in each synthesis can be found in Section 3.8.7.

A flame-dried, round-bottomed flask (250 mL) was charged with the salan ligand (1.0 eq.) and 2-methoxyethanol (50 mL) resulting in an off-white suspension. Et_3N (2.0 eq.) was added to the mixture by syringe, the flask was equipped with a reflux condenser and heated to reflux in an oil bath. Concomitantly, a solution of $CrCl_3 \cdot 6\ H_2O$ (1.0 eq.) in 2-methoxyethanol (50 mL) was prepared. Once reflux was achieved, the solution of $CrCl_3 \cdot 6\ H_2O$ and Zn powder (10 mg) was added in one portion. The resulting reaction mixture was stirred and refluxed for 4 h during which the color changed to purple and a blue-green precipitate formed. The suspension was cooled to room temperature and concentrated to 30 mL *in vacuo*. The suspension was left standing at room temperature overnight before the blue-green precipitate was isolated by suction filtration on a Büchner funnel. The blue-green precipitate was washed with EtOH (2x20 mL) and Et_2O (1x20 mL) and air-dried on the filter for 30 minutes followed by oven-drying at 110 °C for 24 h. The Cr(III)-salan catalyst was characterized by LC-MS and IR.

3.8.4. Data for preparation of L3.1 – L3.10

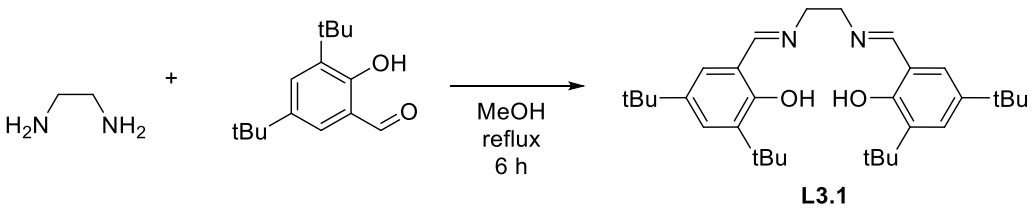

L3.1 was prepared according to the procedure outlined in Section 3.8.3 and isolated as a yellow powder.

V(diamine) / mL	*m*(aldehyde) / g	*V*(MeOH) / mL	Yield / g
1.40 (21.0 mmol)	9.83 (41.9 mmol)	80	9.50 (19.3 mmol, 92%)

^{1}H-NMR (400 MHz, $CDCl_3$): δ 8.40 (s, 2H), 7.37 (d, J = 2.5 Hz, 2H), 7.08 (d, J = 2.5 Hz, 2H), 3.93 (s, 4H), 1.44 (s, 18H), 1.29 (s, 18H). NMR data are in accordance with previously reported values.[210]

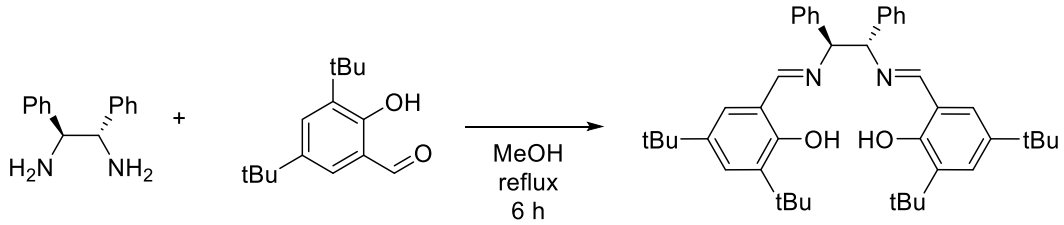

L3.2

L3.2 was prepared according to the procedure outlined in Section 3.8.3 and isolated as a yellow powder.

m(diamine) / g	*m*(aldehyde) / g	*V*(MeOH) / mL	Yield / g
0.85 (4.0 mmol)	1.88 (8.0 mmol)	40	2.46 (3.8 mmol, 95%)

^{1}H-NMR (400 MHz, $CDCl_3$): δ 8.40 (s, 2H), 7.32 (s, 2H), 7.25 – 7.11 (m, 10H) 6.99 (s, 2H), 4.73 (s, 2H), 1.42 (s, 18H), 1.23 (s, 18H). NMR data are in accordance with previously reported values.[211]

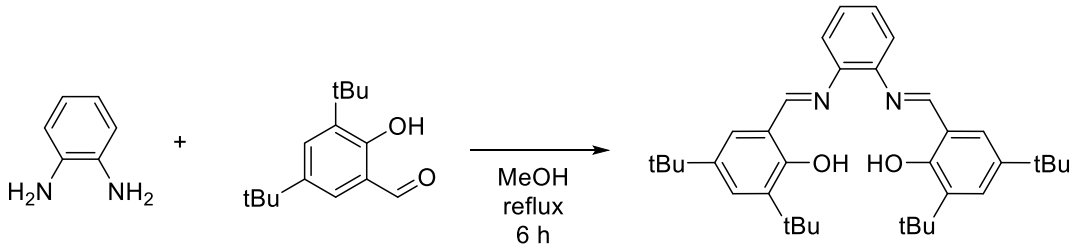

L3.3

L3.3 was prepared according to the procedure outlined in Section 3.8.3 and isolated as a yellow powder.

m(diamine) / g	*m*(aldehyde) / g	*V*(MeOH) / mL	Yield / g
1.0 (9.25 mmol)	4.33 (18.5 mmol)	60	4.40 (8.14 mmol, 88%)

^{1}H-NMR (400 MHz, $CDCl_3$): δ 8.66 (s, 2H), 7.50 – 7.19 (m, 8H), 1.42 (s, 18H), 1.33 (s, 18H). NMR data are in accordance with previously reported values.[212]

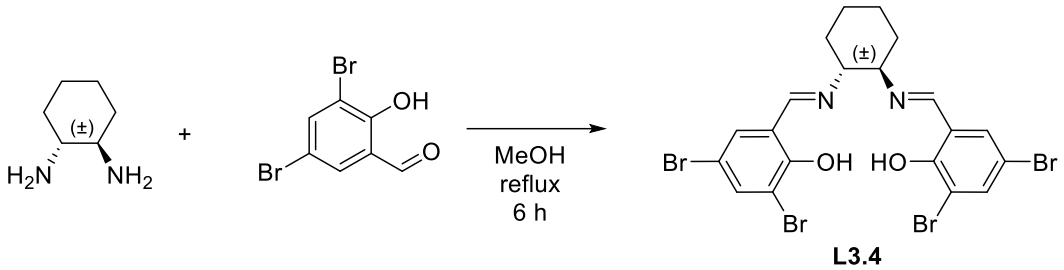

L3.4

L3.4 was prepared according to the procedure outlined in Section 3.8.3 and isolated as a yellow powder.

V(diamine) / mL	*m*(aldehyde) / g	*V*(MeOH) / mL	Yield / g
2.20 (18.3 mmol)	10.26 (36.6 mmol)	100	10.58 (16.5 mmol, 90%)

^{1}H-NMR (400 MHz, $CDCl_3$): δ 8.18 (s, 2H), 7.67 (d, *J* = 2.3 Hz, 2H), 7.29 (d, *J* = 2.3 Hz, 2H), 3.44 – 3.36 (m, 2H), 2.02 – 1.87 (m, 4H), 1.80 – 1.66 (m, 2H), 1.57 – 1.43 (m, 2H). NMR data are in accordance with previously reported values.[213]

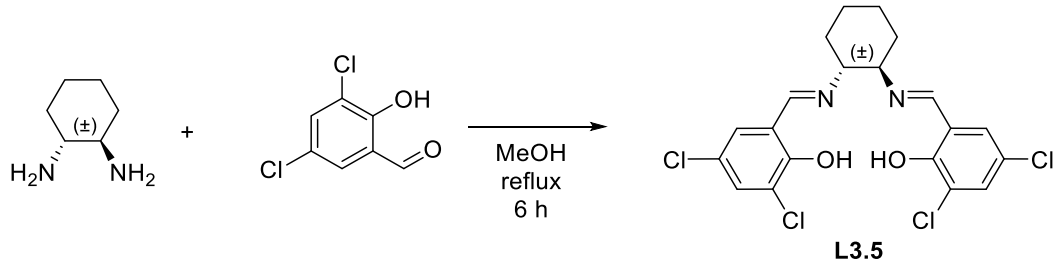

L3.5

L3.5 was prepared according to the procedure outlined in Section 3.8.3 and isolated as a yellow powder.

V(diamine) / mL	*m*(aldehyde) / g	*V*(MeOH) / mL	Yield / g
1.50 (12.5 mmol)	4.77 (25.0 mmol)	70	5.41 (11.8 mmol, 94%)

^{1}H-NMR (400 MHz, $CDCl_3$): δ 8.18 (s, 2H), 7.36 (d, *J* = 2.5 Hz, 2H), 7.08 (d, *J* = 2.5 Hz, 2H), 3.42 – 3.31 (m, 2H), 2.00 – 1.84 (m, 4H), 1.78 – 1.63 (m, 2H), 1.56 – 1.41 (m, 2H). NMR data are in accordance with previously reported values.[213]

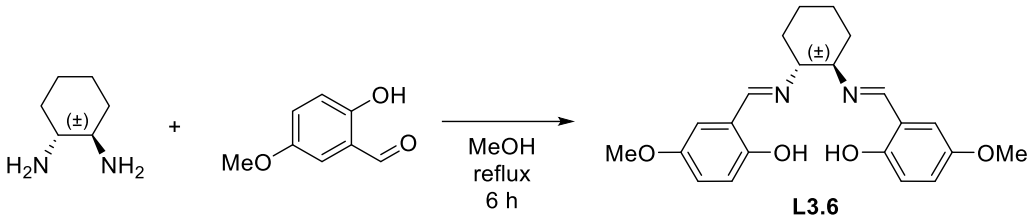

L3.6

L3.6 was prepared according to the procedure outlined in Section 3.8.3 and isolated as a yellow powder.

V(diamine) / mL	*V*(aldehyde) / mL	*V*(MeOH) / mL	Yield / g
2.00 (16.7 mmol)	4.20 (33.3 mmol)	70	5.91 (15.5 mmol, 93%)

^{1}H-NMR (400 MHz, $CDCl_3$): δ 8.21 (s, 2H), 6.90 – 6.80 (m, 4H), 6.66 (d, J = 2.8 Hz, 2H), 3.73 (s, 6H), 3.38 – 3.26 (m, 2H), 2.01 – 1.85 (m, 4H), 1.82 – 1.67 (m, 2H), 1.58 – 1.46 (m, 2H). NMR data are in accordance with previously reported values.[214]

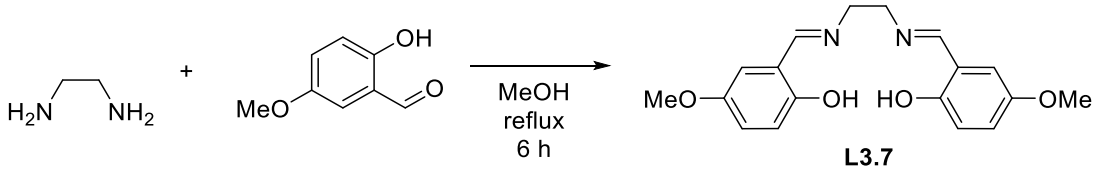

L3.7

L3.7 was prepared according to the procedure outlined in Section 3.8.3 and isolated as a yellow powder.

V(diamine) / mL	*V*(aldehyde) / mL	*V*(MeOH) / mL	Yield / g
1.20 (18.0 mmol)	4.50 (36.0 mmol)	60	5.24 (16.0 mmol, 89%)

^{1}H-NMR (400 MHz, $CDCl_3$): δ 8.31 (s, 2H), 6.95 – 6.82 (m, 4H), 6.74 (d, J = 2.8 Hz, 2H), 3.94 (s, 4H), 3.75 (s, 6H). NMR data are in accordance with previously reported values.[215]

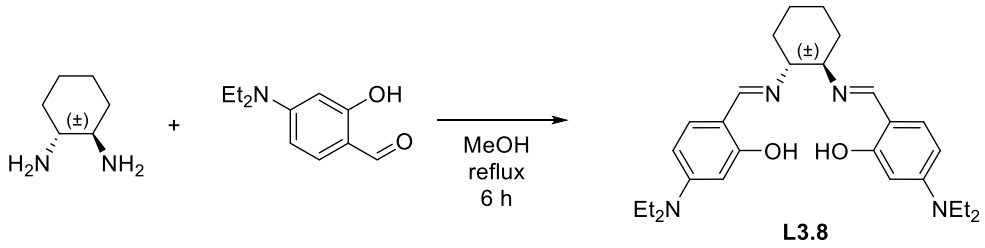

L3.8

L3.8 was prepared according to the procedure outlined in Section 3.8.3 and isolated as a yellow powder.

V(diamine) / mL	*m*(aldehyde) / g	*V*(MeOH) / mL	Yield / g
2.00 (16.7 mmol)	6.44 (33.3 mmol)	60	6.89 (14.8 mmol, 89%)

^{1}H-NMR (400 MHz, $CDCl_3$): δ 7.90 (s, 2H), 6.89 (d, J = 8.7 Hz, 2H), 6.15 – 6.03 (m, 4H), 3.32 (q, J = 7.1 Hz, 8H), 3.24 – 3.11 (m, 2H), 2.01 – 1.90 (m, 2H), 1.86 – 1.80 (m, 2H), 1.68 – 1.56 (m, 2H), 1.47 – 1.35 (m, 2H), 1.14 (t, J = 7.1 Hz, 12H). NMR data are in accordance with previously reported values.[216]

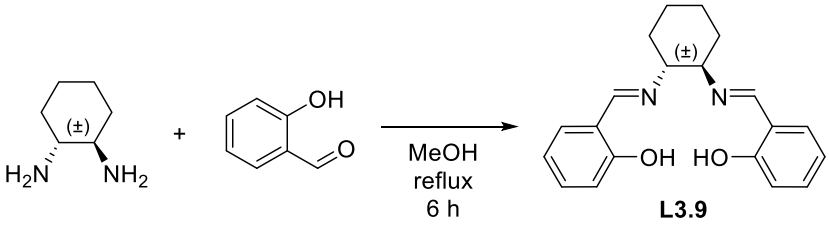

L3.9

L3.9 was prepared according to the procedure outlined in Section 3.8.3 and isolated as a yellow powder.

V(diamine) / mL	*V*(aldehyde) / mL	*V*(MeOH) / mL	Yield / g
2.00 (16.7 mmol)	3.50 (33.3 mmol)	60	4.31 (13.4 mmol, 80%)

^{1}H-NMR (400 MHz, $CDCl_3$): 8.26 (s, 2H), 7.28 – 7.19 (m, 2H), 7.15 (dd, J = 7.7, 1.7 Hz, 2H), 6.89 (dd, J = 8.3, 1.0 Hz, 2H), 6.79 (td, J = 7.4, 1.1 Hz, 2H), 3.38 – 3.26 (m, 2H), 2.00 – 1.82 (m, 4H), 1.80 – 1.66 (m, 2H), 1.56 – 1.41 (m, 2H). NMR data are in accordance with previously reported values.[1]

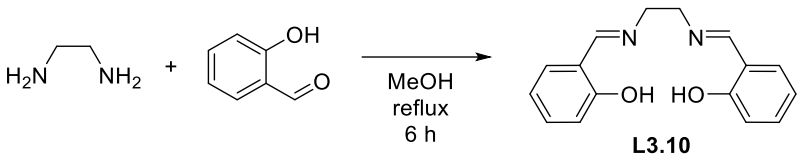

L3.10

L3.10 was prepared according to the procedure outlined in Section 3.8.3 and isolated as a yellow powder.

V(diamine) / mL	*V*(aldehyde) / mL	*V*(MeOH) / mL	Yield / g
1.40 (21.0 mmol)	4.40 (42.0 mmol)	70	5.27 (19.6 mmol, 94%)

^{1}H-NMR (400 MHz, $CDCl_3$): δ 8.38 (s, 2H), 7.32 (t, J = 8.4 Hz, 2H), 7.25 (d, J = 7.7 Hz, 2H), 6.96 (d, J = 8.3 Hz, 2H), 6.88 (t, J = 7.6 Hz, 2H), 3.97 (s, 4H). NMR data are in accordance with previously reported values.[217]

3.8.5. Data for preparation of L3.11 – L3.14

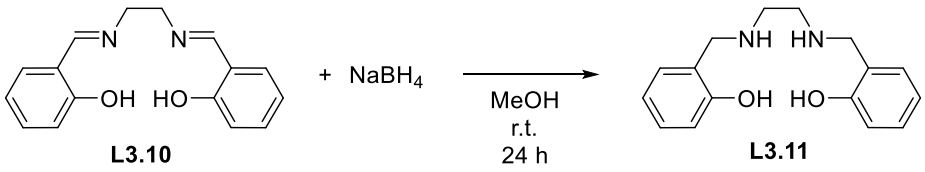

L3.10 L3.11

L3.11 was prepared according to the procedure outlined in Section 3.8.3 and isolated as an off-white powder.

m(**L3.10**) / g	*m*($NaBH_4$) / mg	*V*(MeOH) / mL	Yield / g
4.50 (16.8 mmol)	634 (16.8 mmol)	90	3.63 (13.3 mmol, 79%)

^{1}H-NMR (400 MHz, $CDCl_3$): δ 7.20 (t, J = 7.8 Hz, 2H), 7.00 (d, J = 7.5 Hz, 2H), 6.91 – 6.72 (m, 4H), 3.98 (s, 4H), 2.83 (s, 4H). NMR data are in accordance with previously reported values.[218]

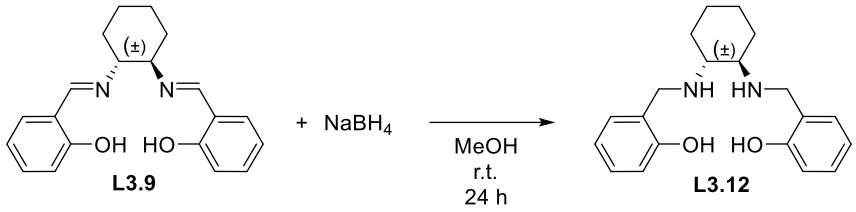

L3.12 was prepared according to the procedure outlined in Section 3.8.3 and isolated as an off-white powder.

m(**L3.9**) / g	*m*($NaBH_4$) / mg	*V*(MeOH) / mL	Yield / g
4.20 (13.0 mmol)	493 (13.0 mmol)	90	4.09 (12.5 mmol, 96%)

^{1}H-NMR (400 MHz, $CDCl_3$): δ 7.16 (td, J = 7.8, 1.7 Hz, 2H), 6.98 (dd, J = 7.5, 1.6 Hz, 2H), 6.89 – 6.75 (m, 4H), 4.04 (d, J = 13.5 Hz, 2H), 3.89 (d, J = 13.5 Hz, 2H), 2.62 – 2.40 (m, 2H), 2.31 – 2.10 (m, 2H), 1.80 – 1.65 (m, 2H), 1.40 – 1.18 (m, 4H). NMR data are in accordance with previously reported values.[1]

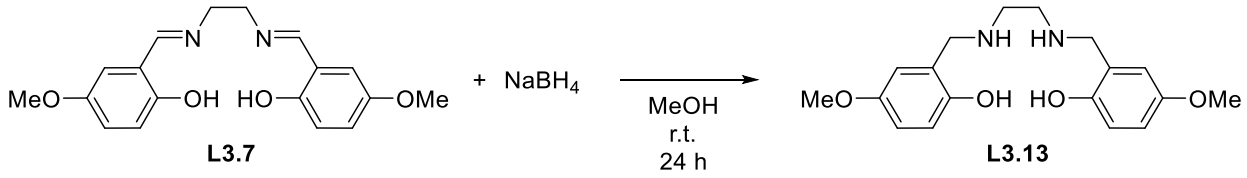

L3.13 was prepared according to the procedure outlined in Section 3.8.3 and isolated as an off-white powder.

m(**L3.7**) / g	*m*($NaBH_4$) / mg	*V*(MeOH) / mL	Yield / g
4.80 (14.6 mmol)	553 (14.6 mmol)	90	4.31 (13.0 mmol, 89%)

^{1}H-NMR (400 MHz, $CDCl_3$): δ 6.76 (d, J = 8.7 Hz, 2H), 6.73 (dd, J = 8.7, 2.7 Hz, 2H), 6.56 (d, J = 2.7 Hz, 2H), 3.95 (s, 4H), 3.74 (s, 6H), 2.83 (s, 4H). NMR data are in accordance with previously reported values.[215]

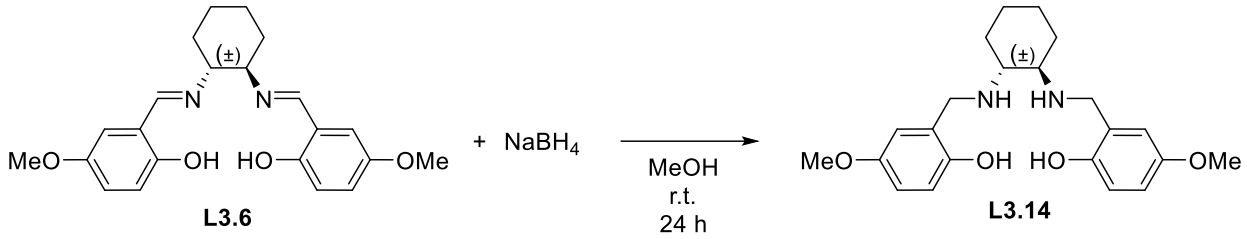

L3.14 was prepared according to the procedure outlined in Section 3.8.3 and isolated as an off-white powder.

m(**L3.6**) / g	*m*($NaBH_4$) / mg	*V*(MeOH) / mL	Yield / g
5.35 (14.0 mmol)	529 (14.0 mmol)	100	4.96 (12.8 mmol, 92%)

^{1}H-NMR (400 MHz, $CDCl_3$): δ 6.77 (d, *J* = 8.7 Hz, 2H), 6.71 (dd, *J* = 8.7, 2.9 Hz, 2H), 6.56 (d, *J* = 2.9 Hz, 2H), 3.98 (d, *J* = 13.8 Hz, 2H), 3.86 (d, *J* = 13.8 Hz, 2H), 3.73 (s, 6H), 2.47 – 2.41 (m, 2H), 2.18 – 2.09 (m, 2H), 1.75 – 1.67 (m, 2H), 1.29 – 1.13 (m, 4H). No NMR data recorded in $CDCl_3$ were found in the literature.

3.8.6. Data for preparation of Cr3.2 – Cr3.10

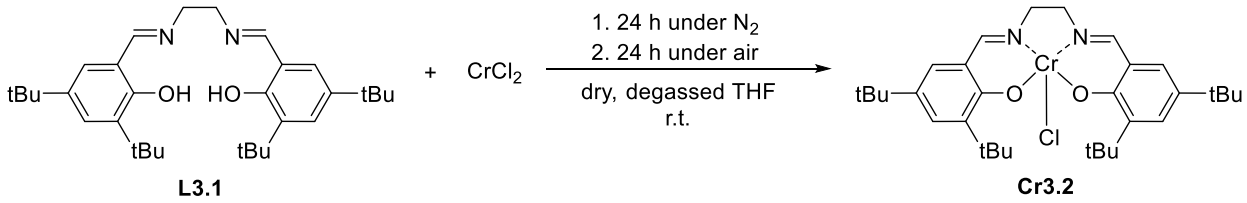

Cr3.2 was prepared according to the procedure outlined in Section 3.8.3. The complex was isolated as a fine brown powder.

m(**L3.1**) / g	*m*($CrCl_2$) / g	*V*(THF) / mL	Yield / g
3.65 (7.41 mmol)	1.0 (8.1 mmol)	150	3.03 (5.24 mmol, 71%)

FTIR, ν/cm^{-1}: 3156 w, 3039 w, 2948 s, 2905 m, 2867 m, 1617 s, 1530 m, 1458 m, 1431 m, 1383 m, 1330 m, 1310 m, 1254 m, 1165 m
MS (ESI+) *m/z*: 542.037 $[M\text{-}Cl]^+$, calc. 542.296.

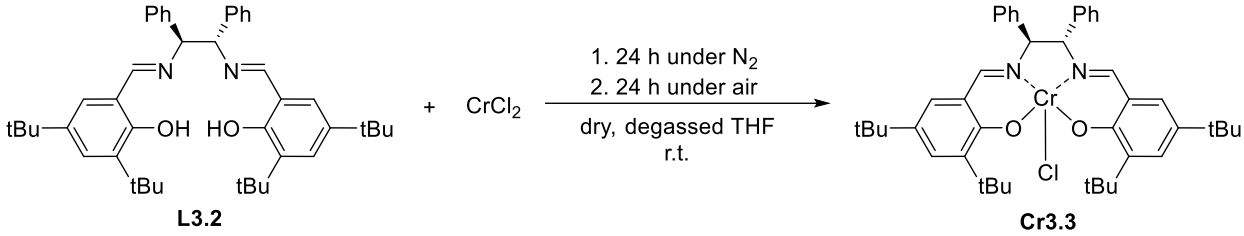

Cr3.3 was prepared according to the procedure outlined in Section 3.8.3. The complex was isolated as a fine brown powder.

m(**L3.2**) / g	*m*($CrCl_2$) / g	*V*(THF) / mL	Yield / g
2.36 (3.66 mmol)	1.0 (8.1 mmol)	150	2.39 (3.27 mmol, 89%)

FTIR, ν/cm^{-1}: 3138 w, 3066 w, 2951 s, 2904 m, 2868 m, 1607 s, 1530 m, 1430 m, 1385 m, 1252 m, 1169 m
MS (ESI+) *m/z*: 694.145 $[M\text{-}Cl]^+$, calc. 694.358.

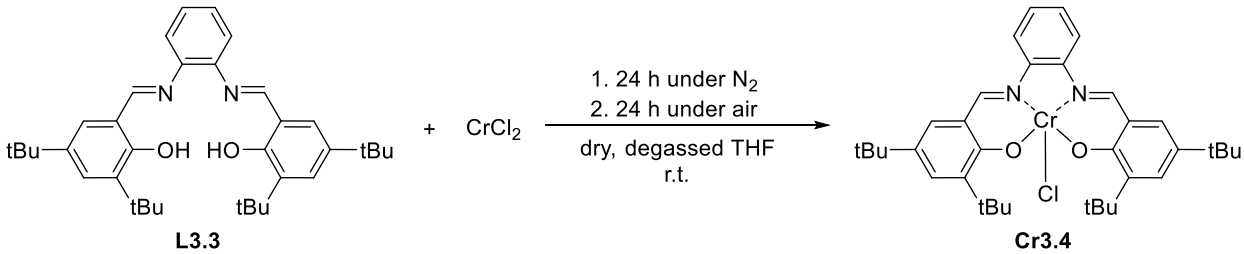

Cr3.4 was prepared according to the procedure outlined in Section 3.8.3. The complex was isolated as a fine brown powder.

m(**L3.3**) / g	*m*($CrCl_2$) / g	*V*(THF) / mL	Yield / g
4.05 (7.49 mmol)	1.0 (8.1 mmol)	150	3.18 (5.08 mmol, 68%)

FTIR, ν/cm^{-1}: 3118 w, 3076 w, 2952 s, 2903 m, 2867 m, 1601 s, 1577 s, 1523 s, 1460 m, 1425 m, 1358 m, 1255 m, 1194 m, 1170 m, 1132 m
MS (ESI+) *m/z*: 590.095 $[M\text{-}Cl]^+$, calc. 590.296.

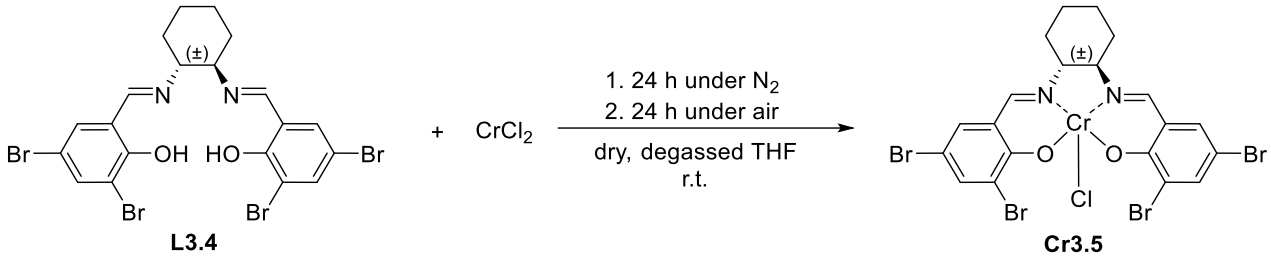

Cr3.5 was prepared according to the procedure outlined in Section 3.8.3. The complex was isolated as a fine light-brown powder.

m(**L3.4**) / g	*m*($CrCl_2$) / g	*V*(THF) / mL	Yield / g
4.76 (7.46 mmol)	1.0 (8.1 mmol)	150	2.96 (4.09 mmol, 55%)

FTIR, ν/cm^{-1}: 3072 m, 3051 m, 2950 m, 2930 m, 2860 w, 1629 s, 1579 m, 1518 m, 1441 s, 1405 m, 1383 m, 1309 s, 1219 m, 1157 s
MS (ESI+) *m/z*: 687.432 $[M\text{-}Cl]^+$, calc. 687.731

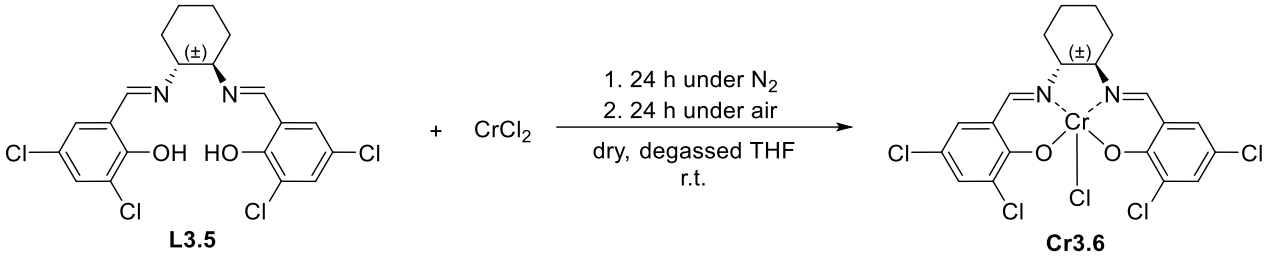

Cr3.6 was prepared according to the procedure outlined in Section 3.8.3. The complex was isolated as a fine light-brown powder.

m(**L3.5**) / g	*m*($CrCl_2$) / g	*V*(THF) / mL	Yield / g
3.38 (7.35 mmol)	1.0 (8.1 mmol)	150	3.06 (5.61 mmol, 76%)

FTIR, ν/cm^{-1}: 3074 m, 3057 m, 2952 m, 2932 m, 2858 w, 1637 s, 1588 m, 1525 m, 1439 s, 1385 m, 1299 s, 1211 m, 1173 m
MS (ESI+) *m/z*: 509.641 $[M\text{-}Cl]^+$, calc. 509.934.

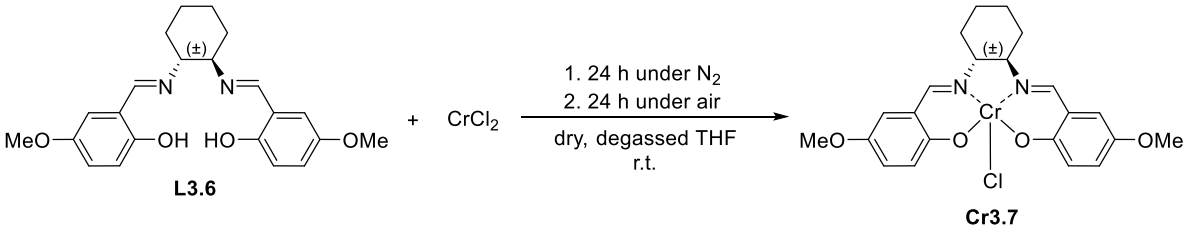

Cr3.7 was prepared according to the procedure outlined in Section 3.8.3. The complex was isolated as a fine brown powder.

m(**L3.6**) / g	*m*($CrCl_2$) / g	*V*(THF) / mL	Yield / g
2.82 (7.37 mmol)	1.0 (8.1 mmol)	150	2.34 (5.00 mmol, 68%)

FTIR, ν/cm^{-1}: 3060 m, 3029 m, 2934 m, 2922 m, 2863 m, 2837 m, 1628 s, 1614 s, 1542 s, 1474 s, 1388 m, 1305 s, 1285 s, 1260 s, 1222 s, 1155 s
MS (ESI+) *m/z*: 431.952 $[M\text{-}Cl]^+$, calc. 432.114.

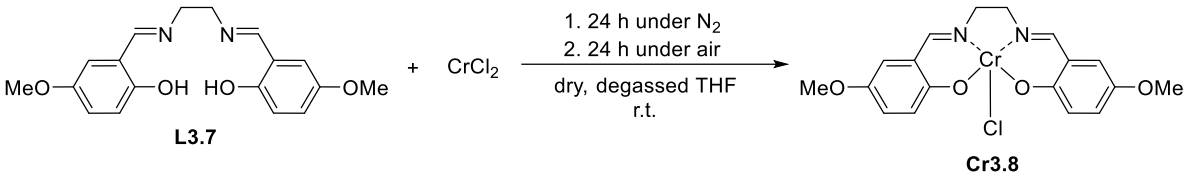

Cr3.8 was prepared according to the procedure outlined in Section 3.8.3. The complex was isolated as a fine brown powder.

m(**L3.7**) / g	*m*($CrCl_2$) / g	*V*(THF) / mL	Yield / g
2.44 (7.43 mmol)	1.0 (8.1 mmol)	150	1.39 (3.36 mmol, 45%)

FTIR, ν/cm^{-1}: 3059 m, 3028 m, 2913 m, 2860 m, 2832 m, 1630 s, 1613 s, 1542 s, 1473 s, 1384 m, 1280 s, 1222 s, 1159 s
MS (ESI+) *m/z*: 377.933 $[M\text{-}Cl]^+$, calc. 378.067.

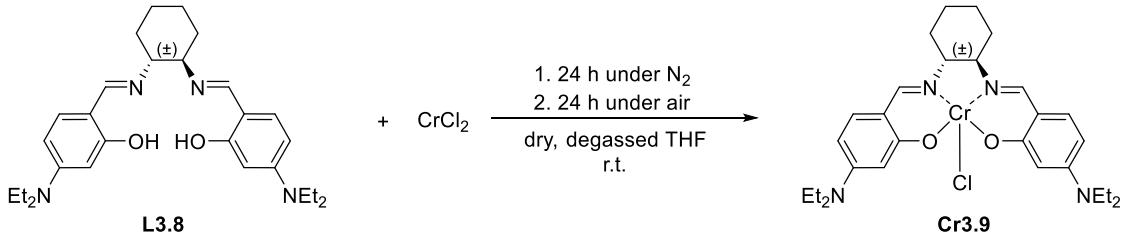

Cr3.9 was prepared according to the procedure outlined in Section 3.8.3. The complex was isolated as a fine brown powder.

m(**L3.8**) / g	*m*($CrCl_2$) / g	*V*(THF) / mL	Yield / g
3.45 (7.42 mmol)	1.0 (8.1 mmol)	150	1.97 (3.58 mmol, 48%)

FTIR, ν/cm^{-1}: 3089 m, 3078 m, 2967 m, 2929 m, 2862 m, 1588 s, 1530 m, 1508 m, 1393 m, 1341 m, 1240 m, 1119 m
MS (ESI+) *m/z*: 513.952 $[M\text{-}Cl]^+$, calc. 514.239

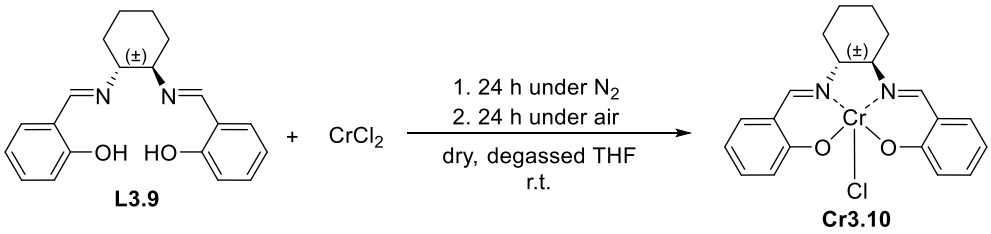

Cr3.10 was prepared according to the procedure outlined in Section 3.8.3. The complex was isolated as a fine brown powder.

m(**L3.9**) / g	*m*($CrCl_2$) / g	*V*(THF) / mL	Yield / g
2.40 (7.44 mmol)	1.0 (8.1 mmol)	150	2.22 (5.44 mmol, 73%)

FTIR, ν/cm^{-1}: 3099 w, 3070 w, 3013 w, 2923 m, 2872 m, 2854 w, 1626 s, 1558 m, 1509 s, 1470 m, 1434 m, 1395 m, 1342 s, 1295 m, 1188 m
MS (ESI+) *m/z*: 371.979 $[M\text{-}Cl]^+$, calc. 372.092.

3.8.7. Data for preparation of Cr3.11 – Cr3.14

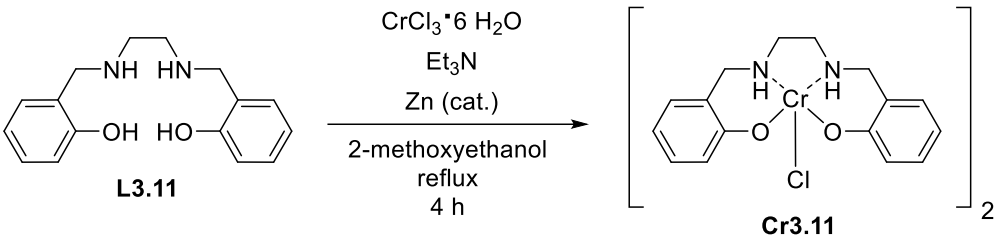

Cr3.11 was prepared according to the procedure outlined in Section 3.8.3. The complex was isolated as a fine, dark blue-green powder.

m(**L3.11**) / g	*V*(Et_3N) / mL	*V*(2-methoxyethanol) / mL	*m*($CrCl_3 \cdot 6H_2O$) / g	Yield / g
3.43 (12.6 mmol)	3.50 (25.2 mmol)	50 + 50	3.36 (12.6 mmol)	3.12 (4.36 mmol, 69%)

FTIR, ν/cm^{-1}: 3211 m, 3181 s, 3066 w, 3032 w, 2985 w, 2928 w, 2872 w, 1597 m, 1568 w, 1482 s, 1446 m, 1295 s, 1276 s, 1220 m, 1194 m
MS (ESI+) *m/z*: 660.885 $[M\text{-}2Cl\text{+}OH]^+$, calc. 661.157.

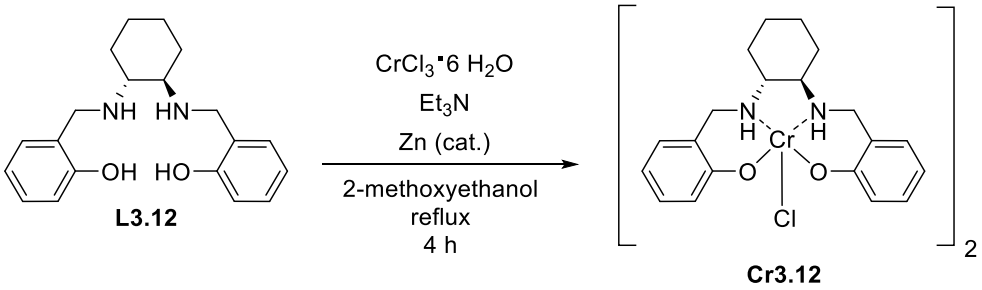

Cr3.12 was prepared according to the procedure outlined in Section 3.8.3. The complex was isolated as a fine, dark blue-green powder.

m(**L3.12**) / g	*V*(Et_3N) / mL	*V*(2-methoxyethanol) / mL	*m*($CrCl_3 \cdot 6H_2O$) / g	Yield / g
3.62 (11.1 mmol)	3.10 (22.2 mmol)	50 + 50	2.95 (11.1 mmol)	3.42 (4.15 mmol, 75%)

FTIR, ν/cm^{-1}: 3191 m, 3155 w, 3056 w, 3009 w, 2934 m, 2858 w, 1596 m, 1570 w, 1479 s, 1450 s, 1282 m, 1226 m
MS (ESI+) *m/z*: 769.011 $[M\text{-}2Cl\text{+}OH]^+$, calc. 769.251.

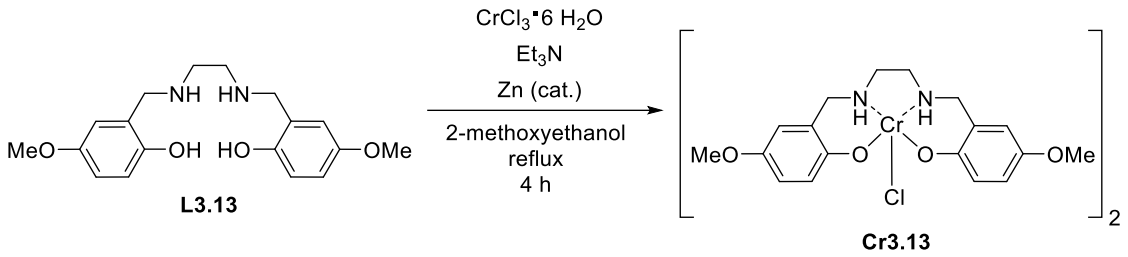

Cr3.13 was prepared according to the procedure outlined in Section 3.8.3. The complex was isolated as a fine, dark violet powder.

m(**L3.13**) / g	*V*(Et_3N) / mL	*V*(2-methoxyethanol) / mL	*m*($CrCl_3 \cdot 6H_2O$) / g	Yield / g
3.58 (10.8 mmol)	3.00 (21.5 mmol)	50 + 50	2.87 (10.8 mmol)	2.39 (2.86 mmol, 53%)

FTIR, ν/cm^{-1}: 3201 w, 3142 m, 3058 w, 3008 w, 2922 m, 2863 w, 1594 m, 1564 w, 1477 s, 1447 s, 1356 w, 1333 w, 1270 s
MS (ESI+) *m/z*: 780.921 $[M\text{-}2Cl\text{+}OH]^+$, calc. 781.199.

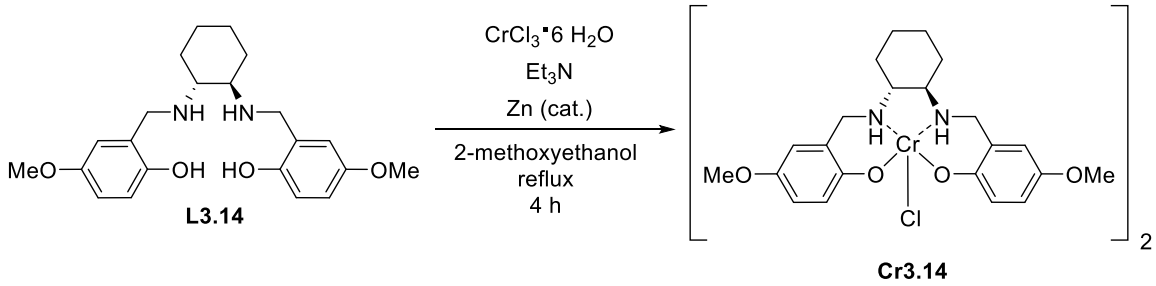

Cr3.14 was prepared according to the procedure outlined in Section 3.8.3. The complex was isolated as a fine, dark blue-green powder.

m(**L3.14**) / g	*V*(Et_3N) / mL	*V*(2-methoxyethanol) / mL	*m*($CrCl_3 \cdot 6H_2O$) / g	Yield / g
3.00 (7.76 mmol)	2.20 (15.8 mmol)	50 + 50	2.07 (7.76 mmol)	2.46 (2.61 mmol, 67%)

FTIR, ν/cm^{-1}: 3192 w, 3147 m, 3011 w, 2981 w, 2934 m, 2858 w, 2827 w, 1592 w, 1563 w, 1485 s, 1455 m, 1429 m, 1410 m, 1262 m, 1218 m, 1203 s
MS (ESI+) *m/z*: 889.051 $[M\text{-}2Cl\text{+}OH]^+$, calc. 889.293.

3.8.8. Optimization experiments performed by me

General procedure for screening experiments:

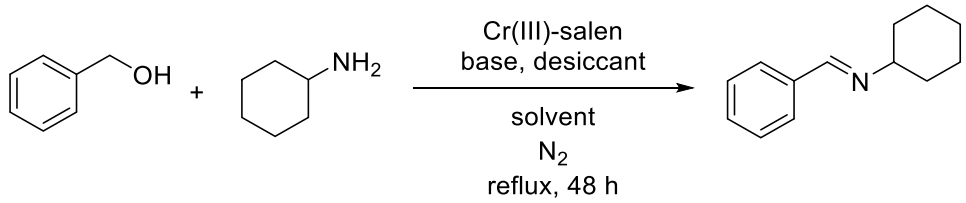

Cr(III)-catalyst and solid additives (bases or desiccants) were weighed into a flame-dried two-necked Schlenk flask equipped with a septum, a magnet and a cold finger. The flask was subjected to vacuum and N_2 refills (repeated three times). Freshly degassed solvent, benzyl alcohol (1.0 mmol), cyclohexylamine (1.0 mmol) and tetradecane (0.5 mmol) were added through the septum. The reaction mixture was heated to reflux and left stirring under a flow of N_2 for 48 hours. After 48 hours, the reaction mixture was cooled to room temperature, an aliquot of the reaction mixture (0.2 mL) was withdrawn through the septum and diluted to 1.0 mL with Et_2O. The sample was filtered through a nylon syringe filter (0.22 μm pore size) into a GC vial and subjected to GC-MS analysis to determine the yield of imine using a recently prepared calibration curve.

Table 3.11: Overview of all optimization experiments performed by me.

Entry[a]	Catalyst	Catalyst load (mol%)	Base	Base load (mol%)	Solvent	Solvent amount (mL)	Desiccant	Yield[b] (%)
NH1	**Cr3.1**	5	KOH	20	toluene	4	4Å MS	15
NH2	**Cr3.1**	5	KOtBu	20	toluene	4	4Å MS	18
NH3	**Cr3.1**	5	K_2CO_3	20	toluene	4	4Å MS	13
NH4	**Cr3.1**	5	Cs_2CO_3	20	toluene	4	4Å MS	14
NH5	**Cr3.1**	5	$CaCO_3$	20	toluene	4	4Å MS	11
NH6	**Cr3.1**	5	KOH	20	1,4-dioxane	4	4Å MS	<10
NH7	**Cr3.1**	5	KOtBu	20	1,4-dioxane	4	4Å MS	<10
NH8	**Cr3.1**	5	K_2CO_3	20	1,4-dioxane	4	4Å MS	<10
NH9	**Cr3.1**	5	Cs_2CO_3	20	1,4-dioxane	4	4Å MS	<10
NH10	**Cr3.1**	5	$CaCO_3$	20	1,4-dioxane	4	4Å MS	<10
NH11	**Cr3.1**	5	KOH	20	mesitylene	4	4Å MS	19
NH12	**Cr3.1**	5	KOtBu	20	mesitylene	4	4Å MS	23
NH13	**Cr3.1**	5	K_2CO_3	20	mesitylene	4	4Å MS	16
NH14	**Cr3.1**	5	Cs_2CO_3	20	mesitylene	4	4Å MS	21
NH15	**Cr3.1**	5	$CaCO_3$	20	mesitylene	4	4Å MS	19
NH16	**Cr3.4**	5	KOH	20	mesitylene	4	4Å MS	21
NH17	**Cr3.4**	5	KOtBu	20	mesitylene	4	4Å MS	24
NH18	**Cr3.4**	5	K_2CO_3	20	mesitylene	4	4Å MS	22
NH19	**Cr3.4**	5	Cs_2CO_3	20	mesitylene	4	4Å MS	23
NH20	**Cr3.4**	5	$CaCO_3$	20	mesitylene	4	4Å MS	18
NH21	**Cr3.1**	5	None	-	mesitylene	4	4Å MS	15
NH22	**Cr3.4**	5	None	-	mesitylene	4	4Å MS	16
NH23	**Cr3.2**	5	KOH	20	toluene	4	4Å MS	10
NH24	**Cr3.2**	5	KOtBu	20	toluene	4	4Å MS	11
NH25	**Cr3.2**	5	K_2CO_3	20	toluene	4	4Å MS	<10
NH26	**Cr3.2**	5	Cs_2CO_3	20	toluene	4	4Å MS	<10
NH27	**Cr3.2**	5	$CaCO_3$	20	toluene	4	4Å MS	<10
NH28	**Cr3.2**	5	None	-	toluene	4	4Å MS	<10
NH29	**Cr3.4**	5	KOH	20	toluene	4	4Å MS	<10
NH30	**Cr3.4**	5	KOtBu	20	toluene	4	4Å MS	13
NH31	**Cr3.4**	5	K_2CO_3	20	toluene	4	4Å MS	<10
NH32	**Cr3.4**	5	Cs_2CO_3	20	toluene	4	4Å MS	11
NH33	**Cr3.4**	5	$CaCO_3$	20	toluene	4	4Å MS	<10
NH34	**Cr3.4**	5	None	-	toluene	4	4Å MS	<10

[a]Conditions: BnOH (1.0 mmol), CyNH2 (1.0 mmol), tetradecane (0.5 mmol, IS), reflux, 48 h. [b]GC-MS yield

NH35	**Cr3.2**	5	KOtBu	20	1,4-dioxane	4	4Å MS	<10
NH36	**Cr3.2**	5	K_2CO_3	20	1,4-dioxane	4	4Å MS	<10
NH37	**Cr3.2**	5	Cs_2CO_3	20	1,4-dioxane	4	4Å MS	<10
NH38	**Cr3.4**	5	KOtBu	20	1,4-dioxane	4	4Å MS	<10
NH39	**Cr3.4**	5	K_2CO_3	20	1,4-dioxane	4	4Å MS	<10
NH40	**Cr3.4**	5	Cs_2CO_3	20	1,4-dioxane	4	4Å MS	<10
NH41[c]	**Cr3.2**	5	KOtBu	20	mesitylene	4	4Å MS	25
NH42[c]	**Cr3.2**	5	K_2CO_3	20	mesitylene	4	4Å MS	23
NH43	**Cr3.2**	5	Cs_2CO_3	20	mesitylene	4	4Å MS	26
NH44	**Cr3.2**	5	KOtBu	20	mesitylene	4	4Å MS	24
NH45	**Cr3.2**	5	K_2CO_3	20	mesitylene	4	4Å MS	19
NH46	**Cr3.2**	5	Cs_2CO_3	20	mesitylene	4	None	19
NH47[c]	**Cr3.2**	5	KOtBu	20	mesitylene	4	None	27
NH48[c]	**Cr3.2**	5	K_2CO_3	20	mesitylene	4	None	26
NH49	**Cr3.2**	5	KOtBu	20	mesitylene	4	None	24
NH50	**Cr3.2**	5	K_2CO_3	20	mesitylene	4	None	16
NH51	**Cr3.2**	5	None	-	mesitylene	4	4Å MS	11
NH52	**Cr3.2**	5	None	-	mesitylene	4	None	<10
NH53	**Cr3.2**	5	KOtBu	20	mesitylene	6	4Å MS	22
NH54	**Cr3.2**	5	KOtBu	20	mesitylene	6	$MgSO_4$ (0.5 eq.)	19
NH55	**Cr3.2**	5	KOtBu	50	mesitylene	6	4Å MS	26
NH56	**Cr3.2**	5	KOtBu	20	mesitylene	3	4Å MS	23
NH57	**Cr3.2**	5	KOtBu	20	toluene	6	4Å MS	16
NH58	**Cr3.2**	5	KOtBu	20	toluene	6	$MgSO_4$ (0.5 eq.)	14
NH59	**Cr3.2**	5	KOtBu	50	toluene	6	4Å MS	18
NH60	**Cr3.2**	5	KOtBu	20	toluene	3	4Å MS	19
NH61	**Cr3.2**	5	KOtBu	20	1,4-dioxane	6	4Å MS	<10
NH62	**Cr3.2**	5	KOtBu	20	1,4-dioxane	6	$MgSO_4$ (0.5 eq.)	<10
NH63	**Cr3.2**	5	KOtBu	50	1,4-dioxane	6	4Å MS	<10
NH64	**Cr3.2**	5	KOtBu	20	1,4-dioxane	3	4Å MS	<10
NH65	**Cr3.11**	5	KOtBu	20	mesitylene	4	4Å MS	<10

[a]Conditions: BnOH (1.0 mmol), CyNH2 (1.0 mmol), tetradecane (0.5 mmol, IS), reflux, 48 h. [b]GC-MS yield. [c]20mol% 18-crown-6 was also added.

NH66[d]	**Cr3.11**	5	KOtBu	20	mesitylene	4	4Å MS	<10
NH67	**Cr3.12**	5	None	-	mesitylene	4	4Å MS	<10
NH68	**Cr3.12**	5	Et_3N	100	mesitylene	4	4Å MS	<10
NH69	**Cr3.12**	5	DMAP	100	mesitylene	4	4Å MS	<10
NH70[d]	**Cr3.12**	5	Et_3N	100	mesitylene	4	4Å MS	<10
NH71	**Cr3.12**	5	KHMDS	15	mesitylene	4	4Å MS	<10
NH72	**Cr3.12**	5	KOtBu	15	mesitylene	4	4Å MS	<10
NH73	**Cr3.12**	5	NaOtBu	15	mesitylene	4	4Å MS	<10
NH74	**Cr3.12**	5	Cs_2CO_3	15	mesitylene	4	4Å MS	<10
NH75	**Cr3.13**	5	KOtBu	15	mesitylene	4	4Å MS	<10
NH76	**Cr3.12**	5	KOtBu	20	DMF	4	4Å MS	<10
NH77	**Cr3.12**	5	KOtBu	20	DMF	4	Na_2SO_4 (0.5 eq.)	<10
NH78	**Cr3.12**	5	$Ca(OH)_2$	20	DMF	4	4Å MS	<10
NH79	**Cr3.12**	5	Cs_2CO_3	20	DMF	4	4Å MS	<10
NH80	**Cr3.11**	5	KOtBu	20	pyridine	4	4Å MS	<10
NH81	**Cr3.12**	5	KOtBu	20	pyridine	4	4Å MS	<10
NH82	**Cr3.12**	5	KOtBu	50	mesitylene	4	4Å MS	<10
NH83	**Cr3.12**	5	KOtBu	20	toluene	4	4Å MS	<10
NH84	**Cr3.12**	5	KOtBu	50	toluene	4	4Å MS	<10
NH85	**Cr3.5**	5	KOtBu	20	toluene	4	4Å MS	13
NH86	**Cr3.5**	5	KOtBu	50	toluene	4	4Å MS	11
NH87	**Cr3.5**	5	KOtBu	20	mesitylene	4	4Å MS	18
NH88	**Cr3.5**	5	KOtBu	50	mesitylene	4	4Å MS	20
NH89	**Cr3.14**	5	None	-	mesitylene	4	4Å MS	<10
NH90	**Cr3.14**	5	DMAP	5	mesitylene	4	4Å MS	<10
NH91	**Cr3.14**	5	KOtBu	20	mesitylene	4	4Å MS	<10
NH92	**Cr3.14**	5	KOtBu	50	mesitylene	4	4Å MS	<10
NH93	**Cr3.14**	5	$Ca(OH)_2$	20	mesitylene	4	4Å MS	<10
NH94	**Cr3.14**	5	Ca_3N_2	20	mesitylene	4	4Å MS	<10
NH95	**Cr3.6**	5	$Ca(OH)_2$	20	mesitylene	4	4Å MS	19
NH96	**Cr3.6**	5	Ca_3N_2	20	mesitylene	4	4Å MS	23
NH97	**Cr3.7**	5	$Ca(OH)_2$	20	mesitylene	4	4Å MS	21
NH98	**Cr3.7**	5	Ca_3N_2	20	mesitylene	4	4Å MS	25
NH99	**Cr3.7**	5	KOtBu	20	mesitylene	4	4Å MS	25
NH100	**Cr3.7**	5	Cs_2CO_3	20	mesitylene	4	4Å MS	23
NH101	**Cr3.1**	5	$Ca(OH)_2$	20	mesitylene	4	4Å MS	23
NH102	**Cr3.1**	5	Ca_3N_2	20	mesitylene	4	4Å MS	24
NH103	**Cr3.1**	5	KOtBu	20	mesitylene	4	4Å MS	25
NH104	**Cr3.1**	5	NaOtBu	20	mesitylene	4	4Å MS	23
NH105	**Cr3.7**	5	KOtBu	20	mesitylene	4	$MgSO_4$ (1.0 eq.)	24

[a]Conditions: BnOH (1.0 mmol), CyNH2 (1.0 mmol), tetradecane (0.5 mmol, IS), reflux, 48 h. [b]GC-MS yield. [d]10mol% DMAP was also added.

NH106	**Cr3.7**	5	KOtBu	20	mesitylene	4	Na_2SO_4 (1.0 eq.)	22
NH107	**Cr3.1**	5	KOtBu	20	mesitylene	4	$MgSO_4$ (1.0 eq.)	25
NH108	**Cr3.1**	5	KOtBu	20	mesitylene	4	Na_2SO_4 (1.0 eq.)	23
NH109	**Cr3.1**	10	DBU	100	mesitylene	4	4Å MS	18
NH110	**Cr3.1**	10	Ca_3N_2	100	mesitylene	4	4Å MS	29
NH111	**Cr3.1**	10	KOtBu	100	mesitylene	4	4Å MS	26
NH112	**Cr3.14**	10	Ca_3N_2	100	mesitylene	4	4Å MS	11
NH113	**Cr3.14**	10	Ca_3N_2	150	mesitylene	4	4Å MS	13
NH114	**Cr3.14**	10	Ca_3N_2	200	mesitylene	4	4Å MS	10
NH115	**Cr3.1**	10	Ca_3N_2	50	mesitylene	4	4Å MS	27
NH116	**Cr3.1**	10	Mg_3N_2	50	mesitylene	4	4Å MS	24
NH117	**Cr3.1**	10	Li_3N	50	mesitylene	4	4Å MS	22
NH118	**Cr3.9**	10	Li_3N	50	mesitylene	4	4Å MS	18
NH119	**Cr3.9**	10	Li_3N	100	mesitylene	4	4Å MS	20
NH120	**Cr3.9**	10	Li_3N	150	mesitylene	4	4Å MS	16
NH121	**Cr3.9**	10	Ca_3N_2	50	mesitylene	4	4Å MS	22
NH122	**Cr3.9**	10	CaO	50	mesitylene	4	4Å MS	16
NH123	**Cr3.2**	10	Ca_3N_2	100	mesitylene	4	4Å MS	27
NH124	**Cr3.2**	10	Li_3N	33	mesitylene	4	4Å MS	24
NH125	**Cr3.3**	10	KOtBu	20	mesitylene	4	4Å MS	22
NH126	**Cr3.3**	10	KOtBu	50	mesitylene	4	4Å MS	19
NH127	**Cr3.3**	10	KOtBu	100	mesitylene	4	4Å MS	24
NH128[e]	**Cr3.3**	10	None	-	mesitylene	4	4Å MS	13
NH129[e]	**Cr3.3**	10	DBU	100	mesitylene	4	4Å MS	18
NH130[e]	**Cr3.3**	10	Ca_3N_2	100	mesitylene	4	4Å MS	27
NH131	**Cr3.1**	5	KOtBu	50	1,4-dioxane	0.5	None	<10

[a]Conditions: BnOH (1.0 mmol), CyNH2 (1.0 mmol), tetradecane (0.5 mmol, IS), reflux, 48 h. [b]GC-MS yield. [e]10mol% $Al(OTf)_3$ was also added.

3.8.9. Table of optimization experiments performed by SLHP

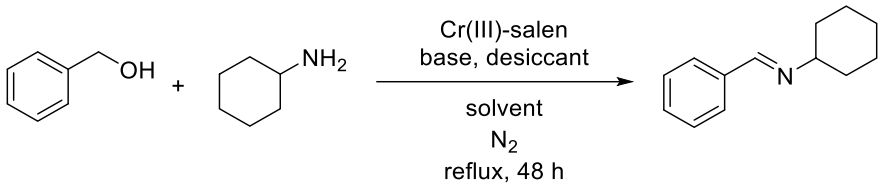

Table 3.12: Overview of all optimization experiments performed by SLHP.

Entry[a]	Catalyst	Catalyst load (mol%)	Base	Base load (mol%)	Solvent	Solvent amount (mL)	Desiccant	Yield[b] (%)
SP1	**Cr3.10**	5	Ca_3N_2	16.7	mesitylene	4	4Å MS	<10
SP2	**Cr3.10**	5	Ca_3N_2	50	mesitylene	4	4Å MS	<10
SP3	**Cr3.10**	5	Ca_3N_2	75	mesitylene	4	4Å MS	<10
SP4	**Cr3.10**	5	Ca_3N_2	100	mesitylene	4	4Å MS	<10
SP5	**Cr3.8**	5	Ca_3N_2	16.7	mesitylene	4	4Å MS	<10
SP6	**Cr3.8**	5	Ca_3N_2	50	mesitylene	4	4Å MS	<10
SP7	**Cr3.8**	5	Ca_3N_2	75	mesitylene	4	4Å MS	<10
SP8	**Cr3.8**	5	Ca_3N_2	100	mesitylene	4	4Å MS	<10
SP9	**Cr3.1**	10	Ca_3N_2	16.7	mesitylene	4	4Å MS	14
SP10	**Cr3.1**	10	Ca_3N_2	50	mesitylene	4	4Å MS	23
SP11	**Cr3.1**	10	Ca_3N_2	100	mesitylene	4	4Å MS	30
SP12	**Cr3.1**	10	Ca_3N_2	133	mesitylene	4	4Å MS	31
SP13	**Cr3.1**	10	Ca_3N_2	167	mesitylene	4	4Å MS	33
SP14	**Cr3.1**	10	Li_3N	50	mesitylene	4	4Å MS	27
SP15	**Cr3.1**	10	Li_3N	100	mesitylene	4	4Å MS	19
SP16	**Cr3.1**	10	Mg_3N_2	50	mesitylene	4	4Å MS	15
SP17	**Cr3.1**	10	Mg_3N_2	100	mesitylene	4	4Å MS	16
SP18	**Cr3.2**	10	Ca_3N_2	50	mesitylene	4	4Å MS	12
SP19	**Cr3.2**	10	Ca_3N_2	100	mesitylene	4	4Å MS	15
SP20	**Cr3.2**	10	Mg_3N_2	50	mesitylene	4	4Å MS	<10
SP21	**Cr3.2**	10	Mg_3N_2	100	mesitylene	4	4Å MS	12
SP22	**Cr3.3**	10	Ca_3N_2	50	mesitylene	4	4Å MS	17
SP23	**Cr3.3**	10	Ca_3N_2	100	mesitylene	4	4Å MS	20
SP24	**Cr3.3**	10	Mg_3N_2	50	mesitylene	4	4Å MS	13
SP25	**Cr3.3**	10	Mg_3N_2	100	mesitylene	4	4Å MS	14
SP26	**Cr3.9**	10	Ca_3N_2	50	mesitylene	4	4Å MS	16
SP27	**Cr3.9**	10	Ca_3N_2	100	mesitylene	4	4Å MS	18
SP28	**Cr3.12**	10	Ca_3N_2	50	mesitylene	4	4Å MS	<10
SP29	**Cr3.12**	10	Ca_3N_2	100	mesitylene	4	4Å MS	<10
SP30	**Cr3.13**	10	Ca_3N_2	50	mesitylene	4	4Å MS	<10
SP31	**Cr3.13**	10	Ca_3N_2	100	mesitylene	4	4Å MS	<10
SP32	**Cr3.10**	5	KOtBu	20	mesitylene	4	4Å MS	14

[a]Conditions: BnOH (1.0 mmol), CyNH2 (1.0 mmol), tetradecane (0.5 mmol, IS), reflux, 48 h. [b]GC-MS yield.

SP33	**Cr3.10**	5	NaOtBu	20	mesitylene	4	4Å MS	18
SP34	**Cr3.8**	5	KOtBu	20	mesitylene	4	4Å MS	<10
SP35	**Cr3.8**	5	NaOtBu	20	mesitylene	4	4Å MS	<10
SP36	**Cr3.1**	10	KOtBu	20	mesitylene	4	4Å MS	18
SP37	**Cr3.1**	10	KOtBu	100	mesitylene	4	4Å MS	22
SP38	**Cr3.1**	10	NaOtBu	20	mesitylene	4	4Å MS	15
SP39	**Cr3.1**	10	NaOtBu	100	mesitylene	4	4Å MS	17
SP40	**Cr3.1**	10	CaO	100	mesitylene	4	4Å MS	12
SP41	**Cr3.1**	10	DBU	50	mesitylene	4	4Å MS	13
SP42	**Cr3.1**	10	DBU	100	mesitylene	4	4Å MS	14
SP43	**Cr3.3**	10	DBU	50	mesitylene	4	4Å MS	11
SP44	**Cr3.3**	10	DBU	100	mesitylene	4	4Å MS	10
SP45	**Cr3.1**	10	$Ca(OH)_2$	25	mesitylene	4	4Å MS	13
SP46	**Cr3.1**	10	$Ca(OH)_2$	50	mesitylene	4	4Å MS	13
SP47	**Cr3.1**	10	$Ca(OH)_2$	100	mesitylene	4	4Å MS	17
SP48	**Cr3.1**	10	$Ca(OH)_2$	150	mesitylene	4	4Å MS	14
SP49	**Cr3.1**	10	NaOH	25	mesitylene	4	4Å MS	<10
SP50	**Cr3.1**	10	NaOH	50	mesitylene	4	4Å MS	<10
SP51	**Cr3.1**	10	NaOH	100	mesitylene	4	4Å MS	14
SP52	**Cr3.1**	10	NaOH	150	mesitylene	4	4Å MS	14
SP53	**Cr3.1**	10	KOH	25	mesitylene	4	4Å MS	<10
SP54	**Cr3.1**	10	KOH	50	mesitylene	4	4Å MS	19
SP55	**Cr3.1**	10	KOH	100	mesitylene	4	4Å MS	17
SP56	**Cr3.1**	10	KOH	150	mesitylene	4	4Å MS	18
SP57	**Cr3.10**	5	NaOtBu	20	mesitylene	4	4Å MS	18
SP58	**Cr3.10**	5	$Ca(OH)_2$	20	mesitylene	4	4Å MS	<10
SP59	**Cr3.10**	5	Cs_2CO_3	20	mesitylene	4	4Å MS	15
SP60	**Cr3.10**	5	KOtBu	20	mesitylene	4	4Å MS	14
SP61	**Cr3.10**	5	NaOtBu	20	mesitylene	4	$MgSO_4$ (1.0 eq.)	12
SP62	**Cr3.10**	5	NaOtBu	20	mesitylene	4	$MgSO_4$ (2.0 eq.)	11
SP63	**Cr3.10**	5	NaOtBu	20	mesitylene	4	K_2CO_3 (1.0 eq.)	16
SP64	**Cr3.10**	5	NaOtBu	20	mesitylene	4	K_2CO_3 (2.0 eq.)	17
SP65	**Cr3.1**	10	KOtBu	100	mesitylene	4	$MgSO_4$ (1.0 eq.)	16
SP66	**Cr3.1**	10	KOtBu	100	mesitylene	4	K_2CO_3 (1.0 eq.)	17
SP67	**Cr3.1**	10	Ca_3N_2	100	mesitylene	4	4Å MS	29
SP68	**Cr3.1**	10	Ca_3N_2	100	mesitylene	4	4Å MS	30
SP69	**Cr3.1**	10	KOH	50	mesitylene	4	4Å MS	19

[a]Conditions: BnOH (1.0 mmol), CyNH2 (1.0 mmol), tetradecane (0.5 mmol, IS), reflux, 48 h. [b]GC-MS yield.

SP70	**Cr3.1**	10	KOH	100	mesitylene	4	4Å MS	17
SP71	**Cr3.1**	10	KOH	50	mesitylene	4	4Å MS	21
SP72	**Cr3.1**	10	KOH	100	mesitylene	4	4Å MS	24
SP73	**Cr3.1**	10	KOtBu	50	mesitylene	4	4Å MS	18
SP74	**Cr3.1**	10	KOtBu	100	mesitylene	4	4Å MS	22
SP75	**Cr3.1**	10	KOtBu	50	mesitylene	4	4Å MS	19
SP76	**Cr3.1**	10	KOtBu	100	mesitylene	4	4Å MS	24
SP77	**Cr3.1**	10	Ca_3N_2	100	mesitylene	2	4Å MS	17
SP78	**Cr3.1**	10	Ca_3N_2	100	mesitylene	4	4Å MS	28
SP79	**Cr3.1**	10	Ca_3N_2	100	mesitylene	6	4Å MS	11
SP80	**Cr3.1**	10	Ca_3N_2	100	*p*-cymene	4	4Å MS	18
SP81	**Cr3.1**	3	KOtBu	50	1,4-dioxane	0.5	4Å MS	<10

[a]Conditions: BnOH (1.0 mmol), CyNH2 (1.0 mmol), tetradecane (0.5 mmol, IS), reflux, 48 h. [b]GC-MS yield.

3.8.10. Mechanistic experiments with the Cr(III)-salen protocol

Gas evolution experiment:

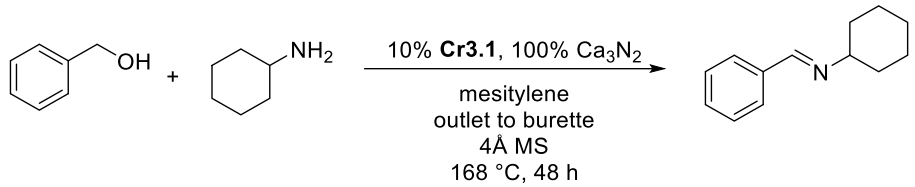

Chromium complex **Cr3.1** (35.0 mg, 0.05 mmol) and freshly activated molecular sieves (4Å, 150 mg) was weighed into a flame-dried two-necked Schlenk flask equipped with a septum, a magnet and a cold finger. The flask was subjected to vacuum and N_2 refills (repeated three times). Freshly degassed anhydrous mesitylene (4 mL), benzyl alcohol (1.0 mmol), cyclohexylamine (1.0 mmol) and tetradecane (0.5 mmol) were added through the septum. At this point, the stopcock of the Schlenk flask was closed, and the connection to the Schlenk line was replaced with vacuum tubing equipped with a syringe and needle at the end. The end of the needle was carefully placed at the opening of an inverted, water-filled burette residing in a water-filled crystallization bowl with a large surface area. The stopcock was reopened and all connections were rigorously reinforced with parafilm to avoid leakages. The reaction mixture was heated to reflux and gas evolution was gradually observed as the temperature rose due to thermal expansion of the dead volume of the Schlenk flask. As the reaction flask reached thermal equilibrium, the bubbling subsided and the initially displaced volume due to thermal expansion was read off the burette. At the 24-hour and 48-hour mark, the gas volume was noted and aliquots of the reaction mixture (0.2 mL) were withdrawn through the septum and diluted to 1.0 mL with Et_2O. The sample was filtered through a nylon syringe filter (0.22 µm pore size) into a GC vial and subjected to GC-MS analysis to determine the yield of imine using a recently prepared calibration curve.

The gas evolution experiment was repeated by SLHP to ensure reliable results and the gas volumes and GC-yields are reported in the table below:

Entry	$V_{0\,h}$ / mL	$V_{24\,h}$ / mL	$V_{48\,h}$ / mL	GC Yield (48 h, %)
1	13.8	13.7	13.7	27
2	11.8	11.8	11.8	19
3^{SLHP}	14.1	14.1	14.1	30

Determination of kinetic isotope effect:

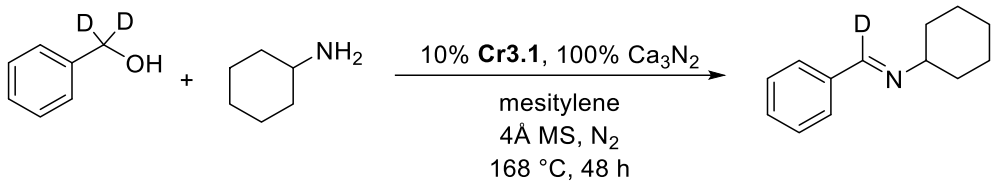

The determination of the kinetic isotope effect of the catalytic imine formation with **Cr3.1** was performed once by me and once by SLHP.

Cr3.1 (35.0 mg, 0.05 mmol) and freshly activated molecular sieves (4Å, 150 mg) was weighed into a flame-dried Schlenk flask equipped with a septum, a magnet and a cold finger. The flask was subjected to vacuum and N_2 refills (repeated three times). Freshly degassed solvent, benzyl alcohol (1.0 mmol), cyclohexylamine (1.0 mmol) and tetradecane (0.5 mmol) were added through the septum. The reaction mixture was heated to reflux and stirred under a flow of N_2. Every 2 hours, for a total of 31 hours (with an overnight break), an aliquot of the reaction mixture (0.2 mL) was taken out through the septum and diluted to 1.0 mL with Et_2O. The sample was filtered through a nylon syringe filter (0.22 µm pore size) into a GC vial and subjected to GC-MS analysis to follow the formation of *N*-benzylidenecyclohexylamine.

The same procedure was repeated using benzyl alcohol-α,α-*d*$_2$ (1.0 mmol) instead of non-deuterated benzyl alcohol. The rate of formation of *N*-benzylidenecyclohexylamine was determined in each experiment and the plot resulting from the experiment performed by me is shown in Figure 3.23 (Section 3.5.3). The plot resulting from the experiment performed by SLHP is shown in Figure 3.24 (Section 3.5.3). The experiment performed by me resulted in a kinetic isotope effect of k_H/k_D = 1.61. The experiment performed by SLHP resulted in a kinetic isotope effect of k_H/k_D = 1.56.

Hammett study:

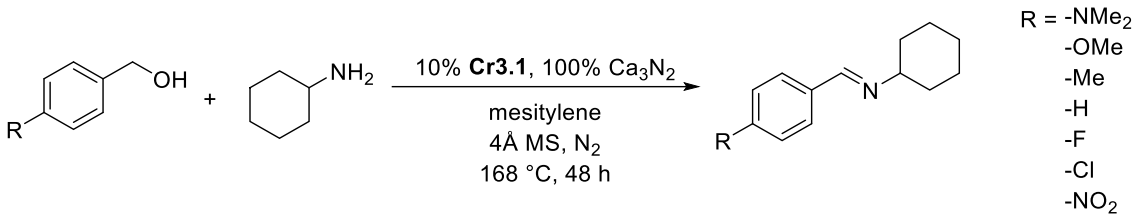

The Hammett study was performed by SLHP.

Cr3.1 (35.0 mg, 0.05 mmol) and freshly activated molecular sieves (4Å, 150 mg) were weighed into a flame-dried two-necked Schlenk flask equipped with a septum, a magnet and a cold finger. The flask was subjected to vacuum and N_2 refills (repeated three times). Freshly degassed anhydrous mesitylene (4 mL), benzyl alcohol (0.5 mmol), 4-substituted benzyl alcohol (0.5 mmol), cyclohexylamine (1.0 mmol) and tetradecane (0.5 mmol) were added. The reaction mixture was heated to reflux in an oil bath set to 168 °C and a GC-MS sample was prepared at 0, 2, 4, 6, 24, 28, 30, 32 and 48 hours. The sampling was done by withdrawing an aliquot (0.2 mL) through the septum followed by dilution to 1.0 mL with Et_2O. The sample was filtered through a nylon syringe filter (0.22 µm pore size) into a GC vial and subjected to GC-MS analysis to follow the formation of *N*-benzylidenecyclohexylamine and the 4-substituted *N*-benzylidenecyclohexylamine to determine k_{rel}. The plots used to determine k_{rel} are shown in Figure 3.53 – 3.58 in Section 3.8.11. The final Hammett plot is shown in Figure 3.26 in Section 3.5.4.

3.8.11. Plots of competition experiments for the Hammett study

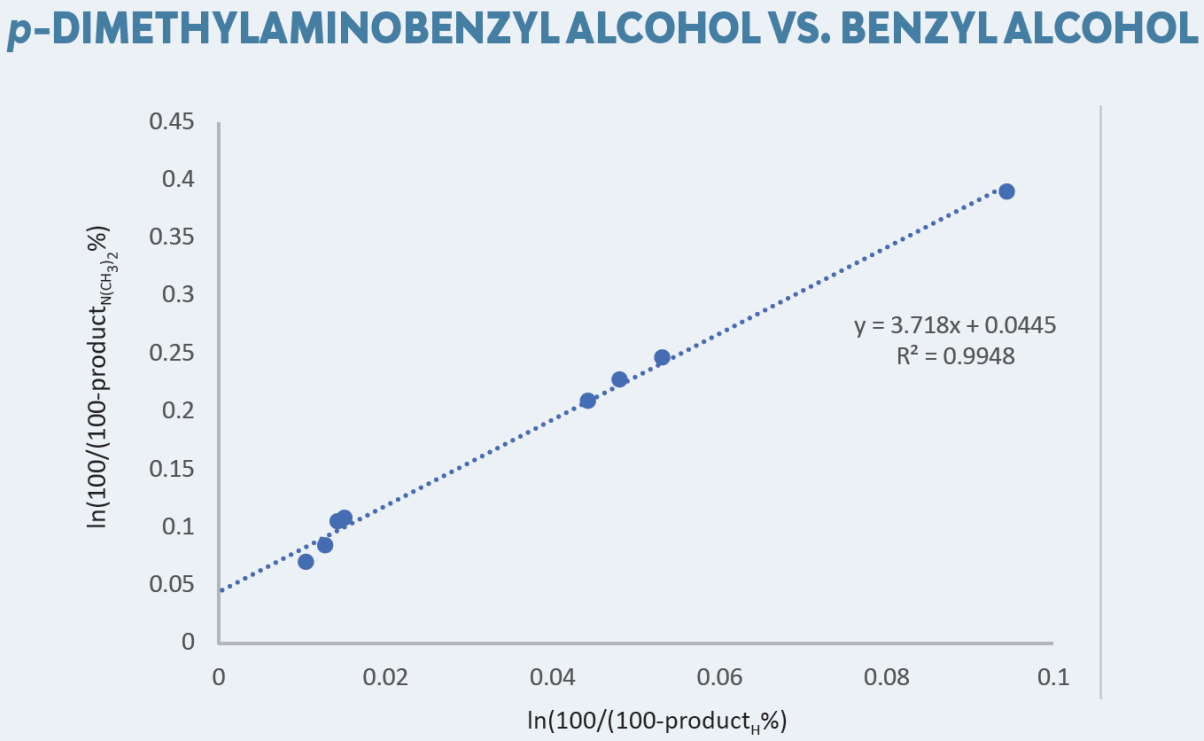

Figure 3.53: Competition experiment between *p*-dimethylaminobenzyl alcohol and benzyl alcohol. Adapted from reference.[205]

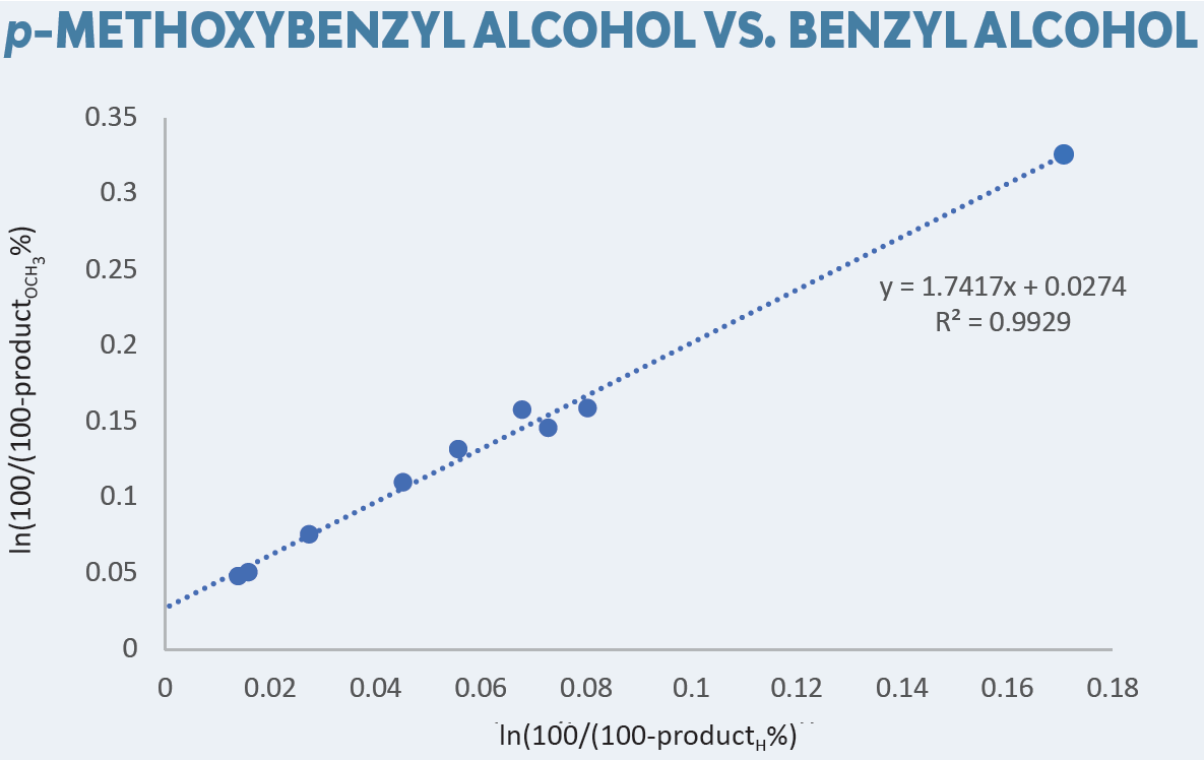

Figure 3.54: Competition experiment between *p*-methoxybenzyl alcohol and benzyl alcohol. Adapted from reference.[205]

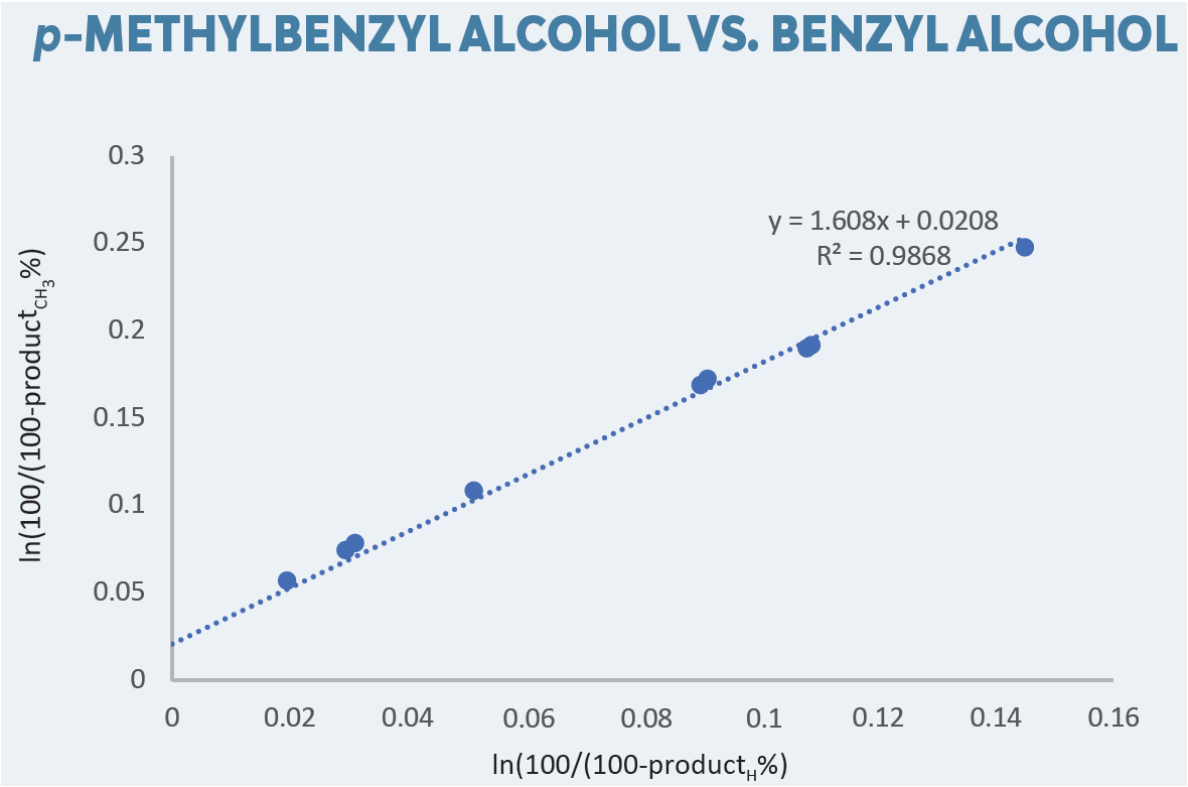

Figure 3.55: Competition experiment between *p*-methylbenzyl alcohol and benzyl alcohol. Adapted from reference.[205]

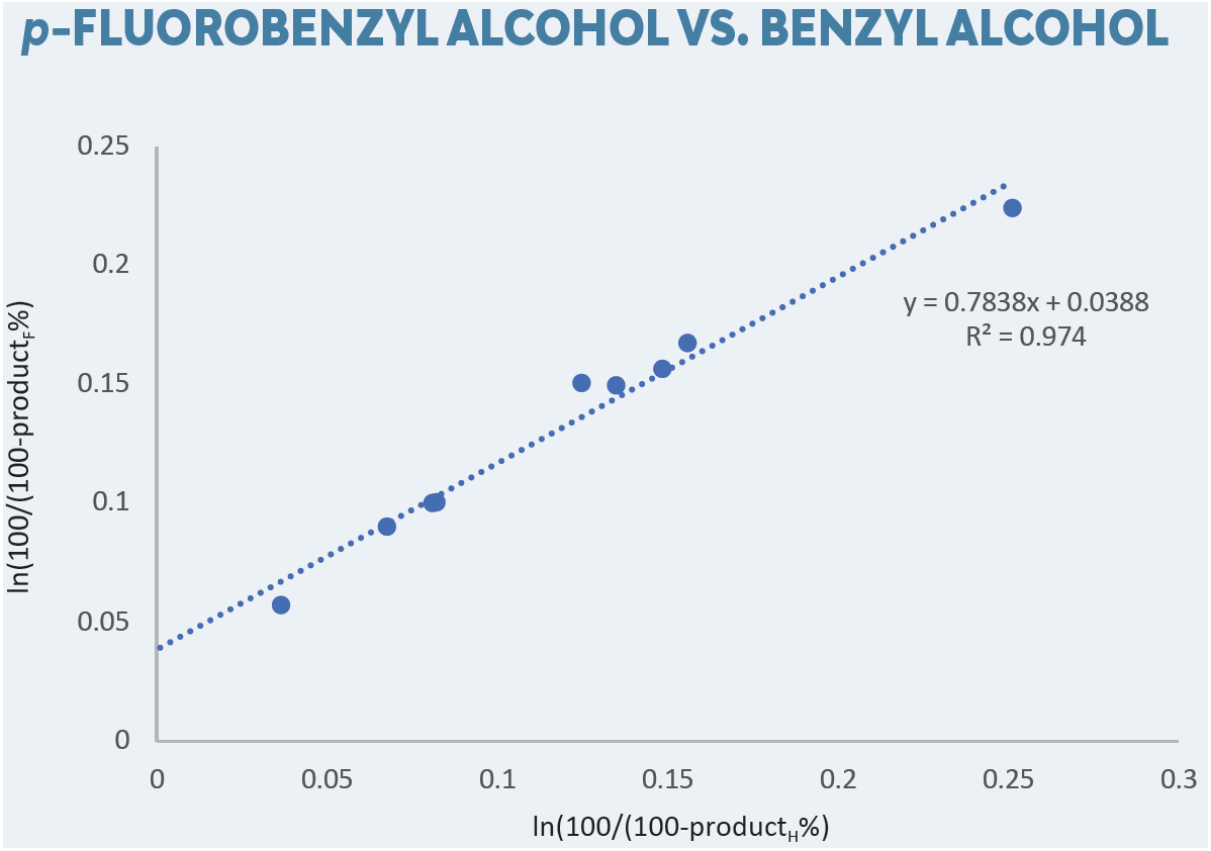

Figure 3.56: Competition experiment between *p*-fluorobenzyl alcohol and benzyl alcohol. Adapted from reference.[205]

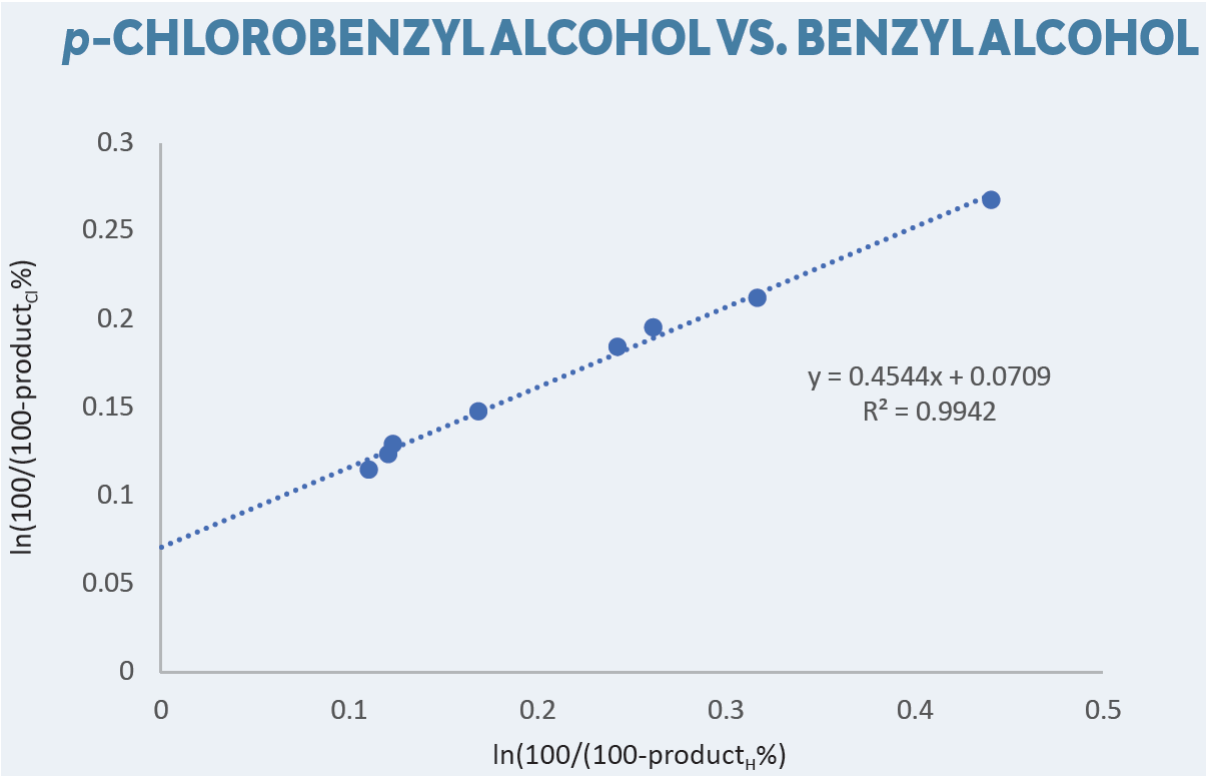

Figure 3.57: Competition experiment between *p*-chlorobenzyl alcohol and benzyl alcohol. Adapted from reference.[205]

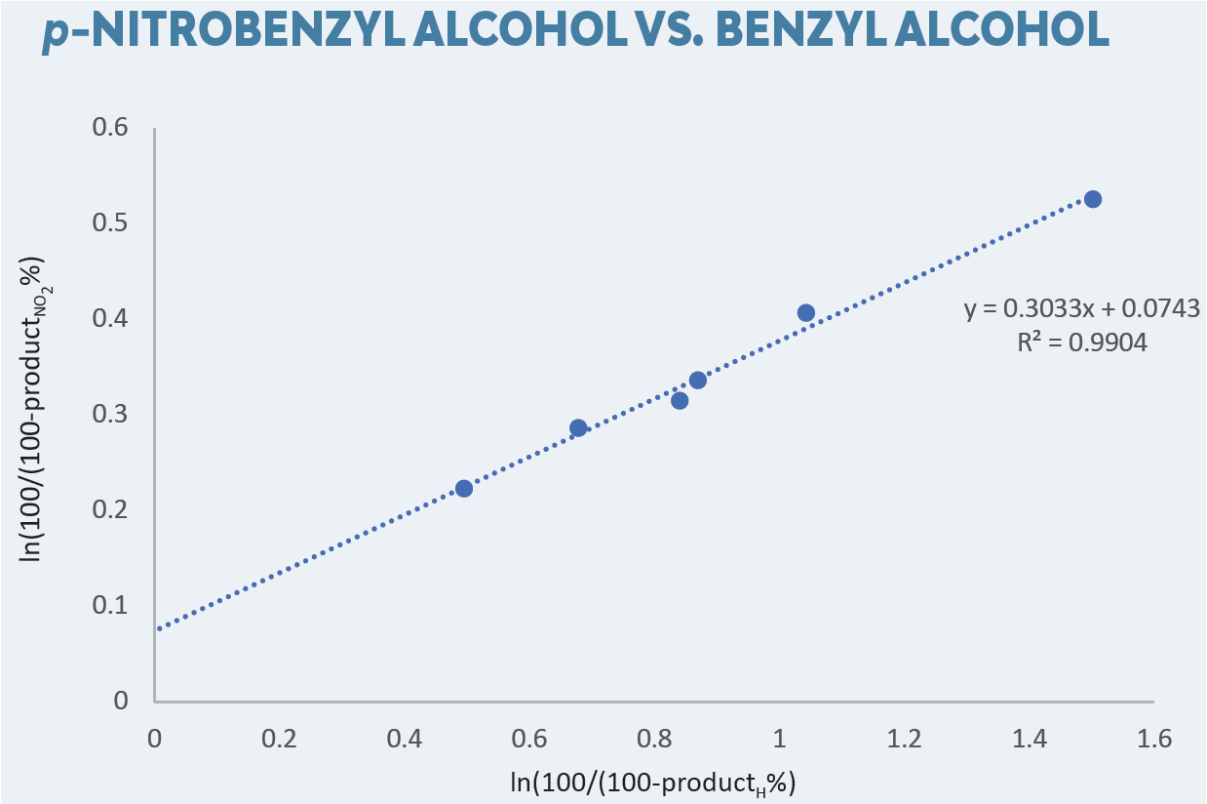

Figure 3.58: Competition experiment between *p*-nitrobenzyl alcohol and benzyl alcohol. Adapted from reference.[205]

3.8.12. Computational details

The initial DFT calculations used to investigate the coordination of benzyl alcohol or cyclohexylamine were performed with ORCA version 4.2.0.[119] All structures were optimized in the gas phase using the B3LYP-D3BJ[120,121,139] \\ def2-TZVP method[140] and unrestricted SCF spin treatment. For all Cr(III) containing structures, a high-spin quartet was assumed. The frequency and thermochemistry calculations were performed at the boiling point of mesitylene (T = 438 K) and at standard state (1 atm), which provided the Gibbs free energy, ΔG_{gas}, directly. The free energy of solvation for each structure was calculated at the B3LYP-D3BJ \\ def2-TZVP level using the SMD model[141] with the standard parameters for toluene. Finally, the solvated Gibbs free energy of each structure was calculated as $\Delta \underline{G}_{tot} = \Delta G_{gas} + \Delta G_{solv}$ and the binding energy of the additional axial ligand was calculated as $\Delta G_{bind} = \Delta G_{tot,\ 6coord} - (\Delta G_{tot,\ 5coord} + \Delta G_{tot,\ ligand})$.

The DFT calculations used to construct the models of the catalysis were performed with Jaguar (version 10.7, release 13) by Schrodinger LLC.[142] All structure optimizations were performed in the gas phase using the B3LYP-D3 method[120,121,143] and the LACVP** basis set. Unrestricted SCF spin treatment was used in all calculations and the multiplicity of all Cr(III) containing structures were assumed to be high-spin quartet. To simulate the experimental conditions, the frequency calculations were performed at the boiling point of mesitylene (438 K) and at standard state (1 atm). The frequencies were checked to ensure that intermediates had no imaginary frequencies and that transitions states had one imaginary frequency. The solvation free energy ΔG_{solv} of structures containing Cr(III) were calculated with the PBF solver in Jaguar using the standard parameters for toluene and the B3LYP-D3 \\ LACVP** method. Solvation free energies of benzyl alcohol, benzaldehyde and hydrogen were calculated using the SM8 model[144] and the B3LYP-D3 \\ 6-31G* method. To obtain more accurate electronic energies, the electronic energy of all complexes was recalculated with the larger basis set LACV3P**++. The final Gibbs free energy of the structures were calculated as the sum $\Delta G_{tot} = E(\text{LACVP3**++}) + \Delta G_{solv} + ZPE + \Delta H - T\Delta S$. In all cases, T was set to the boiling point of mesitylene (438 K).

The computational Hammett study was conducted by calculating the free energy difference ($\Delta G^{\ddagger}$) between the appropriate reactant and transition state using the methodology described above. This calculation was repeated with the appropriate 4-substituted benzyl alkoxide ligands. The ratio of the rate constants was subsequently calculated by $k_x / k_H = \text{EXP}[(\Delta G^{\ddagger}(H) - \Delta G^{\ddagger}(x)) / RT]$ with T = 438 K and R = 0.001987204 kcal K^{-1} mol^{-1}.

The theoretical kinetic isotope effects were calculated by performing frequency calculations on the relevant structures where the weights of the benzylic hydrogen atoms were set to 2. The thermochemistry calculated for the deuterium-containing structures was then employed in the calculation of the free energies using $\Delta G_{tot} = E(\text{LACVP3**++}) + \Delta G_{solv} + ZPE + \Delta H - T\Delta S$. From the calculated $\Delta G^{\ddagger}$(prot) and $\Delta G^{\ddagger}$(deut), the ratio k_H / k_D was calculated using $k_H / k_D = \text{EXP}[(\Delta G^{\ddagger}(\text{deut}) - \Delta G^{\ddagger}(\text{prot})) / RT]$ with T = 438 K and R = 0.001987204 kcal K^{-1} mol^{-1}.

3.8.13. Energies of structures

Table 3.13: Overview of structures and energies calculated in Jaguar.

	E (LACV3P**++)	ZPE	H	S	Solv
BnOH	-346.8832973	83.550	9.174	91.954	-4.494
PhCHO	-345.6767904	69.174	8.891	91.191	-4.014
H_2	-1.179569919	6.388	3.046	33.806	-1.561
Cr1	-1367.723484	273.222	35.382	220.338	-7.2261
Cr1_TS	-1367.678667	270.533	34.625	216.173	-7.0624
Cr2	-1367.694106	272.428	35.573	221.888	-6.9581
Cr3	-1368.912507	287.613	35.959	222.885	-6.9243
Cr3_TS	-1368.906321	286.024	35.513	220.691	-6.9668
Cr4	-1368.931053	288.34	36.081	224.046	-8.0433
Cr4_TS	-1368.887512	285.875	35.114	217.869	-7.8828
Cr5	-1368.901941	287.989	35.99	223.167	-7.7724
Cr6	-1023.18833	217.194	26.782	180.251	-9.4503
Cr7	-1370.119247	303.038	36.358	223.813	-7.2233
Cr7_TS	-1370.115529	301.642	35.809	221.274	-7.148
Cr8	-1370.14309	304.226	36.325	223.6	-8.3783
Cr8_TS	-1370.085339	300.536	36.058	222.158	-10.359
Cr9	-1024.391862	230.142	27.64	183.153	-10.711
Cr9_TS	-1024.354052	228.081	27.099	180.856	-8.7533
Cr10_TS	-1370.074566	297.733	36.105	222.236	-7.9754
Hammett_Cr4_NMe_2_react	-1502.940604	334.399	41.134	247.796	-8.2092
Hammett_Cr4_NMe_2_TS	-1502.901741	331.808	40.196	241.581	-8.5751
Hammett_Cr4_OMe_react	-1483.490869	308.915	39.045	238.096	-8.574
Hammett_Cr4_OMe_TS	-1483.449766	306.395	38.08	231.85	-8.8446
Hammett_Cr4_Me_react	-1408.260981	305.601	38.127	234.24	-8.1922
Hammett_Cr4_Me_TS	-1408.21854	303.101	37.149	227.731	-7.9945
Hammett_Cr4_F_react	-1468.201773	283.236	36.994	228.599	-8.3306
Hammett_Cr4_F_TS	-1468.157974	280.82	35.98	221.847	-8.3543
Hammett_Cr4_Cl_react	-1828.55772	282.376	37.335	230.962	-8.3114
Hammett_Cr4_Cl_TS	-1828.513712	279.946	36.333	224.24	-8.2246
Hammett_Cr4_NO_2_react	-1573.503305	290.255	38.807	237.921	-10.473
Hammett_Cr4_NO_2_TS	-1573.456307	287.797	37.88	231.874	-10.135
Hammett_Cr8_NMe_2_react	-1504.154318	350.265	41.376	246.894	-8.3272
Hammett_Cr8_NMe_2_TS	-1504.09881	346.228	41.208	246.914	-9.5087
Hammett_Cr8_OMe_react	-1484.703035	324.741	39.315	237.83	-9.0681
Hammett_Cr8_OMe_TS	-1484.648104	320.858	39.069	236.458	-10.509
Hammett_Cr8_Me_react	-1409.473214	321.426	38.408	233.888	-8.4082
Hammett_Cr8_Me_TS	-1409.417108	317.777	38.109	232.336	-9.5199
Hammett_Cr8_F_react	-1469.413401	299.091	37.254	228.193	-8.6414
Hammett_Cr8_F_TS	-1469.357032	295.427	37.018	227.017	-9.4307
Hammett_Cr8_Cl_react	-1829.769749	298.253	37.591	230.356	-8.6307

	E (LACV3P**++)	ZPE	H	S	Solv
Hammett_Cr8_Cl_TS	-1829.713493	294.569	37.371	229.286	-9.4089
Hammett_Cr8_NO_2_react	-1574.714694	306.018	39.119	237.046	-10.879
Hammett_Cr8_NO_2_TS	-1574.656489	302.398	38.911	236.593	-10.971
Cr1_Penta_react	-1311.102921	248.597	32.311	206.234	-6.9064
Cr1_Penta_TS	-1311.052046	246.031	31.507	201.167	-7.2266
Cr1_BnO_react	-1657.489235	325.273	41.843	249.629	-25.151
Cr1_BnO_TS	-1657.445591	322.086	41.18	245.312	-24.231
Cr4_Penta_react	-1312.313025	264.098	32.789	208.055	-7.3497
Cr4_Penta_TS	-1312.261679	261.513	32.021	203.372	-7.377
Cr4_BnO_react	-1658.706058	340.729	42.38	252.615	-23.991
Cr4_BnO_TS	-1658.66515	337.669	41.707	247.466	-23.154
Cr8_Penta_react	-1313.523004	279.814	33.256	210.053	-7.9097
Cr8_Penta_TS	-1313.45581	276.711	32.92	208.281	-7.9687
Cr8_BnO_react	-1659.925425	356.571	42.756	253.631	-23.425
Cr8_BnO_TS	-1659.871153	352.484	42.75	253.307	-24.073
Cr1_DiBr_react	-1419.176415	262.538	41.453	256.599	-9.4854
Cr1_DiBr_TS	-1419.13846	260.289	41.201	254.73	-8.5556
Cr1_DiCl_react	-3207.426241	264.43	41.245	252.114	-9.6548
Cr1_DiCl_TS	-3207.388074	262.049	40.228	245.549	-8.6481
Cr1_mCF_3_react	-2043.245603	294.716	44.169	263.479	-8.9326
Cr1_mCF_3_TS	-2043.201192	292.235	43.283	258.24	-8.8329
Cr1_mNMe_2_react	-1636.961404	380.746	46.144	270.901	-9.9044
Cr1_mNMe_2_TS	-1636.910851	377.871	45.384	266.743	-8.6534
Cr1_mNO_2_react	-1778.06682	291.819	41.595	251.104	-13.251
Cr1_mNO_2_TS	-1778.027383	289.547	40.678	245.975	-13.089
Cr1_mOMe_react	-1598.053151	329.286	42.128	252.905	-10.633
Cr1_mOMe_TS	-1598.009549	326.938	41.121	246.532	-9.629
Cr1_pNO_2_react	-1778.076155	292.226	41.655	252.679	-14.713
Cr1_pNO_2_TS	-1778.037716	289.828	40.668	246.51	-14.191
Cr1_pOMe_react	-1598.044769	329.154	42.157	253.318	-10.544
Cr1_pOMe_TS	-1598.000793	326.657	41.198	247.034	-9.7611
Cr8_DiBr_react	-1420.39209	278.463	42.55	261.2	-9.142
Cr8_DiBr_TS	-1420.334539	274.452	42.284	260.107	-10.082
Cr8_DiCl_react	-3208.641004	280.004	41.64	252.731	-9.6349
Cr8_DiCl_TS	-3208.584366	276.213	41.337	251.341	-10.432
Cr8_mCF_3_react	-2044.454763	310.557	44.56	264.322	-9.6841
Cr8_mCF_3_TS	-2044.398592	306.64	44.255	262.69	-10.414
Cr8_mNMe_2_react	-1638.165611	396.149	46.612	272.809	-8.9411
Cr8_mNMe_2_TS	-1638.111059	392.561	46.314	270.771	-9.8986
Cr8_mNO_2_react	-1779.281072	307.789	41.998	252.643	-13.537
Cr8_mNO_2_TS	-1779.225722	303.891	41.692	250.868	-14.412
Cr8_mOMe_react	-1599.264035	345.194	42.389	252.848	-10.234
Cr8_mOMe_TS	-1599.208576	341.52	42.12	251.246	-10.933

	E (LACV3P**++)	ZPE	H	S	Solv
Cr8_pNO$_2$_react	-1779.291956	308.13	41.95	252.648	-14.871
Cr8_pNO$_2$_TS	-1779.233859	304.127	41.629	250.931	-15.609
Cr8_pOMe_react	-1599.256748	345.096	42.408	253.134	-10.065
Cr8_pOMe_TS	-1599.199925	341.342	42.192	251.746	-11.081
Cr4_DiPhenyl_react	-1831.168164	390.648	48.011	277.088	-9.2159
Cr4_DiPhenyl_TS	-1831.131141	388.175	47.165	272.69	-8.2906
Cr4_Cyclohexyl_react	-1525.038268	347.437	40.688	243.211	-8.5322
Cr4_Cyclohexyl_TS	-1524.996218	344.967	39.824	238.37	-7.6813
Cr4_Phenylene_react	-1521.397911	302.82	39.019	236.285	-8.1117
Cr4_Phenylene_TS	-1521.358686	300.414	38.222	231.701	-8.0904
Cr8_DiPhenyl_react	-1832.38415	406.18	48.472	278.932	-8.2721
Cr8_DiPhenyl_TS	-1832.33087	402.798	48.317	278.581	-8.9627
Cr8_Cyclohexyl_react	-1526.251194	362.977	41.115	244.411	-7.0856
Cr8_Cyclohexyl_TS	-1526.196198	359.519	40.881	243.584	-8.3522
Cr8_Phenylene_react	-1522.598026	318.225	39.619	239.278	-9.5297
Cr8_Phenylene_TS	-1522.540748	314.554	39.29	237.442	-10.661
CrSalan_5Coord	-1313.530363	280.394	33.013	207.976	-8.4191
CrSalan_6Coord_CyNH$_2$	-1604.909544	400.633	43.376	254.223	-5.3917
CrSalan_Dimer	-2627.179123	563.637	66.084	354.722	-6.7014

The cartesian coordinates of all listed structures in Table 3.13 can be found by following the link or scanning the QR code below.

https://www.dropbox.com/sh/015kyuog5ukyk6v/AABZ8dMzXy9czautIaXKKiQna?dl=0

Chapter 4. Revisiting alcohol oxidation catalyzed by Chromium(III) Tetraphenylporphine Chloride

Abstract

In this chapter, the AAD protocol using the Cr(III)(TPP)Cl catalyst that was developed by Yulong Miao in the Madsen group has been revisited.[145] The energetics of the proposed reaction mechanism involving outer-sphere H^+/H^- transfer from benzyl alcohol to the CrTPP scaffold has been studied with density functional theory calculations. The best-case scenario with a neutral *N*-donor in the axial position results in an activation energy for the H^+/H^- transfer of 48.4 kcal mol^{-1}, which is prohibitively high. An alternative reaction mechanism relying on H^- transfer to the *meso*-position of the CrTPP scaffold is investigated with DFT, but barriers exceeding 42 kcal mol^{-1} are calculated for this mechanistic proposal.

Key experiments of the original paper have been repeated employing a two-necked Schlenk flask setup and careful exclusion of air. Imine yields in the range 60 – 86% were reported in the original paper, but imine yields ranging from 15 – 20% is observed in the repeat experiments. Additionally, no evolution of hydrogen during the reactions has been detected. Control experiments under an air atmosphere has revealed that aerobic oxidation can be a significant side reaction that also results in byproducts arising from oxidation of mesitylene. Examination of several old chromatograms tied to the original paper has revealed the presence of these byproducts, which indicates that presence of air may have led to erroneous conclusions in the original paper.

4.1. Introduction

The salen/salan ligand scaffold has not been the sole focus in the development of AAD catalysts in the Madsen group. Previously, Mn(III)(TPP)Cl, and derivatives thereof, were found to catalyze the dehydrogenative formation of *N*-benzylidenecyclohexylamine from benzyl alcohol and cyclohexylamine in refluxing mesitylene.[52] More recently, both V(IV)(TPP)Cl_2 and Cr(III)(TPP)Cl were reported as viable catalysts for the dehydrogenative synthesis of imines.[145] Catalysis with the V(IV)(TPP)Cl_2 catalyst was achieved in refluxing toluene (48 hours) using 5% catalyst loading and NaOH (20%) as additive.

Based on the difficulties of achieving adequate reactivity with the Cr(III)-salen based system, it was found surprising that the fairly similar Cr(III)(TPP)Cl catalyst was able to produce imines in >80% yield. The optimal conditions for the CrTPP catalyst were found to be 4% catalyst loading, no basic additives, and 48 hours of refluxing in mesitylene.[145] The kinetic isotope effect of the CrTPP catalyzed reaction was measured to 2.3 and the substrate scope included a wide range of benzylic alcohols. Further details can be found in the original paper.[145]

The proposed mechanism of the dehydrogenation catalyzed by the CrTPP scaffold is shown in Figure 4.1.

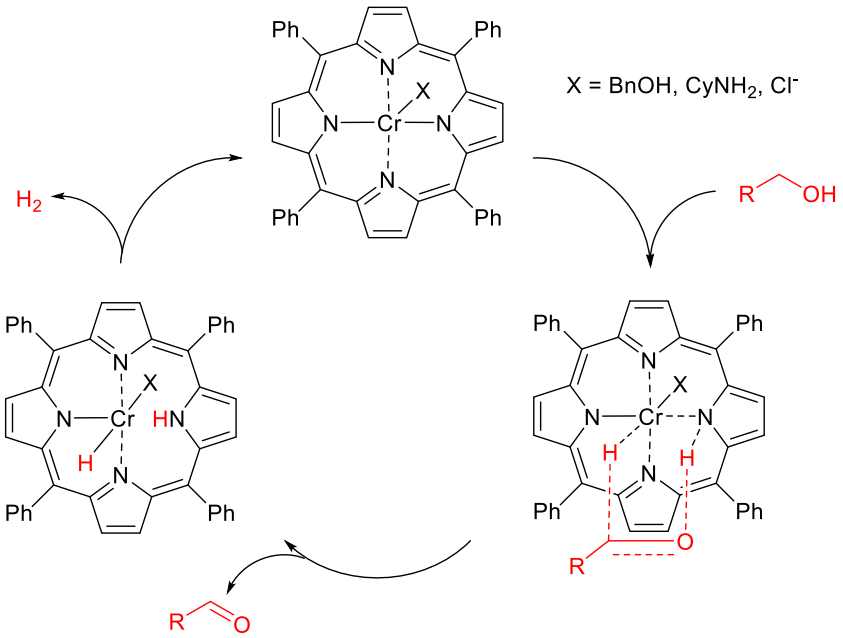

Figure 4.1: Proposed reaction mechanism for AAD with the CrTPP catalyst. The transfer of H^+ and H^- is hypothesized to be concerted as no metal alkoxide species were detected during catalysis. Adapted from reference.[145]

No evidence of metal alkoxide species were detected in either the V(IV) or Cr(III) case, and thus an outer-sphere mechanism with concerted transfer of the alcohol proton to the pyrrole moiety and hydride transfer to the metal center was proposed. The protonated pyrrole and the metal hydride would then release hydrogen gas (either directly or mediated by a proton shuttle) to close the catalytic cycle. In the proposed mechanism, the axial ligand X is hypothesized to be either cyclohexylamine, benzyl alcohol or chloride.

The striking difference in catalytic activity between the CrTPP and the Cr(III)-salen scaffold warranted further investigation. This was done computationally by calculating the energy profile of the proposed CrTPP catalytic cycle and comparing it to the energy profiles calculated for the Cr(III)-salen system. Before delving into the computational study, a short introduction to the structural aspects and catalytic applications of Cr(III)-porphyrin derivatives is given in the following sections.

4.1.1. Structural aspects of Cr(III)-porphyrin complexes

Unlike in the case of Cr(III)-salen and Cr(III)-salan, the possibility of isomerism in the CrTPP ligand scaffold is limited due to the high rigidity of the aromatic ligand. A structural search in the CCDC revealed that all deposited structures of Cr(III)-porphyrin derivatives exhibit octahedral coordination geometry with the *N*-donors of the porphyrin in the same plane and two ligands occupying the axial positions.[219] An example of this geometry is shown in Figure 4.2, where the CrTPP scaffold is axially coordinated by a phenolate and a THF ligand.[220]

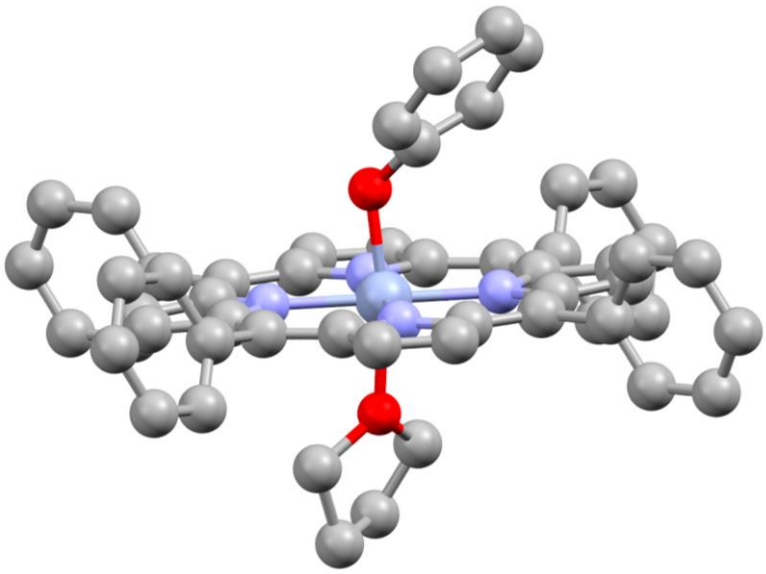

Figure 4.2: Crystal structure of Cr(III)TPP with a phenolate and THF as axial ligands.[220]

The structure of the Cr(III)(TPP)Cl complex has also been studied in solution, where very strong preference for octahedral coordination was found.[221] Furthermore, neutral *N*-donor ligands were found to bind more strongly than neutral *O*- or *S*-donor ligands.[221] These experimental observations are valuable when constructing reliable DFT models of reactions that may be catalyzed by the Cr(III)-porphyrin scaffold.

4.1.2. Catalysis with Cr(III)-porphyrin complexes

Cr(III)-porphyrin derivatives have been used as catalysts for a variety of reactions. Indeed, the similarities between the salen and porphyrin scaffold are reflected in their catalytic applications. Like the Cr(III)-salen scaffold, the Cr(III)-porphyrin scaffold has been used as catalysts for epoxidation of alkenes (Figure 4.3 **a**)[222,223] and coupling of CO_2 and epoxides to form cyclic carbonates or polymers (Figure 4.3 **b**).[224,225] Furthermore, the Cr(III)-porphyrin scaffold has been used as catalyst for the Claisen rearrangement of allyl vinyl ethers (Figure 4.3 **c**)[226] and in the synthesis of phenanthrenes by dehydration cycloaromatization (Figure 4.3 **d**).[227] Figure 4.3 provides an overview of the mentioned transformations catalyzed by the Cr(III)-porphyrin scaffold.

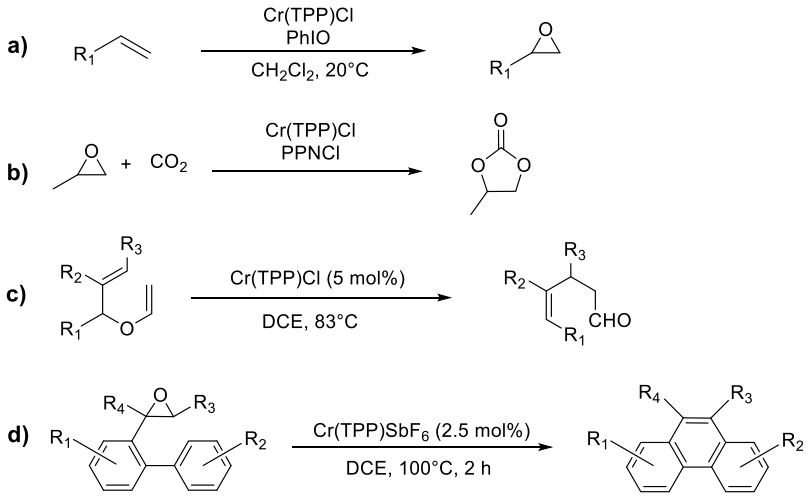

Figure 4.3: Overview of catalytic reactions with the Cr(TPP) catalysts. **a)** Alkene epoxidation with *in situ* generated oxochromium(V).[222] **b)** Synthesis of cyclic carbonates from epoxides and CO_2.[224] **c)** Claisen rearrangement of allyl vinyl ethers.[226] **d)** Synthesis of phenanthrenes by dehydration cycloaromatization.[227]

Evidently, the Cr(III)-porphyrin scaffold has been applied in catalytic transformations, but for oxidation reactions, an external oxidant is typically required.[228] Furthermore, the various reaction mechanisms typically rely on the Lewis acidity of the Cr(III) center and the porphyrin scaffold merely acts as a spectator, stabilizing the Cr(III). Consequently, no examples of metal-ligand cooperativity have been found in the literature of Cr(III)-porphyrin catalysis prior to the AAD paper published by the Madsen group.[145] The general absence of mechanisms involving metal-ligand cooperativity of Cr(III)-porphyrins is in line with my notion of the porphyrin scaffold as a chemically inert scaffold, at least when complexed to Cr(III). Due to the aromaticity of the scaffold, addition of electrophiles or nucleophiles to the ligand is generally not energetically favorable, and the pyrrole nitrogens in Cr(III)-porphyrin derivatives are notoriously difficult to protonate due to their strong interaction with the Cr(III)-center. For example, a study found no indication of protolytic demetallation of a Cr(III)-porphyrin derivative examined by UV-VIS at pH = 7, 4, 3, 2 and 1[229] and Cr(III)(TPP)Cl is attributed the highest stability index, showing incomplete demetallation in conc. sulfuric acid.[230] For future reference, the first and second pK_a, values for the dissociation of protons from two ligated water molecules from a Cr(III)-porphyrin were found to be $pK_{a1} = 9.4$ and $pK_{a1} = 12.4$, respectively.[231]

Based on these reports, the protonation of the pyrrole by benzyl alcohol as proposed in the AAD reaction mechanism does seem unlikely, especially under the basic reaction conditions. However, as the AAD reaction with Cr(III)(TPP)Cl is performed in boiling mesitylene for 48 hours, the high temperature and prolonged reaction time may enable unprecedented reaction mechanisms. Therefore, a range of hypothesized mechanisms are investigated with DFT calculations in the following section.

4.2. Computational study of the CrTPP catalytic cycle

To allow comparison of the energy profiles, the computational methods were kept identical to those used in the Cr(III)-salen case. Further details can be found in Section 4.5.4. As a starting point, the overall $\Delta G_{reaction}$ of the previously proposed mechanism was calculated (Figure 4.4).

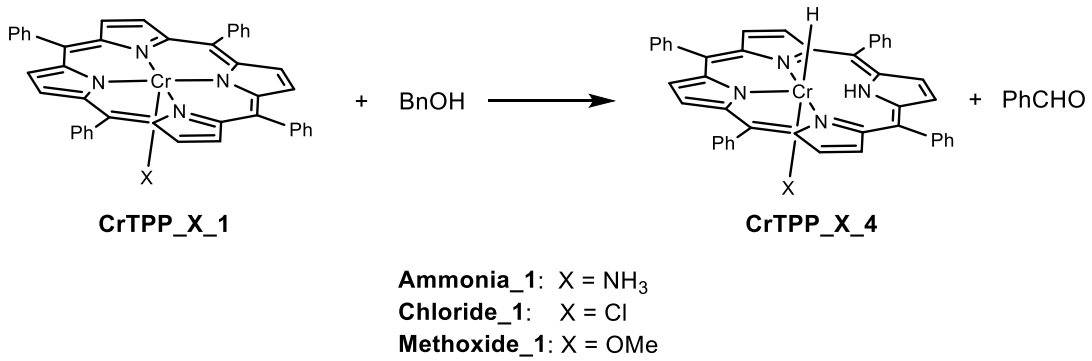

Figure 4.4: Calculation of the overall $\Delta G_{reaction}$ for the H^+/H^- transfer proposed in the original paper. As no experimental evidence regarding the identity of the axial ligand has been obtained, the calculation was repeated for three different axial ligands (ammonia, chloride and methoxide).

The $\Delta G_{reaction}$ was calculated with both ammonia, chloride, and methoxide as axial ligand to probe the most likely coordination modes under the employed reaction conditions. Firstly, the transformation was calculated with an overall cationic CrTPP catalyst containing axially coordinated ammonia to simulate coordination of cyclohexylamine. Secondly, the scenario with overall neutral complexes containing either chloride or methoxide (to simulate coordination of benzyl oxide) as axial ligands were tested. The results are shown in Table 4.1.

Table 4.1: Calculation of $\Delta G_{reaction}$ for the overall H^+/H^- transfer shown in Figure 4.4. The computational details can be found in Section 4.5.4.

Entry	$\Delta G_{reactants}$ / kcal mol^{-1}	$\Delta G_{products}$ / kcal mol^{-1}	$\Delta G_{reaction}$ / kcal mol^{-1}
Ammonia_1	-1507444.06	-1507411.703	32.36
Chloride_1	-1760872.533	-1760835.305	37.23
Methoxide_1	-1544302.332	-1544255.676	46.66

In the three investigated cases, the reaction is highly endergonic. It should be noted that in the best case scenario with axial ammonia, the calculated $\Delta G_{reaction}$ generally exceeds the activation energies calculated in the Cr(III)-salen case. Therefore, the proposed reaction mechanism does not seem likely based on these initial DFT calculations. To gain a full overview of the proposed catalytic

cycle, the a range of intermediates and transition states along the H^+/H^- transfer pathway were located for all three axial ligands. The DFT calculated model of the catalytic cycle with axially coordinated ammonia is shown in Figure 4.5.

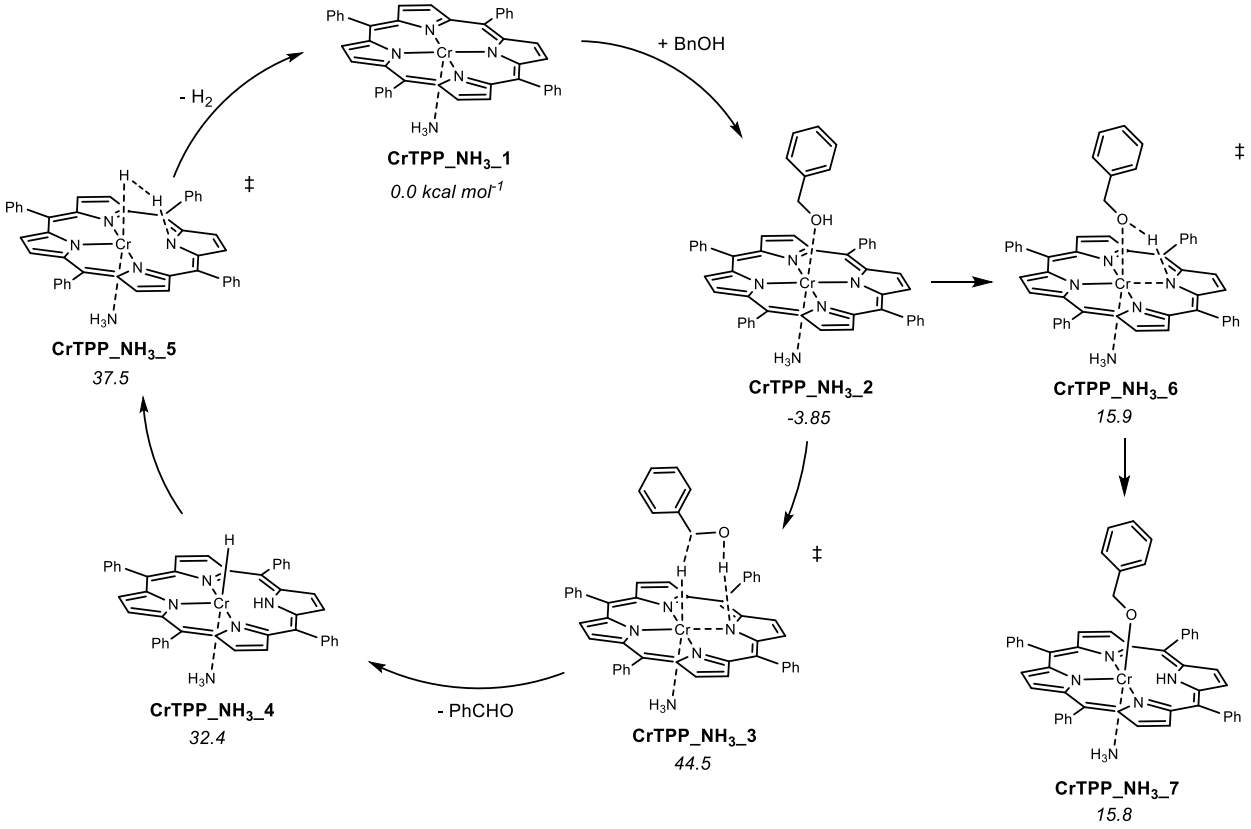

Figure 4.5: DFT model of a hypothesized catalytic cycle with axially coordinated ammonia. The outer-sphere, concerted H^+/H^- transfer presents an energy barrier of 48.4 kcal mol^{-1}, which is much too high.

The initial coordination of benzyl alcohol is energetically favored by ~4 kcal mol^{-1}, and the subsequent concerted outer-sphere transition state **CrTPP_NH3_3** presents an activation energy of 48.4 kcal mol^{-1}, which is prohibitively high. Furthermore, the proton transfer from coordinated benzyl alcohol to the pyrrole moiety (**CrTPP_NH3_2** → **CrTPP_NH3_7**) is endergonic by 19.65 kcal mol^{-1}, which is consistent with the very low basicity of the Cr(III)-coordinated pyrrole reported in Section 4.1.2. Comparatively, the similar proton transfer from coordinated benzyl alcohol to the amido nitrogen in the Cr(III)-salen catalytic cycle was exergonic by 14.8 kcal mol^{-1}. Ultimately, the DFT model predicts that proton transfer from coordinated benzyl alcohol to the pyrrole moiety of the CrTPP scaffold is unfeasible. As a result, any reaction mechanisms relying on proton transfer to the Cr(III)-coordinated pyrrole are considered unlikely to occur.

Catalytic cycles were also modelled with chloride and methoxide as axial ligands and the results are shown in Figure 4.6 and Figure 4.7.

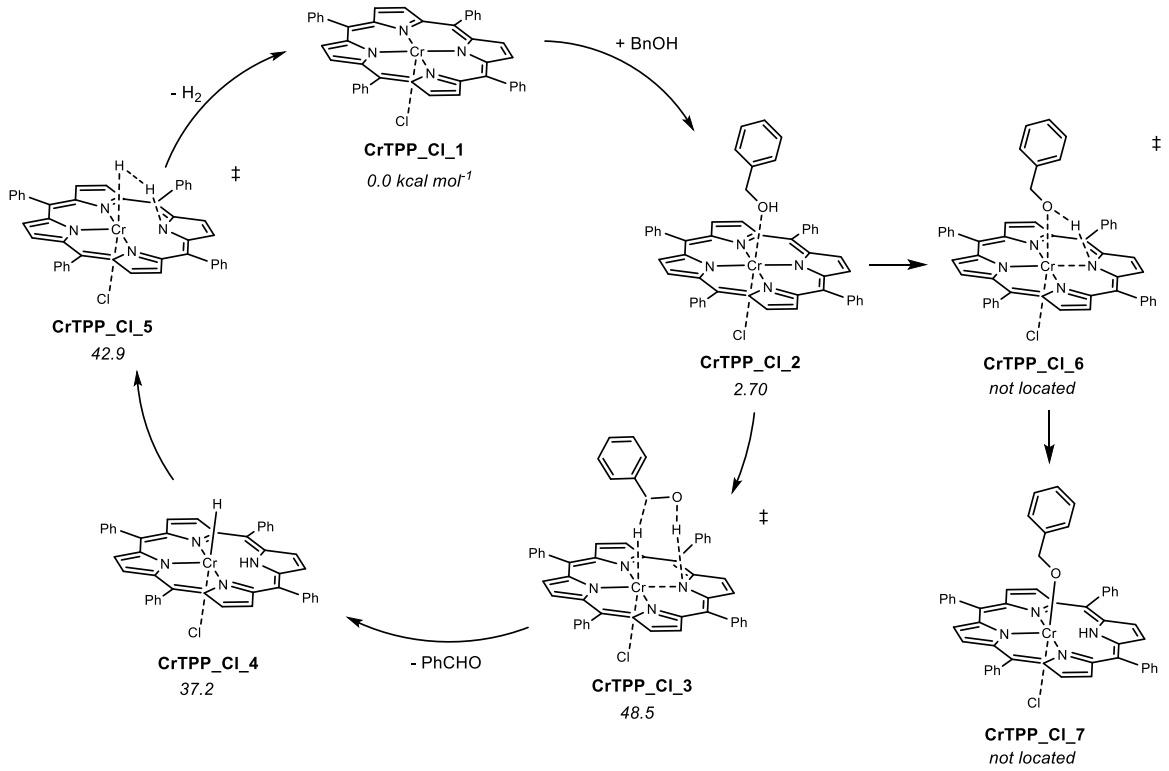

Figure 4.6: DFT model of the hypothesized reaction mechanism with axially coordinated chloride. The calculated activation energy of the outer-sphere, concerted H^+/H^- transfer is 48.5 kcal mol^{-1}.

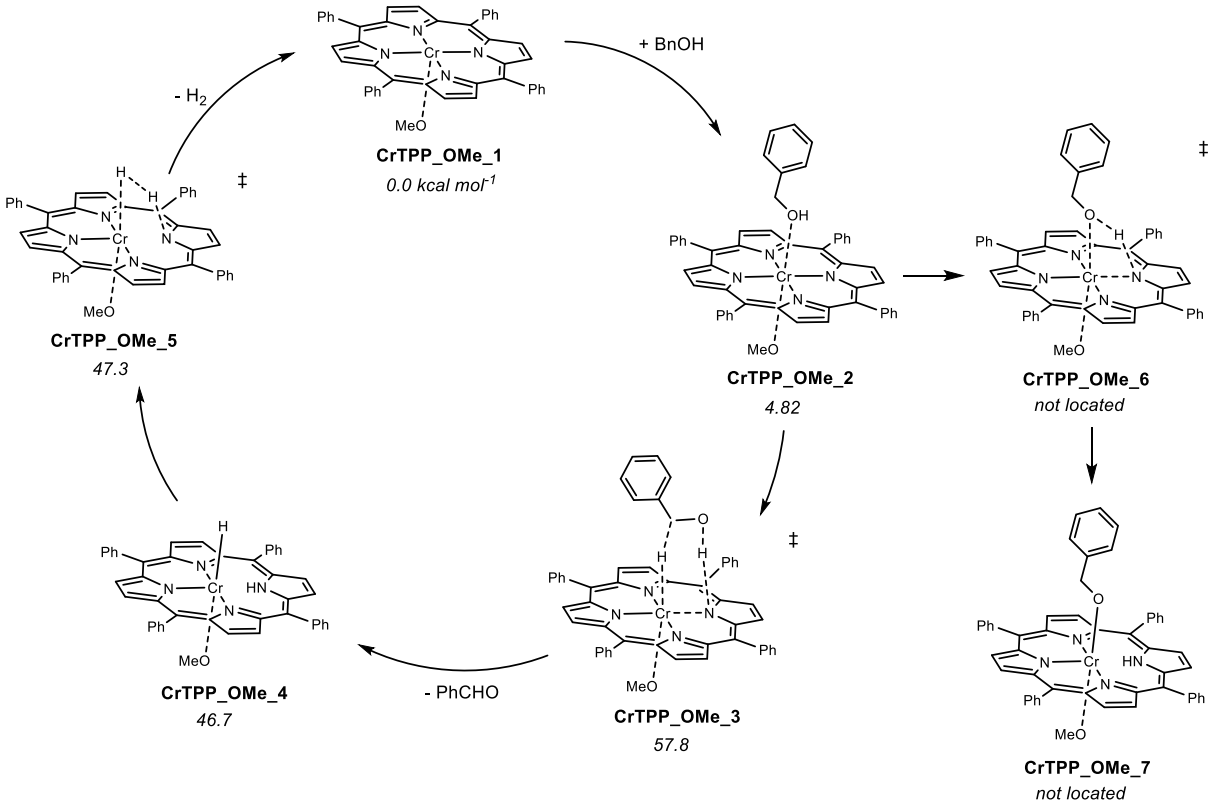

Figure 4.7: DFT model of the hypothesized reaction mechanism with axially coordinated methoxide. The calculated activation energy of the outer-sphere, concerted H^+/H^- transfer is 57.8 kcal mol^{-1}.

For both axial chloride and axial methoxide, the calculated energy barriers are even higher compared to those calculated for the catalytic cycle with axially coordinated ammonia. Despite several attempts, no energy minima were found for **CrTPP_Cl_7** or **CrTPP_OMe_7**; the geometry optimizations consistently moved the proton back from the pyrrole moiety to the alkoxide, thus reforming the alcohol. Based on the calculated energy barriers of the concerted H^+/H^- transfer, alternative reaction mechanisms for the CrTPP-catalyzed dehydrogenative imine synthesis should be considered.

As H^- transfer from coordinated benzyl oxide to the salen ligand had been observed both in the case of Mn(III)-salen and Cr(III)-salen, a similar H^- transfer in the CrTPP case was hypothesized. Transfer of H^- to the *meso*-position of the porphyrin allows delocalization of the negative charge onto a nitrogen, so the *meso*-position was deemed most likely to accept a H^- from a coordinated benzyl oxide. Consequently, a catalytic cycle with H^- transfer to the *meso*-position followed by hydrogen exclusion through reaction with the H^+ of a coordinated benzyl alcohol was modelled for all three axial ligands. The resulting catalytic cycle and the relative energies calculated with DFT are shown in Figure 4.8:

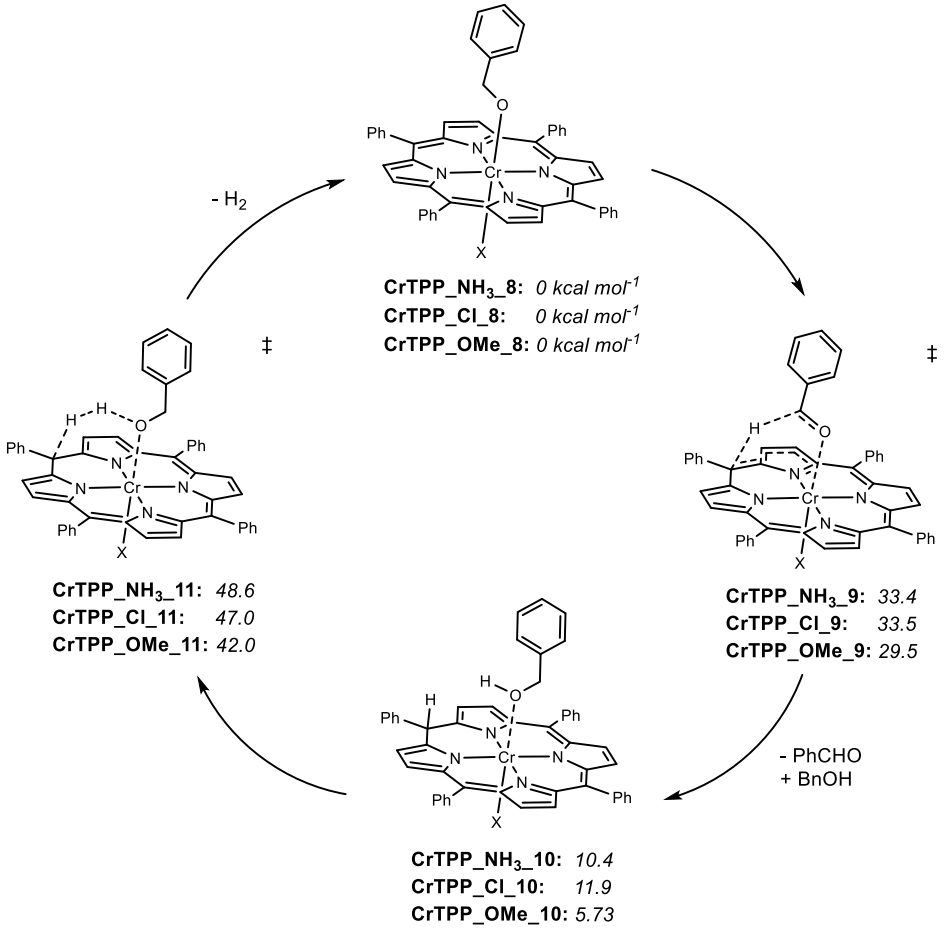

Figure 4.8: DFT model of a reaction mechanism involving transfer of H^- to the *meso*-position of the porphyrin ligand followed by hydrogen exclusion. The hydrogen exclusion step requiring breakage of a stable C-H bond has a prohibitively high activation energy of >42 kcal mol^{-1} in all three cases.

The calculated energy barriers for the initial H^- transfer to the *meso*-position ranges from 29.5 – 33.5 kcal mol^{-1} and the subsequent exclusion of hydrogen presents even higher energy barriers in the range 42.0 – 48.6 kcal mol^{-1}. These barriers are insurmountable, and the mechanism proposed in Figure 4.8 was therefore discarded and no further attempts to devise a likely reaction mechanism were made.

4.3. Repetition of experiments

Due to the inability to propose a reaction mechanism with a reasonable energy profile, it was decided to replicate the results reported in the original paper using the two-necked Schlenk flask setup instead of the Radley carousel, which were found prone to leakages by several members of the research group. The standard imination (Figure 4.9) was run in duplicate according to the conditions used in the original paper and great care was taken to exclude air from the reaction vessel, including thorough degassing of solvent.

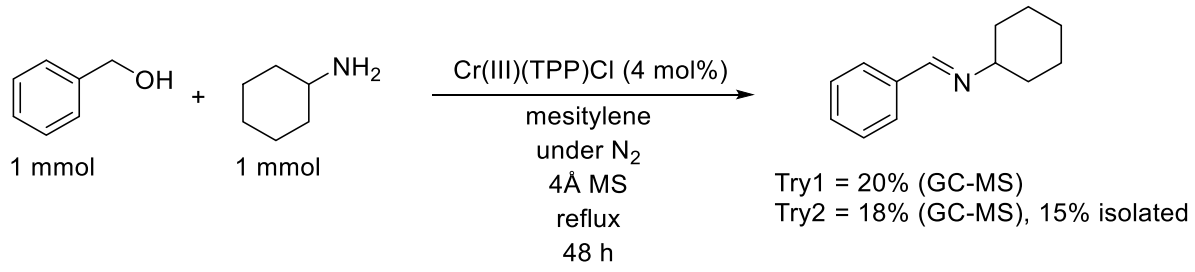

Figure 4.9: Replication of the standard imination in a two-necked Schlenk flask resulted in an isolated yield of 15%.

In the duplicate experiments, the yields of the imine were 20% and 18% respectively (determined by GC-MS, the chromatogram of the first reaction is shown in Figure 4.10). In the second experiment, the imine was isolated by flash column chromatography in a yield of 15%, which supports the GC-MS yields reasonably. These yields were significantly below the previously reported yield of 86%, which was cause for concern.

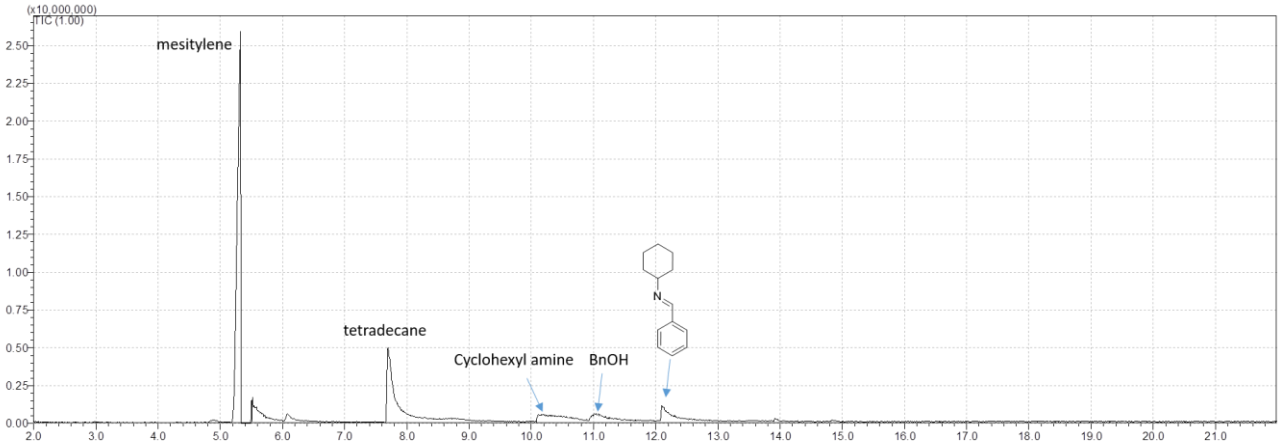

Figure 4.10: GC-MS chromatogram of the CrTPP imination reaction after 48 hours. An incomplete reaction and consequently low yield of *N*-benzylidenecyclohexylamine (20%) is observed.

To test the hypothesis of aerobic oxidation, a control experiment with catalysis in a Schlenk flask open to air was performed according to Figure 4.11.

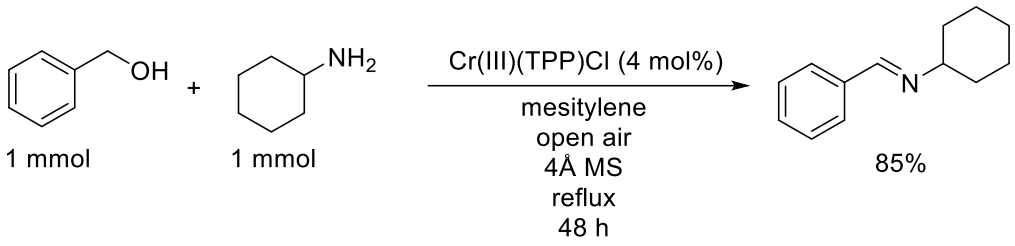

Figure 4.11: Reaction conditions of the CrTPP protocol performed in a Schlenk flask open to air. An 85% yield of *N*-benzylidenecyclohexylamine was determined by GC-MS.

In this control experiment, the GC yield of the imine was determined to 85%, which is more consistent with the yield reported in the paper. This observation clearly indicates that aerobic oxidation of the benzyl alcohol can be a significant side reaction if one is not careful with the reaction setup. Furthermore, some byproducts were observed in the chromatogram of the aerobic oxidation reaction. Through library matching of the fragmentation patterns, the byproducts were identified and the GC-MS chromatogram of the open-air reaction with assigned peaks are shown in Figure 4.12.

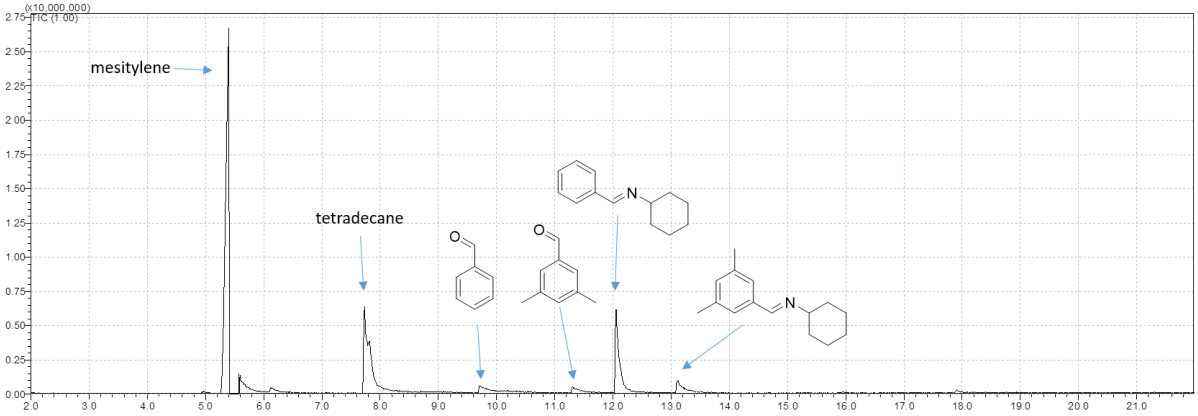

Figure 4.12: GC-MS chromatogram of the open-air CrTPP imination reaction after 48 hours. Higher yield of *N*-benzylidenecyclohexylamine (85%) was observed along with byproducts arising from the aerobic oxidation of mesitylene.

Surprisingly, 3,5-dimethylbenzaldehyde resulting from oxidation of mesitylene (retention time 11.4 minutes) and the corresponding imine resulting from condensation with cyclohexylamine (retention time 13.1 minutes) can be observed. None of these byproducts were observed when the reactions were run with careful exclusion of oxygen (see Figure 4.10). Thus, the presence of these byproducts can act as a marker of oxygen presence during the catalytic reactions.

To test the hypothesis of aerobic oxidation in the experiments presented in the original paper, a selection of old GC-MS chromatograms recorded by Yulong Miao during the original substrate scoping of the CrTPP protocol were re-examined to check for the presence of byproducts related to the aerobic oxidation of mesitylene. Three examples are shown in Figure 4.13.

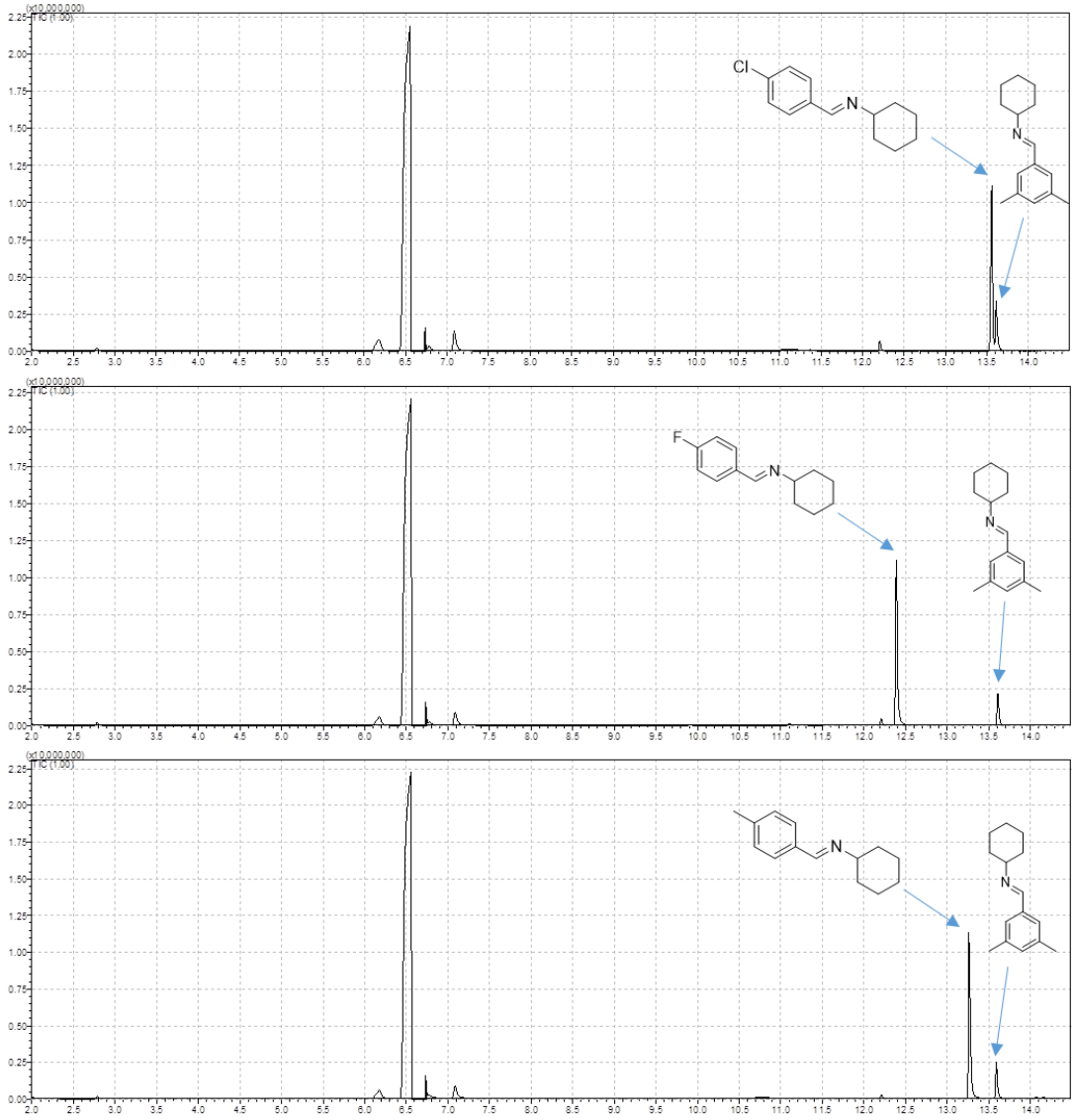

Figure 4.13: Three original chromatograms recorded by Yulong Miao during the original substrate scoping of the CrTPP catalysis. In all three cases, the imine originating from oxidation of mesitylene is present.

In all three shown cases, the imine originating from the oxidation of mesitylene can be detected in the GC-MS chromatogram (retention time 13.6 minutes). It should be noted that Yulong Miao used a different GC-MS method to record the chromatograms shown in Figure 4.13, which is why the retention times differ slightly from those in Figure 4.12. Overall, several old GC-MS chromatograms related to the CrTPP project show evidence of mesitylene oxidation, which indicates that the observed reaction is likely caused by aerobic oxidation.

Indeed, if the alcohol oxidation is caused by the presence of air, no evolution of hydrogen gas is expected during the catalysis. However, evolution of 17 mL of gas identified as hydrogen by ^{1}H NMR were reported in the original paper and this observation does not comply with the hypothesis of aerobic oxidation.[145] Two separate attempts to reproduce the reported gas evolution were made according to Figure 4.14 (further details are provided in Section 4.5.3).

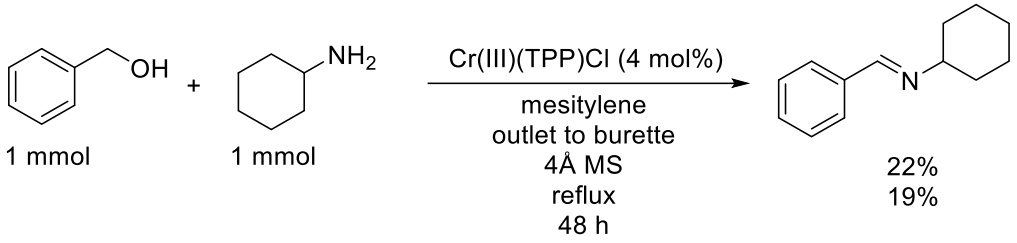

Figure 4.14: Gas evolution experiment using the CrTPP protocol. Duplicate experiments determined imine yields of 22% and 19% respectively and no gas evolution was observed in either experiment.

Unfortunately, only the initial displacement of water related to the thermal expansion of the dead volume during heating was observed. Upon reaching thermal equilibrium, no further water displacement caused by gas evolution was observed in either of the two attempts. The GC-MS chromatograms for both experiments showed an imine yield of around 20%, which is consistent with the previous replication experiments run under inert atmosphere.

4.4. Conclusion

With the struggles of obtaining adequate reactivity from the Cr(III)-salen derivatives, it was surprising to see the relatively similar Cr(III)(TPP)Cl catalyst performing well in refluxing mesitylene, even without the addition of strong inorganic bases that are commonly employed to achieve efficient catalysis. In the original paper, a mechanism relying on the concerted transfer of an alcohol proton to the Cr(III)-coordinated pyrrole moiety and hydride transfer to the metal center was proposed. In this chapter, a DFT model based in this hypothesis was constructed, and in the best-case scenario with axially coordinated ammonia, the activation energy of the concerted transfer was 48.4 kcal mol^{-1}, which is prohibitively high. An alternative mechanism where a hydride was transferred from a coordinated benzyl oxide to the porphyrin ligand followed by reaction with an alcohol proton to release H_2 was modelled by DFT, but the calculated energy barriers for this mechanistic proposal were also too high to explain the observed reactivity.

Due to concerns with leaky carousels and improper reaction setup leading to aerobic oxidation of benzyl alcohol, a series of replication and control experiments were performed. Under careful exclusion of oxygen, an imine yield of 15–20% was observed. Under open-air conditions, an imine yield of 85% along with byproducts stemming from aerobic oxidation of mesitylene was observed. This result led to a re-examination of several old chromatograms recorded by Yulong Miao in relation to the published paper, and evidence of aerobic mesitylene oxidation was found in several cases. This indicated that presence of oxygen could be responsible for the originally reported reactivity. Lastly, two separate gas evolution experiments were made to reproduce the gas evolution reported in the paper. In both cases, no gas evolution was observed.

In conclusion, the CrTPP-catalyzed imination presented in the original paper was found irreproducible and the proposed mechanism was found unlikely based on the high energy barriers calculated by DFT.

4.5. Experimental

In the following section, the details of both the experimental and theoretical investigations can be found. Only details of the experiments carried out by me has been included, the complete account of previously performed experiments related to catalysis with Cr(III)(TPP)Cl can be found in the original paper.[145]

4.5.1. General experimental details

Benzaldehyde, anhydrous benzyl alcohol, cyclohexylamine and mesitylene were purchased from Merck. The catalyst, Cr(III)(TPP)Cl, was purchased from Strem Chemicals and used as received. Degassed, anhydrous mesitylene was prepared by freeze-pump-thaw cycles (repeated three times) followed by sparging with a flow of N_2 for 3 hours minimum. Freshly activated molecular sieves (4Å) was added and the solvent was kept under N_2 and allowed to dry for minimum 24 hours before use. Manual flash column chromatography was performed using HPLC grade heptane and Et_3N. The separations were carried out on silica gel (35 - 70 μm) obtained from VWR Chemicals and pre-saturated with Et_3N before loading the crude product.

All catalytic reactions were performed in two-necked Schlenk flasks using standard Schlenk techniques. The nitrogen feed of the Schlenk line was dried over a column of P_2O_5. To avoid cross-contamination, all glassware and magnets were thoroughly cleaned with *aqua regia* prior to use.

Gas chromatography was carried out on a Shimadzu GCMS-QP2010S instrument equipped with an Rtx-5MS column (30m x 0.25 mm x 0.25 μm). The carrier gas was Helium, and the ionization was performed by electron impact (EI) at 70 eV. The GC settings shown in Table 4.2 were employed in all analyzes:

Table 4.2: Settings employed for GC-MS analysis.

Injection volume	1 μL
Injection mode	Split
Injection temperature	280 °C
Initial oven temperature	60 °C (hold 5 min)
Final oven temperature	300 °C (hold 5 min)
Temperature ramp rate	20 °C / min
Total run time	22 min

Standard ^{1}H and ^{13}C NMR spectra were recorded at 400 MHz and 101 MHz, respectively, on a Bruker Ascend 400 MHz spectrometer using residual $CHCl_3$ signals (δ_H 7.26 ppm, δ_C 77.2 ppm) as reference. All chemical shifts (δ) are quoted in ppm and coupling constants (*J*) are listed in Hz.

4.5.2. Construction of calibration curve

Stock solution **A** (0.100 M *N*-Benzylidenecyclohexylamine in diethyl ether) were prepared by dissolving freshly synthesized *N*-benzylidenecyclohexylamine (188 mg) in Et_2O in a 10 mL volumetric flask. Stock solution **B** (0.050 M tetradecane in diethyl ether) were prepared by dissolving tetradecane (100 mg) in Et_2O in a 10 mL volumetric flask. From the two stock solutions, the GC calibration samples were prepared according to Table 4.3, and the samples were subjected to GC-MS analysis using the standard method.

Table 4.3: Preparation of standards for the construction of the calibration curves.

Vial no.	1	2	3	4	5
V(**StockA**) / mL	0.1	0.2	0.3	0.4	0.5
V(**StockB**) / mL	0.5	0.5	0.5	0.5	0.5
V(Et_2O) / mL	0.4	0.3	0.2	0.1	0.0
c(*N*-Benzylidenecyclohexylamine) / M	0.01	0.02	0.03	0.05	0.05
c(tetradecane) / M	0.025	0.025	0.025	0.025	0.025

The obtained GC-MS chromatograms (example shown in Figure 4.15) were integrated across fixed retention times (reported in Table 4.4) to ensure consistent integration:

Table 4.4: Retention times used for reliable integration of the GC-MS chromatograms.

Compound	Retention time
Tetradecane	7.73 – 9.00 min
N-Benzylidenecyclohexylamine	12.0 – 13.0 min

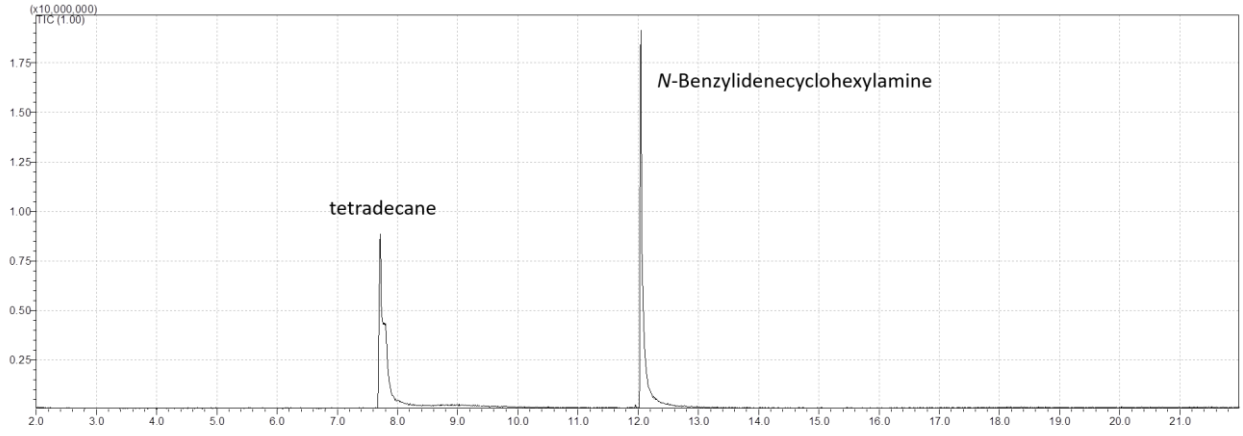

Figure 4.15: Example of a GC-MS chromatogram used to construct the calibration curves.

From the areas obtained by integration of the GC-MS chromatogram, the relative area (A_{imine}/A_{tet}) as a function of the relative concentration (c_{imine}/c_{tet}) were plotted, linear regression with a forced intercept through (0.0) was performed and the obtained slope was used to determine the concentrations of *N*-benzylidenecyclohexylamine in all further experiments.

4.5.3. Synthetic protocols

Synthesis of *N*-benzylidenecyclohexylamine for calibration curves:

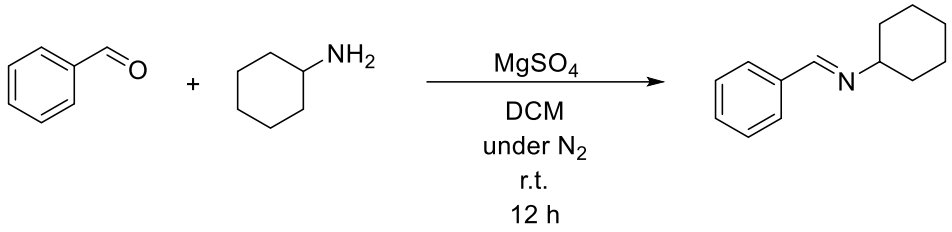

To a round-bottom flask was added CH_2Cl_2 (40 mL), benzaldehyde (2.0 mL, 19.7 mmol), cyclohexylamine (2.25 mL, 19.7 mmol) and $MgSO_4$ (2.4 g, 19.9 mmol). The reaction mixture was stirred for 12 h at room temperature under a flow of N_2. The reaction mixture was filtered, and the solvent was removed *in vacuo*. The crude product was loaded onto a silica gel column saturated with Et_3N and purified by flash chromatography in heptane/Et_3N (98:2). The fractions containing pure product were reduced *in vacuo* and the pure product was further dried under vacuum overnight to remove residual solvent.

Yield: 2.66 g (74%)

^{1}H-NMR (400 MHz, $CDCl_3$): δ 8.32 (s, 1H), 7.75-7.72 (m, 2H), 7.41-7.39 (m, 3H), 3.23-3.16 (m, 1H), 1.86-1.55 (m, 7H), 1.43-1.23 (m, 3H).
^{13}C-NMR (101 MHz, $CDCl_3$): δ 158.9, 136.7, 130.7, 128.7, 128.3, 70.0, 34.4, 25.8, 25.0
NMR data are in accordance with previously reported values.[1]

Catalytic synthesis of *N*-benzylidenecyclohexylamine:

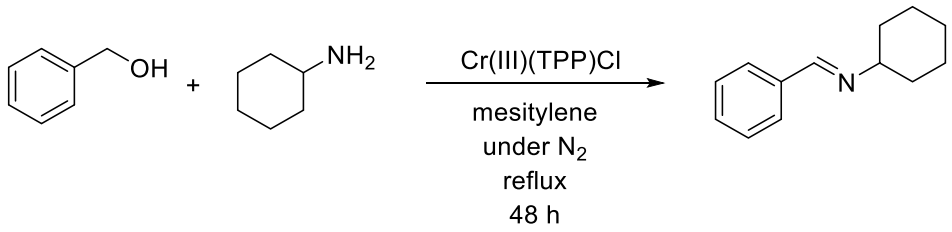

Attempts to reproduce the imine formation were carried out according to the procedure described in the original paper using a two-necked Schlenk flask equipped with a septum and cold finger instead of a Radley carousel.[145]

Freshly opened Cr(III)(TPP)Cl (35.0 mg, 0.05 mmol) and freshly activated molecular sieves (4Å, 150 mg) was weighed into a flame-dried Schlenk flask equipped with a septum and a cold finger. The flask was subjected to vacuum and N_2 refills (repeated three times). Freshly degassed anhydrous mesitylene (4 mL) was added by syringe and the reaction mixture was heated to reflux in an oil bath with stirring. Upon reaching reflux, benzyl alcohol (1.0 mmol), cyclohexylamine (1.0 mmol) and tetradecane (0.5 mmol) were added through the septum and the reaction mixture was refluxed for 48 h under a flow of N_2. At the 24-hour and 48-hour mark, aliquots of the reaction

mixture (0.2 mL) were withdrawn through the septum and diluted to 1.0 mL with Et_2O. The sample was filtered through a nylon syringe filter (0.22 μm pore size) into a GC vial and subjected to GC-MS analysis to determine the yield of imine using a recently prepared calibration curve.

The reaction was repeated twice to ensure reliable results and in the second entry, the imine was isolated by silica gel flash chromatography (heptane/Et_3N, 98:2) to validate the yields determined by GC-MS. The yields are reported in the table below.

Entry	GC Yield (%)	Isolated yield (%)
1	20	-
2	18	15

Open-flask, catalytic synthesis of *N*-benzylidenecyclohexylamine:

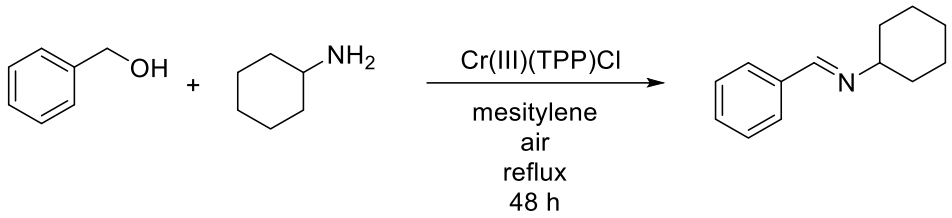

Freshly opened Cr(III)(TPP)Cl (35.0 mg, 0.05 mmol) and freshly activated molecular sieves (4Å, 150 mg) was weighed into a flame-dried two-necked Schlenk flask equipped with a cold finger. Anhydrous mesitylene (4 mL) was added by syringe and the reaction mixture was heated to reflux in an oil bath with stirring. Upon reaching reflux, benzyl alcohol (1.0 mmol), cyclohexylamine (1.0 mmol) and tetradecane (0.5 mmol) were added through the open neck and the reaction mixture was refluxed for 48 h under air. At the 24-hour and 48-hour mark, aliquots of the reaction mixture (0.2 mL) were withdrawn through the septum and diluted to 1.0 mL with Et_2O. The sample was filtered through a nylon syringe filter (0.22 μm pore size) into a GC vial and subjected to GC-MS analysis to determine the yield of imine using a recently prepared calibration curve.

GC Yield: 85%

Gas evolution during the catalytic synthesis of *N*-benzylidenecyclohexylamine:

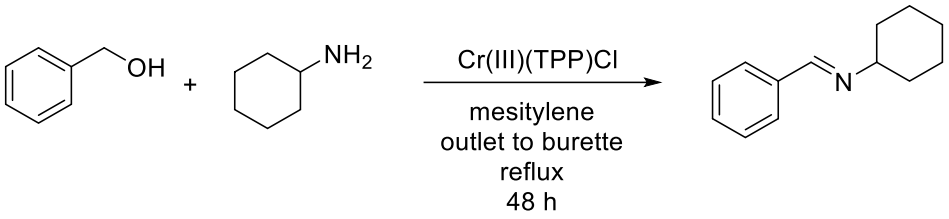

Freshly opened Cr(III)(TPP)Cl (35.0 mg, 0.05 mmol) and freshly activated molecular sieves (4Å, 150 mg) was weighed into a flame-dried two-necked Schlenk flask equipped with a septum and a cold finger. The flask was subjected to vacuum and N_2 refills (repeated three times). Freshly degassed anhydrous mesitylene (4 mL), benzyl alcohol (1.0 mmol), cyclohexylamine (1.0 mmol) and tetradecane (0.5 mmol) were added through the septum. At this point, the stopcock of the Schlenk flask was closed, and the connection to the Schlenk line was replaced with vacuum tubing equipped with a syringe and needle at the end. The end of the needle was carefully placed at the opening of an inverted, water-filled burette residing in a water-filled crystallization bowl with a large surface area. The stopcock was reopened and all connections were rigorously reinforced with parafilm to avoid leakages. The reaction mixture was heated to reflux and gas evolution was gradually observed as the temperature rose due to thermal expansion of the dead volume of the Schlenk flask. As the reaction flask reached thermal equilibrium, the bubbling subsided and the initially displaced volume due to thermal expansion was read off the burette. At the 24-hour and 48-hour mark, the gas volume was noted and aliquots of the reaction mixture (0.2 mL) were withdrawn through the septum and diluted to 1.0 mL with Et_2O. The sample was filtered through a nylon syringe filter (0.22 μm pore size) into a GC vial and subjected to GC-MS analysis to determine the yield of imine using a recently prepared calibration curve.

The gas evolution experiment was repeated twice to ensure reliable results and the gas volumes and GC-yields are reported in the table below.

Entry	$V_{0\,h}$ / mL	$V_{24\,h}$ / mL	$V_{48\,h}$ / mL	GC Yield (%)
1	11.5	11.5	11.4	22
2	11.8	11.8	11.8	19

4.5.4. Computational details

The DFT calculations in this chapter performed with Jaguar (version 10.7, release 13) by Schrodinger LLC[142]. All structure optimizations were performed in the gas phase using the B3LYP-D3 functional[120,121,143] and the LACVP** basis set. Unrestricted SCF spin treatment was used in all calculations and the multiplicity of all Cr(III) containing structures were assumed to be high-spin quartet. To simulate the experimental conditions, the frequency calculations were performed at the boiling point of mesitylene (438 K) and at standard state (1 atm). The frequencies were checked to ensure that intermediates had no imaginary frequencies and that transitions states had one imaginary frequency. The solvation free energy ΔG_{solv} of structures containing Cr(III) were calculated with the PBF solver in Jaguar using the standard parameters for toluene and the B3LYP-D3\\LACVP** method. Solvation free energies of benzyl alcohol and benzaldehyde were calculated using the SM8 model[144] and the B3LYP-D3\\6-31G* method. To obtain more accurate electronic energies, the electronic energy of all structures was recalculated with the larger basis set LACV3P**++. The final Gibbs free energy of the structures were calculated as the sum $\Delta G_{tot} = E$(LACVP3**++) + $\Delta G_{solv} + ZPE + \Delta H - T\Delta S$. In all cases, T was set to the boiling point of mesitylene (438 K).

4.5.5. Energies of structures

Table 4.5: Overview of structures and energies calculated in Jaguar.

	E (LACV3P**++)	ZPE	H	S	Solv
BnOH	-346.8832973	83.550	9.174	91.954	-4.4940
PhCHO	-345.6767904	69.174	8.891	91.191	-4.0140
CrTPP_NH$_3$_1	-2055.977599	402.463	51.683	294.372	-25.8127
CrTPP_NH$_3$_2	-2402.912912	488.267	61.751	338.883	-23.5476
CrTPP_NH$_3$_3	-2402.828643	482.828	61.331	337.505	-22.8186
CrTPP_NH$_3$_4	-2057.1307	413.52	52.868	299.054	-23.3144
CrTPP_NH$_3$_5	-2057.121476	411.296	52.198	295.652	-22.5987
CrTPP_NH$_3$_6	-2402.881491	486.489	60.854	334.544	-22.7150
CrTPP_NH$_3$_7	-2402.882795	487.677	61.317	336.663	-22.7680
CrTPP_NH$_3$_8	-2402.489081	479.582	61.226	336.174	-7.4870
CrTPP_NH$_3$_9	-2402.432378	475.845	46.772	298.999	-7.7116
CrTPP_NH$_3$_10	-2403.677956	494.426	62.082	339.670	-8.4880
CrTPP_NH$_3$_11	-2403.609582	488.128	61.674	337.383	-7.4600
CrTPP_Cl_1	-2459.837811	377.978	50.573	289.419	-8.5773
CrTPP_Cl_2	-2806.758054	463.882	60.601	334.486	-9.0354
CrTPP_Cl_3	-2806.677184	459.82	60.015	331.608	-10.5724
CrTPP_Cl_4	-2460.975436	389.465	51.519	293.047	-11.5719
CrTPP_Cl_5	-2460.971765	390.004	50.956	290.877	-9.1327
CrTPP_Cl_8	-2806.231432	454.462	60.239	332.672	-27.9964
CrTPP_Cl_9	-2806.174944	451.035	59.842	329.731	-27.3947
CrTPP_Cl_10	-2807.42013	469.132	61.290	337.650	-26.9662
CrTPP_Cl_11	-2807.357629	463.038	60.765	334.282	-25.9687
CrTPP_OMe_1	-2114.744532	403.351	52.556	298.264	-7.8904
CrTPP_OMe_2	-2461.662257	489.085	62.624	343.413	-7.6360
CrTPP_OMe_3	-2461.571277	484.688	62.073	340.692	-8.0068
CrTPP_OMe_4	-2115.868425	414.108	53.575	302.576	-9.1172
CrTPP_OMe_5	-2115.869064	413.444	52.95	299.898	-8.0028
CrTPP_OMe_8	-2461.121969	479.263	62.188	341.057	-25.6552
CrTPP_OMe_9	-2461.071775	476.133	61.765	338.035	-25.3780
CrTPP_OMe_10	-2462.320163	494.193	63.327	346.882	-24.8131
CrTPP_OMe_11	-2462.255221	487.972	62.816	343.338	-24.0844

The cartesian coordinates of all listed structures in Table 4.5 can be found by following the link or scanning the QR code below.

https://www.dropbox.com/sh/e5mlv2pzne8zo0r/AABhB4eWaV8I2c-kJMs0bbbpa?dl=0

Conclusions and outlook

In this thesis, new approaches to acceptorless alcohol dehydrogenation (AAD) using cheap and readily available Fe(III)-salen and Cr(III)-salen catalysts were investigated.

In the first project, the effectiveness of an Fe(III)-salen catalyst system for the coupling of benzylic alcohols and amines to produce imines was demonstrated. Initial studies suggested that the reaction was enabled by homogeneous, molecular catalysis. DFT calculations were employed to rationalize the experimental results and suggest a plausible catalytic cycle. Unfortunately, the calculated catalytic cycles revealed insurmountable energy barriers and poor correlation between the experimental and computational results.

Heterogeneous catalysis was suspected, so poisoning studies with PMe_3 and Hg were conducted, which resulted in inhibition of the catalytic activity. Furthermore, LC-MS studies revealed extensive degradation of the Fe(III)-salen catalyst. It was ultimately concluded that the catalytically active species were not molecular Fe(III)-salen derivatives but rather heterogeneous small iron particles, as shown in Figure iii.

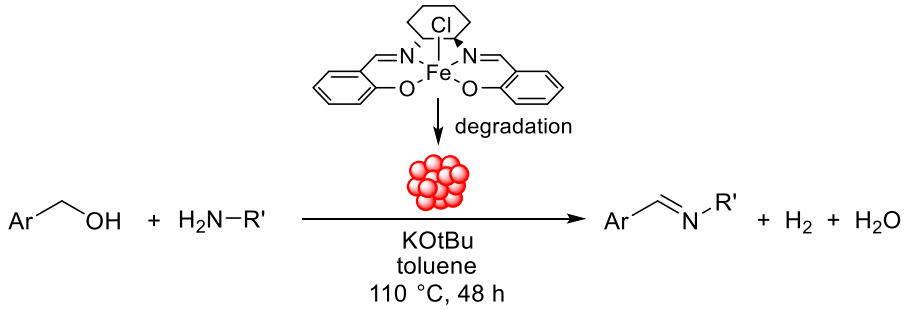

Figure iii: Heterogeneous small iron particles were suggested as the most likely catalyst for the coupling of benzylic alcohols and amines.

In the second project, a range of Cr(III)-salen and Cr(III)-salan complexes were synthesized and investigated as possible catalysts for the dehydrogenative coupling of benzyl alcohol and cyclohexylamine. After extensive optimization of reaction conditions, a maximum imine yield of only 30% was achieved.

No evolution of hydrogen gas was detected during the reactions, which excluded the operation of an AAD reaction mechanism. LC-MS studies confirmed the *in situ* reduction of Cr(III)-salen to Cr(III)-salan and provided evidence of catalyst dimerization. Furthermore, an extensive DFT study was conducted to explore different reaction mechanisms and possible catalyst optimizations. Once again, no low-energy AAD pathways were identified, which correlated well with the low reactivity of the catalyst system. Ultimately, both experimental and computational findings pointed towards highly stable alkoxo-Cr(III)-salan intermediates as resting states that inhibit catalytic activity.

In the final chapter, a previously published AAD protocol using a Cr(III)(TPP)Cl catalyst was revisited. DFT calculations were used to investigate several proposed reaction mechanisms, but no low-energy pathways were identified.

Key experiments from the original report were replicated under carefully controlled conditions, which resulted in much lower imine yields compared to the original paper. Additionally, no evolution of hydrogen gas was detected during the reactions. Lastly, performing the reactions under an air atmosphere revealed that aerobic oxidation was a significant side reaction, leading to high imine yields and the formation of byproducts. Examination of several old chromatograms associated with the original paper indicated the presence of these byproducts, suggesting that the presence of air may have led to inflated imine yields.

Overall, the projects presented in this thesis shed light on the substantial challenges and potential pitfalls encountered during the development of homogeneously catalyzed reactions. The Fe(III)-salen project serves as a notable example, as the consideration of heterogeneous catalysis only emerged in the late stages of the project, ultimately leading to a complete revision of the project's conclusions. In hindsight, it would have been advantageous to investigate the possibility of heterogeneous catalysis at an earlier stage, potentially saving valuable time spent on DFT modeling of the molecular pathway. Nonetheless, the DFT studies played a vital role in discounting the viability of the molecular pathways and ultimately contributed to the realization of heterogeneous catalysis as the most likely process.

On a similar note, the Cr(III)-salen and Cr(III)(TPP)Cl projects highlight the significance of conducting catalytic experiments under meticulously controlled conditions. Notably, initial investigations of the Cr(III)-salen catalyst system reported near-quantitative imine yields in Radley carousels, whereas imine yields of no more than ~30% were realized using the Schlenk-flask setup. Since the preferred substrate, benzyl alcohol, is susceptible to oxidation by oxygen, particularly at elevated temperatures, insufficient control over the oxygen content can substantially skew the imine yields towards inflated values.

A similar observation was made in relation to previous studies involving the Cr(III)(TPP)Cl catalyst, where the previously reported high imine yields could not be achieved in the Schlenk-flask setup. Clearly, minimizing the presence of oxygen by thorough degassing and proper implementation of Schlenk techniques is vital to obtain reliable results. However, it should be acknowledged that the human factor in reaction setups remains a challenge. Therefore, it is crucial to verify catalytic results by repeating the experiments using different operators, glassware, and setups to ensure the reproducibility of the reported reactions.

In future investigations, the use of glove boxes to ensure completely air-free conditions could be highly advantageous. This approach has the potential to save valuable time and effort that would otherwise be spent unraveling misleading reaction yields. By implementing such measures, we can enhance the reliability and accuracy of catalytic research, thereby advancing our understanding of complex reaction systems.

Publications

Development and mechanistic investigation of the dehydrogenation of alcohols with an iron(III) salen catalyst

N. S. B. Hansen, F. Monda, F. S. Bro, X. Liu, M. S. G. Ahlquist, R. Madsen, *Org. Biomol. Chem.* **2023**, *21*, 4794 – 4800.

Bibliography

[1] S. V. Samuelsen, C. Santilli, M. S. G. Ahlquist, R. Madsen, *Chem. Sci.* **2019**, *10*, 1150–1157.

[2] P. T. Anastas, J. C. Warner, *Green Chemistry: Theory and Practice*, Oxford University Press, **1998**.

[3] B. Trost, *Science* **1991**, *254*, 1471–1477.

[4] R. A. Sheldon, *ACS Sustain. Chem. Eng.* **2018**, *6*, 32–48

[5] R. A. Sheldon, *Green Chem.* **2017**, *19*, 18–43.

[6] W. L. Evans, J. E. Day, *J. Am. Chem. Soc.* **1919**, *41*, 1267–1285.

[7] D. B. Dess, J. C. Martin, *J. Org. Chem.* **1983**, *48*, 4155–4156.

[8] C. Gunanathan, D. Milstein, *Science* **2013**, *341*, DOI 10.1126/science.1229712.

[9] G. E. Dobereiner, R. H. Crabtree, *Chem. Rev.* **2010**, *110*, 681–703.

[10] P. Pandey, I. Dutta, J. K. Bera, *Proc. Natl. Acad. Sci. India - Phys. Sci.* **2016**, *86*, 561–579.

[11] T. Irrgang, R. Kempe, *Chem. Rev.* **2019**, *119*, 2524–2549.

[12] D. Morton, D. J. Cole-Hamilton, *J. Chem. Soc., Chem. Commun.* **1987**, 248–249.

[13] D. Morton, D. J. Cole-Hamilton, *J. Chem. Soc., Chem. Commun.* **1988**, 1154.

[14] H. Junge, B. Loges, M. Beller, *Chem. Commun.* **2007**, 522–524.

[15] L. U. Nordstrøm, H. Vogt, R. Madsen, *J. Am. Chem. Soc.* **2008**, *130*, 17672–17673.

[16] J. H. Dam, G. Osztrovszky, L. U. Nordstrøm, R. Madsen, *Chem. Eur. J.* **2010**, *16*, 6820–6827.

[17] C. Santilli, I. S. Makarov, P. Fristrup, R. Madsen, *J. Org. Chem.* **2016**, *81*, 9931–9938.

[18] A. Maggi, R. Madsen, *Organometallics* **2012**, *31*, 451–455.

[19] A. Sølvhøj, R. Madsen, *Organometallics* **2011**, *30*, 6044–6048.

[20] I. S. Makarov, R. Madsen, *J. Org. Chem.* **2013**, *78*, 6593–6598.

[21] J. S. M. Samec, J.-E. Bäckvall, P. G. Andersson, P. Brandt, *Chem. Soc. Rev.* **2006**, *35*, 237.

[22] S. E. Clapham, A. Hadzovic, R. H. Morris, *Coord. Chem. Rev.* **2004**, *248*, 2201–2237.

[23] J.-E. Bäckvall, *J. Organomet. Chem.* **2002**, *652*, 105–111.

[24] O. Pàmies, J.-E. Bäckvall, *Chem. Eur. J.* **2001**, *7*, 5052–5058.

[25] I. S. Makarov, P. Fristrup, R. Madsen, *Chem. Eur. J.* **2012**, *18*, 15683–15692.

[26] J. R. Khusnutdinova, D. Milstein, *Angew. Chem. Int. Ed.* **2015**, *54*, 12236–12273.

[27] G. A. Filonenko, R. van Putten, E. J. M. Hensen, E. A. Pidko, *Chem. Soc. Rev.* **2018**, *47*, 1459–1483.

[28] K.-J. Haack, S. Hashiguchi, A. Fujii, T. Ikariya, R. Noyori, *Angew. Chem. Int. Ed. Engl.* **1997**, *36*, 285–288.

[29] R. Noyori, S. Hashiguchi, *Acc. Chem. Res.* **1997**, *30*, 97–102.

[30] D. A. Alonso, P. Brandt, S. J. M. Nordin, P. G. Andersson, *J. Am. Chem. Soc.* **1999**, *121*, 9580–9588.

[31] M. Yamakawa, H. Ito, R. Noyori, *J. Am. Chem. Soc.* **2000**, *122*, 1466–1478.

[32] C. P. Casey, J. B. Johnson, *J. Org. Chem.* **2003**, *68*, 1998–2001.

[33] P. A. Dub, J. C. Gordon, *Nat. Rev. Chem.* **2018**, *2*, 396–408.

[34] P. A. Dub, J. C. Gordon, *Dalton Trans.* **2016**, *45*, 6756–6781.

[35] P. A. Dub, J. C. Gordon, *ACS Catal.* **2017**, *7*, 6635–6655.

[36] P. A. Dub, N. J. Henson, R. L. Martin, J. C. Gordon, *J. Am. Chem. Soc.* **2014**, *136*, 3505–3521.

[37] M. Nielsen, E. Alberico, W. Baumann, H.-J. Drexler, H. Junge, S. Gladiali, M. Beller, *Nature* **2013**, *495*, 85–89.

[38] M. Nielsen, A. Kammer, D. Cozzula, H. Junge, S. Gladiali, M. Beller, *Angew. Chem. Int. Ed.* **2011**, *50*, 9593–9597.

[39] M. Nielsen, H. Junge, A. Kammer, M. Beller, *Angew. Chem. Int. Ed.* **2012**, *51*, 5711–5713.

[40] E. Alberico, A. J. J. Lennox, L. K. Vogt, H. Jiao, W. Baumann, H.-J. Drexler, M. Nielsen, A. Spannenberg, M. P. Checinski, H. Junge, M. Beller, *J. Am. Chem. Soc.* **2016**, *138*, 14890–14904.

[41] C. Gunanathan, D. Milstein, *Acc. Chem. Res.* **2011**, *44*, 588–602.

[42] D. Milstein, *Top. Catal.* **2010**, *53*, 915–923.

[43] C. Gunanathan, Y. Ben-David, D. Milstein, *Science* **2007**, *317*, 790–792.

[44] B. Gnanaprakasam, J. Zhang, D. Milstein, *Angew. Chem. Int. Ed.* **2010**, *49*, 1468–1471.

[45] H. Li, X. Wang, F. Huang, G. Lu, J. Jiang, Z.-X. Wang, *Organometallics* **2011**, *30*, 5233–5247.

[46] H. Li, X. Wang, M. Wen, Z. Wang, *Eur. J. Inorg. Chem.* **2012**, *2012*, 5011–5020.

[47] B. G. Reed-Berendt, K. Polidano, L. C. Morrill, *Org. Biomol. Chem.* **2019**, *17*, 1595–1607.

[48] S. Rösler, M. Ertl, T. Irrgang, R. Kempe, *Angew. Chem. Int. Ed.* **2015**, *54*, 15046–15050.

[49] S. P. Midya, J. Pitchaimani, V. G. Landge, V. Madhu, E. Balaraman, *Catal. Sci. Technol.* **2018**, *8*, 3469–3473.

[50] A. Takallou, N. Mesgarsaravi, S. S. Beigbaghlou, N. Sakhaee, A. Z. Halimehjani, *Asian J. Org. Chem.* **2021**, *10*, 506–536.

[51] S. Elangovan, J. Neumann, J.-B. Sortais, K. Junge, C. Darcel, M. Beller, *Nat. Commun.* **2016**, *7*, 12641.

[52] K. Azizi, S. Akrami, R. Madsen, *Chem. Eur. J.* **2019**, *25*, 6439–6446.

[53] W. M. C. Sameera, F. Maseras, *Wiley Interdiscip. Rev. Comput. Mol. Sci.* **2012**, *2*, 375–385.

[54] S. Chakraborty, P. O. Lagaditis, M. Förster, E. A. Bielinski, N. Hazari, M. C. Holthausen, W. D. Jones, S. Schneider, *ACS Catal.* **2014**, *4*, 3994–4003.

[55] D. H. Nguyen, X. Trivelli, F. Capet, J.-F. Paul, F. Dumeignil, R. M. Gauvin, *ACS Catal.* **2017**, *7*, 2022–2032.

[56] G. Henrici-Olivé, S. Olivé, *Angew. Chem. Int. Ed. Engl.* **1976**, *15*, 136–141.

[57] M. E. Dry, *Catal. Today.* **2002**, *71*, 227–241.

[58] R. Schlögl, *Angew. Chem. Int. Ed.* **2003**, *42*, 2004–2008.

[59] A. Fürstner, *ACS. Cent. Sci.* **2016**, *2*, 778–789.

[60] K. S. Egorova, V. P. Ananikov, *Angew. Chem. Int. Ed.* **2016**, *55*, 12150–12162.

[61] W. M. Haynes, *CRC Handbook of Chemistry and Physics*, CRC Press, **2016**.

[62] E. Balaraman, A. Nandakumar, G. Jaiswal, M. K. Sahoo, *Catal. Sci. Technol.* **2017**, *7*, 3177–3195.

[63] T. Yan, B. L. Feringa, K. Barta, *ACS Catal.* **2016**, *6*, 381–388.

[64] T. Yan, B. L. Feringa, K. Barta, *Nat. Commun.* **2014**, *5*, 5602.

[65] G. Bottari, A. Afanasenko, A. A. Castillo-Garcia, B. L. Feringa, K. Barta, *Adv. Synth. Catal.* **2021**, *363*, 5436–5442.

[66] S. Chakraborty, W. W. Brennessel, W. D. Jones, *J. Am. Chem. Soc.* **2014**, *136*, 8564–8567.

[67] S. Weber, J. Brünig, V. Zeindlhofer, C. Schröder, B. Stöger, A. Limbeck, K. Kirchner, K. Bica, *ChemCatChem* **2018**, *10*, 4386–4394.

[68] M. Mastalir, B. Stöger, E. Pittenauer, M. Puchberger, G. Allmaier, K. Kirchner, *Adv. Synth. Catal.* **2016**, *358*, 3824–3831.

[69] M. Mastalir, M. Glatz, N. Gorgas, B. Stöger, E. Pittenauer, G. Allmaier, L. F. Veiros, K. Kirchner, *Chem. Eur. J.* **2016**, *22*, 12316–12320.

[70] M. Peña-López, H. Neumann, M. Beller, *ChemCatChem* **2015**, *7*, 865–871.

[71] S. Budweg, Z. Wei, H. Jiao, K. Junge, M. Beller, *ChemSusChem* **2019**, *12*, 2988–2993.

[72] E. Alberico, P. Sponholz, C. Cordes, M. Nielsen, H.-J. Drexler, W. Baumann, H. Junge, M. Beller, *Angew. Chem. Int. Ed.* **2013**, *52*, 14162–14166.

[73] S. Chakraborty, H. Dai, P. Bhattacharya, N. T. Fairweather, M. S. Gibson, J. A. Krause, H. Guan, *J. Am. Chem. Soc.* **2014**, *136*, 7869–7872.

[74] R. Langer, G. Leitus, Y. Ben-David, D. Milstein, *Angew. Chem. Int. Ed.* **2011**, *50*, 2120–2124.

[75] D. E. Prokopchuk, R. H. Morris, *Organometallics* **2012**, *31*, 7375–7385.

[76] W. Zuo, D. E. Prokopchuk, A. J. Lough, R. H. Morris, *ACS Catal.* **2016**, *6*, 301–314.

[77] A. A. Mikhailine, M. I. Maishan, A. J. Lough, R. H. Morris, *J. Am. Chem. Soc.* **2012**, *134*, 12266–12280.

[78] K. Z. Demmans, C. S. G. Seo, A. J. Lough, R. H. Morris, *Chem. Sci.* **2017**, *8*, 6531–6541.

[79] C. Sui-Seng, F. N. Haque, A. Hadzovic, A.-M. Pütz, V. Reuss, N. Meyer, A. J. Lough, M. Zimmer-De Iuliis, R. H. Morris, *Inorg. Chem.* **2009**, *48*, 735–743.

[80] W. Zuo, A. J. Lough, Y. F. Li, R. H. Morris, *Science* **2013**, *342*, 1080–1083.

[81] P. J. Bonitatibus, S. Chakraborty, M. D. Doherty, O. Siclovan, W. D. Jones, G. L. Soloveichik, *Proc. Natl. Acad. Sci. U.S.A.* **2015**, *112*, 1687–1692.

[82] H. Song, B. Kang, S. H. Hong, *ACS Catal.* **2014**, *4*, 2889–2895.

[83] M. Minakawa, M. Okubo, M. Kawatsura, *Bull. Chem. Soc. Jpn.* **2015**, *88*, 1680–1682.

[84] S. Enthaler, B. Spilker, G. Erre, K. Junge, M. K. Tse, M. Beller, *Tetrahedron* **2008**, *64*, 3867–3876.

[85] G. Jaiswal, V. G. Landge, D. Jagadeesan, E. Balaraman, *Nat. Commun.* **2017**, *8*, 2147.

[86] G. Jaiswal, V. G. Landge, D. Jagadeesan, E. Balaraman, *Green Chem.* **2016**, *18*, 3232–3238.

[87] M. Nallagangula, C. Sujatha, V. T. Bhat, K. Namitharan, *Chem. Comm.* **2019**, *55*, 8490–8493.

[88] R. Martínez, D. J. Ramón, M. Yus, *Org. Biomol. Chem.* **2009**, *7*, 2176.

[89] S. Verma, S. Kujur, R. Sharma, D. D. Pathak, *ACS Omega* **2022**, *7*, 9754–9764.

[90] B. J. Gregori, F. Schwarzhuber, S. Pöllath, J. Zweck, L. Fritsch, R. Schoch, M. Bauer, A. Jacobi von Wangelin, *ChemSusChem* **2019**, *12*, 3864–3870.

[91] C. Bäumler, C. Bauer, R. Kempe, *ChemSusChem* **2020**, *13*, 3110–3114.

[92] M. Subaramanian, G. Sivakumar, E. Balaraman, *Chem Rec* **2021**, *21*, 3839–3871.

[93] J. F. Sonnenberg, N. Coombs, P. A. Dube, R. H. Morris, *J. Am. Chem. Soc.* **2012**, *134*, 5893–5899.

[94] J. F. Sonnenberg, R. H. Morris, *Catal. Sci. Technol.* **2014**, *4*, 3426–3438.

[95] M. D. Hobday, T. D. Smith, *Coord. Chem. Rev.* **1973**, *9*, 311–337.

[96] P. Pfeiffer, E. Breith, E. Lübbe, T. Tsumaki, *Liebigs Ann.* **1933**, *503*, 84–130.

[97] M. Gerloch, F. E. Mabbs, *J. Chem. Soc. A* **1967**, 1598–1608.

[98] M. Gerloch, J. Lewis, F. E. Mabbs, A. Richards, *Nature* **1966**, *212*, 809–810.

[99] M. Gerloch, J. Lewis, F. E. Mabbs, A. Richards, *J. Chem. Soc. A* **1968**, 112–116.

[100] R. B. Lauffer, R. H. Heistand, L. Que, *Inorg. Chem.* **1983**, *22*, 50–55.

[101] P. Coggon, A. T. McPhail, F. E. Mabbs, V. N. McLachlan, *J. Chem. Soc. A* **1971**, 1014–1019.

[102] T. Kurahashi, K. Oda, M. Sugimoto, T. Ogura, H. Fujii, *Inorg. Chem.* **2006**, *45*, 7709–7721.

[103] T. M. Ross, S. M. Neville, D. S. Innes, D. R. Turner, B. Moubaraki, K. S. Murray, *Dalton Trans.* **2010**, *39*, 149–159.

[104] D. J. Harding, P. Harding, W. Phonsri, *Coord. Chem. Rev.* **2016**, *313*, 38–61.

[105] L. Borer, L. Thalken, C. Ceccarelli, M. Glick, J. H. Zhang, W. M. Reiff, *Inorg. Chem.* **1983**, *22*, 1719–1724.

[106] R. Viswanathan, M. Palaniandavar, P. Prabakaran, P. T. Muthiah, *Inorg. Chem.* **1998**, *37*, 3881–3884.

[107] J. B. H. Strautmann, C.-G. Freiherr von Richthofen, G. Heinze-Brückner, S. DeBeer, E. Bothe, E. Bill, T. Weyhermüller, A. Stammler, H. Bögge, T. Glaser, *Inorg. Chem.* **2011**, *50*, 155–171.

[108] C. J. Whiteoak, R. Torres Martin de Rosales, A. J. P. White, G. J. P. Britovsek, *Inorg. Chem.* **2010**, *49*, 11106–11117.

[109] N. S. B. Hansen, F. Monda, F. S. Bro, X. Liu, M. S. G. Ahlquist, R. Madsen, *Org. Biomol. Chem.* **2023**, *21*, 4794 – 4800.

[110] L. Carneiro, A. R. Silva, *Catal. Sci. Technol.* **2016**, *6*, 8166–8176.

[111] F. Monda, First-Row Transition Metal-Catalyzed Dehydrogenation Reactions, Ph.D. thesis, Technical University of Denmark, **2019**.

[112] C. P. Casey, S. W. Singer, D. R. Powell, R. K. Hayashi, M. Kavana, *J. Am. Chem. Soc.* **2001**, *123*, 1090–1100.

[113] N. Sieffert, R. Réocreux, P. Lorusso, D. J. Cole-Hamilton, M. Bühl, *Chem. Eur. J.* **2014**, *20*, 4141–4155.

[114] J. B. Johnson, J.-E. Bäckvall, *J. Org. Chem.* **2003**, *68*, 7681–7684.

[115] C. S. Yi, Z. He, I. A. Guzei, *Organometallics* **2001**, *20*, 3641–3643.

[116] K. Azizi, R. Madsen, *Chem. Sci.* **2020**, *11*, 7800–7806.

[117] J. P. Barham, G. Coulthard, K. J. Emery, E. Doni, F. Cumine, G. Nocera, M. P. John, L. E. A. Berlouis, T. McGuire, T. Tuttle, J. A. Murphy, *J. Am. Chem. Soc.* **2016**, *138*, 7402–7410.

[118] K. Emery, A. Young, J. Arokianathar, T. Tuttle, J. Murphy, *Molecules* **2018**, *23*, 1055.

[119] F. Neese, *Wiley Interdiscip. Rev. Comput. Mol. Sci.* **2018**, *8*, DOI 10.1002/wcms.1327.

[120] A. D. Becke, *J. Chem. Phys.* **1993**, *98*, 5648–5652.

[121] C. Lee, W. Yang, R. G. Parr, *Phys. Rev. B* **1988**, *37*, 785–789.

[122] J. Sirirak, D. Sertphon, W. Phonsri, P. Harding, D. J. Harding, *Int. J. Quantum. Chem.* **2017**, *117*, e25362.

[123] P. Verma, Z. Varga, J. E. M. N. Klein, C. J. Cramer, L. Que, D. G. Truhlar, *Phys. Chem. Chem. Phys.* **2017**, *19*, 13049–13069.

[124] M. A. Blagov, V. B. Krapivin, S. V. Simonov, N. G. Spitsyna, *Dalton Trans.* **2018**, *47*, 16040–16043.

[125] D. Coskun, S. V. Jerome, R. A. Friesner, *J. Chem. Theory. Comput.* **2016**, *12*, 1121–1128.

[126] C. Adamo, V. Barone, *J. Chem. Phys.* **1999**, *110*, 6158–6170.

[127] J. P. Perdew, K. Burke, M. Ernzerhof, *Phys. Rev. Lett.* **1996**, *77*, 3865–3868.

[128] N. C. Handy, A. J. Cohen, *Mol. Phys.* **2001**, *99*, 403–412.

[129] M. Swart, *J. Chem. Theory. Comput.* **2008**, *4*, 2057–2066.

[130] M. Swart, A. W. Ehlers, K. Lammertsma, *Mol. Phys.* **2004**, *102*, 2467–2474.

[131] D. J. Darensbourg, C. G. Ortiz, D. R. Billodeaux, *Inorganica Chim. Acta* **2004**, *357*, 2143–2149.

[132] M. Gerloch, E. D. McKenzie, A. D. C. Towl, *J. Chem. Soc. A* **1969**, 2850–2858.

[133] J. F. Sonnenberg, D. Pichugin, N. Coombs, R. H. Morris, *Top. Catal.* **2013**, *56*, 1199–1207.

[134] J. F. Sonnenberg, R. H. Morris, *ACS Catal.* **2013**, *3*, 1092–1102.

[135] P. Foley, R. DiCosimo, G. M. Whitesides, *J. Am. Chem. Soc.* **1980**, *102*, 6713–6725.

[136] D. R. Anton, R. H. Crabtree, *Organometallics* **1983**, *2*, 855–859.

[137] X. Cui, Y. Li, S. Bachmann, M. Scalone, A.-E. Surkus, K. Junge, C. Topf, M. Beller, *J. Am. Chem. Soc.* **2015**, *137*, 10652–10658.

[138] T. L. Andersen, A. S. Donslund, K. T. Neumann, T. Skrydstrup, *Angew. Chem. Int. Ed.* **2018**, *57*, 800–804.

[139] S. Grimme, S. Ehrlich, L. Goerigk, *J. Comput. Chem.* **2011**, *32*, 1456–1465.

[140] F. Weigend, R. Ahlrichs, *Phys. Chem. Chem. Phys.* **2005**, *7*, 3297.

[141] A. V. Marenich, C. J. Cramer, D. G. Truhlar, *J. Phys. Chem. B* **2009**, *113*, 6378–6396.

[142] A. D. Bochevarov, E. Harder, T. F. Hughes, J. R. Greenwood, D. A. Braden, D. M. Philipp, D. Rinaldo, M. D. Halls, J. Zhang, R. A. Friesner, *Int. J. Quantum. Chem.* **2013**, *113*, 2110–2142.

[143] S. Grimme, J. Antony, S. Ehrlich, H. Krieg, *J. Chem. Phys.* **2010**, *132*, 154104.

[144] A. V. Marenich, R. M. Olson, C. P. Kelly, C. J. Cramer, D. G. Truhlar, *J. Chem. Theory. Comput.* **2007**, *3*, 2011–2033.

[145] Y. Miao, S. V. Samuelsen, R. Madsen, *Organometallics* **2021**, *40*, 1328–1335.

[146] F. Kallmeier, R. Fertig, T. Irrgang, R. Kempe, *Angew. Chem. Int. Ed.* **2020**, *59*, 11789–11793.

[147] Y. Miao, 3d Transition Metal Catalyzed Dehydrogenation of Alcohols, Ph.D. thesis, Technical University of Denmark, **2021**.

[148] F. H. Westheimer, *Chem. Rev.* **1949**, *45*, 419–451.

[149] R. Ratcliffe, R. Rodehorst, *J. Org. Chem.* **1970**, *35*, 4000–4002.

[150] J. C. Collins, W. W. Hess, F. J. Frank, *Tetrahedron Lett.* **1968**, *9*, 3363–3366.

[151] E. J. Corey, G. Schmidt, *Tetrahedron Lett.* **1979**, *20*, 399–402.

[152] E. J. Corey, J. W. Suggs, *Tetrahedron Lett.* **1975**, *16*, 2647–2650.

[153] M. Costa, *Crit. Rev. Toxicol.* **1997**, *27*, 431–442.

[154] D. G. Barceloux, *J. Toxicol. Clin. Toxicol.* **1999**, *37*, 173–194.

[155] R. A. Sheldon, I. W. C. E. Arends, G.-J. ten Brink, A. Dijksman, *Acc. Chem. Res.* **2002**, *35*, 774–781.

[156] M. Trincado, J. Bösken, H. Grützmacher, *Coord. Chem. Rev.* **2021**, *443*, 213967.

[157] F. Bottaro, R. Madsen, *ChemCatChem* **2019**, *11*, 2707–2712.

[158] F. Bottaro, A. Takallou, A. Chehaiber, R. Madsen, *Eur. J. Org. Chem.* **2019**, *2019*, 7164–7168.

[159] K. Azizi, R. Madsen, *ChemCatChem* **2018**, *10*, 3703–3708.

[160] R. F. Schulte, *2017 Minerals Yearbook − Chromium*, US Geological Survey, Reston, VA, **2020**.

[161] M. Weller, T. Overton, J. Rourke, F. Armstrong, *Inorganic Chemistry*, Oxford University Press, London, England, **2014**.

[162] P. G. Cozzi, *Chem. Soc. Rev.* **2004**, *33*, 410–421.

[163] T. L. DesMarias, M. Costa, *Curr. Opin. Toxicol.* **2019**, *14*, 1–7.

[164] T. Pavesi, J. C. Moreira, *J. Appl. Toxicol.* **2020**, *40*, 1183–1197.

[165] A. Levina, P. A. Lay, *Chem. Res. Toxicol.* **2008**, *21*, 563–571.

[166] N. S. Raja, B. Unni. Nair, *Toxicology* **2008**, *251*, 61–65.

[167] E. G. Samsel, K. Srinivasan, J. K. Kochi, *J. Am. Chem. Soc.* **1985**, *107*, 7606–7617.

[168] K. Srinivasan, J. K. Kochi, *Inorg. Chem.* **1985**, *24*, 4671–4679.

[169] C. Bousquet, D. G. Gilheany, *Tetrahedron Lett.* **1995**, *36*, 7739–7742.

[170] C. T. Dalton, K. M. Ryan, V. M. Wall, C. Bousquet, D. G. Gilheany, *Top. Catal.* **1998**, *5*, 75–91.

[171] J. F. Larrow, S. E. Schaus, E. N. Jacobsen, *J. Am. Chem. Soc.* **1996**, *118*, 7420–7421.

[172] B. D. Brandes, E. N. Jacobsen, *Synlett* **2011**, 1013–1015.

[173] L. E. Martinez, J. L. Leighton, D. H. Carsten, E. N. Jacobsen, *J. Am. Chem. Soc.* **1995**, *117*, 5897–5898.

[174] W. Adam, F. G. Gelalcha, C. R. Saha-Möller, V. R. Stegmann, *J. Org. Chem.* **2000**, *65*, 1915–1918.

[175] Y. Nieves-Quinones, T. J. Paniak, Y. E. Lee, S. M. Kim, S. Tcyrulnikov, M. C. Kozlowski, *J. Am. Chem. Soc.* **2019**, *141*, 10016–10032.

[176] R. L. Paddock, S. T. Nguyen, *J. Am. Chem. Soc.* **2001**, *123*, 11498–11499.

[177] Donald. J. Darensbourg, R. M. Mackiewicz, J. L. Rodgers, C. C. Fang, D. R. Billodeaux, J. H. Reibenspies, *Inorg. Chem.* **2004**, *43*, 6024–6034.

[178] D. J. Darensbourg, J. C. Yarbrough, *J. Am. Chem. Soc.* **2002**, *124*, 6335–6342.

[179] D. J. Darensbourg, R. M. Mackiewicz, J. L. Rodgers, A. L. Phelps, *Inorg. Chem.* **2004**, *43*, 1831–1833.

[180] B. Li, G.-P. Wu, W.-M. Ren, Y.-M. Wang, D.-Y. Rao, X.-B. Lu, *J. Polym. Sci. A Polym. Chem.* **2008**, *46*, 6102–6113.

[181] D. J. Darensbourg, M. Ulusoy, O. Karroonnirum, R. R. Poland, J. H. Reibenspies, B. Çetinkaya, *Macromolecules* **2009**, *42*, 6992–6998.

[182] T. Katsuki, *Chem. Soc. Rev.* **2004**, *33*, 437.

[183] K. Matsumoto, B. Saito, T. Katsuki, *Chem. Comm.* **2007**, 3619.

[184] F. Lloret, M. Julve, M. Mollar, I. Castro, J. Latorre, J. Faus, X. Solans, I. Morgenstern-Badarau, *J. Chem. Soc., Dalton Trans.* **1989**, 729–738.

[185] D. J. Darensbourg, E. B. Frantz, J. R. Andreatta, *Inorganica Chim. Acta* **2007**, *360*, 523–528.

[186] M. Ohba, H. Tamaki, N. Matsumoto, H. Okawa, *Inorg. Chem.* **1993**, *32*, 5385–5390.

[187] P. Coggon, A. T. McPhail, F. E. Mabbs, A. Richards, A. S. Thornley, *J. Chem. Soc. A* **1970**, 3296–3303.

[188] B. Liu, J. Chai, S. Feng, B. Yang, *Spectrochim. Acta A Mol. Biomol. Spectrosc.* **2015**, *140*, 437–443.

[189] D. J. Darensbourg, in *Synthetic Biodegradable Polymers*, Springer, Berlin, Heidelberg, **2012**, pp. 1–27.

[190] A. Böttcher, H. Elias, J. Glerup, M. Neuburger, C. E. Olsen, H. Paulus, J. Springborg, M. Zehnder, G. W. Francis, *Acta Chem. Scand.* **1994**, *48*, 967–980.

[191] H. Golchoubian, L. Rostami, B. Kariuki, *Polyhedron* **2010**, *29*, 1525–1533.

[192] A. Böttcher, H. Elias, J. Glerup, M. Neuburger, C. E. Olsen, J. Springborg, H. Weihe, M. Zehnder, G. W. Francis, *Acta Chem. Scand.* **1994**, *48*, 981–988.

[193] S.-W. Lee, S. Chang, D. Kossakovski, H. Cox, J. L. Beauchamp, *J. Am. Chem. Soc.* **1999**, *121*, 10152–10156.

[194] M. K. Kumar, S. Prabhakar, M. R. Kumar, T. J. Reddy, S. Premsingh, S. Rajagopal, M. Vairamani, *Rapid Commun. Mass Spectrom.* **2004**, *18*, 1103–1108.

[195] D.-Y. Rao, B. Li, R. Zhang, H. Wang, X.-B. Lu, *Inorg. Chem.* **2009**, *48*, 2830–2836.

[196] D. J. Darensbourg, A. D. Yeung, *Polym. Chem.* **2015**, *6*, 1103–1117.

[197] D. J. Darensbourg, A. I. Moncada, W. Choi, J. H. Reibenspies, *J. Am. Chem. Soc.* **2008**, *130*, 6523–6533.

[198] E. W. Ainscough, A. G. Bingham, A. M. Brodie, J. M. Husbands, J. E. Plowman, *J. Chem. Soc., Dalton Trans.* **1981**, 1701.

[199] P. D. Knight, P. Scott, *Coord. Chem. Rev.* **2003**, *242*, 125–143.

[200] J. C. Pessoa, I. Correia, *Coord. Chem. Rev.* **2019**, *388*, 227–247.

[201] L. Chiang, L. E. N. Allan, J. Alcantara, M. C. P. Wang, T. Storr, M. P. Shaver, *Dalton Trans.* **2014**, *43*, 4295–4304.

[202] A. Ben Jrad, H. Kanso, D. Raviglione, T. Noguer, N. Inguimbert, C. Calas-Blanchard, *Chem. Comm.* **2019**, *55*, 12821–12824.

[203] R. Sanzenbacher, A. Böttcher, H. Elias, M. Hüber, W. Haase, J. Glerup, T. B. Jensen, M. Neuburger, M. Zehnder, J. Springborg, C. E. Olsen, *Inorg. Chem.* **1996**, *35*, 7493–7499.

[204] C. Kleeberg, *Z. Anorg. Allg. Chem.* **2011**, *637*, 1790–1794.

[205] S. L. H. Pedersen, Chromium-Catalyzed Dehydrogenation of Alcohols, Master's Thesis, Technical University of Denmark, **2023**.

[206] A. P. Bruins, *J. Chromatogr. A* **1998**, *794*, 345–357.

[207] E. M. McGarrigle, D. G. Gilheany, *Chem. Rev.* **2005**, *105*, 1563–1602.

[208] T. Wu, T. Wang, L. Sun, K. Deng, W. Deng, R. Lu, *ChemistrySelect* **2017**, *2*, 4533–4537.

[209] G. A. Luinstra, G. R. Haas, F. Molnar, V. Bernhart, R. Eberhardt, B. Rieger, *Chem. Eur. J.* **2005**, *11*, 6298–6314.

[210] A. Thevenon, A. Cyriac, D. Myers, A. J. P. White, C. B. Durr, C. K. Williams, *J. Am. Chem. Soc.* **2018**, *140*, 6893–6903.

[211] F. P. Ballistreri, L. Brinchi, R. Germani, G. Savelli, G. A. Tomaselli, R. M. Toscano, *Tetrahedron* **2008**, *64*, 10239–10243.

[212] M. Sanz, T. Cuenca, M. Galakhov, A. Grassi, R. K. J. Bott, D. L. Hughes, S. J. Lancaster, M. Bochmann, *Organometallics* **2004**, *23*, 5324–5331.

[213] X. Yao, M. Qiu, W. Lü, H. Chen, Z. Zheng, *Tetrahedron Asymmetry* **2001**, *12*, 197–204.

[214] T. Achard, Y. N. Belokon', J. A. Fuentes, M. North, T. Parsons, *Tetrahedron* **2004**, *60*, 5919–5930.

[215] T. A. Immel, M. Grützke, E. Batroff, U. Groth, T. Huhn, *J. Inorg. Biochem.* **2012**, *106*, 68–75.

[216] M. Klarner, P. Blach, H. Wittkämper, N. Jonge, C. Papp, R. Kempe, *ChemCatChem* **2021**, *13*, 3257–3261.

[217] N. Otto, T. Opatz, *Beilstein J. Org. Chem.* **2012**, *8*, 1105–1111.

[218] X. Zhao, D. Zhang, R. Yu, S. Chen, D. Zhao, *Eur. J. Inorg. Chem.* **2018**, *2018*, 1185–1191.

[219] A. Kechiche, T. Fradi, O. Noureddine, M. Guergueb, F. Loiseau, V. Guerineau, N. Issoui, A. Lemeune, H. Nasri, *J. Mol. Struct.* **2022**, *1250*, 131801.

[220] A. L. Balch, L. Latos-Grazynski, B. C. Noll, M. M. Olmstead, E. P. Zovinka, *Inorg. Chem.* **1992**, *31*, 1148–1151.

[221] D. A. Summerville, R. D. Jones, B. M. Hoffman, F. Basolo, *J. Am. Chem. Soc.* **1977**, *99*, 8195–8202.

[222] J. T. Groves, W. J. Kruper, *J. Am. Chem. Soc.* **1979**, *101*, 7613–7615.

[223] T. G. Traylor, A. R. Miksztal, *J. Am. Chem. Soc.* **1989**, *111*, 7443–7448.

[224] O. M. Chukanova, G. P. Belov, *Kinet. Catal.* **2017**, *58*, 397–401.

[225] S. Mang, A. I. Cooper, M. E. Colclough, N. Chauhan, A. B. Holmes, *Macromolecules* **2000**, *33*, 303–308.

[226] T. Takanami, M. Hayashi, K. Suda, *Tetrahedron Lett.* **2005**, *46*, 2893–2896.

[227] R. Wakabayashi, T. Kurahashi, S. Matsubara, *Synlett* **2013**, *24*, 2297–2301.

[228] J. Muzart, *Chem. Rev.* **1992**, *92*, 113–140.

[229] N. Schaefle, R. Sharp, *J. Phys. Chem. A* **2005**, *109*, 3276–3284.

[230] J. W. Buchler, in *The Porphyrins*, Elsevier, **1978**, pp. 389–483.

[231] S. Jeon, T. C. Bruice, *Inorg. Chem.* **1991**, *30*, 4311–4315.